Experimental modeling of sloshing at small-scale
Relevance at full-scale through analysis of the physics of impacts

Karimi, Reza

DOI
10.4233/uuid:f1498c73-5caa-4858-904b-7cbbf9c04d9b

Publication date
2017

Document Version
Final published version

Citation (APA)
Karimi, R. (2017). *Experimental modeling of sloshing at small-scale: Relevance at full-scale through analysis of the physics of impacts*. [Dissertation (TU Delft), Delft University of Technology]. https://doi.org/10.4233/uuid:f1498c73-5caa-4858-904b-7cbbf9c04d9b

Experimental Modeling of Sloshing at Small-Scale:

Relevance at Full-Scale
Through Analysis of the Physics of Impacts

M.R. Karimi

Experimental Modeling of Sloshing at Small-Scale: *Relevance at Full-Scale Through Analysis of the Physics of Impacts* M.R. Karimi

Experimental Modeling of Sloshing at Small-Scale:

Relevance at Full-Scale Through Analysis of the Physics of Impacts

Proefschrift

ter verkrijging van de graad van doctor
aan de Technische Universiteit Delft,
op gezag van de Rector Magnificus prof. Prof. ir. K.C.A.M. Luyben
voorzitter van het College voor Promoties,
in het openbaar te verdedigen op
donderdag 6 juli 2017 om 10:00 uur

Door

Mohammad Reza KARIMI
Master of Science in Offshore and Dredging Engineering
geboren te Zanjan, Iran

This dissertation has been approved by the:

promotor: Prof. dr. ir. M.L. Kaminski and
promotor: Prof. J.-M. Ghidaglia

Composition of the doctoral committee:

Rector Magnificus Prof. ir. K.C.A.M. Luyben, TU Delft
Prof. dr. ir. M.L. Kaminski (promotor), TU Delft
Prof. J.-M. Ghidaglia (promotor), ENS Paris-Saclay-CMLA
Prof. dr. ir. A.P. van 't Veer, TU Delft

Independent members:

Prof. O.M. Faltinsen, Norwegian University of Science and Technology (NTNU)
Prof. F. Dias, University College Dublin (UCD)
Dr. O. Kimmoun, École centrale de Marseille (ECM)
Prof. dr. ir. B. Koren, Technische Universiteit Eindhoven (TU/e)

The doctoral research has been carried out in the context of an agreement on joint doctoral supervision between École normale supérieure Paris-Saclay, Cachan, France and Delft University of Technology, the Netherlands.

To Farhad and Akhtar

To Elnaz and Niki Shirin

Contents

Chapter 1

Introduction

LNG sloshing and its dynamic loads on the containment system are of importance for LNG shipping industry. The applied loads must not lead to any damage or serious deformation which could endanger the structural integrity or serviceability of the containment system or the LNG carrying vessel. The common goal of the designers of containment system technologies as well as the class societies which verify and approve of such designs is to make sure that the installed structures offer safe and conservative solutions to LNG transport challenges. LNG carrier owners as well as owners of the vessels in which LNG is used as fuel are as well mindful of the potential risks and try to avoid the catastrophic conditions that their vessels might face due to sloshing impacts.

Sloshing loads are highly variable and full-scale loads on the containment system have not yet been measured very accurately (an attempt to do so has been described by Pasquier and Berthon [2009]). Even if such loads are measured accurately the associated variability cannot be addressed properly since the same voyage cannot be exactly repeated. Due to the variability of sloshing loads deterministic estimations are not considered to be realistic. Sloshing load variability is due to different phenomena which are not mastered completely. Partial lack of knowledge about physical phenomena which influence sloshing and variability of sloshing loads leave no better choice than the use of probabilistic methods based on model test results at smaller scales. Such small-scale tests are convenient and each test can be repeated several times in order to address variability of sloshing loads and achieve a certain convergence (depending on how such convergence is defined). The details of how sloshing model tests should be performed are frequently mentioned in the literature Gervaise et al. [2009], Kuo et al. [2009], LR [2009] ,BV [2011] and DNV [2014] and are not repeated here.

When sloshing loads of model tests performed at small-scale are used to esti-

mate sloshing loads at full-scale, serious assumptions are made. Most importantly it is assumed that model tests at small-scale are relevant or at least conservative after applying a proper scale factor. Even though those assumptions are made, in practice there is an awareness concerning involved biases that exist which can (and will) distort the estimations. To work around part of those problems and mainly for classical ship and tank designs and after estimation of the loads at full-scale based on model test results, a more practical scale factor based on feedback at sea is applied to the measured loads. For less classical designs the scale factor found from dimensional analysis is used. The tolerated fill levels for the LNG carrier tanks are taken to be 0%-10% and 70%-98% of the tank height for the three membrane CCS NO96, MarkIII and CS1 according to BV [2011]. The uncertainty about sloshing loads, relevance of the model tests and load scale factors leads to serious limitations in serviceability of the vessels.

The goal of this study has been to bring insight on sloshing through experimental studies i.e. sloshing model tests. The first issue to be addressed was: *the relevance of model tests*. The model tests at small-scale are supposed to model sloshing at full-scale. Those model tests should satisfy similarity laws and provide measurements that can be translated into full-scale loads. If the tests do not satisfy basic similarity requirements they should be abandoned or at least the degree of bias should be determined.

Secondly and being aware of some of the biases that could interfere the question was: *To what extent are the model test results distorted and biased?* A complete answer to this question would have given an idea about how those biases should be dealt with or compensated. It was clear from the beginning that there would be multiple biases caused by multiple phenomena that had to be taken care of separately. Nevertheless even the sum of all those biases if measured would be considered quite valuable.

The third issue was considering *the variability of sloshing loads*. These loads can only be dealt with as statistical distributions and not absolute values.

The last question was *How answers to the previous questions could help improve or modify the current sloshing assessment methodologies?* In order to address the raised questions it was necessary to start from the end or in other words the sloshing assessment methodology. The current sloshing assessment methodologies combine the latest findings about sloshing physics and statistics, practical limitations and engineering shortcuts that are tolerated among the specialists after all.

There were several reasons for being critical towards the current sloshing assessment methodology which can be summarized as,

– No study regarding the relevance of model tests with full-scale has ever been performed which could decisively prove that sloshing model tests are justified. One problem is due to the lack of exact repetitions of full-scale sea

states which makes it impossible to study variability of full-scale sloshing loads. A workaround is to make a sample of pressures over time equivalent of the sample for each impact. This seems to be the only possible way to study the full-scale results but during model tests the impacts must be studied in a more careful way,

– With the assumption of partial relevance and in order to study sloshing loads due to each sea state, speed and heading that a ship will encounter throughout her lifetime, scaled tank motions due to that condition are applied to the model tanks with the same fill level. The tests are repeated a couple of times each to have better statistical convergence. Due to the large variability of impact pressures, multiple repetitions are needed to achieve convergence. Those repetitions are time consuming and as a result finding a faster approach would be beneficial. This potentially faster approach should not of course reduce the accuracy of load estimation which would consequently lead to less certainty about the structural integrity of the containment system,

– In studying the loads caused by every sea state, the repetitions are performed to have better statistical convergence. The question would be that are the long repetitions enough for reaching the desired convergence,

– In making the collections of pressure peaks out of many repetitions of long tests, data obtained from different impact types with potentially different statistics are mixed together. Flip-through, gas pocket, slosh and broken wave impacts seem not to be of the same intensity, variability and statistics and a statistical sample made by mixing the pressure peaks caused by different impact types might not be the best way to obtain relevant statistics,

– Scaling the impact pressures is a key step in studying the integrity of the LNG containment system. It is well known than there is no single scale factor for sloshing pressures caused by different phenomena (Bogaert et al. [2010b]). Scale factors are different and depend on the type of phenomena which cause the pressures. Too much information is lost when considering only the collection of all the pressure peaks from several repetitions of the same test including the impact types which are crucial as explained. After the mixture one scale factor is applied on all the pressure peaks and is supposed to make up for all the neglected phenomena.

One necessary step to address the cited issues was to perform sloshing model tests at different scales. For this purpose three scales of 1:10, 1:20 and 1:40 were chosen. Due to the advantage of observation and comparative simplicity of 2D tanks compared to 3D ones, all tests were envisaged to be performed in 2D. The

details of those model tests can be found repeatedly in the next chapters and are not mentioned here. The list of all the performed campaigns can be found in Table. 1.1.

Table 1.1. List of all of the 2D sloshing test campaigns performed in the framework of this PhD research

No.	Start Date	End Date	Scale	Highlights
1	04/11/2011	15/12/2011	1:10	Heaviest tank ever mounted in GTT
2	28/09/2012	29/01/2013	1:40	Start of testing different gases
3	31/05/2013	08/07/2013	1:20	Monitoring global flow
4	30/08/2013	03/10/2013	1:40	Database completion
5	14/03/2014	01/04/2014	1:20	Databse completion
4	08/09/2014	13/10/2014	1:40	Singularization tested successfully
7	17/07/2015	12/09/2015	1:20	Dedicated to singularization

After performing two initial comparisons which were basically based on the current methodology assumptions and were published in Karimi et al. [2013b] and Karimi et al. [2014b] the first independent study based on the aforementioned discussion was performed in order to monitor the proper scaling of global fluid flow between the model tests at two different scales of 1:20 and 1:40. This comparison was to investigate the very fundamental basis of sloshing model tests. There was also the possibility for changing the ullage gas and study the effect of gas-liquid density ratio on the global flow. Th results of this study are presented in Ch. 2 which is based on: *Effect of Ullage Gas on Sloshing - Part I. Global Effects of Gas-Liquid Density Ratio.* M. R. Karimi, L. Brosset, J.-M. Ghidaglia and M. L. Kaminski.European Journal of Mechanics - B/Fluids. Volume 53, September-October 2015, Pages 213-228. *doi:10.1016/j.euromechflu.2015.05.006*. In this chapter not only the global flow scaling is verified, it is used to find an impact by impact correlation between the model tests at two different scales. This is called then *impact coincidence* which can be used to track down any impact at any scale. The significance is because fundamentally in order for a model test to be relevant every impact in the model test should be properly scaled. In other words if a flip-through impact at real-scale becomes a broken wave at model test, the model test would be considered as (strictly) irrelevant.

After verifying the global flow scaling, the local flow right before the impact and before any interference from compressibility effects was considered. The influence of gas-liquid density ratio at this stage was studied with highly repeatable breaking waves and using different ullage gases. This study is summarized in Ch. 3 which is based completely on: *Effect of Ullage Gas on Sloshing - Part II. Local Effects of Gas-Liquid Density Ratio.* M. R. Karimi, L. Brosset, J.-M. Ghidaglia and M. L. Kaminski. European Journal of Mechanics - B/Fluids. Volume 57,

May-June 2016, Pages 82-100. *doi:10.1016/j.euromechflu.2015.11.011*. The original idea behind this study was to compare single impact waves (SIW) and the impact pressures at two different scales of 1:40 and 1:20 but due to the encountered complexities it was dedicated to demonstrate the local effects of gas-liquid density ratio and mainly based on the results at scale 1:20. It showed the clear role of DR on wave shape and geometry right before the impact. For the first time this the study confirmed previous numerical studies (see Braeunig et al. [2009]) that had demonstrated that keeping the same DR between the model-scale and full-scale is necessary to keep matching wave shapes and kinematics at both scales.

Ch. 4 addressed statistics of sloshing model tests at three different scales and specially at two scales of 1:20 and 1:40 where at each scale several different ullage gases were used. This chapter is based on : *Effects of Ullage Gas and Scale on Sloshing Loads.* M. R. Karimi, L. Brosset, M. L. Kaminski and J.-M. Ghidaglia. European Journal of Mechanics - B/Fluids. Volume 62, March-April 2017, Pages 59-85. *http://dx.doi.org/10.1016/j.euromechflu.2016.11.017*. Based on *Impact Coincidence* that was observed in Ch. 2, *Impact ID* is defined to compare impact pressures corresponding to the same ID but at different scales and with different ullage gases. Variability of sloshing loads as a function of ullage gas and scale is addressed. *Dominant IDs* are found and demonstrated. Some of the advantages of focusing on single IDs rather than the whole collections can be cited as:

- The main goal of any sloshing model test (or any model test in general) is to downscale the real phenomena which take place at full-scale. This would strictly mean that any breaking wave impact and all the physical phenomena should also be scaled. This has been proven to be impossible when the scale factor is large (Braeunig et al. [2009]). Studying wave impacts ID per ID enables more accurate comparisons of scaling biases which are involved,
- It makes it possible to focus on statistical and physical properties of every single impact alone rather than mixing impact pressures obtained from different impact types hence making the statistical analysis more relevant,
- Studying impact IDs separately would enable making a difference between severe impacts and impacts which are not as important from a structural point of view,
- If certain impacts are considered to be *dominant* and if those impacts can be generated independently (see Karimi et al. [2015a]) with short sequences of tank motions, sloshing analysis can be focused on those impacts which would in turn lead to less time consuming model tests and more repetitions or in other words more relevant statistics,

- Focusing on IDs makes another bridge between physics and statistics of sloshing assessment which could bring more insight about the involved phenomena. Without considering IDs too much information about the physics of impacts are lost and the only remaining way to study them will be through statistics,

- It challenges and consequently benefits the numerical simulation codes with thousands of different and complicated impact types that can be regenerated using those codes for validation purposes.

Ch. 5 studies the so called *dominant IDs* that were already introduced in ch. 4, more in detail. This chapter discusses that the loads due to every *impact ID* have a unique statistical distribution which is different from the distributions of the other IDs or a mixture of all IDs over time. It is shown that the dominant impacts can be used to estimate the ultimate sloshing loads rather than relying on extrapolations based on a few long model tests. This chapter is based on: *Dominant Impacts in Sloshing Model Tests.* M. R. Karimi, L. Brosset, M. L. Kaminski and J.-M. Ghidaglia which has been submitted to the European Journal of Mechanics - B/Fluids.

Having all the mentioned points in mind one difficulty was to show that regenerating every selected ID was possible with short sequences of tank motions rather than the complete long model test. Demonstrating this possibility was one thing but the outcomes would also open new doors to studying sloshing impacts. The struggle to define the envisaged challenges and demonstrate the outcomes are shown in the last chapter, Ch. 5. This chapter is based on: *Singularization of Sloshing Impacts.* M. R. Karimi, L. Brosset, M. L. Kaminski and J.-M. Ghidaglia which has also been submitted to the European Journal of Mechanics - B/Fluids. The statistical distributions of the same impact ID at two different scales of 1:20 and 1:40 are shown and compared. Since all the chapters in this document have been prepared based on papers, some repetitions especially in the test setup and introduction sections could not be avoided. I hope that this small attempt would be usable for the researchers of this field as well as the engineers who have to deal with similar issues regularly.

I want to take this chance to thank Dr. ir. Karim Shiati and Prof. dr. ir. Majid Hassanizadeh who inspired me and showed me the way.

I want to thank many individuals who helped me finalize this research. Firstly I would like to thank Laurent Brosset as a mentor, colleague and friend. Without his support and trust this study would never be possible. The memories of the nice discussions and conversations, casual or formal, technical or non-technical would always be with me. I thank my dear professors, Prof. Miroslaw Lech (Mirek) Kaminski and Prof. Jean-Michel Ghidaglia who were always unbelievably positive and helpful at every stage of this Ph.D. I would like to one by one thank

many colleagues and friends at Gaztransport&Technigaz (GTT), TU Delft, and the university of Paris-Saclay (ENS Cahchan) but the list is too long that if I start to mention names, it is certain that many will be forgotten. I am forever grateful and I humbly thank you all.

M.R. Karimi, Delft
June 27, 2017

Chapter 2

Global Effects of Gas-Liquid Density Ratio

Abstract

[1] Previous analytical, numerical, and experimental studies have proved that properties of ullage gas influence sloshing wave impacts and induced pressures. One of those properties is ullage gas density (ρ_g), also considered in dimensionless form as gas-liquid density ratio (DR). Previous studies intended to study the effects of DR sometimes mixed DR effects with gas compressibility and ullage gas pressure effects and attributed them only to DR. This study is based on experiments and is meant to focus only on the effects of DR far from impact zones which will be addressed as global effects. Effects of DR near impact zones and before detection of any compressibility effects are addressed as local effects and will be treated in part II. Quantitative and statistical comparisons will be presented in part III.

Test setup consisted of two 2D tanks as transverse slices of tank 2 of a membrane LNG carrier with total capacity of $152\,000\,\mathrm{m}^3$ at scales 1:20 and 1:40 at 20% fill level. Using two liquids of water and sodium polytungstate (SPT) and different ullage gases of helium (He), air, two mixtures of sulfur hexafluoride (SF_6) and nitrogen (N_2) , and pure SF_6, all at atmospheric pressure, provided a range of DRs from 0.0002 to 0.0060.

For the tested range of DR, the global effects of DR on sloshing geometry (free surface) are small when comparing at the same scale or at two different scales. Small discrepancies exist even between two exact repetitions with the same DR at the same scale. Global flow keeps the same phase regardless of tested DRs which implies that all breaking wave impacts take place at the exact same time instants, considering a small time window (usually smaller than 100 ms). This was confirmed by verifying the recorded impact times.

Based on this, scaling in sloshing model tests as well as the effect of changing the ullage gas can be investigated impact by impact as opposed to the solely statistical approaches adopted so far. It also helps to track down impacts measured at full-scale (on board the ship) and to

[1]This chapter is based on: *Effect of Ullage Gas on Sloshing - Part I. Global Effects of Gas-Liquid Density Ratio.* M. R. Karimi, L. Brosset, J.-M. Ghidaglia and M. L. Kaminski.European Journal of Mechanics - B/Fluids. Volume 53, September-October 2015, Pages 213-228. *doi:10.1016/j.euromechflu.2015.05.006*

further verify whether sloshing model tests are representative for them or not. The stochastic nature of sloshing can be studied more in depth also with the help of high-speed video recordings for corresponding wave impacts. Reevaluations of the current statistical sloshing assessment methodologies can be envisaged.

2.1 Introduction

Gas-liquid density ratio (DR) defined as, $DR = \rho_g/\rho_l$ where ρ_g is ullage gas density, and ρ_l is liquid density, is a dimensionless number of interest in studying sloshing wave impacts and induced pressures (see DNV [2014] and BV [2011]). So far the importance of DR for sloshing has been investigated by analytical works, numerical simulations, and sloshing model tests.

Dias et al. [2007] divide sloshing impacts on the wall into three categories of direct impact, jet flow and gas pocket impact. For each category, an analytical model is given and expressions to find impact pressures on the wall are proposed. This analytical approach does not explain several experimental observations as why impact pressures are generally less when heavy gases are used with water instead of air. The method does not differentiate between possibilities of different impact geometries due to different DR. In other words it is assumed that the geometry and impact category (gas pocket, direct impact, and jet effects) is identical while varying the DR.

Lee et al. [2007] did a sensitivity study at first to determine the most relevant dimensionless numbers in sloshing. The numerical simulations were performed by FLOW3D to model sloshing impacts for 25% and 50% fill levels with harmonic roll motion excitations. The study concludes that DR effect is not significant on dimensionless impact pressure. Further studies revealed that DR is on the contrary an important factor. Braeunig et al. [2009] simulated the free fall of a rectangular of liquid under gravity, surrounded by gas and inside a rectangular tank. The calculations were in 2D and done with compressible two-fluid software (FLUX-IC). The study shows that increasing the DR (varied in the range of $0.0001 \leq DR \leq 0.005$) reduces impact pressures significantly. It also shows that varying the DR changes the impact nature in such a way that small ratios lead to creation of shock waves in the liquid, while large ratios give more weight to gas compressibility and result in pressure oscillations. The study also suggests that for perfect scaling at model tests, other than respecting the same Froude number, DR must also be kept the same and liquid and gas compressibility at model test should be relevantly scaled. It is discussed that having liquids or gases with scaled compressibility is impractical. It is stated that keeping the same DR is possible using a heavy gas instead of air as ullage gas with water. Moreover as a heavy gas is generally more compressible than a light one (smaller speed of sound), the requirement on gas compressibility is better fulfilled with the heavy

gas and results would be more conservative. The study differentiates between the effect of DR and gas and liquid compressibility. It defines a theoretical basis for scaling with a simple geometry. In Scolan et al. [2014], a comparison between the wave shapes obtained before impact for a large breaking wave with the bi-fluid (water + air) and with the mono-fluid (water + vacuum) version of FSID code (see Scolan [2010]) was presented. The gas flow seems to impede slightly the breaking process leading to a delay of the wave front and a deviation upwards of the wave crest. Same trends were noticed by Guilcher et al. [2014] when comparing breaking wave shapes simulated on the one hand by a SPH bi-fluid solver and on the other hand by the mono-fluid version of FSID.

Several dedicated sloshing experiments have also been conducted to study the effects of DR. Maillard and Brosset [2009] explain such an experiment with different condensable and non-condensable gases covering a range of DRs. The studied range of DR was $0.00005 \leq DR \leq 0.0058$ and included water as liquid and vapor at different temperatures and pressures as well as other ullage gases of helium, air, and two mixtures of N_2 and SF_6 with DRs of 0.0036 and 0.0046. The study assumes that by keeping the same Froude number and DR between the full-scale and model-scale, the flow (impact geometry) would be completely scaled even during impacts. The pressure measurements are treated statistically. The results present a severe influence of DR for both condensable and non-condensable gases. According to the results, increasing the DR seriously decreases the expected pressures (see Maillard and Brosset [2009]). By using the results of this study and the results presented by Braeunig et al. [2009], an assessment methodology for sloshing impacts in LNG carrier tanks is proposed (Gervaise et al. [2009]) and implemented which is based on performing model tests with the same Froude number and density ratio as full-scale. Yung et al. [2009] and Yung et al. [2010] introduced a new dimensionless number as *interaction index* which combines the effect of DR and the polytropic index of gas. The study explains that by keeping the same Froude number, Euler number (defined as $Eu = P/\rho U^2$ where P is taken to be dynamic pressure, ρ is the media density, and U is the reference velocity), and interaction index, dynamic similitude between the model test and full-scale can be established and the pressures can be directly scaled. Based on this, an assessment methodology for sloshing impacts is proposed (Kuo et al. [2009]) which is also based on performing model tests with the same Froude number and density ratio as full-scale. Ahn et al. [2012] describe a small scale sloshing experiment to study the effect of DR. For this experiment 2D and 3D tanks with different fill levels and $0.0012 \leq DR \leq 0.0040$ were used. The paper notices the effect of DR on the resultant impact pressures and rise-times and recommends that the DR for sloshing model tests should be kept the same as in the real LNG tanks. Lugni et al. [2010] discusses the effect of ullage gas pressure (which naturally influences the DR) on the impact geometry

and kinematics based on model tests with a model tank which is found to be important.

It has been accepted that DR plays an important role and the consensus is that higher density ratios (by keeping the same liquid) lead to less severe impacts and lower density ratios are associated with more violent ones. The sensitivity of such changes is obvious by considering potential disastrous effects due to pressure underestimations from the model tests. A few comments can be made on the former studies:

- All the mentioned experiments were done at one scale yet the results addressed scaling issues. Numerical works consider different scales but for simplified geometries and simplified liquid and gas properties,
- Experiments designed to study the effects of DR, mixed the effects of DR and gas compressibility and attributed them only to DR,
- The experiments do not discuss the effect of DR on wave impact geometry which is crucial for the resultant pressures.

It seemed necessary to perform model tests at two or more scales, try different density ratios at each scale, have a high density of pressure sensors near impact zones, have very accurate synchronized comparisons of visual and measured data and pay attention to the evolution of impact geometries far from impact zones until the moment of impact.

In order to verify the evolution of impact geometry and kinematics at model test, one would need to monitor the free surface far from the impact zone up to the impact moment. Observing the gradual development of the free surface until a few milliseconds before the impact and at the moment of impact, one can think of imaginary borders which define the influence regions of different and sometimes overlapping physical properties of gas and liquid. At each region of influence there are only a few parameters that can affect the free surface and impact geometry. An effort trying to define such regions and summarize the influential parameters is elaborated by Lafeber et al. [2012a] based on the analysis of breaking wave impacts in large flume tanks. The study explains that before (and in general also after) the wave breaking process and far from the breaking zone which can be near the tank walls or in the middle of tank, the fluid flow will only be governed by Froude number and DR. In this zone the influence of gas compressibility is negligible since no compression occurs. In the regions far from the impact location the effects of DR on geometry can be considered as global.

As the flow approaches the tank wall, gas will be forced to escape and might be partially entrapped. At this time, gas compressibility, DR, phase transition and free surface instabilities (Kelvin Helmholtz instabilities) could all be of importance in determining the final impact geometry and possible increase of pressure

on impact zone. As all this is taking place near the final impact location, the effects of DR and other parameters are considered local at this time.

This study is dedicated to the global effects of DR on fluid flow and in particular on impact geometry and kinematics. It was investigated whether such effects exist or not. These effects were studied at each scale as well as at two different scales. The incompressible gas assumption for the regions far from the tank walls and constant ullage pressure with varying DRs helped to focus only on the effect of DR. The investigations and comparisons of this study are both qualitative using normal-speed HD videos (to observed global flow) and high-speed videos (to observe local flow) and quantitative by looking at pressure measurements and impact times.

2.2 Test Setup

Two model test campaigns were performed with 2D tanks and 3DOF motions. Different fill levels are of interest in sloshing model tests but for the studied cases a low fill level of 20% of the tank height was chosen as lower fill levels are associated with more severe impacts and higher induced pressures (see BV [2011]) and also different wave shapes could be studied. The larger tank was the scale 1:20 model of a transverse slice in the middle of tank 2 (see Fig. 2.1) of a membrane LNG carrier with total capacity of $152\,000\,\mathrm{m}^3$ (see Fig. 2.2(a) for the shape and internal dimensions at scale 1:20). The smaller tank was scale 1:40 model of the same slice. The tanks were made of thick plexiglass to reduce structural flexibility and enable observation. There were openings in the tanks to allow gas and water injection and also temperature and density measurements. There were openings to install pressure sensor modules on the tank. After gas injection and reaching the desired DR, the tanks were made tight to avoid leakage. Two different hexapods were used for the two campaigns. The choice of different hexapods was due to the requirements of each test and the capabilities and limitations of each hexapod in terms of maximum allowable weight, translations, rotations, velocities and accelerations in 3 DOF. Test at scale 1:20 was performed with a Sirocco type hexapod of Symétrie with max payload of 2 tons whereas the test at scale 1:40 was carried out with a Mistral type hexapod of Symétrie with max payload of 1 ton. Further detailed specifications and limitations of the hexapods are included in manufacturer's website. Dedicated verifications of tank alignment on the hexapods were performed by installing laser beams on vertical tank walls.

Two liquids of water and a solution (with water) of sodium polytungstate (SPT) (with a density of $1800\,\mathrm{kg/m}^3$) and different ullage gases of helium, air, two mixtures of sulfur hexafluoride (SF_6) and N_2 (Mix_2 with a density of $2\,\mathrm{kg/m}^3$ and Mix_4 with a density of $4\,\mathrm{kg/m}^3$), and pure SF_6 enabled to verify a range of DRs at two scales in multiple groups of tests as listed in Table 2.1 and Table

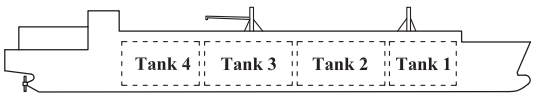

Fig. 2.1. Location and numbering of storage tanks in a schematic starboard view of the 152 000 m^3 LNG carrier using GTTs containment system technology which was the basis for defining tank dimensions and motions for the model tests. The tank capacities are 23 000 m^3 for tank 1 and 43 000 m^3 for the rest

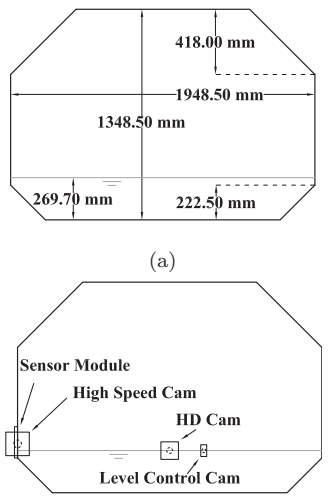

Fig. 2.2. (a) Internal dimensions of the 2D tank at scale 1:20 with the internal depth of 150 mm (b) Schematic camera and sensor module locations at both scales

2.2. Ullage pressure for all *DR*s was atmospheric in order to avoid any possible influence of pressure change.

For each group of tests, 3 types of irregular motions were applied on the tank. Those irregular motions were based on the real tank motions at full scale calculated by DIODORE for 5 hour sea states based on Jonswap spectrum found from the assumption of zero crossing period T_z of 8.5 s, heading of 270 ° and significant wave heights H_s of 2, 4 and 6 m. Jonswap spectrum is an enhanced form of Pierson-Moskowitz spectrum which can be used to describe any sea state

Table 2.1. Liquids and gases, nominal densities, and density ratios used for tests at scale 1:20

Group	Gas	Liquid	$\rho_g(kg/m^3)$	$\rho_l(kg/m^3)$	DR(−)
1	helium	water	0.18	997	0.0002
2	air	water	1.15	997	0.0012
3	Mix_2	water	2.00	997	0.0020
4	Mix_4	water	4.00	997	0.0040
5	air	SPT	1.15	1800	0.0006
6	Mix_2	SPT	2.00	1800	0.0011

Table 2.2. Liquids and gases, nominal densities, and density ratios used for tests at scale 1:40

Group	Gas	Liquid	$\rho_g(kg/m^3)$	$\rho_l(kg/m^3)$	DR(−)
1	helium	water	0.18	997	0.0002
2	air	water	1.15	997	0.0012
3	Mix_2	water	2.00	997	0.0020
4	SF_6	water	6.00	997	0.0060

using the characteristic values of T_z and significant wave height with the addition of wave direction information. After calculating the real ship motions at the location of the desired tank slice, only sway, heave, and roll motions were kept and scaled. During the campaigns all three irregular conditions were repeated several times to obtain better statistical samples for further studies. The repetitions were done for each different gas as well. In this study only the tank motions corresponding to H_s of 6 m will be studied.

Other than the mentioned irregular motions, single impact waves (SIW), corresponding to only one oscillation period and amplitude and with duration of only one period were applied (corresponding to only sway motion) to study a wide variety of simpler and more repetitive wave shapes. Those single impact waves were also created with different gas mixtures. Each SIW was repeated several times with at least one impact with recorded high-speed video. All the mentioned motions were defined for the center of the tank bottom which was taken to be the motion reference point.

At scale 1:20, 126 PCB pressure sensors were used, installed on a 21×6 arrays on two opposite vertical walls. At scale 1:40, 60 PCB pressure sensors were used, installed on a 15×4 arrays. All the pressure sensors sampled at 40 kHz. The use of many pressure sensors provided clearer pressure maps and helped to understand the ongoing phenomena. During the tests, the pressure measurement system was being activated with the definition of a pressure threshold which triggered the

system. All wave impacts on the module with maximum pressures lower than this threshold were not measured.

Three types of cameras were used at both test campaigns. High-speed cameras were used to visually capture the impact geometry a few milliseconds before and after the impact. For test at scale 1:20, a Photron SA5 high-speed camera was installed, looking at the sensor array. This camera had a resolution of 1024×1024 pixels with ~ 2.66 pix/mm and the global electronic shutter was adjustable from 16.7 ms to 1 μs independent of the frame rate. At scale 1:40, a Phantom V7.2 high-speed camera was used at the corresponding side. For this camera the resolution was 704×600 pixels with ~ 3.56 pix/mm and the exposure of 130 μs. Both high-speed cameras recorded at 4000 fps. To capture global videos of fluid free surface, the same HD camera (Canon XF105) was used for both tests without capturing close-up details of impacts. This camera's shutter speed could have been adjusted between 1/18 and 1/2000 of a second depending on the frame rate. At both scales the same frame rate of 25 fps was used. The resolution at scale 1:20 was 960×576 pixels with ~ 0.5 pix/mm whereas at scale 1:40 the resolution was 1920×1080 pixels with ~ 1 pix/mm. The recordings of this HD camera were mainly used for qualitative comparisons presented in this paper. A simple camera was also used to control the fill level. For all the cameras, dedicated wooden supports were made and installed. All the cameras were kept completely fixed on the supports throughout the tests (see Fig. 2.2(b) for Camera and sensor module locations at scale 1:20). There was a secondary pressure threshold used for the camera system. The high-speed cameras are only activated when the impact pressure is higher than this secondary threshold.

At each test campaign, in order to make sure that the adjusted fill level was accurate enough, the required water was weighed and transferred to the tanks, a photo was taken by a camera mounted on a fixed support and that level was taken to be the reference throughout the whole campaign. Regular photos were taken by the same stationary camera twice per day to make sure that the fixed level remained unchanged.

At each campaign, after fixing the fill level, a leakage test was performed with Nidron 5 (a mixture of 95% nitrogen and 5% hydrogen). Since tests with helium were more prone to leakage, dedicated leakage tests with helium were also performed. Changing the gas was done without emptying the tanks in order not to change the fill level. Gas density was regularly controlled using a mobile density meter.

Multiple arrays of LED lights were used to illuminate the video backgrounds. LED lights produced less heat as opposed to customary halogen lights. Less heat favored less water evaporation during the campaigns and so consistent testing conditions. Dedicated supports were used for the lighting system.

2.3 Accuracy Level

The accuracy level of the model tests can be discussed with regard to tank alignment control, definition of the center of rotation for the tank, fill level control, tank motions, and ambient conditions such as liquid temperature, gas temperature, ambient temperature, ullage gas pressure, ambient pressure, and ullage gas density.

2.3.1 Tank Alignment Verification

Ideal geometrical alignment of test tank on hexapod meant that the 2D tank axes were all aligned with the hexapod axes so that translations and rotations imposed by the hexapod could be properly applied to the tank, inducing the desired tank motions. The real situation is that misalignments are always observed.

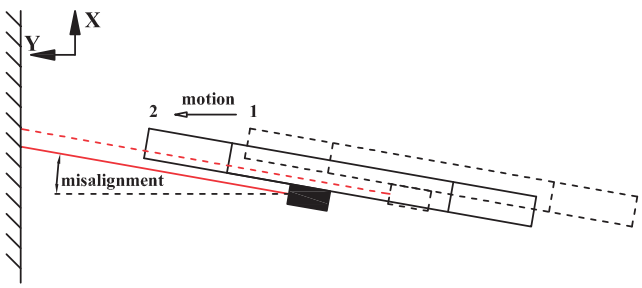

Fig. 2.3. Detection of misalignment between tank axis and hexapod axis using a laser beam

This was investigated for the two test setups used in this study using a laser beam. A laser distance finder (Bosch GLM 150) was installed on the vertical tank wall to generate the laser beam. Projection of this laser beam was tracked on the front wall. In case of moving the hexapod in Y direction, and in case of perfect alignment between the beam, tank, and the hexapod, the mark does not move on the wall. On the other hand if there is a misalignment between the tank and the hexapod (Fig. 2.3), the mark would move on the wall in X direction. For both tanks, the misalignment angle was detected to be less than 0.1°. This was checked by correcting the misalignment in XY plane by 0.1°, repeating the same translations in Y direction and observing that the mark moved this time in the opposite direction in X.

2.3.2 Definition of the Center of Rotation

Definition of a center of rotation was of importance in the model tests. The center of rotation was the point for which the tank motions (sway, heave, and roll for the 2D test) were defined. As those motions included rolling, all the rotations were also defined around this point. As a convention, the center of rotation was taken to be the centroid of the tank floor at both scales. This enabled to simply scale the motions from scale 1:20 to scale 1:40. After definition of the motions, those motions should have been respected exactly. One single important unknown was the location of this centroid in space with respect to the hexapod origin. In the 2D cases which were studied, the unknowns were two distances in Y and Z. This relative location should have been given to the hexapod to ensure the right motions at the right location at one scale and subsequently correctly scaled motions at the corresponding point at the other scale.

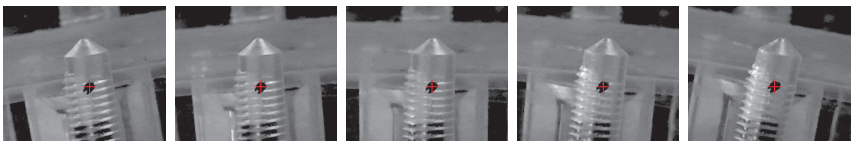

$\phi = +10°$ (a) $\phi = +5°$ (b) $\phi = 0°$ (c) $\phi = -5°$ (d) $\phi = -10°$ (e)

Fig. 2.4. Rotating the tank with 5° increments to verify whether the mark (the tank floor centroid) is the center of rotation

In order to find this point, first tank floor was measured and the centroid location was marked, then several relative positions were fed to the hexapod software and for each relative position, the tank was rotated with roll angles of $+10°$, $+5°$, $-5°$, and $-10°$ as depicted by Fig. 2.4. At each step an image was taken from the marker on the tank. The right relative position was chosen to be the one for which the center of the mark did not experience any translations, i.e. it was the center of rotation. The last step was done with a high-resolution camera triggered by bluetooth in order not to move the image frame and the marker position in the image.

In following the mentioned steps, one of the difficulties was actually finding the centroid which was not straightforward due to certain geometrical irregularities especially in the inner tank edges. Size of the marker was also important which was taken to be less than 2-3 mm. Another difficulty was a small unavoidable tank alignment problem which would anyhow affect the measurements although the discrepancy was less than 0.1°. The step including taking and comparing the images was the most accurate as following the center of the mark was done in the pixel level. That said, the process yielded an error which was less than ± 5

mm in finding the tank centorid location relative to the hexapod origin.

2.3.3 Tank Fill Level

The water level in the tank was monitored constantly to make sure it was reasonably constant throughout the model tests. Using arrays of LED lights enabled to maintain the variations of ambient temperature reasonably small in order to avoid evaporation. The use of halogen lights was avoided due to associated temperature rise, evaporation and the consequent water level changes. Nevertheless small changes were observed after each test due to liquid splashing which left multiple droplets on tank walls and also due to free surface stabilization process.

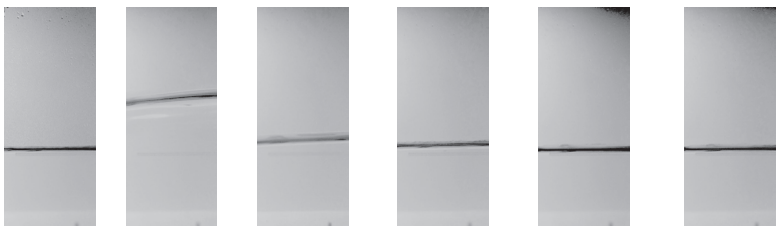

Ref. (a) | $t = 0$ (b) | $t = +1$ min (c) | $t = +2$ min (d) | $t = +5$ min (e) | $t = +10$ min (f)

Fig. 2.5. Idle time needed between two tests was determined by monitoring the free surface variations and stabilization time after each test. Images correspond to verification at scale 1:20.

In order to always have repeatable test conditions, a minimum idle time which was required to reach a constant fill level was respected between every two consecutive tests. The idle time was especially important for SIW tank motions which were used especially to have better repeatability. Based on monitoring the free surface variations and stabilization time after each test, the idle time was determined to be 10 min between each two tests at both scales.

2.3.4 Tank Motions

In order to ensure that the tank motions were accurate, those motions were verified by an independent measurement system. The motion command signals were then compared with measured motions to examine possible discrepancies. By comparing the command and motion signals, an increasing time shift was observed between the two signals. Discrepancies with respect to the motion amplitudes were also found. This time shift at both scales was progressively found for all common zero crossings of command and motion signals as $\Delta t_{ZC,i} =$

$t_{ZC,m,i} - t_{ZC,c,i}$ where $t_{ZC,c,i}$ is the i_{th} zero crossing time for any of the 3 DOF motions of the command signals, $t_{ZC,m,i}$ is the i_{th} (corresponding) zero crossing time for the same DOF of the measured motion signal and Δt_i is the i_{th} time shift between the two signals. The calculated time shifts for roll motion signals at both scales, were found as a function of the corresponding zero crossing times of the command signal as shown in Fig. 2.6.

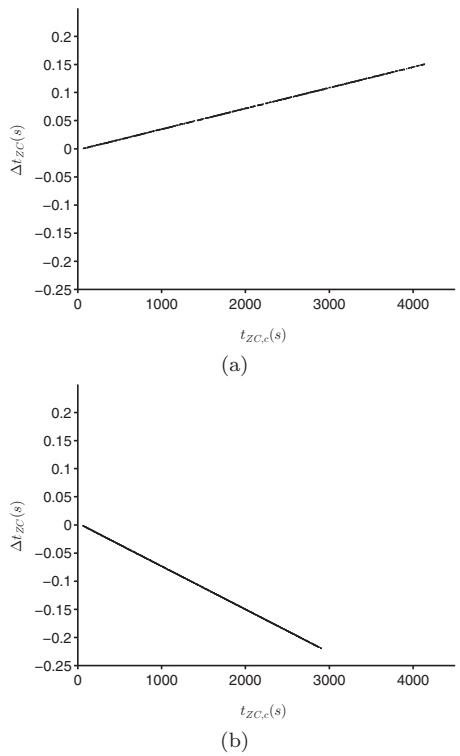

Fig. 2.6. Linear time shift between command and motion as a function of command signal time, found based on roll motion at (a) scale 1:20 (b) scale 1:40

The time shift was linear with respect to time. This time shift was positive at scale 1:20 which meant that real motions were delayed with respect to the original command signal and was negative at scale 1:40 which implies that real motions were ahead with respect to the commands. The linear trend of the time shift was found to be similar based on sway, heave or roll motions but with clearly less scatter when found based on roll. Due to this reason roll signals were used

as a basis for further signal manipulations in order to compare command and motion signals. Based on the linear time shift found for both motions, a linear correction coefficient as m was defined which enabled to relate to motions of both scales to one another. This correction coefficient was also used later on to find the corresponding video frames at both scales and correct the impact times of tests at scale 1:40 during scaling.

Table 2.3. Average and standard deviation of absolute error of motion amplitude at scale 1:20 and 1:40 based on 10 repetitions at each scale

		Scale 1:20		Scale 1:40	
Motion	Unit	$\mu_{\lvert\epsilon_{max}\rvert}$	$\sigma_{\lvert\epsilon_{max}\rvert}$	$\mu_{\lvert\epsilon_{max}\rvert}$	$\sigma_{\lvert\epsilon_{max}\rvert}$
X	(mm)	0.360	0.070	0.17	0.005
Y	(mm)	0.790	0.040	0.48	0.056
Z	(mm)	0.490	0.290	0.37	0.102
ϕ	(°)	0.015	0.006	0.016	0.005
θ	(°)	0.009	0.003	0.007	0.001
ψ	(°)	0.020	0.010	0.009	0.001

In order to verify the accuracy of motion amplitudes, the time shifts were linearly corrected for the command signal based on the trend found from the graphs depicted in Fig. 2.6. The discrepancy between command and motion could then be found directly. The maximum calculated motion errors for two tests at scale 1:20 and 1:40 with the largest tank motions (corresponding to Hs = 6m) are listed in Table 2.3. Note that even though the motions were 2D, i.e. the commands for surge, pitch, and yaw motions were null, negligible motions for those degrees of freedom were also observed.

2.3.5 Ambient Conditions

Ambient conditions such as temperature, pressure, and density were controlled throughout the model tests (see Table 2.4 and Table 2.5). Temperatures were stable during the tests. Small variations were mainly due to the change of ambient temperature. The same statement is valid for the measured pressures.

Controlled environmental conditions and tightness of the tank resulted in minimal gas density variations. This enabled us to look at the effects of changing the density without conflicts from possible ullage pressure effects. Furthermore the gases or gas mixtures that provided the desired densities inevitably contained water vapor. This vapor proportion could be estimated and will be taken into account whenever in the future compressibility effects will be studied.

Table 2.4. Controlled ambient conditions as liquid temperature (T_l), ullage gas temperature (T_g), ambient temperature (T_a), ullage gas pressure (P_g), ambient pressure (P_a), and ullage gas density (ρ_g) for different groups of tests (see Table 2.1) at scale 1:20

Group	T_l (°C)		T_g (°C)		T_a (°C)		P_g (mbar)		P_a (mbar)		ρ_g (kg/m^3)	
	μ	σ	μ	σ	μ	σ	μ	σ	μ	σ	μ	σ
1	25.9	0.45	25.7	0.53	25.4	0.98	1023.5	3.36	1007.2	2.64	0.182	0.002
2	27.2	0.59	27.2	0.47	27.1	0.83	994.6	0.76	994.9	0.71	-	-
3	25.9	0.64	25.9	0.64	25.6	1.12	1036.6	2.34	1004.3	2.29	1.976	0.015
4	25.1	0.63	25.1	0.58	24.7	0.76	1001.4	1.78	1000.6	4.78	4.004	0.022
5	29.2	1.04	29.2	1.03	28.8	1.36	1009.1	0.63	1009.3	0.66	-	-
6	26.9	0.71	26.8	0.71	26.2	1.09	1007.6	2.64	999.9	6.75	2.014	0.004

Table 2.5. Controlled ambient conditions as liquid temperature (T_l), ullage gas temperature (T_g), ambient temperature (T_a), ullage gas pressure (P_g), ambient pressure (P_a), and ullage gas density (ρ_g) for different groups of tests (see Table 2.2) at scale 1:40

Group	T_l (°C)		T_g (°C)		T_a (°C)		P_g (mbar)		P_a (mbar)		ρ_g (kg/m^3)	
	μ	σ	μ	σ	μ	σ	μ	σ	μ	σ	μ	σ
1	25.2	0.28	24.0	0.30	22.8	0.35	997.7	13.24	994.4	0.86	0.189	0.003
2	-	-	25.5	2.08	23.6	1.73	-	-	1000.9	5.63	-	-
3	24.5	1.31	24.2	1.35	22.1	1.13	1023.5	4.48	997.4	7.26	2.070	0.010
4	22.9	0.52	22.7	0.48	20.9	0.2	1027.8	7.30	996.7	7.05	5.820	0.150

2.4 Visual Investigation of Global Effects of DR

The effect of DR on the global flow (far from wave breaking zones) was studied visually by monitoring liquid free surface using the HD camera for the duration of irregular tank motions corresponding to $H_s = 6$ m at both scales. The irregular motions which corresponded to 5h sea states at full-scaled lasted 4195 s at scale 1:20 and 2966 s at scale 1:40. Both motions included ramps in the beginning and at the end to make a smooth transition from stationary conditions to the desired motions and vice versa to avoid motion discontinuities. Camera's frame rate as 25 fps was enough to capture the global effects.

In order to compare the corresponding frames at scale 1:20, the videos were visually synchronized in the beginning after which they were considered to be with the same time reference. As a result when a frame, which was a known number of frames after this time reference, was selected from one of the videos, the corresponding frames for the other videos were simply the same number of frames after the common time reference for those videos. The procedure for

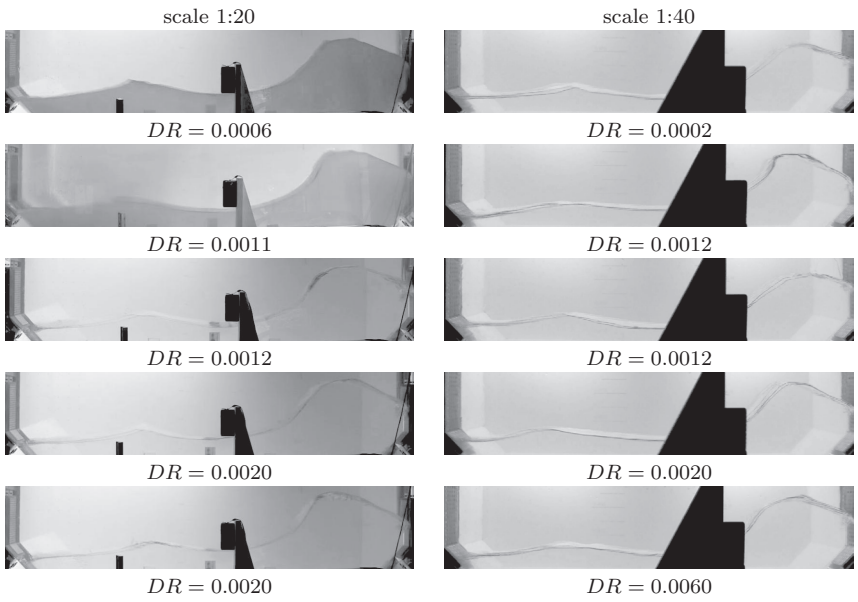

Fig. 2.7. Free surface with the same (at scale 1:20) and scaled (at scale 1:40) tank motions and different DR at time t_A at scale 1: 20 and time t'_A at scale 1: 40

selecting the corresponding frame at scale 1:40 included more steps. The first step, similar to the previous procedure was to visually synchronize the scale 1:40 videos at the beginning with the already synchronized videos at scale 1:20. Next it was necessary to scale the time and at the same time correct the linear time shift between the tank motions at both scales as already discussed in Section 2.3.4 and depicted in Fig. 2.6. For a random time t_X at scale 1:20, this step can be summarized to find the corresponding time at scale 1:40, t'_X, as:

$$t'_X = t_X/\sqrt{2}/(1+m) \tag{2.1}$$

Eq.2.1 scales the time based on Froude similarity between the two model tests and the factor 2 between the geometrical scales. It also corrects the time shift caused by linear time shift of the motions of each hexapod.

Also knowing that any selected time instant t_X corresponds to F_X number frames after the common time reference at scale 1:20, the previous equation can also be rewritten to find the corresponding frame number at scale 1:40 (F'_X) for any frame random frame number at scale 1:20 (F_X) as,

$$F'_X = round(F_X/\sqrt{2}/(1+m)) \tag{2.2}$$

The procedure for video comparison as mentioned has potentially two sources of error. Firstly matching the videos in the beginning is done visually which is inherently not so accurate. As a result, an error of ± 1 frame can present which due to the camera frame rate could lead to ± 40 ms time difference. Furthermore it should be noted that the procedure shown by Eq.2.2 is approximate as it finds the best match at scale 1:40 and not necessarily the exact match. Being aware of the mentioned shortcomings comparison of the fluid free surface was done at 3 time instants of t_A, t_B, and t_C, measured at scale 1:20, and from a common time reference for all the videos. The three time instants were chosen only to be able to compare distinctive and visible global flow geometries and no other criterion was involved.

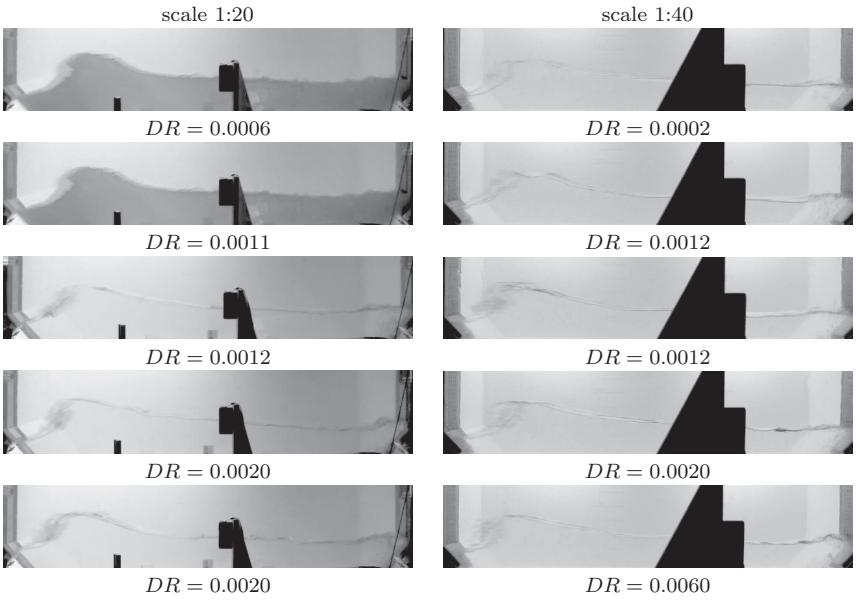

Fig. 2.8. Free surface with the same (at scale 1:20) and scaled (at scale 1:40) tank motions and different DR at the time t_B at scale $1:20$ and time t'_B at scale $1:40$

In terms of global flow geometry, the fluid free surface was observed to have a very similar shape regardless of DR and scale, for the whole duration of the motions. Small discrepancies were still observed. Such discrepancies were not

due to DR as similar differences were observed with the same DR (see Fig. 2.7 for images corresponding to $DR = 0.0012$ at scale 1:40). There were no residual or accumulating effects of local phenomena on the global flow geometry. In other words even if there are different local effects due to the use of several different combinations of gas and liquid, such effects did not seem to influence the global flow geometry which seemed to be independent of DR from the beginning up to the end of the motions. In between two successive impacts, when the wave front is far from the impact areas, the shape of the free surface repeats pretty well when repeating the same condition. This is also true when changing the gases for the range of DR studied although the shape variations can still be observed. The sources of variability seem to have come directly from the free surface instabilities that develop just before the impacts during the gas escaping phase while the wave front approaches the wall. Nevertheless, the perturbations caused by these instabilities disappear quickly enough to prevent a progressive deterioration of the flow that would induce an increasing variability.

It was also observed that, the global flow was in phase regardless of DR and scale and for the whole duration of the videos. In other words, the flow memory of tank motions is short and global flow complying with Froude similarity makes sense. The local effects of changing the gas or liquid, did not influence or change the phase which implied that wave impacts should occur at exactly the same time instants (considering a very small time window). This could potentially provide a basis for comparing different tests with different gases impact by impact instead of comparing them statistically. Of course this can be investigated further by looking at the times of the measured impacts.

2.5 Verification Based on Pressure Recordings

The observation of in-phase fluid flow regardless of tested DRs and scale provides a basis for deterministic comparison of wave impacts at different model tests. Based on this observation if the model tank motions are exactly repeated (or scaled and repeated), wave impacts should be occurring at literally the same expected time instants for all the repetitions regardless of DR and scale. This way individual impacts can be studied under the influence of varying parameters and at different scales. This idea was further investigated by comparing the recorded wave impact times for the repetitions of the same irregular tank motions at the same scale or at different scales while changing DR. Before going through the results, a few terms should be defined.

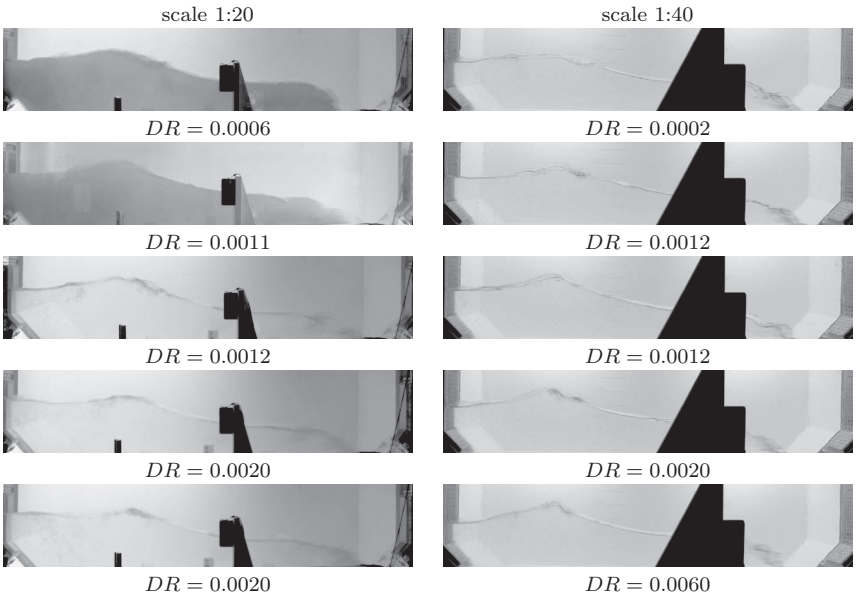

Fig. 2.9. Free surface with the same (at scale 1:20) and scaled (at scale 1:40) tank motions and different DR at the time t_C at scale 1: 20 and time t'_C at scale 1: 40

2.5.1 Definitions

The introduced definitions and symbols are only the ones which will be used in the coming discussions and graphs.

Pressure Threshold (P_{th})

During sloshing model tests, wave impacts occur, potentially when waves break on tank walls but only wave impacts with maximum induced pressures higher than a threshold (P_{th}) are recorded and the less severe impacts are filtered (this is common practice for standard sloshing model tests). For each severe impact, measured pressures and time are recorded for a predefined duration and for all sensors on the sensor module where the impact took place.

Impact Time (t_i)

In this comparison and for each test, wave impact times t_i, $i = 1, 2, ..., N$ where N is the number of the last recorded impact for the test, were defined as the

moments when measured pressure by any pressure sensor on the sensor module exceeded the threshold, subtracted by 20 ms for tests at scale 1:20 and 12.5 ms at scale 1:40 as pre-trigger times. Pre- and Post-trigger times were intended to cover all the relevant pressure data of each recorded wave impact. Impact times defined this way are also considered as impact start times. The whole data recording duration for each wave impact was 40 ms at scale 1:20 and 52.5 ms at scale 1:40.

Maximum impact pressure ($P_{max,i}$)

Every record of a wave impact is a collection of pressure time histories recorded by all the pressure sensors. Maximum instantaneous measured pressure in this collection will be referred to as $P_{max,i}$ which reflects the more local phenomena that occurred during the corresponding impact.

Reference Time Window (Δt)

In order to compare the impact times of any two tests with the same (or scaled) tank motions, wave impact times of one test were taken as reference times as $t_{i,ref}$ with i varying from 1, corresponding to the first recorded impact up to N, the number of the last recorded impact for the reference test. A time window as Δt was defined around the reference event times defining the N reference time slots as $t_{i,ref} \pm \Delta t$ and for any other test repetition it was checked whether the event times fit in the defined reference time slots.

Number of Impact Coincidences (NC)

When comparing event times of any two tests if impact times of one fit in time slots defined for the reference test as $t_{i,ref} \pm \Delta t$, the couples of impacts at two tests were considered as coincident events. Any coincidence was accepted only if it was impact by impact with a reasonable reference time window size. With the defined criterion two exceptions were considered as

- If two or more impact times of the second test lied in one time slot defined by the reference test, only the closest to the reference impact time was taken to be the right match for the reference impact and the rest were disregarded,

- If a wave impact time of the second test fits in the reference time slot of two or more impacts of the reference tests, only the one coincidence with smallest time difference was kept and the rest were neglected.

Extended Recorded Wave Impacts

Occasionally during the tests at both scales and in case of continuously high pressures, some wave impacts were recorded as two. This created close impact times (as close as 30 ms) which were not both necessary for the comparison as both close impact times imply the same breaking wave. In order to find the extended events, all events which were closer than 100 ms were found and the maximum impact pressures were compared, and finally only the one with higher induced pressure was kept and the other was neglected in the later comparisons.

Pseudo Impacts

In every model test, depending on how small a (P_{th}) is adopted and eespecially for very low values of pressure threshold, a handful of impacts could be recorded which are not necessarily representative of wave breaking processes and could be caused due to sudden increase of pressure at one sensor as a result of stochastic and very local water droplets. Such impacts are known to exist and are expected to interfere with comparison of real wave impact times which are governed by global flow but this effect is not expected to be affecting the number of coincidences to a considerable extent. Pressure fluctuations due to the change of hydrostatic pressure can also be registered as impacts if threshold is very low. These types of impacts are not considered to be interfering with the number of coincidences as they are considered to be repeatable and as such captured in other repetitions as well.

Maximum Reference Time Window (Δt_{max})

The maximum meaningful reference time window (Δt_{max}) for comparison of any two tests needed to be considered carefully as very large time windows could lead to the recognition of invalid coincidences. For two random tests, this maximum time window is defined to be equal to the minimum event time difference found from all consecutive impact times of both tests. This guarantees that the chance of considering two different but close impacts at two tests as coincidences is minimal and is convenient for comparing couples of tests with no other repetitions available. That said, this criterion is based on only two compared tests and might still generate some error for a serious comparison because,

- When comparing two tests, it is clear that not all the wave impacts were recorded (pressure threshold effect) so minimum impact time difference found from all consecutive events might not be the real minimum,
- The minimum impact time difference is found knowing that pseudo impacts exist which might affect Δt_{max}.

Aware of the aforementioned limitations, the mentioned criterion for defining Δt_{max} was used for initial data examinations but for serious comparisons an optimum and reasonably small time window should be selected and adopted.

2.5.2 Selected Tests for Comparison

For doing the comparisons, recorded pressure measurements of 40 tests at scale 1:20 and 40 tests at scale 1:40 were selected according to Table 2.6 and Table 2.7. For all those tests, the same tank 2D motions corresponding to a sea state with H_s of 6m had been applied. 40 tests at each scale were put in 4 different groups, corresponding to different gases and DRs (see Table 2.1 and Table 2.2 for gas and liquid list and properties in each group). Each test that was selected to be used for the comparison is given a number to facilitate further reference.

Table 2.6. 40 selected tests to study event coincidence at scale 1:20 and the number of recorded impacts for those tests

Group 1			Group 2			Group 3			Group 4		
No.	p_{th} **(bar)**	**N**	**No.**	p_{th} **(bar)**	**N**	**No.**	p_{th} **(bar)**	**N**	**No.**	p_{th} **(bar)**	**N**
1	0.25	429	**11**	0.16	509	**21**	0.25	218	**31**	0.25	175
2	0.25	390	**12**	0.16	527	**22**	0.25	243	**32**	0.25	150
3	0.25	411	**13**	0.16	521	**23**	0.25	224	**33**	0.25	154
4	0.25	420	**14**	0.16	491	**24**	0.25	219	**34**	0.25	146
5	0.25	429	**15**	0.16	492	**25**	0.25	234	**35**	0.25	165
6	0.25	410	**16**	0.16	528	**26**	0.25	234	**36**	0.25	146
7	0.25	398	**17**	0.16	504	**27**	0.25	207	**37**	0.25	162
8	0.25	399	**18**	0.16	503	**28**	0.25	229	**38**	0.25	172
9	0.25	433	**19**	0.16	506	**29**	0.25	213	**39**	0.25	157
10	0.25	425	**20**	0.25	267	**30**	0.25	208	**40**	0.25	162

Any combination of tests of Table 2.6 and Table 2.7 could have been considered for impact coincidence verification. In case of comparing impact times at scale 1:40 with those of a test at scale 1:20, impact times of the smaller scale were linearly corrected based on the linear time shift of tank motions and scaled with a factor $\sqrt{2}$ based on Eq. 2.1.

2.5.3 Initial Impact Coincidence Verification

Impact coincidence was first verified by simply plotting the maximum impact pressures ($P_{max,i}$) versus their corresponding impact times (t_i), separately at scale 1:20 and 1:40 as shown in Fig. 2.10(a) and 2.10(b) respectively. In order to make both figures comparable, the impact times at scales 1:40 were scaled according to the procedure mentioned in Eq. 2.1. At each scale 40 tests were

Table 2.7. 40 selected tests to study event coincidence at scale 1:40 and the number of recorded impacts for those tests

Group 1			Group 2			Group 3			Group 4		
No.	p_{th} **(bar)**	**N**	**No.**	p_{th} **(bar)**	**N**	**No.**	p_{th} **(bar)**	**N**	**No.**	p_{th} **(bar)**	**N**
1	0.20	216	**11**	0.08	482	**21**	0.07	528	**31**	0.05	567
2	0.20	200	**12**	0.08	488	**22**	0.07	515	**32**	0.05	556
3	0.20	192	**13**	0.08	514	**23**	0.07	526	**33**	0.05	559
4	0.20	181	**14**	0.08	512	**24**	0.07	490	**34**	0.05	576
5	0.20	190	**15**	0.08	486	**25**	0.07	487	**35**	0.05	575
6	0.20	189	**16**	0.08	482	**26**	0.07	514	**36**	0.05	583
7	0.20	197	**17**	0.08	516	**27**	0.07	505	**37**	0.05	568
8	0.20	184	**18**	0.08	482	**28**	0.07	501	**38**	0.05	573
9	0.20	205	**19**	0.08	489	**29**	0.07	499	**39**	0.05	559
10	0.20	205	**20**	0.08	488	**30**	0.07	509	**40**	0.05	575

available according to Table 2.6 and Table 2.7. Only a small time duration compared to the total test duration was used in this figure for better visibility and this window is chosen to be the same at both scales.

The figures both show that impacts only happen at specific time instants. Changing the gas, does not affect those specific times. In other words impact times are governed by the global flow in the tank and not very much influenced and affected, by ullage gas properties including the DR. It is also noted by comparing Fig. 2.10(a) and Fig. 2.10(b) that the specific impact time instants do not depend on scale either as literally the same specific impact times are also observed at both scales.

It can be seen that there are some impact times, for which only one measurement exists considering all the tests (80 tests) at both scales. This could be an indication of pseudo-impacts or impacts which normally generate very low pressures, except for only one exception which is recorded for all 80 repetitions. This can be verified by monitoring the global flow videos and observing whether an impact occurred at those times or not.

The impact coincidence was observed to exist and to be independent of ullage gas or scale for the tested DRs and scales. The nature and accuracy of this coincidence is yet to be investigated further more accurately. It was also interesting to verify how close the observed coincident impacts were and to verify the randomness of coincidences.

Sensitivity of NC as a function of reference time window (Δt)

An important parameter in studying coincident impacts is reference time window (Δt). Very small sizes of Δt will lead to detection of no coincidences. Large sizes of Δt will be misleading by detecting wrong coincidences. First the sensitivity of

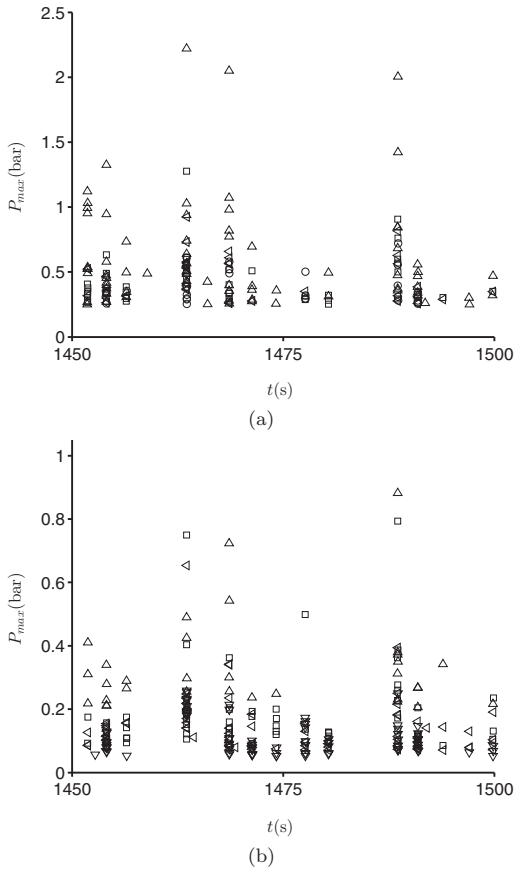

Fig. 2.10. plot of the maximum induced impact pressure (P_{max}) vs. impact time (t) for the recorded impacts of tests 1 to 40 at (a) scale 1:20 ($\triangle$: $DR = 0.0002$, $\square$: $DR = 0.0012$, $\triangleleft$: $DR = 0.002$, $\circ$: $DR = 0.004$), (b) scale 1:40 ($\triangle$: $DR = 0.0002$, $\square$: $DR = 0.0012$, $\triangleleft$: $DR = 0.002$, $\triangledown$: $DR = 0.006$). Impact times at scale 1:40 have been scaled with a factor $\sqrt{2}$ and linearly corrected based on the known relative time shift of tank motions at two different scales. Impacts occur at the same time instants regardless of DR and scale.

the number of coincidences (NC) as a function of Δt needs to be investigated. Based on this study an idea of the reasonable value for Δt can be developed.

When studying impact coincidence of any two tests at the same scale or at two different scales with exactly scaled conditions, variation of NC as function of Δt was similar to the schematic curve presented in Fig. 2.11. Varying Δt from 0 to Δt_{max} increases NC from 0 to NC_{100}. This increase could be sharp in the beginning and for small reference time window sizes, 95% of the NC_{100} could be reached. The Δt corresponding to 95% of the NC_{100} is named Δt_{95}. Increasing the time window size will cause the remaining 5% increase of NC which is often stepwise. Depending on Δt_{max} which could be much larger than Δt_{95}, this stepwise and small variation could dominate most of such curve.

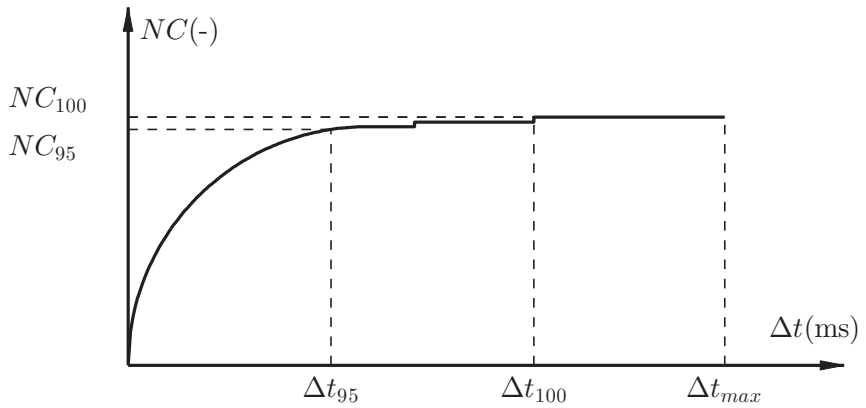

Fig. 2.11. A schematic curve showing the change of NC as a function of Δt. While Δt_{100} and Δt_{max} yield NC_{100}, Δt_{95} corresponds to 95% of NC_{100} which is depicted by NC_{95}

On this curve, the region between Δt_{95} and Δt_{max} could well be including uncertainties. As mentioned before defining Δt_{max} as the minimum impact time difference of consecutive impacts for the two tests is only accurate if all the possible wave impacts are captured. As this is not the case due to the adoption of p_{th}, every Δt_{max} could lead to the recognition of invalid coincidences. A curve similar to the one presented in Fig. 2.11 can be established for any couples of tests at scale 1:20 listed in Table 2.6 (1560 possible comparisons), or couples of tests at scale 1:40 (1560 possible comparisons) listed in Table 2.7 or in comparing tests at scale 1:20 with tests at scale 1:40 (1600 possible comparisons). At each comparison 3 parameters of Δt_{95}, Δt_{100}, and Δt_{max} can be found and the collections can be used to examine each parameter (See Table 2.8). The results show that the difference between Δt_{95} on the one hand and Δt_{100} and Δt_{max} on the other hand is considerable. Furthermore Δt_{100} and Δt_{max} vary a lot which

was expected as they depend on p_{th} which varies for each group of tests. Δt_{95} is proven to be much smaller with a small standard deviation for all 3 collections of comparisons. Among all the parameters introduced in Fig. 2.11, Δt_{95} and NC_{100} were considered to be the best ones in order to give more insight about the nature of coincidences.

Table 2.8. Variation of Δt_{max}, Δt_{100} and Δt_{95}, found from comparisons similar to Fig. 2.11 for all the possible couples of tests at scale 1:20 (according to Table 2.6), 1:40 (according to Table 2.7), and two scales versus each other

	Scale 1:20				Scale 1:40				Scale 1:20 vs. Scale 1:40			
Δt (ms)	μ	σ	Min	Max	μ	σ	Min	Max	μ	σ	Min	Max
Δt_{max}	857.2	729.6	100.0	2184.8	440.9	212.9	100.7	1486.6	619.7	517.1	100.0	2216.5
Δt_{100}	149.2	254.1	40.0	2060.0	141.8	174.6	30.0	1450.0	191.2	252.7	40.0	2200.0
Δt_{95}	46.8	8.3	30.0	70.0	31.4	5.8	20.0	50.0	63.3	17.4	30.0	110.0

It is worthwhile to study the selected parameters of Δt_{95} and NC_{100} in more detail. Fig. 2.12 shows the two parameters calculated for all the possible couples of tests at scale 1:20. Before performing the comparisons and for tests $11-19$, only the impacts with pressures higher than $0.25bar$ are kept to have the same basis of comparison for all the tests. 1560 combinations could be done. Fig. 2.12(a) and Fig. 2.12(b) are both symmetrical as expected. In other words the parameters are independent of the order of the compared tests. Based on Fig. 2.12(a), NC_{100} is largest when comparing tests with helium with one another and is smallest when comparing tests with Mix_4 with each other. As the number of potential impacts with every gas should be exactly the same (because global flow was shown to be independent of the ullage gas in the tested range of DR) and since NC_{100} must be theoretically identical for all the comparisons, this effect could be attributed only to the influence of p_{th}. According to Table 2.6, p_{th} is the same for all 40 tests with different gases (except initially for tests $11-19$ which were then corrected) but with this constant threshold, the number of recorded impacts is reduced with heavier ullage gases. As a result and since for heavy gases less impacts are recorded, NC_{100} is expected to be smaller in comparisons involving heavier gases. The opposite statement is also valid for the comparisons involving lighter gas of helium results in larger NC_{100} since more impacts have originally been recorded for those tests. Also comparisons within the same groups of tests yield more or less similar number of coincidences. With regard to this, Fig. 2.12 can be seen as 16 blocks with nearly unique colors for each block due to the nearly constant number of coincidences within each block.

Fig. 2.12(b) summarizes Δt_{95}s for all the possible comparisons at scale 1:20. The figure shows a change of Δt_{95} for comparisons with similar and different gases. Δt_{95} is smallest when comparing tests with the heaviest gas of Mix_4 with

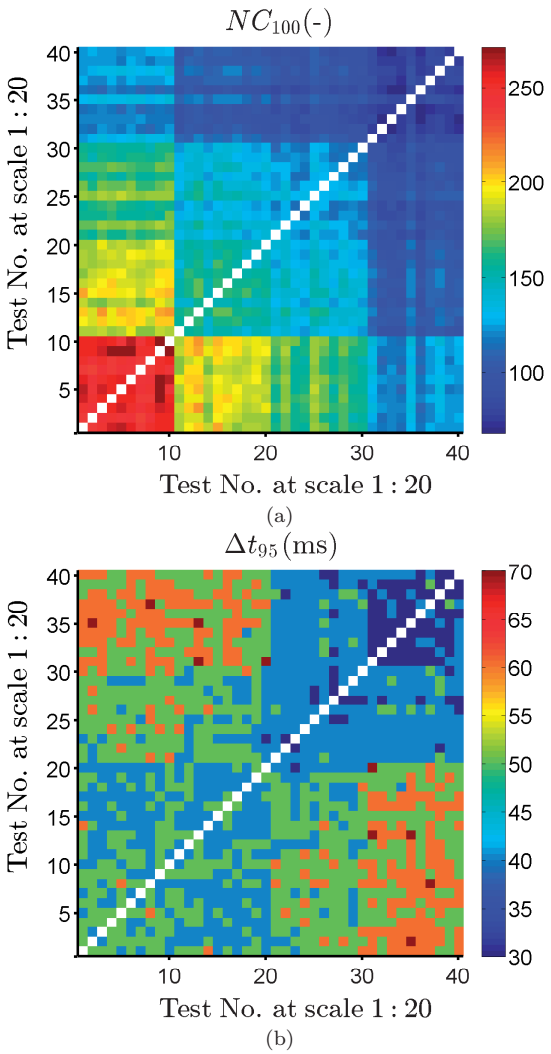

Fig. 2.12. (a) NC_{100} for all the possible comparisons between the tests at scale 1:20 (b) Δt_{95} for all the possible comparisons between the tests at scale 1:20. Increments of 10 ms were used to find Δt_{95}.

each other and is largest when comparing the tests with the heaviest gas of Mix_4 with tests with lightest gas which is helium. This could imply that by using the

same gas, impact times are at the closest and as a result with a very small time window, 95% of the detectable coincidences are found. It also implies that by comparing tests with a large difference in DR, impact time differences are the largest and there is a need for Δt to detect 95% of the coincidences. This idea can further be investigated for all the compared gases.

For tests with helium with test numbers of $1-10$, Δt_{95}s are not minimum when comparing tests with the same DR. It appears from Fig. 2.12(b) that Δt_{95}s are minimum when comparing them with tests with air. It should be noted that according to Table 2.6, p_{th} is smaller for most of the tests with air which affects the impact time. Nevertheless Δt_{95} increases by doing comparisons with the heavier gas of Mix_2 and is the largest when comparing with the heaviest gas of Mix_4.

In case of tests with air with test numbers of $11-20$, Δt_{95}s are minimum when comparing tests with the same DR. Δt_{95}s are slightly larger when comparing the tests with air, with tests with helium. Δt_{95}s are also larger while comparing tests with air with tests with Mix_2 and again largest when comparing with tests with the largest DR difference i.e. with Mix_4.

In case of heavy gases of Mix_2 and Mix_4 the behavior is as predicted. Smallest values of Δt_{95} for test numbers $21-30$ and $31-40$ with respectively Mix_2 and Mix_4 are obtained when comparing them with themselves. Δt_{95}s increase in comparisons with different DR and are the largest while making comparisons with the largest difference of DR.

The same study was performed comparing the tests at scale 1:40. Fig. 2.13 summarizes the two parameters of NC_{100} and Δt_{95} calculated for all the possible couples of tests at scale 1:40. 1560 combinations could have been studied. According to Table 2.7 different p_{th} had been adopted for different gases. The goal was to be able to capture more and more impacts with heavy gases. Before making the comparisons presented in Fig. 2.13, a common threshold of $0.08bar$ was applied to the measurements in order to bring them to the same basis for comparison. This threshold clearly did not influence the number of the impacts in Group 1 and Group 2. It did not change the basis for definition of impact times of the corrected tests either. Similar to Fig. 2.12(a) and Fig. 2.12(b), Fig. 2.13(a) and Fig. 2.13(b) are symmetrical. In Fig. 2.13(a), NC_{100} is largest when comparing tests with air with one another and is smallest when comparing tests with SF_6 with each other. This is in contradiction with what was previously concluded at scale 1:20. At that scale comparison of tests with helium showed larger coincidences. Here the reason is that large value of adopted p_{th} for tests with helium ($0.2bar$) which automatically filtered many impacts and naturally reduced the chance of detecting more coincidences. On the other hand for tests with air the p_{th} was $0.08bar$ and for this threshold about three times more impacts were captured which naturally increased the chance of coincidence detection and led

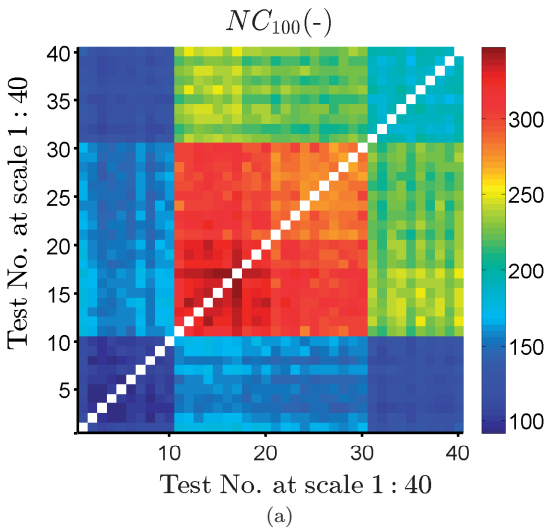

Fig. 2.13. (a) NC_{100} for all the possible comparisons between the tests at scale 1:40 (b) Δt_{95} for all the possible comparisons between the tests at scale 1:40. Increments of 10 ms were used to find Δt_{95}.

to larger values of N_{100} in comparisons with air. For tests $11 - 40$ where the comparisons were based on the same p_{th} of $0.08bar$ the smallest value of NC_{100}

was detected for comparisons with the heaviest ullage gas of SF_6 with the less recorded coincidences after applying the common threshold of $0.08bar$.

Fig. 2.13(b) summarizes Δt_{95}s for all the possible comparisons at scale 1:40. The idea developed from the results of Fig. 2.12(b) that smallest Δt_{95}s are when the tests with the same gas are compared with each other was tested here as well. According to Fig. 2.13(b), Δt_{95} is smallest when comparing tests with helium with each other as well as while comparing tests with SF_6 with one another.

For tests with helium with test numbers of $1-10$, Δt_{95}s are indeed minimum when comparing tests with the same DR. Comparing tests with helium with tests with air and Mix_2 however result in no considerable difference. On the other hand Δt_{95}s increase substantially in comparisons with the heaviest gas of SF_6 where they are the highest. For tests with air with test numbers of $11-20$, Δt_{95}s are maximum when comparing them with tests with the heaviest gas of SF_6. In comparison with each other and with tests with helium and Mix_2 Δt_{95}s are in the in average in the same range. For tests with Mix_2 with test numbers of $21-30$, Δt_{95}s are minimum when comparing them with each other and are maximum when comparing them with tests with SF_6. In comparison with tests with helium again small values for Δt_{95} are recorded which was not expected. In case of the heaviest gas of SF_6 the variation of Δt_{95} is more according the previous observations at scale 1:20. Smallest values of Δt_{95} are obtained for comparisons of tests $31-40$ with each other. Δt_{95} increases by making comparison with tests of other DRs but is not maximum while comparing with helium. Instead Δt_{95} is highest when comparing with tests with air.

In making the comparisons at scale 1:40, an important point is that even though a secondary and common threshold was applied to all the measurements, all the impact times were still found based on different initial thresholds which could affect the measurements. This effect could be more influential if the thresholds are more different. This would be the case in comparisons involving tests with helium with a much larger p_{th}. Apart from comparisons made with helium, the idea developed earlier would be valid with only one exception of air-air comparisons.

An interesting study would be to monitor the variations of NC_{100} and Δt_{95} for comparisons between tests at scale 1:20 and tests at scale 1:40. Impact times at scale 1:40 were first scaled and corrected based on Eq. 2.1 for this comparison. The results are summarized in Fig. 2.14. Both figures are asymmetrical since every comparison is unique. According to Fig. 2.14, NC_{100} is higher whenever the number of recorded events is larger. This is in accordance with was observed previously in Fig. 2.12, and Fig. 2.13.

Fig. 2.14(b) is not coherent with what was already observed in Fig. 2.12(b) and Fig. 2.13(b). In the previous figures, it was shown that Δt_{95} was usually lowest when comparing tests with the same ullage gases and was highest when

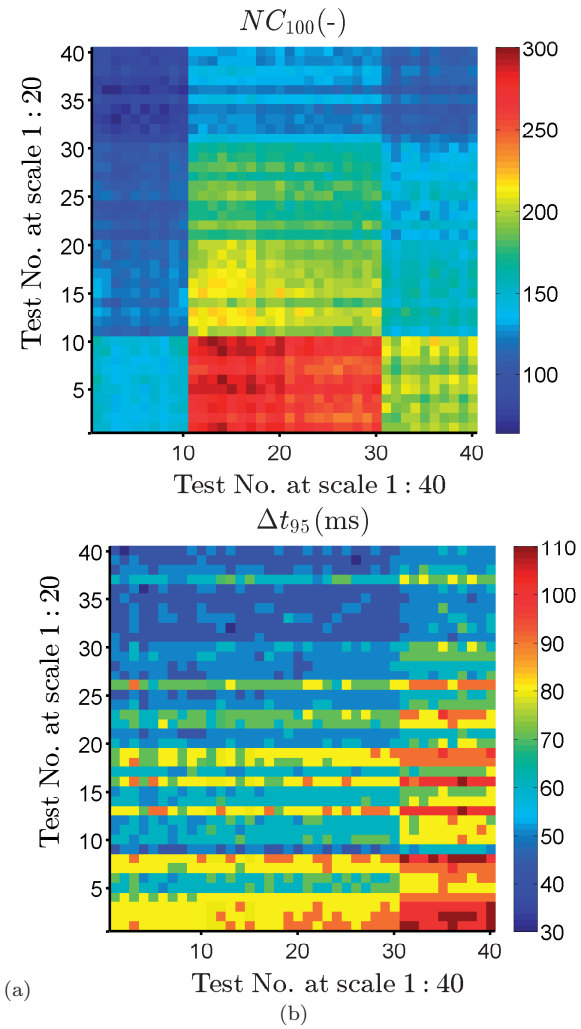

Fig. 2.14. (a) NC_{100} for all the possible comparisons between the tests at scale 1:20 and tests at scale 1:40 (b) Δt_{95} for all the possible comparisons between the tests at scale 1:20 and tests at scale 1:40. Increments of 10 ms were used to find Δt_{95}.

comparing tests with the largest ullage pressure difference. In Fig. 2.14(b), Δt_{95} is lowest when comparing tests with helium at scale 1:40 with tests with Mix_2 at

scale 1:20 and is highest when comparing tests with SF_6 at scale 1:40 with tests with helium at scale 1:20. This is believed to be due to the adoption of different p_{th} at different scales and tests with different gases as well as inaccuracies in defining the correct and corresponding reference time ($t = 0$) at different scales. The latter is believed to play a more important role which did not interfere in comparisons at the same scale.

Sensitivity of NC as a function of shifting impact times of one test by $\Delta\tau$

In studying impact coincidence at each or different scales it is important to verify whether the coincidences are random or real. In other words it is of importance to be able to say random coincidences from the real ones. In order to study this, it was tested in a comparison of impact times of two tests as to how the number of coincidences vary if the impact times of one the tests is shifted by $\Delta\tau$ and as such, introducing wrong impact times. It was also interesting to see the joint influence of reference time window (Δt) in combination with the effect of applying a time shift. Applying a time shift introduced an error in impact times whereas varying the reference time window changed the tolerance in considering the impacts at two tests as coincidences. Such a comparison is shown in Fig. 2.15 for tests 5 and 35 at scale 1:20. In this figure, Δt is varied in the range of $0 - \Delta t_{max} = 0.32s$ whereas $\Delta\tau$ is varied in the range of $-10s - +10s$. Both variations are applied with an increment of $0.01s$.

As both tests use the same time reference, the maximum number of coincidences (NC_{100}) is achieved with $\Delta\tau = 0s$. This is valid for all values of Δt. Applying a small time shift to the impact times of one test leads to a sudden drop in the number of coincidences to zero. However there are several local peaks of the NC which are much smaller compared to NC_{100} but are still considerable. If three sections of Fig. 2.15 are considered corresponding to $\Delta t_{95} = 50ms$, $\Delta t_{100} = 80ms$, and $\Delta t_{max} = 350ms$ as depicted in Fig. 2.16, those peaks can be seen as rather symmetrical, around the main peak in the curves. The peaks are considered to be detected when a $\Delta\tau$ close to the multiples of average zero crossing period of the sway tank motions are applied to data. At scale 1:20, average zero down crossing periods for sway, heave, and roll tank motions are 2.72 s, 2.41 s, and 3.17 s respectively whereas two first local peaks with positive time shifts and calculated for Δt_{95} are at $\Delta\tau = 2.4$ s and 5.12 s.

Comparisons similar to what was presented in Fig. 2.15 and Fig. 2.16 show that observed coincidences according to earlier definitions are not random and are so sensitive to errors in the definition of the impact times. By adopting an appropriate reference time window, number of the detected false coincidences is reduced. Furthermore not any local peak in a comparison similar to what was presented in Fig. 2.16 can be attributed to the real coincidences.

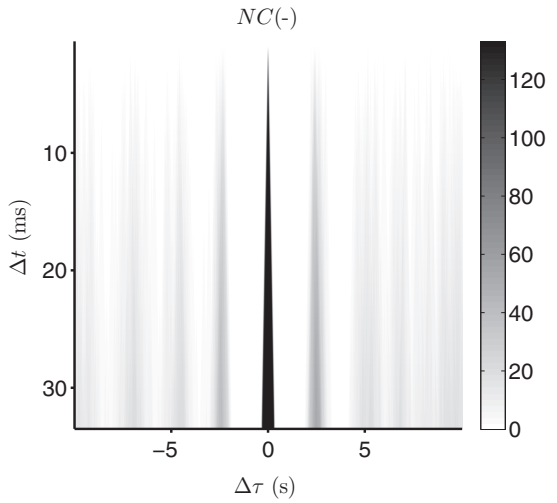

Fig. 2.15. Variation of NC as a function of both Δt and $\Delta\tau$ for tests 5 and 35 at scale 1:20. Δt is varied in the range of $0 - \Delta t_{max} = 0.32s$ whereas $\Delta\tau$ is varied in the range of $-10s - +10s$. Both variations are applied with an increment of $0.01s$

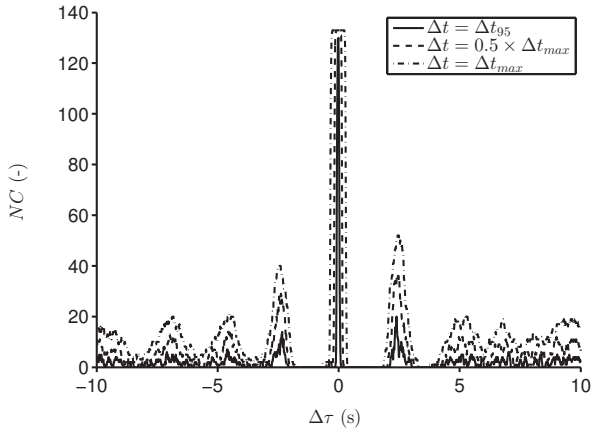

Fig. 2.16. Variation of NC as a function of $\Delta\tau$ for three values of Δt for tests 22 and 31 at scale 1:20

In a study at any scale(s), it seems necessary to perform a study on the sensitivity of NC as a function of both Δt and $\Delta\tau$ before trying to establish a coincidence curve as presented in Fig. 2.17.

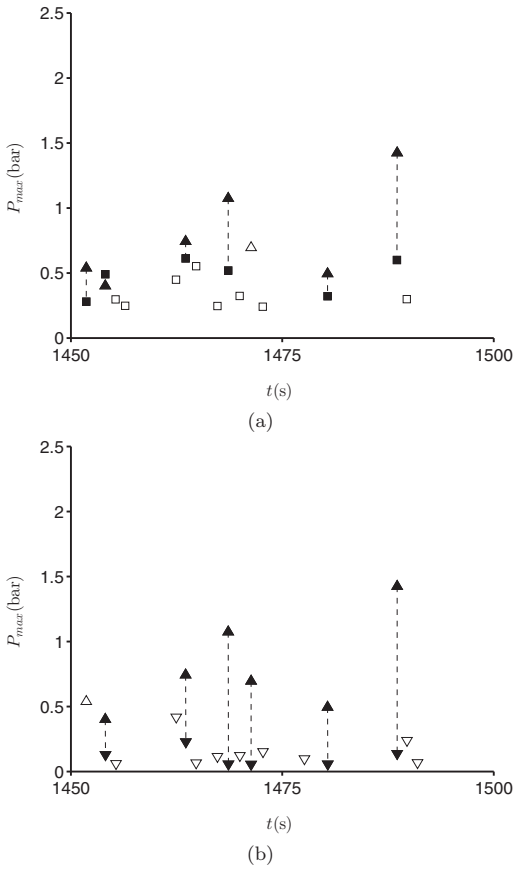

Fig. 2.17. Corresponding wave impacts with different density ratios at (a) scale 1: 20 (tests 5 and test 15)and (b) scale 1: 20 and 1: 40 (tests 5 and test 35 respectively).($\triangle$: $DR = 0.0002$ at scale 1: 20 , $\square$: $DR = 0.0012$ at scale 1: 20, $\triangledown$: $DR = 0.006$ scale 1: 40. Filled markers indicate common impacts)

2.6 Local Effects of DR

An application of the observed coincidence is that the corresponding wave impacts in different repetitions of the same irregular tank motions can be compared visually, given that there are high-speed video recordings available for all those corresponding impacts. The comparison is very interesting as the variations of the same impacts from one repetition to the other, both with the same gas and liquid can be examined. Observed changes could be described as the source of large variations of resultant loads during sloshing model tests. This is what is usually explained as stochastic behavior of sloshing. With the same basis for comparing the corresponding impacts, the effect of changing the ullage gas on every single impact can be studied visually. It can be seen what the local effects of changing the DR are. All the previous comparisons are very relevant for tracking the same impacts and comparing the effect of scaling and change of ullage gas.

Such a comparison was done for one impact at scale 1:20 as shown in Fig. 2.18 and another impact at scale 1:40 as shown in Fig. 2.19. Fig. 2.18(a) to (f) shows an impact captured in two repetitions with helium, two repetition with air, and finally two repetitions with Mix_2 respectively at scale 1:20. For all the images, wave trough is at the same level, so that the wave geometry can be compared. Free surface instabilities are different for different gases. A similarity between the wave geometries with the same gas is observed. This similarity is more obvious with air and Mix_2. It can be seen that the distance between wave front and the wall is smaller with the lighter gas of helium and larger for heavier gases. This cannot be considered as a final verdict about the local effect of DR on the wave shapes (even though gas compressibility is not into play yet for the compared moments) mainly because even between repetitions with the same gas, considerable differences are also observed which cannot be attributed to the effect of DR. Such differences give a clue as why repeating the same sloshing model tests with very controlled conditions does not give exactly the same pressure signature.

Fig. 2.19(a) to (f) shows another impact captured in two repetitions with helium, two repetitions with air, and finally two repetitions with SF_6 respectively at scale 1:40. Again for all the images, the wave trough is at the same level. Free surface instabilities are different comparing impacts with SF_6 with those with helium and air. A similarity between the wave geometries with the same gas is observed except for two repetitions with helium (This was also observed in Fig. 2.18(a) and (b)). This similarity is more obvious with air and SF_6. The distance between the wave front and the wall is larger with SF_6 than with air even before any gas compressibility influence is present. The comparison with helium is not so obvious due to already large differences in repetitions with helium. Again

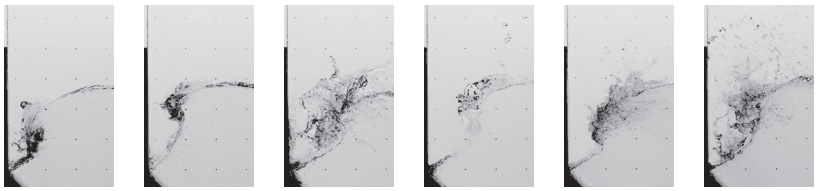

(a) (b) (c) (d) (e) (f)

Fig. 2.18. One wave impact, captured in 6 repetitions with 3 different gases at scale 1:20. (a) and (b) with helium, (c) and (d) with air, and , (e) and (f) with Mix_2. For better geometrical comparison, wave trough is at the same level in all 6 images.

between repetitions with the same gas, some differences are observed (especially with helium) which makes it difficult to draw a conclusion about the local effects of DR which as was the case for the previous figure give a hint about load variations, while repeating the same sloshing model.

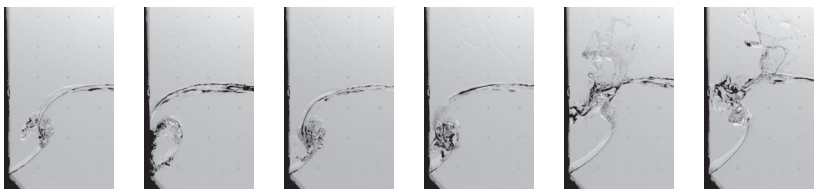

(a) (b) (c) (d) (e) (f)

Fig. 2.19. One wave impact (different from the impact depicted by Fig. 2.18), captured in 6 repetitions with 3 different gases at scale 1:40. (a) and (b) with helium, (c) and (d) with air, and , (e) and (f) with SF_6. For better geometrical comparison, wave trough is at the same level in all 6 images.

It can be concluded that one source of stochastic behavior in sloshing model tests is that exact test repetitions do not exactly generate the same impact geometries which will necessarily lead to different loading conditions. This can be studied further by comparing more impacts with many repetitions. Also concluding on the local effects of DR can not be done due to this variation of the geometry of the same exact impact event with the same gas. It is necessary (as foreseen before) to study such effects by generating single and repetitive waves as briefly introduced in Section 2.2.

2.7 Conclusions and Recommendations

By performing 2D model tests campaigns at 2 different scales of 1:20 and 1:40 at low fill level of 20% with irregular tank motions and by using water as liquid and different gases and gas mixtures in order to vary ullage gas properties while keeping the ullage gas pressure as atmospheric, wave impact times were measured by the pressure sensors and were partially also captured visually by high-speed cameras. A normal-speed HD camera captured the global fluid flow in the tanks for the duration of the irregular tests. The main focus was to study the effect of gas-liquid density ratio (DR) on the fluid flow and sloshing in a global sense. The following results could be deduced based on the results:

- The global influence of gas-liquid density ratio (DR) on sloshing wave shapes seemed to be small for the tested range of density ratios ($0.0002 - 0.006$) regardless of scale and DR which meant similar global wave shapes throughout the duration of irregular tests.

- With the same or scaled irregular tank motions, global flow keeps the same phase regardless of tested DR and scale. The notion of in phase flow enabled to recognize an accurate impact-by-impact relation (coincidence) between model tests at similar and different scales.

- The impact coincidence found based on in phase flow was investigated and confirmed by comparing recorded wave impact times of different tests,

- In the study of impact coincidence the most important parameters were proven to be firstly pressure threshold (P_{th}), triggering the measurements system which influences the number of captured impacts as well as the recorded impact times and secondly reference time window (Δt) which is crucial in detecting right or false impact coincidences. The optimum size of the reference time window for any comparison depends on scale and on the basis for defining impact times. In the performed comparisons, time window sizes of $30.0-70.0$ ms at scale 1:20, $20.0-50.0$ ms at scale 1:40, and $30.0 - 120.0$ ms for studying the coincidences between the two scales were enough to obtain at least 95% of all the detectible coincidences. Larger time window sizes are susceptible to detection of false coincidences,

- Based on the concept of coincidence, recorded high-speed videos of coincident impacts could be compared at the same or two different scales. The preliminary results show that during the same irregular tests with the same exact tank motions and with the same ullage gas, coincident impacts have similar geometries with small differences. This could be considered as one of the reasons behind the stochastic nature of pressure measurements in

sloshing model tests. Local differences between coincident impacts with different DR were observed but those cannot yet be attributed to DR since as mentioned even coincident impacts with the same DR are not always identical. Further investigation of the local effects of DR shall be done with single impact waves which are more repeatable. This will be covered in Part II of this paper.

It is suggested that based on the concept of coincidence, statistical post-processing of sloshing model test results are revisited and complemented with more deterministic comparisons. With this regard it is suggested that,

- Scaling in irregular tests is studied impact by impact. Corresponding impact pressures and forces measured in corresponding model tests at different scales can be compared with the notion of impact coincidence. This will give a better idea of the representativeness of the model tests. Statistical methods that are in use are still valuable tools but can only verify the conservatism of the model tests rather than their representativeness.
- Stochastic behavior of sloshing model tests in terms of resultant loads is studied further using the notion of impact coincidence.
- Scaling biases in irregular tests introduced by different properties of gas and liquid are studied impact by impact.
- The effect of ullage gas on impact pressures is studied impact by impact. So far the consensus is that increasing the DR will result in lower impact pressures and reducing the ullage pressure will cause more violent impacts with higher resultant pressures.
- Impact coincidence is used in relating the full-scale measurement (see Pasquier and Berthon [2009]) results of the real LNG tanks with the corresponding model tests measurements.

Chapter 3

Local Effects of Gas-Liquid Density Ratio

Abstract

[1]Gas-liquid density ratio (DR) is a key dimensionless number in sloshing assessment methodologies of membrane containment systems for LNG tanks of floating structures. Earlier studies on the effect of DR were mainly statistical and effects of DR were usually mixed with those of gas compressibility and ullage gas pressure but attributed only to DR. In an attempt to separately study such effects, part I of this work studied the effects of DR far from impact zones (global effects of gas-liquid density ratio) which proved to be small in the studied range of DR (0.0002 to 0.0060). The effects of DR near impact zones and in the instants prior to the detection of any compressibility effects are referred to as local effects and are treated in the current paper (part II).

The test setup was identical to the one presented in Part I and consisted of two 2D model tanks representing transverse slices of tank 2 (out of 4) of a membrane LNG carrier with total capacity of 152 000 m^3 at scales 1:20 and 1:40. Both model tests were performed at 20% fill level of the tank heights. Water was the main liquid that was used. In some tests at scale 1:20 a solution of sodium polytungstate (SPT) was also used which had a higher density compared to water. Different ullage gases of helium (He), air, two mixtures of sulfur hexafluoride (SF_6) and nitrogen (N_2) , and pure SF_6, all at atmospheric pressure with a range of DRs from 0.0002 to 0.0060 were utilized. Synchronized high-speed video cameras (@4000 fps) and arrays of piezoelectric PCB (112A21 and 112M361) pressure sensors (@40 kHz) monitored and measured impacts on the tank walls. In Part II of the study short and more regular tank motions which generated highly repeatable single impact waves (SIW) were used instead of long irregular tank motions which were considered in part I.

By comparing the single impact waves (SIW) generated by identical tank motions but with different DR, it was observed that DR clearly modifies wave shapes prior to the moment of wave

[1]This chapter is based on: *Effect of Ullage Gas on Sloshing - Part II. Local Effects of Gas-Liquid Density Ratio.* M. R. Karimi, L. Brosset, J.-M. Ghidaglia and M. L. Kaminski. European Journal of Mechanics - B/Fluids. Volume 57, May-June 2016, Pages 82-100. *http://dx.doi.org/10.1016/j.euromechflu.2015.11.011*

breaking. Larger DRs tend to slow down the wave front and delay breaking. It was also observed that larger DRs slightly slow down wave trough runup as well. Those effects would also lead to a mild shift of impact types by changing the DR (for example Flip-through to slosh or large gas-pocket to small gas-pocket impacts). By comparing single impact waves (SIW) generated by identical tank motions and the same DR but with different gas and liquid densities it was shown that keeping the same DR is essentially needed to keep the same impact geometry as recommended by the existing sloshing assessment methodologies. Free surface instabilities were also very similar for those waves generated with the same tank motions and similar DR but with different gases and liquids. Considering the reduction of wave kinetic energy by heavier[2] ullage gases as a relevant source of the statistical reduction of impact pressures and having in mind the mild shift of wave impact types caused by the change of DR it is still to be studied further why the heavier gas leads to smaller statistical pressures.

3.1 Introduction

3.1.1 General context of sloshing model tests and scaling issues

Sloshing model tests represent the basic tool for any sloshing assessment in LNG (liquefied natural gas) tanks of floating structures involving membrane containment systems. Among others, Gervaise et al. [2009], Kuo et al. [2009], ABS [2014], BV [2011], LR [2009] and classification note No.30.9 from DNV [2014] describe methodologies developed for such assessments. These methodologies have a lot in common. The model tank, built with smooth rigid walls generally made of transparent PMMA[3], is partially filled with water and installed on the platform of a six degree-of-freedom sloshing rig, usually an accurate Stewart platform (hexapod). Many pressure sensors (usually 300 sensors in a typical GTT[4] sloshing study) acquiring at high frequency (> 20 kHz) are arranged in rectangular arrays located in the tank areas where the most important wave impacts are expected to take place. The tests mimic at small scale all conditions that the floating structure is expected to experience during its life, covering different possible loading conditions, sea states, ship speeds, ship-wave incidences and fill levels in the studied tank. Samples of pressure peaks are gathered in order to enable long term statistics and, after a scaling process, derive design loads at a suitably low probability. Up-scaling the measured pressures is the crux of the problem as it involves large uncertainties.

Internal dimensions of model tanks are downscaled from the real internal tank geometry according to a geometric scale, λ, defined as the ratio of the dimensions

[2]throughout the paper the term *heavy gas* would refer to gases with higher density and the term *light gas* would refer to gases with lower density. This was thought to make the text easier to read (and write) compared to the terms *dense* and *less dense* although dense and less dense are more scientific. Nonetheless wherever needed, the value of DR is mentioned explicitly

[3]Poly(methyl methacrylate) commonly known under the trademark **Plexiglas**

[4]Gaztransport et Technigaz, Saint-Rémy-lès-Chevreuse, France

at full-scale (prototype) and the dimensions at model-scale. This scale is recommended not to be less than 50 according to ABS [2014], BV [2011], LR [2009] and DNV [2014]. The geometrical scale of 40 is the scale adopted by GTT. The motions of the floating structure are calculated at real scale, usually by a 3D boundary element method (BEM) and downscaled according to Froude similarity before being applied by the sloshing rig to the model tank. This means that the time scale τ is the square root of the geometric scale ($\tau = \sqrt{\lambda}$). This does not mean that the flow inside the model tank is rigorously in similarity with the real flow for a given condition. Liquid and gas properties like density, compressibility, viscosity or surface tension at the interface may be involved during certain sequences of the flow. The liquid and the gas inside the model tank should therefore have their properties relevantly scaled with regard respectively to those of LNG and of natural gas (NG) in order to comply with all similarity laws involved or, in other words, in order that the small scale flow is described by the same dimensionless problem as the full scale flow. As in reality all these requirements cannot be simultaneously fulfilled, the similarity that is expected to be imposed by Froude-scaled excitations is necessarily biased.

According to the Vaschy-Buckingham theorem (π theorem) and considering the sloshing problem with a liquid surrounded by a gas inside a tank, the gas density (ρ_g^{ms} at model scale and ρ_g^{fs} at full sale) will necessarily intervene and a new dimensionless number is to be introduced combining the gas density with the liquid density. This dimensionless number could be the Atwood number $At = \frac{\rho_l - \rho_g}{\rho_l + \rho_g}$ but, as the liquid is much denser than the gas, it is preferred, as proposed for instance by Yung et al. (2010), to introduce the density ratio $DR = \frac{\rho_g}{\rho_l}$.

Several authors studied the influence of DR on impact pressures during sloshing model tests statistically. Based on such tests performed in Marintek, Maillard and Brosset [2009] for GTT or Yung et al. [2010] for ExxonMobil observed a significant reduction of the statistical pressures when increasing the DR. They concluded that keeping the same DR at model test as at full scale ($DR \approx 0.004$) is a requirement and proposed to perform sloshing model tests with water and a right mixture of N_2 and SF_6 in order to meet this requirement. Ahn et al. [2012] drew the same conclusions based on sloshing model tests performed in Seoul National University (SNU).

3.1.2 Context of the paper

In order to experimentally study scaling issues associated with sloshing and more specifically some biases brought to Froude similarity by improperly scaled gas properties, three model tanks have been built with internal dimensions representing those of a transverse slice of the tank 2^5 of a 152 000 m^3 LNG carrier (2D

[5] Among 4 LNG tanks

tank), respectively at scales 1:40, 1:20 and 1:10. Sloshing test campaigns have been carried out with the three tanks at the same filling ratio of 20% of the tank height and for Froude-similar forced excitations in the plane of the tank (3 DOF). Mostly the tests have been performed with water and different ullage gases providing a large range of gas-liquid density ratios (DR). Some tests at scale 1:20 have also been performed with a solution of Sodium Polytungstate (SPT) with a density of $1800 kg/m^3$ with different gases. Whatever the scale, a high speed video camera was fixed to one side of the tank to capture the shape of the waves right before and during impacts. An array of pressure sensors was installed on the same side covering the impacted area. Additionally, an high definition(HD) camera also fixed to the tank recorded global deformations of free surface during the complete duration of the tests. As a result, these sloshing test campaigns allowed the study of the variability of the flow when accurately repeating the same conditions. Furthermore, the influence of liquid and gas properties, and the influence of scale, could also be studied.

This paper is the second of a series of four papers, gathering the most important results from these test campaigns. The first paper (Karimi et al. [2015b]) is based on the results at scales 1:40 and 1:20 for irregular excitations derived from calculated ship motions on a given sea state with a significant wave have height of 6 m. It showed that, if a small tolerance (tolerance in terms of impact times) is introduced, impacts always happen at about the same instants when the same condition is repeated at a given scale regardless of the utilized ullage gas. When comparing similar sloshing model tests at two different scales with Froude-similar excitations, the impacts happen at Froude-similar instants. This observation is done regularly from the beginning up to the end of long sloshing model tests and does not deteriorate over time. The impacts that happen almost at the same instants (considering the accepted tolerance) regardless of scale or the utilized ullage gas, are referred to as *coincident impacts*. In between two successive impacts, when the wave front is far from the impact areas, the shape of the free surface repeats pretty well when repeating the same condition. This is also true when changing the gases for the range of DR studied. Nevertheless, the shape variations can still be clearly distinguished. The sources of variability seem to come firstly from free surface instabilities that develop just before the impacts during the gas escaping phase while the wave front approaches the wall and secondly from the fall of droplets after the splashing following wave impacts. Nevertheless, the perturbations brought by these different sources vanish quickly enough to prevent a progressive deterioration of the flow that would induce an increasing variability. In brief, the effective memory of the flow is short and the notion of a global flow complying with Froude similarity makes sense.

Part III of this study will be presented in a third paper in preparation. It will show the comparison of statistics from measured pressure peaks at the three

different scales. Part IV will be presented in a fourth paper also in preparation. Taking benefit of the short *effective memory* observed by Karimi et al. [2015b], it will show that the characteristics of a given impact obtained during irregular tests could be conserved when generated by a short excitation corresponding to the original motions before the impact time. The influence of the excitation duration on the variability, therefore on the pressure statistics, will be presented. Possible changes on the way to perform sloshing model tests will be envisaged. Some of these results have already been presented in Karimi et al. [2015a].

3.1.3 Objectives of this paper and overview

In the final section of Karimi et al. [2015b], comparisons of the wave shapes obtained just before impact (actually before any compression of the gas) for coincident impacts generated by repetitions of the same irregular excitation but for different ullage gases were introduced. Fig. 3.1 is extracted from this section and shows wave shapes for a coincident impact at scale 1:20 obtained with water and three different gases. Two repetitions with the same gas are given at each time, leading to six different snapshots.

Despite some obvious variations observed when comparing the wave shapes obtained by repeating the condition with the same gas, it seems that a distinctive influence of ullage gas is present. First, free surface instabilities (Kelvin-Helmholtz and Rayleigh-Plateau, see Drazin and Reid [2004]), especially present at the crest level where the shearing gas flow is supposed to be the most violent, appear differently with the different gases. Their development was believed to depend mainly on surface tension and viscosity. But focusing on the overall wave shape from the trough to the base of the crest, other differences are observed that can only be attributed to the different DRs. In Braeunig et al. [2009], the authors explain that there is a transfer of momentum from the liquid to the gas before any liquid impact when the liquid forces the gas to escape in between the wave and the wall. By a parametric numerical study of a simple liquid impact they illustrate that the heavier the gas, the larger this transfer of momentum is.

Scolan et al. [2014] presented the bi-fluid version of a 2D code FSID, simulating the generation and propagation of waves along a wave canal. FSID[6] is a non-linear potential solver for incompressible flows based on a succession of conformal mappings and a desingularized technique (Scolan [2010]). In Scolan et al. [2014], showing the breaking wave shapes introduced by Karimi and Brosset [2014] , a comparison between the wave shapes obtained before impact for a large breaking wave with the bi-fluid (water and air) and with the mono-fluid (water and vacuum) version of FSID was presented. The gas flow seems to impede slightly the breaking process leading to a delay of the wave front and a deviation

[6]Free Surface IDendification

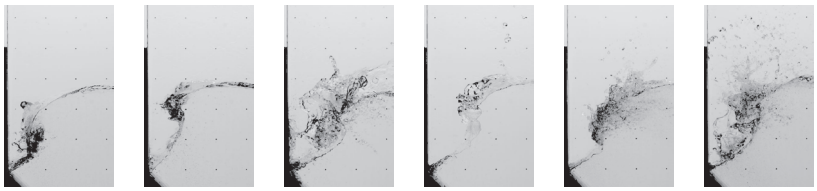

(a) (b) (c) (d) (e) (f)

Fig. 3.1. Snapshots obtained for a coincident impact (for the definition of coincident impact see Karimi et al. [2015b]) at scale 1:20 with three different ullage gases. (a) and (b) with helium, (c) and (d) with air, (e) and (f) with a mixture of nitrogen and SF_6 with a density ratio $DR = 0.002$.

upwards of the wave crest. Same trends were obtained by Guilcher et al. [2014] when comparing breaking wave shapes simulated on the one hand by a SPH[7] bi-fluid solver and on the other hand by the mono-fluid version of FSID.

This paper presents the influence of DR on the wave shapes just before impacts but prior to any compression of the gas. This influence is investigated using sloshing tests at scale 1:20 with short regular tank excitations. Every short regular tank excitation is designed to generate one unique impact. Such a short excitation is referred to as a Single Impact Wave excitation, or SIW and leads to a highly repeatable wave shape before impact which enables us to make a deterministic study on the influence of DR on the local flow. This local influence can be observed in slightly different wave shapes generated by the same tank motion but with different ullage gases.

The wave shapes are compared through snapshots captured by the high speed camera at instants before any compression in the escaping gas in between the wave crest and the wall. This is checked through the pressure signals recorded by the sensors at the wall. Before the selected instant, the loads on the wall are only induced by the runup of the wave trough. This type of load is a typical hydrodynamic load induced by the change of momentum imposed by the wall to the liquid. According to the classification proposed by **?**, this is a pure ELP2 (Elementary Loading Process, type 2: building jet) characterized by an easily identifiable upward moving pressure pulse.

After checking the repeatability of the generated wave shapes, the paper presents results for four different SIW excitations leading to different types of breaking waves before impact. At each time the test is repeated with water and three different gases, therefore for four different DRs.

Finally, results are also given for four different SIW excitations repeated twice:

[7] smoothed particle hydrodynamics

firstly with water and air, secondly with SPT (Sodium Polytungstate) and a mixture of gases tuned in order to keep the same DR.

3.2 Test Setup

The test setup and all measures taken to insure the maximum accuracy have been described in detail by Karimi et al. [2015b]. A summary of the test setup elements and those measures will also be outlined here. Two model test campaigns were performed at scales 1:20 and 1:40 with 2D tanks and 3DOF motions at 20% fill level (of the tank height). The internal dimensions of the tanks at both scale are shown in Fig. 3.2. The tanks were made out of PMMA due to its rigidity and transparency to enable observation.

High-speed cameras (Photron at scale 1:20 and Phantom (Vision Research) at scale 1:40) and an high definition(HD) camera (Canon XF105) were used to capture the local impacts and the global fluid flow in the tank respectively. High-speed cameras recorded at 4000 fps at both scales. A simple camera was also used to verify the fill level. See Fig. 3.2 for a schematic presentation of the locations of the cameras and the pressure sensor modules with respect to the tank.

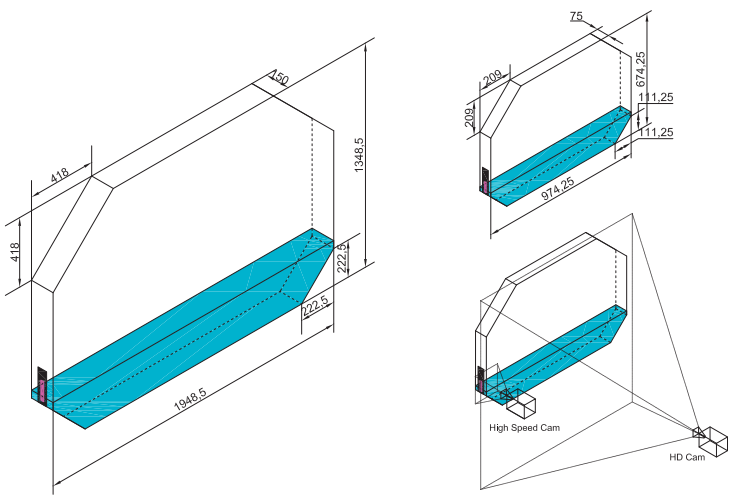

Fig. 3.2. Isometric illustrations of internal tank dimensions and pressure sensor module locations at scales 1:40 and 1:20 and the schematic positioning of cameras demonstrated at scale 1:40

At scale 1:20, 126 PCB (112A21 and 112M361) pressure sensors were used,

installed on a 21 × 6 array on one side of the tank. At scale 1:40, 60 PCB (112A21 and 112M361) pressure sensors were used, installed on a 15 × 4 array on the corresponding side of the tank. The sampling rate of all the pressure sensors was 40 kHz. The vertical and horizontal distance between the centers of all sensors were 10 mm at both scales. The sensing area of each circular sensor had a diameter of 5.5 mm. The sensors were triggered with a pressure threshold which meant that only wave impacts with a maximum local pressure higher than this threshold were measured. The pressure threshold was adjusted to be able to record the desired impacts. Sensor modules at both scales are shown in *Fig.* 3.3 separately and superimposed after upscaling the module geometry at scale 1:40 by the geometrical scale factor of 2.

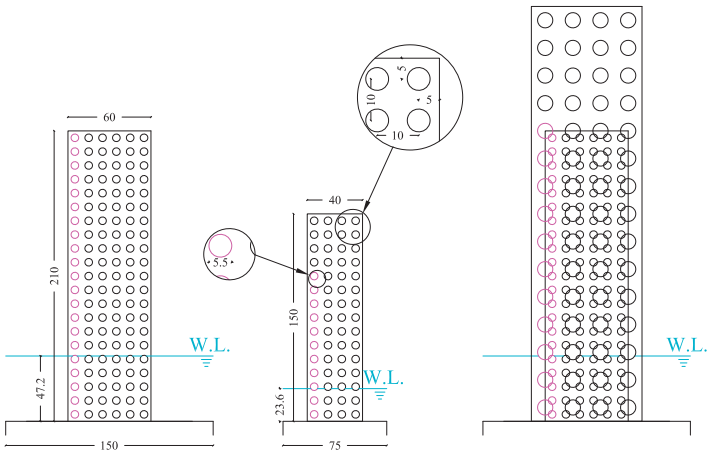

Fig. 3.3. Sensor modules at scale 1:20 and scale 1:40 and their superimposition after scaling the geometries to scale 1:20

In this paper the measurements of one column of pressure sensors highlighted magenta as shown in Fig. 3.3 were used. This column of pressure sensors was closest to the observation window and could be used for the best synchronization between the high-speed camera recordings and pressure measurements. Throughout the paper 3 color gray-scale legends are superimposed on the left side of each of the images recorded by high-speed cameras in order to help identify the location of corresponding sensors (see Fig. 3.6 together with Fig. 3.7 as an example).

Since the local effects of DR were of interest different ullage gases were tested at both scales. Water was used as the main liquid at both scales. At scale 1:20

a solution of sodium polytungstate (SPT) with a density of 1800 kg/m^3 was also utilized. The tested liquids and gases as well as the achieved range of DRs at the two scales are listed in Table 3.1 and Table 3.2. Ullage pressure for all DRs was atmospheric to avoid any possible influence due to ullage pressure fluctuation.

Table 3.1. Liquids and gases, nominal densities, and density ratios used for tests at scale 1:20. Mix_2 and Mix_4 are two mixtures of N_2 and SF_6 with densities of 2 and 4 kg/m^3 respectively.

Group	Gas	Liquid	$\rho_g(kg/m^3)$	$\rho_l(kg/m^3)$	$DR(-)$
1	helium	water	0.18	997	0.0002
2	air	water	1.15	997	0.0012
3	Mix_2	water	2.00	997	0.0020
4	Mix_4	water	4.00	997	0.0040
5	air	SPT	1.15	1800	0.0006
6	Mix_2	SPT	2.00	1800	0.0011

Table 3.2. Liquids and gases, nominal densities, and density ratios used for tests at scale 1:40. Mix_2 is a mixture of N_2 and SF_6 with a density of 2 kg/m^3.

Group	Gas	Liquid	$\rho_g(kg/m^3)$	$\rho_l(kg/m^3)$	$DR(-)$
1	helium	water	0.18	997	0.0002
2	air	water	1.15	997	0.0012
3	Mix_2	water	2.00	997	0.0020
4	SF_6	water	6.00	997	0.0060

Long duration irregular tank motions based on simulated and scaled ship motions were used to study the global effects of density ratio detailed by Karimi et al. [2015b]. To study the local effects of density ratio, short excitations enabling the generation of repeatable single impact waves were utilized. The single impact wave motions were based on 1 DOF sway motions of the tank with no roll or heave.

A range of single impact waves were generated and tested with the theoretical period of $T = 2.4692s$ at scale 1:20 ($T = 1.746s$ at scale 1:40) corresponding to the estimation of the lowest natural sloshing frequency and different sway motion amplitudes. The estimation of the lowest natural frequency was given by the equation $\omega_0 = \sqrt{(g\pi/b) \times \tanh(\pi h/b)}$ were $b = 1.9485m$ and $h = 0.2697m$ (see Abramson [1966]). The beginning and the end of the motion signals (the first and the last quarter) were not harmonic but generated by cubic splines to provide a smooth transition from/to stationary tank conditions and only the middle section was completely half a period of a harmonic as depicted by Fig. 3.4. Four representative tank motion signals which were also used in the comparisons in this paper are given in Table 3.3, Table 3.4, Table 3.5 and Table 3.6. Since all

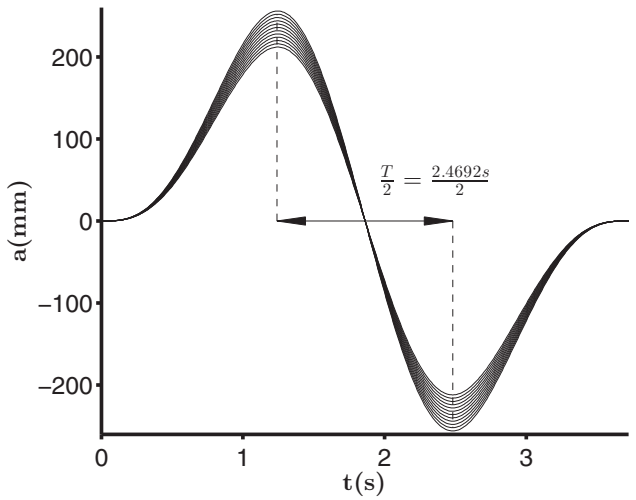

Fig. 3.4. Sway motion signals at scale 1:20 which were used to perform a sweep of motion amplitudes corresponding to a period of $T = 2.4692\,s$ and different amplitudes to create different single impact waves (SIW).

the generated waves corresponded to the same period, wave periods would not be outlined in the text unless necessary in order to avoid repetition.

The resulting wave shapes covered a range from mild slosh, flip through (see Cooker and D.H.Peregrine [1990]) and gas pocket impact types as shown by Fig. 3.5 which was ideal for studying the local effects of density ratio. In a slosh impact wave does not break on the wall and tends to virtually break after the wall hence no gas pocket is entrapped. The flip through impact type is associated with the formation of a high-speed vertical jet and is the intermediate impact type between slosh and gas pocket impact types. In a gas pocket impact type a gas pocket, small or large, is entrapped between the wave front and the wall.

Before performing the tests, tank alignment, fill level, accurate tank motions and environmental conditions were verified and confirmed to be sufficiently accurate. The procedure for those steps has been described in more detail by Karimi et al. [2015b].

It should be noted that throughout the following comparisons, the time references adopted in pressure signal graphs are unique to the corresponding comparisons and do not correspond to the tank motion time references.

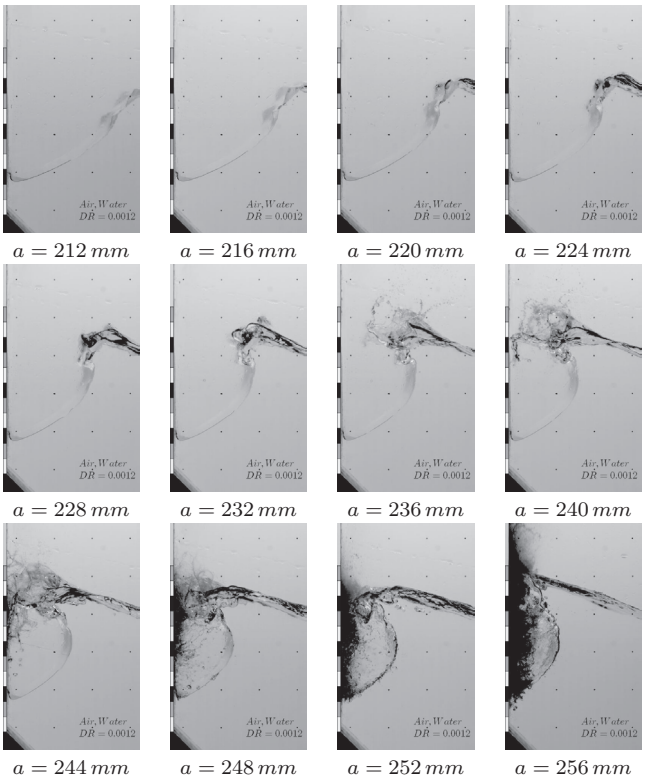

Fig. 3.5. Distinctive breaking wave shapes generated at scale 1:20 using the sway motion signals given in Fig. 3.4

3.3 Repeatability

Repeatability of breaking wave geometries, wave kinematics and resulting pressures were of importance in this study. Accuracy and controlled test conditions led to highly repeatable wave shapes. This repeatability as verified is presented here by comparing breaking shapes in two cases at scale 1:40 in Fig. 3.6 and Fig. 3.8 and one case at scale 1:20 in Fig. 3.9. Impact pressures are also shown for one of the cases at scale 1:40 in Fig. 3.7. Less repetitions were available at scale 1:20.

Fig. 3.6 shows 4 breaking waves generated by repetitions of the same tank motions with an amplitude of $a = 114mm$ at scale 1:40. The same tank motions lead to breaking wave shapes which compare reasonably well as far as the wave

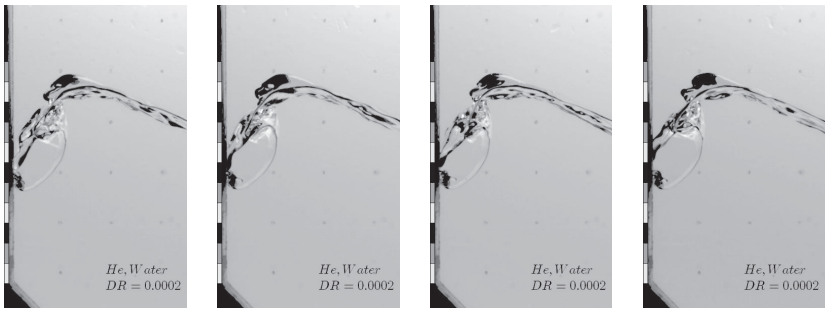

$a = 114\,mm$ (a) *Rep. 1* | $a = 114\,mm$ (b) *Rep. 2* | $a = 114\,mm$ (c) *Rep. 3* | $a = 114\,mm$ (d) *Rep. 4*

Fig. 3.6. Repeatable breaking wave shapes demonstrated with snapshots from high-speed camera recordings, obtained from 4 repetitions of the same tank motions with $a = 114\,mm$ and $T = 1.746\,s$ at scale 1:40

trough and front are considered. The free surface instabilities are comparable but still different for all the repetitions. Such free surface instabilities are considered to be a source of variability of measured pressures.

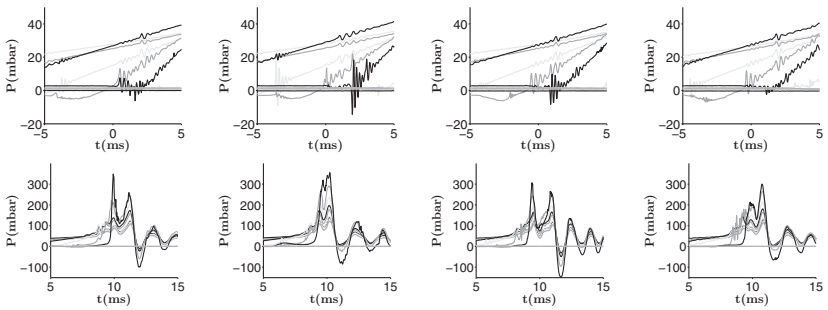

(a) *Rep. 1* (b) *Rep. 2* (c) *Rep. 3* (d) *Rep. 4*

Fig. 3.7. Pressure signals measured for four repeatable SIW presented in Fig. 3.6

In order to compare the pressure signals corresponding to these four repetitions, the signals are studied in two time intervals which respectively reflect a phase were the load is due to the upward runup and the following phase of the impact when oscillatory loads due to gas pocket entrapment are measured as shown by Fig. 3.7. For each repetition the right image is selected and then the time scale for pressure signals is adjusted such that $t = 0$ corresponds to the chosen image in order to facilitate comparison. In other words the wave shapes

shown by Fig. 3.6 correspond to $t = 0$ on pressure signals i.e. the time reference at each graph is selected to correspond to the chosen image.

For the period of $t = -5$ to $t = +5\,ms$, the pressure signals compare reasonably well in terms of amplitude. For $t = 5\,ms$ to $t = 15\,ms$ which actually corresponds to the main impact, larger variations can be seen as expected since very small variations in wave shape and free surface instabilities still exist which will mostly influence this part of the pressure signals. Besides, the limited number of pressure sensors will lead to an incomplete pressure map which is unavoidable.

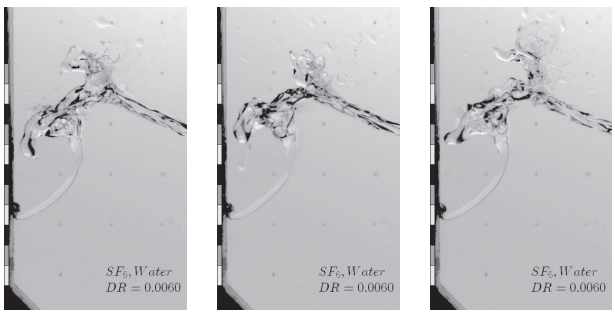

$a = 118\,mm$ (a) *Rep. 1* $a = 118\,mm$ (b) *Rep. 2* $a = 118\,mm$ (c) *Rep. 3*

Fig. 3.8. Repeatable breaking wave shapes demonstrated with snapshots from high-speed camera recordings, obtained from 3 repetitions of the same tank motions with $a = 118\,mm$ and $T = 1.746\,s$ at scale 1:40

Fig. 3.8 shows 3 breaking waves which were obtained by the same tank motions corresponding to $a = 118mm$ at scale 1:40. Again repeatability of the wave front shape is good even though differences due to free surface instabilities still exist.

Fig. 3.9 shows 2 breaking waves which were obtained by the same tank motions corresponding to $a = 240mm$ at scale 1:20. Free surface instabilities are the main source of variability but wave fronts are still repeatable.

Despite small differences of wave shapes as depicted for 3 cases, the differences are not substantial and can be neglected in later comparisons especially since the differences are observed less in wave front region which will be compared later on. Differences of pressure measurements are inevitable and do not concern the following comparisons.

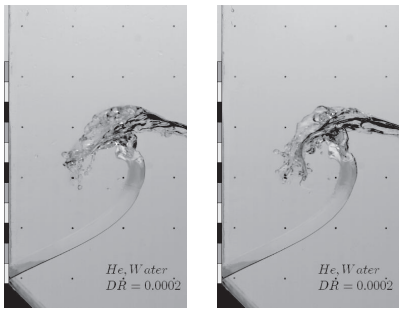

$a = 240\,mm$ (a) *Rep. 1* $a = 240\,mm$ (b) *Rep. 2*

Fig. 3.9. Repeatable breaking wave shapes demonstrated with snapshots from high-speed camera recordings, obtained from 3 repetitions of the same tank motions with $a = 240\,mm$ and $T = 2.4692\,s$ at scale 1:20

3.4 Local Effects of DR

The local effects of DR were investigated by varying the DR while keeping the same tank SIW excitations and all the other environmental conditions including the ullage gas pressure. Wave shapes were regularly monitored and the induced pressures were recorded for each generated wave in a synchronized manner. It was important to record the induced pressures to make sure that compressibility effects were not yet present in every comparison otherwise possible observed differences could not be attributed solely to DR. In this paper the comparisons were only made at scale 1:20.

3.4.1 Scale 1:20, $T = 2.4692\,s$, $a = 228\,mm$

Fig. 3.10 shows four SIW waves, all corresponding to the period of $T = 2.4692\,s$ and the amplitude of $a = 228\,mm$. Water is the common liquid for all four waves whereas different gases of helium, air, Mix_2, and Mix_4 provide a range of density ratios. In order to be able to compare the wave shapes, the corresponding times of the snapshots have been chosen in order that the wave troughs on the wall are at the same level.

Fig. 3.11 shows the pressure signals measured from $15\,ms$ before until the depicted moment in Fig. 3.10. The moment captured by each image corresponds to $t = 0\,ms$ on pressure signals. By looking at the high-speed video images the differences are in terms of wave shapes. The differences are more obvious considering the wave fronts. The lowest DR of 0.0002 corresponds to a further

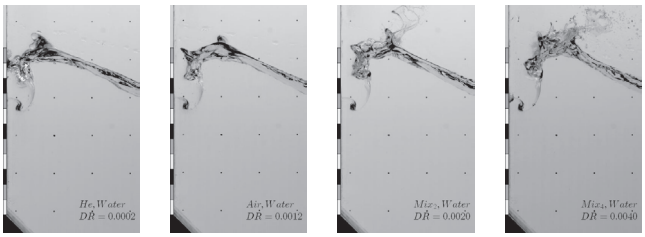

$a = 228\,mm$ (a) $a = 228\,mm$ (b) $a = 228\,mm$ (c) $a = 228\,mm$ (d)

Fig. 3.10. The same tank motions with different DR and the generated breaking waves at scale 1:20 for a motion amplitude of $a = 228\,mm$ and the period of $T = 2.4692\,s$. Corresponding tank motion time history is given by Table 3.4.

progressed wave front which has started to break whereas the highest DR of 0.004 corresponds to a less progressed front which has not yet started to break. The two intermediate density ratios of 0.0012 and 0.0020 lead to intermediate wave shapes. Free surface instabilities appear to be more pronounced with higher DR.

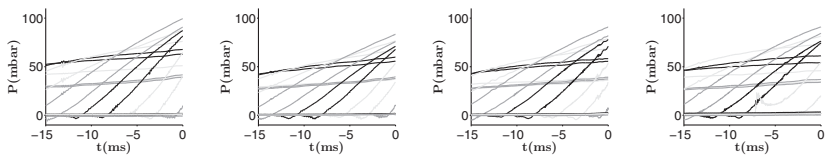

(a) (b) (c) (d)

Fig. 3.11. Measured pressure signals corresponding to the impacts demonstrated in Fig.3.10 from 15 ms before up to the moment shown by Fig.3.10. $t = 0$ corresponds to images shown in Fig.3.10.

By looking at the pressure signals as shown in Fig. 3.11, the measured loads are merely induced by the trough and no gas compression is recorded yet in the upper areas of the pressure sensor module. In other words the shape differences observed in Fig. 3.10 can only be attributed to a difference in DR. Transfer of momentum between approaching liquid (wave front) and escaping gas changes by varying density ratio which leads to different impact geometry and kinematics thus wave impacts with the same excitations but different density ratios are not the same geometrically and kinematically.

3.4.2 Scale 1:20, $T = 2.4692\,s$, $a = 236\,mm$

Fig. 3.12 shows another group of four SIW waves, all corresponding to the period of $T = 2.4692\,s$ and the amplitude of $a = 236\,mm$. In order to be able to compare the wave shapes, the corresponding times of the snapshots have been chosen in order that the wave troughs on the wall are at the same level.

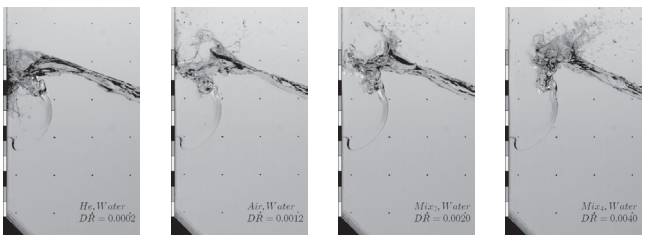

$a = 236\,mm$ (a) $a = 236\,mm$ (b) $a = 236\,mm$ (c) $a = 236\,mm$ (d)

Fig. 3.12. The same tank motions with different DR and the generated breaking waves at scale 1:20 for a motion amplitude of $a = 236\,mm$ and the period of $T = 2.4692\,s$. Corresponding tank motion time history is given by Table 3.5.

As shown in Fig. 3.12 with the lowest DR of 0.0002 obtained with helium, the wave has already started to break as the droplets touch the sensors and the applied load can be seen as pressure increase shown in Fig. 3.13(a). For the same wave with the same tank motions but the highest DR of 0.0040 corresponding to Mix_4 the wave is still far from the wall and breaking. The depicted snapshots correspond to $t = 0\,ms$ on the pressure signals. The wave is slowed down more by the heavier gas. This is only due to the effect of DR without any intervention from gas compressibility yet as the pressure sensors in the gas pocket zone has not yet measured any compression. Free surface instabilities are clearly distinctive with different DR.

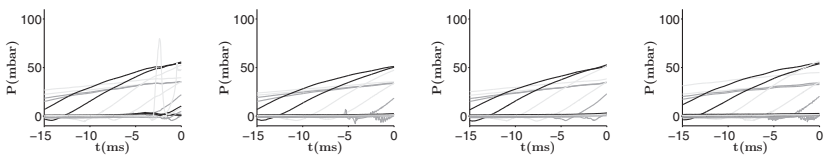

(a) (b) (c) (d)

Fig. 3.13. Measured pressure signals corresponding to the impacts demonstrated in Fig.3.12 from 15 ms before up to the moment shown by Fig.3.12. $t = 0$ corresponds to images shown in Fig.3.12.

In Fig. 3.12 (a) as the wave tends to break earlier, instabilities disturb the impact region whereas in Fig. 3.12 (d) due to the effect of higher DR, the geometry near the impact zone is more regular and less disturbed by the instabilities and instead the instabilities are blown and pushed backwards by the stream of escaping gas.

3.4.3 Additional Comparisons

The local effects of DR on breaking wave geometry can be investigated with a range of SIW impacts as presented before. Two additional examples are given by Fig. 3.14 to Fig. 3.17.

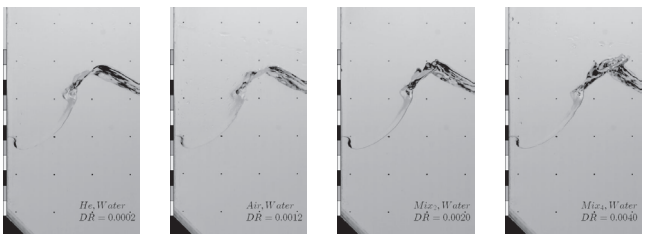

$a = 216\,mm$ (a) $a = 216\,mm$ (b) $a = 216\,mm$ (c) $a = 216\,mm$ (d)

Fig. 3.14. The same tank motions with different DR and the generated breaking waves at scale 1:20 for a motion amplitude of $a = 216\,mm$ and the period of $T = 2.4692\,s$. Corresponding tank motion time history is given by Table 3.3.

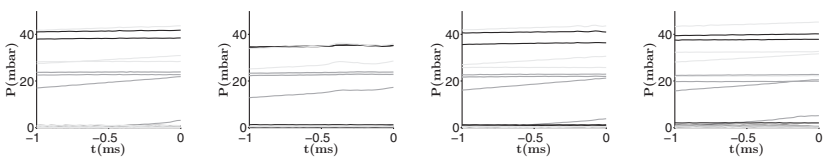

(a) (b) (c) (d)

Fig. 3.15. Measured pressure signals corresponding to the impacts demonstrated in Fig.3.14 from 1 ms before up to the moment shown by Fig.3.14. $t = 0$ corresponds to images shown in Fig.3.14.

In both cases and as expected increasing the density ratio leads to less and less advanced wave fronts. Again this influence is observed where gas compressibility is not yet in action. In Fig. 3.16 similar to that observed in Fig. 3.12 the waves tend to break earlier with lighter gases and so instabilities disturb the

impact region more with lower DR whereas with higher DR impact region is more regular and less disturbed by the instabilities which are blown backwards by the escaping gas.

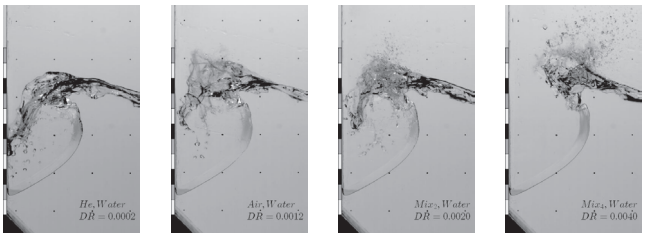

$a = 244\,mm$ (a) $a = 244\,mm$ (b) $a = 244\,mm$ (c) $a = 244\,mm$ (d)

Fig. 3.16. The same tank motions with different DR and the generated breaking waves at scale 1:20 for a motion amplitude of $a = 244\,mm$ and the period of $T = 2.4692\,s$. Corresponding tank motion time history is given by Table 3.6

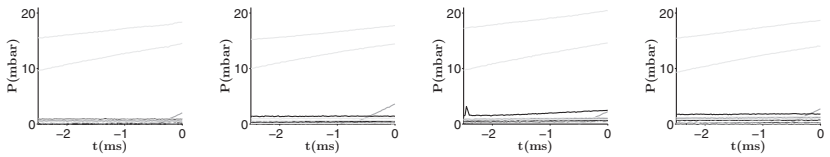

(a) (b) (c) (d)

Fig. 3.17. Measured pressure signals corresponding to the impacts demonstrated in Fig.3.16 from 2.5 ms before up to the moment shown by Fig.3.16. $t = 0$ corresponds to images shown in Fig.3.16.

Fig. 3.18 summarizes the wave geometry comparisons for all the four considered SIW by extracting and superimposing the wave profiles with different density ratios for each SIW. In this figure and for all the four considered amplitudes, there is a clear difference between the profiles obtained by the lowest and the highest density ratios as explained earlier but the difference between the wave profiles with the intermediate density ratios of 0.0012 and 0.0020 is not that obvious. In this figure wave profiles are plotted without considering the free surface instabilities.

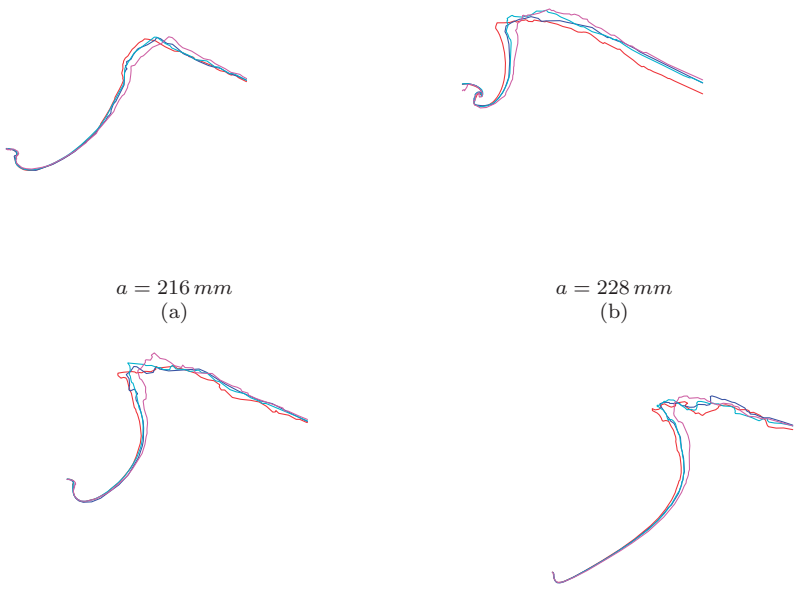

Fig. 3.18. Superimposed wave profiles for two SIW motions and different gases and liquids at scale 1:20 (a) $a = 216\ mm$ (based on Fig. 3.14) (b) $a = 228\ mm$ (based on Fig. 3.10) (c) $a = 236\ mm$ (based on Fig. 3.12) (d) $a = 244\ mm$ (based on Fig. 3.16) ($DR = 0.0002$: —, $DR = 0.0012$: —, $DR = 0.0020$: —, $DR = 0.0040$: —)

3.5 Local Effect of DR on Vertical Trough Speed

The effect of DR on wave kinematics was further investigated by monitoring wave trough position and average velocity. To do this a small observation window on the original snapshots was selected as depicted by Fig. 3.19. For sequences of images the vertical trough position could be monitored in this observation window. In order to compare trough positions for waves generated with identical tank motions but with different DR, initial snapshots of high-speed camera recordings were selected at first for those waves in such a way that for all of them troughs were at the same level. Those images defined a new time reference denoted by t' with $t' = 0$ corresponding to the moment where troughs were all at the same level. By monitoring the next frames and placing the observation windows of different gases next to each other, the effect of DR could be visually observed as

shown in Fig. 3.20 for the waves already shown in Fig. 3.10.

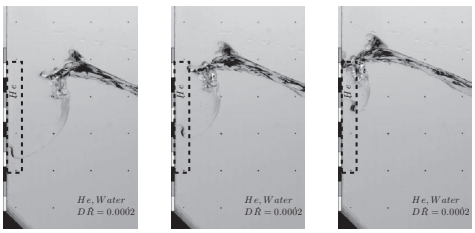

$a = 228\,mm$ $t' = 0$ *(a)*

$a = 228\,mm$ $t' = +9.25\,ms$ *(b)*

$a = 228\,mm$ $t' = +18.5\,ms$ *(c)*

Fig. 3.19. Observation window defined to track vertical runup and find the trough position and speed for waves presented in Fig. 3.10 and the studied time instants demonstrated for the case of Fig. 3.10 (a). It should be noted that the time references and the chosen instants are different in this figure and Fig. 3.10.

Fig. 3.20(a) shows the reference time where troughs are set at the same level for all the waves. After $9.25\,ms$ the trough level for four waves changes slightly showing a faster trough with the lowest density ratio and a slower trough with the highest density ratio. After $18.5\,ms$ this difference is more pronounced as shown in 3.20(c).

This comparison from the beginning to the end involved 75 frames captured at 4000 fps. Using those frames and knowing the camera's frame rate, an estimation of the average trough speed could be given. Due to change of image contrast in the images, finding the exact trough position included errors and was slightly subjective. This meant that over small distances, the estimation included bigger errors. Over larger distances on the other hand errors were much less pronounced. Average vertical trough speed was found using 75 available frames, by finding the speed on the basis of distance travelled every 10, 20, 40 and 50 frames and the corresponding average vertical trough speed could be given respectively in parts (a), (b), (c) and (d) of Fig. 3.21.

As shown in Fig. 3.21 (a) it is not quite clear whether the more local speed is higher with lighter gas. By calculating the average vertical trough speed based on a larger number of frames (Fig. 3.21(d)), the dependence of trough speed on DR becomes more obvious.

Trough position and velocity were similarly checked for the condition presented previously in Fig. 3.12. Again an observation window is defined as shown in Fig. 3.22 and a new time reference is introduced. Fig. 3.23 compares wave trough positions for four waves presented in Fig. 3.12 at three time instants. After $8.25\,ms$ the trough levels for four waves change again showing the fastest

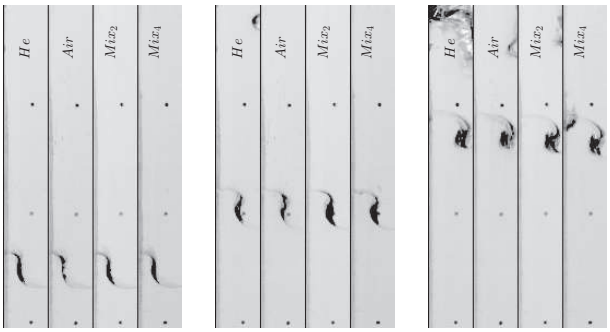

$a = 228\,mm$ $t' = 0$ *(a)*

$a = 228\,mm$ $t' = +9.25\,ms$ *(b)*

$a = 228\,mm$ $t' = +18.5\,ms$ *(c)*

Fig. 3.20. Trough speed is compared for four SIW demonstrated in Fig. 3.10 by selecting a time instant at the beginning so that the troughs are at the same level and then monitoring their vertical motion. Larger density ratios appear to slightly slow down to trough.

trough with the lowest density ratio and a slower trough with the highest density ratio. After $16.5\,ms$ this difference is larger as depicted in 3.23(c). In total 67 frames were used in this comparison.

3.6 The Same DR with Different Gas and/or Liquid

For the state of the art sloshing model tests, gas-liquid density ratio is kept the same between the model-scale and full-scale (along with the essential Froude similar tank geometry and motions) in order to have the scaled transfer of momentum between the liquid and gas. In this study by keeping the same DR and identical tank motions but with different gases and liquids it was also verified whether DR was indeed an influential dimensionless number.

For this comparison the same SIW were generated with a solution of SPT (Sodium Plytungstate) as liquid and Mix_2 as gas which corresponded to approximately the same DR as obtained with water and air. The chosen cases for comparison correspond to four amplitudes of $a = 212\,mm$, $a = 224\,mm$, $a = 236\,mm$, and $a = 248\,mm$ as depicted by Fig. 3.24.

Similar to the previous comparisons, every couple of waves is considered while the trough is at the same level for both waves in that couple. Fig. 3.24 summarizes the comparison in which the wave geometry and kinematic seem very

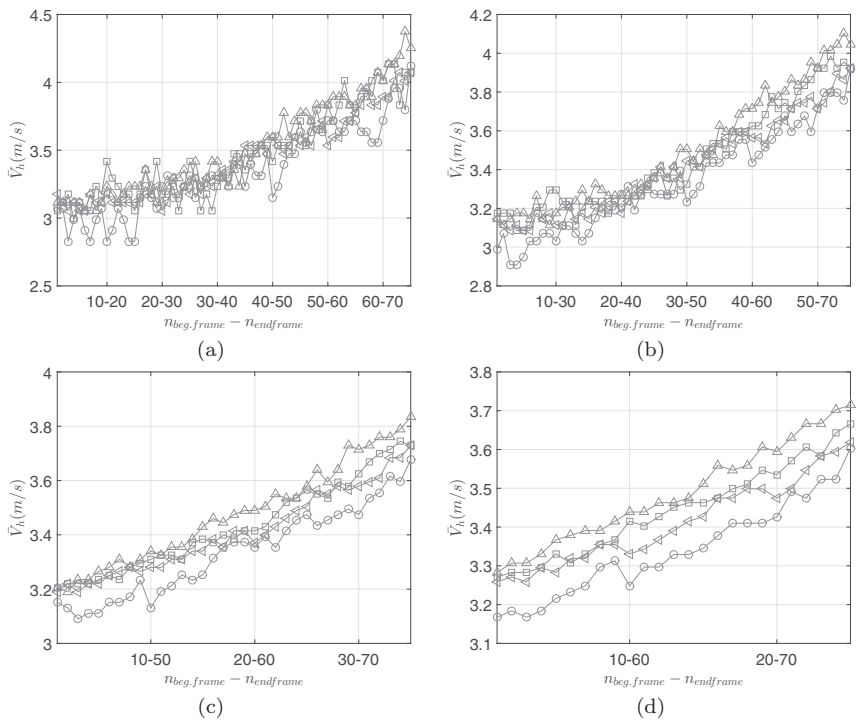

Fig. 3.21. Average vertical trough speed $\bar{V}_h$ calculated based on tracking the trough edge in 75 frames of high-speed video recordings corresponding to the comparisons shown in Fig. 3.19 and Fig. 3.20. The time difference between two consecutive frames is $0.25\,ms$. The average speed is found between (a) 10, (b) 20, (c) 40 and (d) 50 consecutive frames. ($\triangle:\ DR = 0.0002$, $\square:\ DR = 0.0012$, $\triangleleft:\ DR = 0.002$, $\circ:\ DR = 0.004$)

similar by keeping the same tank motions and geometry as well as DR regardless of the liquid and gas. This comparison is more emphasized comparing the superimposed wave profiles as presented in Fig. 3.25.

Regarding Fig. 3.24 it is also observed that by keeping the same DR not only the overall wave shapes are preserved, free surface instabilities are also quite comparable regardless of utilized gases and liquids.

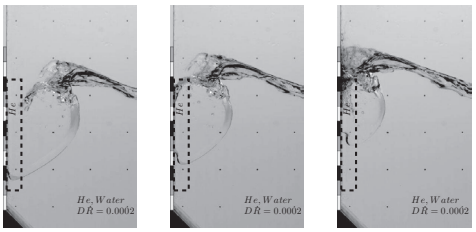

$a = 236\,mm$ $t' = 0$ *(a)*

$a = 236\,mm$ $t' = +8.25\,ms$ *(b)*

$a = 236\,mm$ $t' = +16.5\,ms$ *(c)*

Fig. 3.22. Observation window defined to track vertical runup and find the trough position and speed for waves presented in Fig. 3.12 and the studied time instants demonstrated for the wave shown in Fig. 3.12 (a). It should be noted that the time references and the chosen instants are different in this figure and Fig. 3.12.

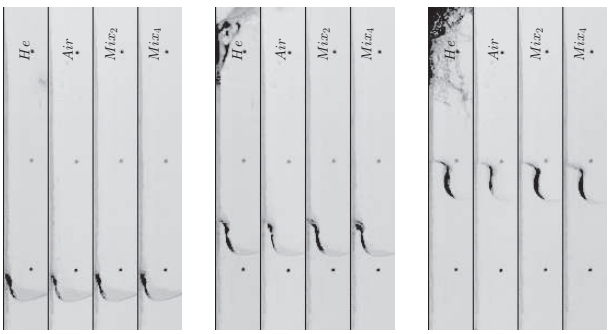

$a = 236\,mm$ $t' = 0$ *(a)*

$a = 236\,mm$ $t' = +8.25\,ms$ *(b)*

$a = 236\,mm$ $t' = +16.5\,ms$ *(c)*

Fig. 3.23. Trough speed is compared for four SIW demonstrated in Fig. 3.12 by selecting a time instant at the beginning so that the troughs are at the same level and then monitoring the vertical motion. Larger density ratios appear to slightly slow down the trough.

3.7 Conclusion and Discussion

2D Sloshing model tests were performed at scales 1:40 and 1:20 at 20% fill level (of the tank height). The model tanks represented a transverse slice of tank 2 of a LNG carrier with a capacity of 152 000 m^3 with 4 tanks. At scale 1:20, either water or a solution of sodium polytungstate (SPT) with a density of $1800 kg/m^3$

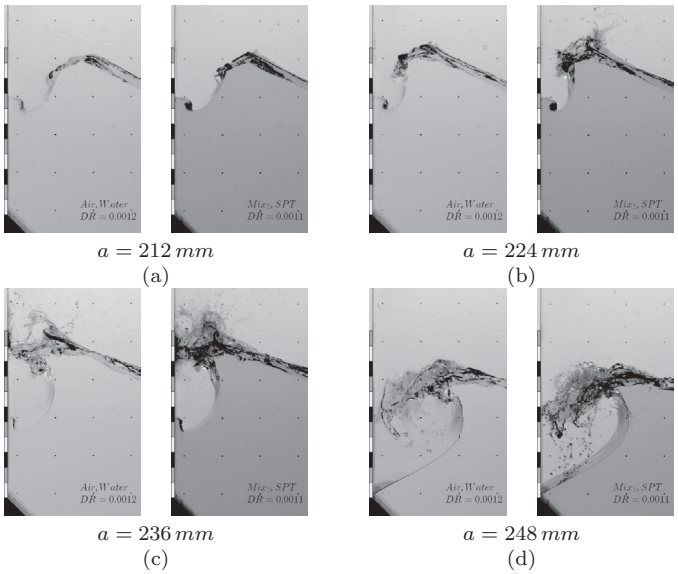

Fig. 3.24. Comparison between wave impacts created with the same tank motions and close DR for 4 motion amplitudes and the period of $T = 2.4692\,s$ at scale 1:20.

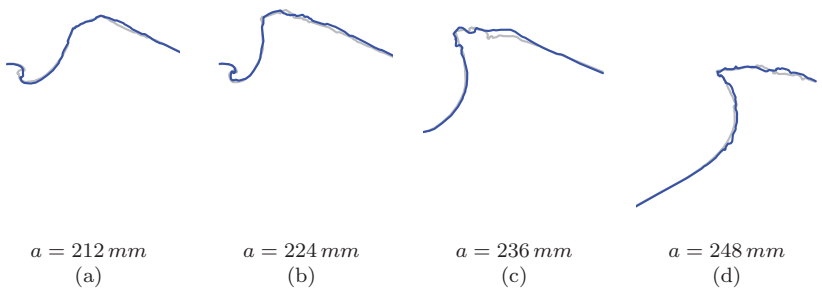

Fig. 3.25. Superimposed wave profiles for breaking waves presented in Fig. 3.24 ($DR = 0.0012$: —, $DR = 0.0011$: —)

were used as liquid whereas at scale 1:40 only water was utilized. Different ullage gases of helium, air, two mixtures of N_2 and SF_6 with densities of $2kg/m^3$ and $4kg/m^3$ and pure SF_6 were used. For each model tank the main instrumentation consisted of a rectangular array of pressure sensors with the acquisition frequency

of 40 kHz and a high speed camera recording at 4000 fps. The sensor array was installed on one side of the tank and covered the impact areas. The video camera was fixed to the tank on the same side as the sensor array in order to capture wave shapes before and during impacts. The camera and the data acquisition system were synchronized.

Short sway excitations were used to enable generation of single impacts (SIW) in the tanks. The sway motions were designed by the composition of a half period of sine and two cubic splines as ending ramps respectively from/to rest. The variations of the harmonic amplitude led to various breaking wave shapes ranging from soft slosh to large gas pocket and including flip-through impact types, as could be obtained in a flume by moving the focal point when generating the waves by a focusing technique (see Bogaert et al. [2010a] for instance). Wave shapes were compared before the impacts, prior to any compression of the escaping gas in between the wave and the wall. During this phase whatever the kind of wave impact studied, the load recorded by the sensors is induced by a building jet runup from the trough along the wall.

Such SIW excitations led to accurate repetitions of wave shapes before impact when the test conditions were repeated, as shown on Fig. 3.6, Fig. 3.8 and Fig. 3.9. By those examples it was shown that wave fronts remain smooth and precisely repeatable from the trough to the base of the crest. The corresponding pressures induced by the building jet at the trough are also repeatable. Only around the crest, where free surface instabilities develop due to the shearing gas flow, some differences can be distinguished. As a consequence, variations of the pressure signals induced by the crest impact are significant. The free surface instabilities seemed to be the main source of variability.

Four different cases at scale 1:20 were presented to demonstrate the local effects of DR. At each case, 4 waves were generated with water and four different ullage gases of helium, air, Mix_2 and Mix_4. The following trends were observed at each case:

- The free surface remains smooth from trough to the base of the crest whatever the ullage gas,
- Free surface instabilities develop around the crest. Their development depends on the ullage gas,
- For the smooth part of the wave front, the higher the DR, the less advanced the breaking process is. The denser gas seems to slow down the process and reduce the wave front velocity,
- The influence of DR increases from trough to crest,

- For higher DRs, the speed of the upward building jet from the trough is slightly reduced. This should also lead to slightly smaller pressures in this region for higher DRs.

- There is a reduction of wave kinetic energy right before impact caused by heavier ullage gases. This can be considered as one of the reasons why statistically heavier ullage gases lead to lower impact pressures.

The numerical results presented in Scolan et al. [2014] and in Guilcher et al. [2014] fit qualitatively well with the experimental conclusions. Braeunig et al. [2009] explained the influence of DR on the wave shape before any compression of the gas by a transfer of mechanical energy from the liquid to the gas. The higher the DR, the larger this transfer is, therefore the remaining energy of the liquid is more reduced. This explanation is in line with our experimental conclusions. It can be considered as a global explanation for the reduction of the statistical pressures when using a ullage gas with higher DR during sloshing model tests, as observed by by Maillard and Brosset [2009], Yung et al. [2010] and Ahn et al. [2012].

As stated also in Braeunig et al. [2009], changing the DR leads to changing the impact conditions and therefore the nature of impact as it is considered that impact type and shape influences the loads. The impeding of the breaking process, as it has been observed during our study, could magnify the impact pressures or mitigate them when increasing the DR depending on the initial wave shape chosen: a broken wave could potentially become a large gas pocket impact, a large gas pocket impact could become a small gas pocket impact and a small gas pocket impact could become a flip-through. This sequence would generally lead to larger impact pressures. But, on the other hand, a flip-through could become a sharp slosh, a sharp slosh could become a mild slosh and so forth. And this sequence would generally lead to smaller impact pressures. Therefore, the impeding of the breaking process is not sufficient to explain the detailed mechanism of the statistical pressure reduction.

For waves obtained with lower DR, impact areas were in general more disturbed due to the presence of free surface instabilities as a result of earlier wave breaking which can potentially lead to more stochasticity in pressure measurements. In case of higher DR impact areas were more regular and less disturbed as instabilities were blown and pushed away from the impact regions by the escaping gas flow. This in turn can potentially lead to less stochastic impact pressures. The intensity of the observed effect is also a function of the studied wave shape and could be more or less pronounced.

By generating the same waves with identical tank motions, using two different liquids and choosing the ullage gases in order to get the same DR, the wave shapes are found to be reasonably repeatable. Therefore it is found that adjusting the

DR is a key parameter in sloshing model tests in order to obtain the desired impact conditions. It was observed that by adjusting the same DR free surface instabilities were also reasonably similar regardless of utilized gases and liquids. This means that adjusting the DR is influential in order to get the same free surface instabilities.

These results help to understand that there is a hierarchy among the different similarity laws to comply with when performing sloshing model tests. Froude similarity for the forced excitations is the foundation on which the experimental model is built. As a result of Karimi et al. [2015b], when considering repetitions of the same condition at a given scale, the variability brought during each impact by both the generation of free surface instabilities and splashing damp quickly enough to prevent a progressive deterioration of the global flow. Moreover, when considering tests at two different scales with Froude-scaled excitations, the biases brought to Froude similarity during each impact by the improperly scaled properties of the fluids also damp quickly enough to prevent a progressive deterioration of Froude similarity for the global flow. Without this property, sloshing model tests would not have any relevance. As a result of the current paper, density ratio similarity is also necessary to prevent any systematic bias in the impact conditions.

The other similarity laws related to gas and liquid properties such as compressibility and viscosity or surface tension at the free surface or phase transition phenomenon come later in the list. Most of the time, viscosity and surface tension are disregarded and considered as secondary properties. As these properties are directly linked to free surface instabilities generated by shearing gas flow prior to every impact, they should be considered as important sources of variability for sloshing and therefore the related similarity laws should also be studied as they are crucial for statistics of sloshing loads.

3.8 Sway Motion Signals at Scale 1:20

Table 3.3. Sway tank motions at scale 1:20 corresponding to SIW with the amplitude of 216 mm

t(s)	Y(mm)	t(s)	Y(mm)	t(s)	Y(mm)	t(s)	Y(mm)	t(s)	Y(mm)	t(s)	Y(mm)
0.00	-000.0000	0.63	+067.3520	1.26	+215.8540	1.89	+001.0100	2.52	-215.9180	3.15	-068.3250
0.01	-000.0000	0.64	+070.0110	1.27	+215.9860	1.90	-004.4860	2.53	-215.7000	3.16	-065.6920
0.02	-000.0000	0.65	+072.7080	1.28	+215.9790	1.91	-009.9790	2.54	-215.3500	3.17	-063.0980
0.03	-000.0000	0.66	+075.4410	1.29	+215.8330	1.92	-015.4660	2.55	-214.8690	3.18	-060.5470
0.04	-000.0000	0.67	+078.2080	1.30	+215.5470	1.93	-020.9430	2.56	-214.2630	3.19	-058.0390
0.05	+000.0010	0.68	+081.0080	1.31	+215.1220	1.94	-026.4060	2.57	-213.5330	3.20	-055.5760
0.06	+000.0050	0.69	+083.8390	1.32	+214.5570	1.95	-031.8520	2.58	-212.6840	3.21	-053.1590
0.07	+000.0150	0.70	+086.6990	1.33	+213.8540	1.96	-037.2780	2.59	-211.7180	3.22	-050.7900
0.08	+000.0360	0.71	+089.5860	1.34	+213.0110	1.97	-042.6790	2.60	-210.6390	3.23	-048.4690
0.09	+000.0700	0.72	+092.4970	1.35	+212.0310	1.98	-048.0530	2.61	-209.4510	3.24	-046.1990
0.10	+000.1200	0.73	+095.4320	1.36	+210.9140	1.99	-053.3960	2.62	-208.1560	3.25	-043.9790
0.11	+000.1880	0.74	+098.3880	1.37	+209.6600	2.00	-058.7040	2.63	-206.7580	3.26	-041.8120
0.12	+000.2790	0.75	+101.3630	1.38	+208.2700	2.01	-063.9740	2.64	-205.2600	3.27	-039.6970
0.13	+000.3930	0.76	+104.3540	1.39	+206.7460	2.02	-069.2020	2.65	-203.6650	3.28	-037.6360
0.14	+000.5350	0.77	+107.3590	1.40	+205.0870	2.03	-074.3860	2.66	-201.9780	3.29	-035.6300
0.15	+000.7060	0.78	+110.3760	1.41	+203.2960	2.04	-079.5220	2.67	-200.2000	3.30	-033.6790
0.16	+000.9080	0.79	+113.4030	1.42	+201.3730	2.05	-084.6060	2.68	-198.3360	3.31	-031.7850
0.17	+001.1450	0.80	+116.4380	1.43	+199.3200	2.06	-089.6350	2.69	-196.3880	3.32	-029.9470
0.18	+001.4170	0.81	+119.4770	1.44	+197.1380	2.07	-094.6070	2.70	-194.3590	3.33	-028.1670
0.19	+001.7280	0.82	+122.5190	1.45	+194.8280	2.08	-099.5170	2.71	-192.2540	3.34	-026.4440
0.20	+002.0780	0.83	+125.5610	1.46	+192.3920	2.09	-104.3620	2.72	-190.0750	3.35	-024.7790
0.21	+002.4700	0.84	+128.6000	1.47	+189.8310	2.10	-109.1400	2.73	-187.8260	3.36	-023.1720
0.22	+002.9060	0.85	+131.6340	1.48	+187.1480	2.11	-113.8480	2.74	-185.5080	3.37	-021.6250
0.23	+003.3870	0.86	+134.6600	1.49	+184.3430	2.12	-118.4820	2.75	-183.1270	3.38	-020.1360
0.24	+003.9150	0.87	+137.6760	1.50	+181.4190	2.13	-123.0390	2.76	-180.6840	3.39	-018.7060
0.25	+004.4910	0.88	+140.6790	1.51	+178.3770	2.14	-127.5160	2.77	-178.1840	3.40	-017.3340
0.26	+005.1160	0.89	+143.6660	1.52	+175.2200	2.15	-131.9110	2.78	-175.6280	3.41	-016.0220
0.27	+005.7920	0.90	+146.6350	1.53	+171.9500	2.16	-136.2200	2.79	-173.0210	3.42	-014.7680
0.28	+006.5200	0.91	+149.5820	1.54	+168.5680	2.17	-140.4410	2.80	-170.3650	3.43	-013.5730
0.29	+007.3010	0.92	+152.5060	1.55	+165.0770	2.18	-144.5710	2.81	-167.6630	3.44	-012.4360
0.30	+008.1360	0.93	+155.4020	1.56	+161.4790	2.19	-148.6080	2.82	-164.9190	3.45	-011.3560
0.31	+009.0260	0.94	+158.2680	1.57	+157.7760	2.20	-152.5480	2.83	-162.1350	3.46	-010.3330
0.32	+009.9720	0.95	+161.1020	1.58	+153.9720	2.21	-156.3900	2.84	-159.3140	3.47	-009.3670
0.33	+010.9730	0.96	+163.9000	1.59	+150.0670	2.22	-160.1300	2.85	-156.4590	3.48	-008.4570
0.34	+012.0320	0.97	+166.6590	1.60	+146.0660	2.23	-163.7670	2.86	-153.5730	3.49	-007.6020
0.35	+013.1480	0.98	+169.3770	1.61	+141.9700	2.24	-167.2970	2.87	-150.6600	3.50	-006.8010
0.36	+014.3220	0.99	+172.0500	1.62	+137.7820	2.25	-170.7190	2.88	-147.7210	3.51	-006.0540
0.37	+015.5540	1.00	+174.6760	1.63	+133.5050	2.26	-174.0310	2.89	-144.7600	3.52	-005.3590
0.38	+016.8450	1.01	+177.2510	1.64	+129.1410	2.27	-177.2300	2.90	-141.7790	3.53	-004.7150
0.39	+018.1950	1.02	+179.7720	1.65	+124.6940	2.28	-180.3140	2.91	-138.7820	3.54	-004.1210
0.40	+019.6030	1.03	+182.2360	1.66	+120.1660	2.29	-183.2820	2.92	-135.7700	3.55	-003.5760
0.41	+021.0700	1.04	+184.6400	1.67	+115.5600	2.30	-186.1310	2.93	-132.7470	3.56	-003.0780
0.42	+022.5970	1.05	+186.9810	1.68	+110.8790	2.31	-188.8590	2.94	-129.7160	3.57	-002.6250
0.43	+024.1810	1.06	+189.2560	1.69	+106.1270	2.32	-191.4650	2.95	-126.6780	3.58	-002.2170
0.44	+025.8250	1.07	+191.4620	1.70	+101.3060	2.33	-193.9470	2.96	-123.6370	3.59	-001.8520
0.45	+027.5260	1.08	+193.5940	1.71	+096.4190	2.34	-196.3040	2.97	-120.5950	3.60	-001.5270
0.46	+029.2860	1.09	+195.6510	1.72	+091.4700	2.35	-198.5330	2.98	-117.5540	3.61	-001.2410
0.47	+031.1030	1.10	+197.6290	1.73	+086.4610	2.36	-200.6340	2.99	-114.5180	3.62	-000.9910
0.48	+032.9760	1.11	+199.5250	1.74	+081.3970	2.37	-202.6050	3.00	-111.4880	3.63	-000.7760
0.49	+034.9070	1.12	+201.3350	1.75	+076.2800	2.38	-204.4440	3.01	-108.4670	3.64	-000.5940
0.50	+036.8920	1.13	+203.0560	1.76	+071.1130	2.39	-206.1520	3.02	-105.4570	3.65	-000.4420
0.51	+038.9330	1.14	+204.6850	1.77	+065.9010	2.40	-207.7260	3.03	-102.4600	3.66	-000.3180
0.52	+041.0280	1.15	+206.2190	1.78	+060.6460	2.41	-209.1650	3.04	-099.4790	3.67	-000.2190
0.53	+043.1760	1.16	+207.6540	1.79	+055.3510	2.42	-210.4690	3.05	-096.5170	3.68	-000.1420
0.54	+045.3770	1.17	+208.9870	1.80	+050.0210	2.43	-211.6370	3.06	-093.5740	3.69	-000.0860
0.55	+047.6290	1.18	+210.2150	1.81	+044.6580	2.44	-212.6670	3.07	-090.6530	3.70	-000.0470
0.56	+049.9310	1.19	+211.3340	1.82	+039.2660	2.45	-213.5600	3.08	-087.7570	3.71	-000.0220
0.57	+052.2820	1.20	+212.3420	1.83	+033.8490	2.46	-214.3150	3.09	-084.8870	3.72	-000.0080
0.58	+054.6820	1.21	+213.2340	1.84	+028.4100	2.47	-214.9300	3.10	-082.0450	3.73	-000.0010
0.59	+057.1280	1.22	+214.0090	1.85	+022.9530	2.48	-215.4070	3.11	-079.2340	3.74	-000.0000
0.60	+059.6200	1.23	+214.6610	1.86	+017.4810	2.49	-215.7440	3.12	-076.4540	3.75	-000.0000
0.61	+062.1550	1.24	+215.1880	1.87	+011.9970	2.50	-215.9420	3.13	-073.7080	3.76	-000.0000
0.62	+064.7330	1.25	+215.5870	1.88	+006.5060	2.51	-215.9990	3.14	-070.9980	3.77	-000.0000

Table 3.4. Sway tank motions at scale 1:20 corresponding to SIW with the amplitude of 228 mm

t(s)	Y(mm)	t(s)	Y(mm)	t(s)	Y(mm)	t(s)	Y(mm)	t(s)	Y(mm)	t(s)	Y(mm)
0.00	-000.0000	0.63	+071.0940	1.26	+227.8460	1.89	+001.0660	2.52	-227.9130	3.15	-072.1210
0.01	-000.0000	0.64	+073.9010	1.27	+227.9850	1.90	-004.7350	2.53	-227.6840	3.16	-069.3410
0.02	-000.0000	0.65	+076.7470	1.28	+227.9780	1.91	-010.5340	2.54	-227.3130	3.17	-066.6040
0.03	-000.0000	0.66	+079.6320	1.29	+227.8240	1.92	-016.3250	2.55	-226.8070	3.18	-063.9100
0.04	-000.0000	0.67	+082.5530	1.30	+227.5220	1.93	-022.1060	2.56	-226.1660	3.19	-061.2630
0.05	+000.0010	0.68	+085.5080	1.31	+227.0730	1.94	-027.8730	2.57	-225.3960	3.20	-058.6630
0.06	+000.0050	0.69	+088.4970	1.32	+226.4770	1.95	-033.6220	2.58	-224.4990	3.21	-056.1120
0.07	+000.0160	0.70	+091.5150	1.33	+225.7340	1.96	-039.3490	2.59	-223.4800	3.22	-053.6110
0.08	+000.0380	0.71	+094.5630	1.34	+224.8450	1.97	-045.0500	2.60	-222.3410	3.23	-051.1620
0.09	+000.0740	0.72	+097.6360	1.35	+223.8110	1.98	-050.7230	2.61	-221.0870	3.24	-048.7650
0.10	+000.1260	0.73	+100.7340	1.36	+222.6310	1.99	-056.3620	2.62	-219.7200	3.25	-046.4220
0.11	+000.1990	0.74	+103.8540	1.37	+221.3080	2.00	-061.9650	2.63	-218.2440	3.26	-044.1340
0.12	+000.2940	0.75	+106.9940	1.38	+219.8410	2.01	-067.5280	2.64	-216.6630	3.27	-041.9020
0.13	+000.4150	0.76	+110.1510	1.39	+218.2320	2.02	-073.0470	2.65	-214.9800	3.28	-039.7270
0.14	+000.5650	0.77	+113.3230	1.40	+216.4810	2.03	-078.5190	2.66	-213.1990	3.29	-037.6100
0.15	+000.7450	0.78	+116.5080	1.41	+214.5910	2.04	-083.9400	2.67	-211.3220	3.30	-035.5510
0.16	+000.9590	0.79	+119.7030	1.42	+212.5610	2.05	-089.3060	2.68	-209.3540	3.31	-033.5510
0.17	+001.2080	0.80	+122.9060	1.43	+210.3940	2.06	-094.6150	2.69	-207.2980	3.32	-031.6110
0.18	+001.4960	0.81	+126.1150	1.44	+208.0900	2.07	-099.8630	2.70	-205.1570	3.33	-029.7310
0.19	+001.8240	0.82	+129.3250	1.45	+205.6520	2.08	-105.0450	2.71	-202.9350	3.34	-027.9130
0.20	+002.1940	0.83	+132.5360	1.46	+203.0800	2.09	-110.1600	2.72	-200.6350	3.35	-026.1550
0.21	+002.6080	0.84	+135.7440	1.47	+200.3780	2.10	-115.2040	2.73	-198.2600	3.36	-024.4600
0.22	+003.0680	0.85	+138.9470	1.48	+197.5450	2.11	-120.1730	2.74	-195.8140	3.37	-022.8260
0.23	+003.5750	0.86	+142.1410	1.49	+194.5840	2.12	-125.0640	2.75	-193.3010	3.38	-021.2540
0.24	+004.1320	0.87	+145.3250	1.50	+191.4980	2.13	-129.8740	2.76	-190.7230	3.39	-019.7450
0.25	+004.7400	0.88	+148.4950	1.51	+188.2870	2.14	-134.6000	2.77	-188.0830	3.40	-018.2980
0.26	+005.4010	0.89	+151.6480	1.52	+184.9550	2.15	-139.2390	2.78	-185.3860	3.41	-016.9120
0.27	+006.1140	0.90	+154.7810	1.53	+181.5030	2.16	-143.7880	2.79	-182.6340	3.42	-015.5890
0.28	+006.8830	0.91	+157.8920	1.54	+177.9330	2.17	-148.2430	2.80	-179.8300	3.43	-014.3270
0.29	+007.7070	0.92	+160.9780	1.55	+174.2480	2.18	-152.6030	2.81	-176.9780	3.44	-013.1260
0.30	+008.5880	0.93	+164.0350	1.56	+170.4500	2.19	-156.8640	2.82	-174.0810	3.45	-011.9870
0.31	+009.5280	0.94	+167.0610	1.57	+166.5420	2.20	-161.0230	2.83	-171.1420	3.46	-010.9070
0.32	+010.5260	0.95	+170.0520	1.58	+162.5260	2.21	-165.0780	2.84	-168.1650	3.47	-009.8880
0.33	+011.5830	0.96	+173.0060	1.59	+158.4050	2.22	-169.0260	2.85	-165.1510	3.48	-008.9270
0.34	+012.7000	0.97	+175.9180	1.60	+154.1810	2.23	-172.8650	2.86	-162.1050	3.49	-008.0240
0.35	+013.8780	0.98	+178.7870	1.61	+149.8570	2.24	-176.5910	2.87	-159.0300	3.50	-007.1790
0.36	+015.1180	0.99	+181.6090	1.62	+145.4360	2.25	-180.2040	2.88	-155.9280	3.51	-006.3900
0.37	+016.4180	1.00	+184.3800	1.63	+140.9220	2.26	-183.6990	2.89	-152.8020	3.52	-005.6570
0.38	+017.7810	1.01	+187.0980	1.64	+136.3160	2.27	-187.0760	2.90	-149.6560	3.53	-004.9770
0.39	+019.2060	1.02	+189.7590	1.65	+131.6210	2.28	-190.3320	2.91	-146.4920	3.54	-004.3500
0.40	+020.6920	1.03	+192.3600	1.66	+126.8420	2.29	-193.4640	2.92	-143.3130	3.55	-003.7740
0.41	+022.2410	1.04	+194.8980	1.67	+121.9800	2.30	-196.4710	2.93	-140.1220	3.56	-003.2490
0.42	+023.8520	1.05	+197.3690	1.68	+117.0390	2.31	-199.3510	2.94	-136.9220	3.57	-002.7710
0.43	+025.5250	1.06	+199.7710	1.69	+112.0230	2.32	-202.1020	2.95	-133.7160	3.58	-002.3410
0.44	+027.2600	1.07	+202.0980	1.70	+106.9340	2.33	-204.7220	2.96	-130.5060	3.59	-001.9550
0.45	+029.0560	1.08	+204.3500	1.71	+101.7760	2.34	-207.2090	2.97	-127.2950	3.60	-001.6120
0.46	+030.9130	1.09	+206.5210	1.72	+096.5510	2.35	-209.5630	2.98	-124.0850	3.61	-001.3090
0.47	+032.8310	1.10	+208.6080	1.73	+091.2650	2.36	-211.7800	2.99	-120.8800	3.62	-001.0460
0.48	+034.8080	1.11	+210.6090	1.74	+085.9190	2.37	-213.8610	3.00	-117.6820	3.63	-000.8190
0.49	+036.8460	1.12	+212.5200	1.75	+080.5180	2.38	-215.8020	3.01	-114.4930	3.64	-000.6270
0.50	+038.9420	1.13	+214.3370	1.76	+075.0640	2.39	-217.6050	3.02	-111.3150	3.65	-000.4670
0.51	+041.0960	1.14	+216.0560	1.77	+069.5620	2.40	-219.2660	3.03	-108.1520	3.66	-000.3350
0.52	+043.3070	1.15	+217.6750	1.78	+064.0150	2.41	-220.7850	3.04	-105.0060	3.67	-000.2310
0.53	+045.5750	1.16	+219.1900	1.79	+058.4260	2.42	-222.1620	3.05	-101.8790	3.68	-000.1500
0.54	+047.8980	1.17	+220.5970	1.80	+052.8000	2.43	-223.3940	3.06	-098.7720	3.69	-000.0910
0.55	+050.2750	1.18	+221.8930	1.81	+047.1390	2.44	-224.4820	3.07	-095.6900	3.70	-000.0490
0.56	+052.7050	1.19	+223.0750	1.82	+041.4480	2.45	-225.4240	3.08	-092.6320	3.71	-000.0230
0.57	+055.1870	1.20	+224.1390	1.83	+035.7300	2.46	-226.2210	3.09	-089.6030	3.72	-000.0080
0.58	+057.7200	1.21	+225.0810	1.84	+029.9890	2.47	-226.8710	3.10	-086.6030	3.73	-000.0020
0.59	+060.3020	1.22	+225.8980	1.85	+024.2280	2.48	-227.3740	3.11	-083.6360	3.74	-000.0000
0.60	+062.9320	1.23	+226.5860	1.86	+018.4520	2.49	-227.7300	3.12	-080.7020	3.75	-000.0000
0.61	+065.6080	1.24	+227.1430	1.87	+012.6640	2.50	-227.9390	3.13	-077.8030	3.76	-000.0000
0.62	+068.3300	1.25	+227.5640	1.88	+006.8670	2.51	-228.0000	3.14	-074.9430	3.77	-000.0000

Table 3.5. Sway tank motions at scale 1:20 corresponding to SIW with the amplitude of 236 mm

t(s)	Y(mm)	t(s)	Y(mm)	t(s)	Y(mm)	t(s)	Y(mm)	t(s)	Y(mm)	t(s)	Y(mm)
0.00	-000.0000	0.63	+073.5890	1.26	+235.8400	1.89	+001.1040	2.52	-235.9110	3.15	-074.6520
0.01	-000.0000	0.64	+076.4940	1.27	+235.9840	1.90	-004.9010	2.53	-235.6730	3.16	-071.7740
0.02	-000.0000	0.65	+079.4400	1.28	+235.9770	1.91	-010.9030	2.54	-235.2890	3.17	-068.9410
0.03	-000.0000	0.66	+082.4260	1.29	+235.8180	1.92	-016.8980	2.55	-234.7650	3.18	-066.1530
0.04	-000.0000	0.67	+085.4490	1.30	+235.5050	1.93	-022.8820	2.56	-234.1020	3.19	-063.4130
0.05	+000.0010	0.68	+088.5090	1.31	+235.0410	1.94	-028.8510	2.57	-233.3050	3.20	-060.7220
0.06	+000.0050	0.69	+091.6020	1.32	+234.4240	1.95	-034.8020	2.58	-232.3770	3.21	-058.0810
0.07	+000.0170	0.70	+094.7260	1.33	+233.6550	1.96	-040.7290	2.59	-231.3210	3.22	-055.4930
0.08	+000.0390	0.71	+097.8800	1.34	+232.7350	1.97	-046.6310	2.60	-230.1430	3.23	-052.9570
0.09	+000.0760	0.72	+101.0620	1.35	+231.6640	1.98	-052.5020	2.61	-228.8440	3.24	-050.4760
0.10	+000.1310	0.73	+104.2690	1.36	+230.4430	1.99	-058.3400	2.62	-227.4300	3.25	-048.0510
0.11	+000.2060	0.74	+107.4980	1.37	+229.0730	2.00	-064.1390	2.63	-225.9020	3.26	-045.6830
0.12	+000.3040	0.75	+110.7480	1.38	+227.5550	2.01	-069.8970	2.64	-224.2650	3.27	-043.3730
0.13	+000.4300	0.76	+114.0160	1.39	+225.8890	2.02	-075.6100	2.65	-222.5230	3.28	-041.1210
0.14	+000.5840	0.77	+117.2990	1.40	+224.0770	2.03	-081.2740	2.66	-220.6790	3.29	-038.9290
0.15	+000.7710	0.78	+120.5960	1.41	+222.1200	2.04	-086.8850	2.67	-218.7370	3.30	-036.7980
0.16	+000.9920	0.79	+123.9040	1.42	+220.0190	2.05	-092.4400	2.68	-216.7000	3.31	-034.7280
0.17	+001.2510	0.80	+127.2190	1.43	+217.7760	2.06	-097.9350	2.69	-214.5720	3.32	-032.7200
0.18	+001.5480	0.81	+130.5400	1.44	+215.3920	2.07	-103.3670	2.70	-212.3560	3.33	-030.7750
0.19	+001.8880	0.82	+133.8630	1.45	+212.8680	2.08	-108.7310	2.71	-210.0560	3.34	-028.8920
0.20	+002.2700	0.83	+137.1870	1.46	+210.2060	2.09	-114.0260	2.72	-207.6750	3.35	-027.0730
0.21	+002.6990	0.84	+140.5070	1.47	+207.4080	2.10	-119.2460	2.73	-205.2170	3.36	-025.3180
0.22	+003.1750	0.85	+143.8220	1.48	+204.4760	2.11	-124.3890	2.74	-202.6850	3.37	-023.6270
0.23	+003.7010	0.86	+147.1290	1.49	+201.4120	2.12	-129.4520	2.75	-200.0830	3.38	-022.0000
0.24	+004.2770	0.87	+150.4240	1.50	+198.2170	2.13	-134.4310	2.76	-197.4150	3.39	-020.4380
0.25	+004.9070	0.88	+153.7050	1.51	+194.8940	2.14	-139.3230	2.77	-194.6820	3.40	-018.9400
0.26	+005.5900	0.89	+156.9690	1.52	+191.4440	2.15	-144.1250	2.78	-191.8900	3.41	-017.5060
0.27	+006.3290	0.90	+160.2120	1.53	+187.8710	2.16	-148.8330	2.79	-189.0420	3.42	-016.1360
0.28	+007.1240	0.91	+163.4330	1.54	+184.1760	2.17	-153.4450	2.80	-186.1400	3.43	-014.8300
0.29	+007.9780	0.92	+166.6260	1.55	+180.3620	2.18	-157.9570	2.81	-183.1880	3.44	-013.5870
0.30	+008.8900	0.93	+169.7910	1.56	+176.4310	2.19	-162.3680	2.82	-180.1890	3.45	-012.4070
0.31	+009.8620	0.94	+172.9230	1.57	+172.3850	2.20	-166.6730	2.83	-177.1470	3.46	-011.2900
0.32	+010.8950	0.95	+176.0190	1.58	+168.2280	2.21	-170.8700	2.84	-174.0650	3.47	-010.2350
0.33	+011.9890	0.96	+179.0760	1.59	+163.9630	2.22	-174.9570	2.85	-170.9460	3.48	-009.2400
0.34	+013.1460	0.97	+182.0910	1.60	+159.5910	2.23	-178.9300	2.86	-167.7930	3.49	-008.3060
0.35	+014.3650	0.98	+185.0600	1.61	+155.1150	2.24	-182.7880	2.87	-164.6100	3.50	-007.4310
0.36	+015.6480	0.99	+187.9810	1.62	+150.5400	2.25	-186.5270	2.88	-161.3990	3.51	-006.6150
0.37	+016.9950	1.00	+190.8500	1.63	+145.8660	2.26	-190.1450	2.89	-158.1640	3.52	-005.8550
0.38	+018.4050	1.01	+193.6630	1.64	+141.0990	2.27	-193.6400	2.90	-154.9070	3.53	-005.1520
0.39	+019.8790	1.02	+196.4170	1.65	+136.2390	2.28	-197.0100	2.91	-151.6320	3.54	-004.5030
0.40	+021.4180	1.03	+199.1100	1.66	+131.2920	2.29	-200.2520	2.92	-148.3420	3.55	-003.9070
0.41	+023.0210	1.04	+201.7370	1.67	+126.2600	2.30	-203.3650	2.93	-145.0390	3.56	-003.3630
0.42	+024.6890	1.05	+204.2950	1.68	+121.1460	2.31	-206.3460	2.94	-141.7270	3.57	-002.8690
0.43	+026.4200	1.06	+206.7800	1.69	+115.9530	2.32	-209.1930	2.95	-138.4080	3.58	-002.4230
0.44	+028.2160	1.07	+209.1900	1.70	+110.6860	2.33	-211.9050	2.96	-135.0850	3.59	-002.0230
0.45	+030.0750	1.08	+211.5200	1.71	+105.3470	2.34	-214.4800	2.97	-131.7610	3.60	-001.6680
0.46	+031.9970	1.09	+213.7670	1.72	+099.9390	2.35	-216.9160	2.98	-128.4390	3.61	-001.3550
0.47	+033.9830	1.10	+215.9280	1.73	+094.4670	2.36	-219.2110	2.99	-125.1210	3.62	-001.0830
0.48	+036.0300	1.11	+217.9990	1.74	+088.9340	2.37	-221.3640	3.00	-121.8110	3.63	-000.8480
0.49	+038.1390	1.12	+219.9770	1.75	+083.3430	2.38	-223.3740	3.01	-118.5100	3.64	-000.6490
0.50	+040.3080	1.13	+221.8570	1.76	+077.6980	2.39	-225.2400	3.02	-115.2210	3.65	-000.4830
0.51	+042.5380	1.14	+223.6370	1.77	+072.0030	2.40	-226.9590	3.03	-111.9470	3.66	-000.3470
0.52	+044.8270	1.15	+225.3130	1.78	+066.2610	2.41	-228.5320	3.04	-108.6910	3.67	-000.2390
0.53	+047.1740	1.16	+226.8810	1.79	+060.4760	2.42	-229.9570	3.05	-105.4530	3.68	-000.1560
0.54	+049.5780	1.17	+228.3380	1.80	+054.6520	2.43	-231.2330	3.06	-102.2380	3.69	-000.0940
0.55	+052.0390	1.18	+229.6790	1.81	+048.7930	2.44	-232.3590	3.07	-099.0470	3.70	-000.0510
0.56	+054.5540	1.19	+230.9020	1.82	+042.9020	2.45	-233.3340	3.08	-095.8830	3.71	-000.0240
0.57	+057.1230	1.20	+232.0030	1.83	+036.9830	2.46	-234.1590	3.09	-092.7470	3.72	-000.0080
0.58	+059.7450	1.21	+232.9790	1.84	+031.0410	2.47	-234.8310	3.10	-089.6420	3.73	-000.0020
0.59	+062.4180	1.22	+233.8240	1.85	+025.0780	2.48	-235.3520	3.11	-086.5700	3.74	-000.0000
0.60	+065.1400	1.23	+234.5370	1.86	+019.0990	2.49	-235.7210	3.12	-083.5330	3.75	-000.0000
0.61	+067.9100	1.24	+235.1130	1.87	+013.1080	2.50	-235.9360	3.13	-080.5330	3.76	-000.0000
0.62	+070.7270	1.25	+235.5480	1.88	+007.1080	2.51	-236.0000	3.14	-077.5720	3.77	-000.0000

Table 3.6. Sway tank motions at scale 1:20 corresponding to SIW with the amplitude of 244 mm

t(s)	Y(mm)	t(s)	Y(mm)	t(s)	Y(mm)	t(s)	Y(mm)	t(s)	Y(mm)	t(s)	Y(mm)
0.00	-000.0000	0.63	+076.0830	1.26	+243.8350	1.89	+001.1410	2.52	-243.9070	3.15	-077.1820
0.01	-000.0000	0.64	+079.0870	1.27	+243.9840	1.90	-005.0670	2.53	-243.6610	3.16	-074.2070
0.02	-000.0000	0.65	+082.1330	1.28	+243.9770	1.91	-011.2730	2.54	-243.2650	3.17	-071.2770
0.03	-000.0000	0.66	+085.2200	1.29	+243.8120	1.92	-017.4710	2.55	-242.7230	3.18	-068.3950
0.04	-000.0000	0.67	+088.3460	1.30	+243.4890	1.93	-023.6580	2.56	-242.0370	3.19	-065.5620
0.05	+000.0010	0.68	+091.5090	1.31	+243.0080	1.94	-029.8290	2.57	-241.2130	3.20	-062.7800
0.06	+000.0050	0.69	+094.7070	1.32	+242.3700	1.95	-035.9810	2.58	-240.2540	3.21	-060.0500
0.07	+000.0170	0.70	+097.9370	1.33	+241.5750	1.96	-042.1100	2.59	-239.1630	3.22	-057.3740
0.08	+000.0410	0.71	+101.1990	1.34	+240.6240	1.97	-048.2120	2.60	-237.9440	3.23	-054.7520
0.09	+000.0790	0.72	+104.4880	1.35	+239.5170	1.98	-054.2820	2.61	-236.6020	3.24	-052.1870
0.10	+000.1350	0.73	+107.8030	1.36	+238.2550	1.99	-060.3170	2.62	-235.1390	3.25	-049.6800
0.11	+000.2130	0.74	+111.1420	1.37	+236.8380	2.00	-066.3130	2.63	-233.5600	3.26	-047.2320
0.12	+000.3150	0.75	+114.5020	1.38	+235.2680	2.01	-072.2670	2.64	-231.8680	3.27	-044.8430
0.13	+000.4440	0.76	+117.8810	1.39	+233.5460	2.02	-078.1730	2.65	-230.0660	3.28	-042.5150
0.14	+000.6040	0.77	+121.2760	1.40	+231.6730	2.03	-084.0290	2.66	-228.1600	3.29	-040.2490
0.15	+000.7970	0.78	+124.6840	1.41	+229.6500	2.04	-089.8300	2.67	-226.1520	3.30	-038.0450
0.16	+001.0260	0.79	+128.1040	1.42	+227.4770	2.05	-095.5730	2.68	-224.0460	3.31	-035.9050
0.17	+001.2930	0.80	+131.5310	1.43	+225.1580	2.06	-101.2550	2.69	-221.8450	3.32	-033.8290
0.18	+001.6010	0.81	+134.9650	1.44	+222.6930	2.07	-106.8710	2.70	-219.5540	3.33	-031.8180
0.19	+001.9520	0.82	+138.4010	1.45	+220.0840	2.08	-112.4170	2.71	-217.1760	3.34	-029.8710
0.20	+002.3470	0.83	+141.8370	1.46	+217.3320	2.09	-117.8910	2.72	-214.7150	3.35	-027.9910
0.21	+002.7910	0.84	+145.2700	1.47	+214.4390	2.10	-123.2880	2.73	-212.1730	3.36	-026.1760
0.22	+003.2830	0.85	+148.6980	1.48	+211.4080	2.11	-128.6060	2.74	-209.5560	3.37	-024.4280
0.23	+003.8260	0.86	+152.1160	1.49	+208.2390	2.12	-133.8400	2.75	-206.8660	3.38	-022.7460
0.24	+004.4220	0.87	+155.5230	1.50	+204.9360	2.13	-138.9880	2.76	-204.1070	3.39	-021.1310
0.25	+005.0730	0.88	+158.9150	1.51	+201.5000	2.14	-144.0460	2.77	-201.2820	3.40	-019.5820
0.26	+005.7800	0.89	+162.2900	1.52	+197.9340	2.15	-149.0100	2.78	-198.3950	3.41	-018.0990
0.27	+006.5430	0.90	+165.6430	1.53	+194.2400	2.16	-153.8780	2.79	-195.4500	3.42	-016.6830
0.28	+007.3660	0.91	+168.9730	1.54	+190.4190	2.17	-158.6460	2.80	-192.4500	3.43	-015.3320
0.29	+008.2480	0.92	+172.2750	1.55	+186.4760	2.18	-163.3120	2.81	-189.3980	3.44	-014.0480
0.30	+009.1910	0.93	+175.5460	1.56	+182.4110	2.19	-167.8720	2.82	-186.2970	3.45	-012.8280
0.31	+010.1960	0.94	+178.7840	1.57	+178.2290	2.20	-172.3230	2.83	-183.1520	3.46	-011.6730
0.32	+011.2640	0.95	+181.9850	1.58	+173.9310	2.21	-176.6620	2.84	-179.9660	3.47	-010.5820
0.33	+012.3960	0.96	+185.1460	1.59	+169.5210	2.22	-180.8880	2.85	-176.7410	3.48	-009.5530
0.34	+013.5920	0.97	+188.2630	1.60	+165.0010	2.23	-184.9960	2.86	-173.4810	3.49	-008.5880
0.35	+014.8520	0.98	+191.3330	1.61	+160.3730	2.24	-188.9840	2.87	-170.1900	3.50	-007.6830
0.36	+016.1790	0.99	+194.3530	1.62	+155.6430	2.25	-192.8500	2.88	-166.8700	3.51	-006.8390
0.37	+017.5710	1.00	+197.3190	1.63	+150.8110	2.26	-196.5910	2.89	-163.5250	3.52	-006.0540
0.38	+019.0290	1.01	+200.2280	1.64	+145.8820	2.27	-200.2040	2.90	-160.1580	3.53	-005.3260
0.39	+020.5530	1.02	+203.0760	1.65	+140.8580	2.28	-203.6880	2.91	-156.7720	3.54	-004.6550
0.40	+022.1440	1.03	+205.8590	1.66	+135.7430	2.29	-207.0410	2.92	-153.3700	3.55	-004.0390
0.41	+023.8020	1.04	+208.5750	1.67	+130.5400	2.30	-210.2590	2.93	-149.9550	3.56	-003.4770
0.42	+025.5260	1.05	+211.2200	1.68	+125.2530	2.31	-213.3410	2.94	-146.5310	3.57	-002.9660
0.43	+027.3160	1.06	+213.7890	1.69	+119.8840	2.32	-216.2850	2.95	-143.0990	3.58	-002.5050
0.44	+029.1720	1.07	+216.2810	1.70	+114.4380	2.33	-219.0880	2.96	-139.6640	3.59	-002.0920
0.45	+031.0950	1.08	+218.6900	1.71	+108.9180	2.34	-221.7500	2.97	-136.2280	3.60	-001.7250
0.46	+033.0820	1.09	+221.0130	1.72	+103.3270	2.35	-224.2690	2.98	-132.7930	3.61	-001.4010
0.47	+035.1340	1.10	+223.2480	1.73	+097.6690	2.36	-226.6420	2.99	-129.3630	3.62	-001.1200
0.48	+037.2510	1.11	+225.3890	1.74	+091.9480	2.37	-228.8680	3.00	-125.9400	3.63	-000.8770
0.49	+039.4310	1.12	+227.4330	1.75	+086.1680	2.38	-230.9470	3.01	-122.5270	3.64	-000.6710
0.50	+041.6750	1.13	+229.3780	1.76	+080.3320	2.39	-232.8750	3.02	-119.1270	3.65	-000.4990
0.51	+043.9800	1.14	+231.2180	1.77	+074.4430	2.40	-234.6530	3.03	-115.7420	3.66	-000.3590
0.52	+046.3460	1.15	+232.9500	1.78	+068.5070	2.41	-236.2790	3.04	-112.3750	3.67	-000.2470
0.53	+048.7730	1.16	+234.5720	1.79	+062.5260	2.42	-237.7520	3.05	-109.0280	3.68	-000.1610
0.54	+051.2590	1.17	+236.0780	1.80	+056.5050	2.43	-239.0710	3.06	-105.7040	3.69	-000.0970
0.55	+053.8030	1.18	+237.4650	1.81	+050.4470	2.44	-240.2350	3.07	-102.4050	3.70	-000.0530
0.56	+056.4040	1.19	+238.7290	1.82	+044.3560	2.45	-241.2440	3.08	-099.1330	3.71	-000.0240
0.57	+059.0600	1.20	+239.8680	1.83	+038.2370	2.46	-242.0960	3.09	-095.8910	3.72	-000.0090
0.58	+061.7700	1.21	+240.8760	1.84	+032.0930	2.47	-242.7920	3.10	-092.6810	3.73	-000.0020
0.59	+064.5340	1.22	+241.7500	1.85	+025.9280	2.48	-243.3300	3.11	-089.5050	3.74	-000.0000
0.60	+067.3480	1.23	+242.4870	1.86	+019.7470	2.49	-243.7110	3.12	-086.3650	3.75	-000.0000
0.61	+070.2120	1.24	+243.0830	1.87	+013.5520	2.50	-243.9340	3.13	-083.2630	3.76	-000.0000
0.62	+073.1250	1.25	+243.5330	1.88	+007.3490	2.51	-243.9990	3.14	-080.2020	3.77	-000.0000

Chapter 4

Effects of Ullage Gas and Scale on Sloshing Loads

Abstract

[1] Gas-liquid density ratio (DR) is a key dimensionless number in sloshing assessment methodologies of membrane containment systems for LNG tanks of floating structures. Earlier studies on the effect of DR were mainly statistical and effects of DR were usually mixed with those of gas compressibility and ullage gas pressure but attributed only to DR. In an attempt to separately study such effects, Karimi et al. [2015b] studied the effects of DR far from impact zones (global effects of gas-liquid density ratio) which proved to be small in the studied range of DR (0.0002 to 0.0060). The effects of DR near impact zones and before detection of any compressibility effects are referred to as local effects and correspond to modifications of wave shape before impact. They were treated in Karimi et al. [2016]. This paper studies the influence of ullage gas at the same scale as well as scaling of sloshing loads at different scales.

The test setups were similar to those presented in Karimi et al. [2015b] and Karimi et al. [2016] and consisted of three 2D model tanks as transverse slices of tank 2 (out of 4) of a membrane LNG carrier with total capacity of 152000 m^3 at scales 1:10, 1:20 and 1:40. All model tests were performed at a fill level corresponding to 20% of the tank heights. Water as liquid and different ullage gases of helium (He), air, two mixtures of sulfur hexafluoride (SF_6) and nitrogen (N_2), and pure SF_6, all at atmospheric pressure with a range of DRs from 0.0002 to 0.0060 were used. Synchronized High-speed video cameras (@4000 fps) and arrays of piezoelectric PCB pressure sensors (@40 kHz) monitored and measured impacts on the tank walls. The study was mainly based on the definition of *Impact ID* based on impact coincidence.

The results are presented at 4 main stages. First, in the same way that sloshing loads measured in irregular model tests are treated in the current methodologies, the measured pressure peaks are studied as statistical samples. Next by the notion of impact ID, the effect of change of ullage gas at the same scale is verified. Thirdly with the same notion of impact ID,

[1]This chapter is based on: *Effects of Ullage Gas and Scale on Sloshing Loads.* M. R. Karimi, L. Brosset, M. L. Kaminski and J.-M. Ghidaglia . European Journal of Mechanics - B/Fluids. Volume 62, March-April 2017, Pages 59-85. *http://dx.doi.org/10.1016/j.euromechflu.2016.11.017*

impacts are tracked down through three scales to verify scaling. At last dominant impact IDs are introduced. It is shown that the most severe impacts are generated by only a few dominant IDs.

4.1 Introduction

When stored in tanks equipped with membrane containment systems as those proposed by GTT[2], liquefied natural gas (LNG) remains in a state close to a thermodynamic equilibrium with its vapor at atmospheric pressure (the gas pressure is intentionally kept slightly above the atmospheric pressure), corresponding to a temperature of $-163°C$. Any new project of a floating structure storing or transporting LNG in membrane tanks is assessed for sloshing loads by means of sloshing model tests. A model tank made of smooth rigid walls of PMMA[3], reproducing the inner dimensions of the real tank at a smaller geometrical scale $1 : \lambda$ (usually $\lambda = 40$), is placed on the platform of a 6 degree of freedom (DOF) motion rig. The tank is filled with water and a heavy gas. As the density of water is more than twice the density of LNG, a density scale $1 : \mu$ (μ is defined as ρ_{LNG}/ρ_{water}) is to be introduced in the dimensional analysis. The heavy gas is made of a mixture of sulfur hexafluoride (SF_6) and nitrogen (N_2) tuned in order to match the same gas-to-liquid density ratio (DR) as in a real tank with natural gas and LNG. The motions of the floating structure are calculated at scale 1 usually by means of a classical boundary element method (BEM) taking into account the possible speed of the ship (usually under the approximation of the encounter frequency) and the coupling between the floating structure and the cargo motions. These motions are imposed by the rig to the model tank after having been down-scaled. As the gravity is the same at both scales, all forced accelerations at small scale must be the same as at full scale, which imposes a time scale $1 : \tau$ related to the geometric scale by $\tau = \sqrt{\lambda}$. Many pressure sensors (typically 300 sensors for every sloshing test campaign) acquiring at high frequency (¿ 20 kHz) are regularly arranged in rectangular arrays located in the most exposed areas of the tank. The tests mimic at small scale all conditions that the floating structure is expected to experience during its life, screening different possible loading conditions, sea states, ship speeds, wave incidences with regard to the floating structure and fill levels in the studied tank. Samples of pressure peaks are gathered in order to enable long term statistics and, after a scaling process, derive design loads at a suitably low probability. Among others, ABS [2014], BV [2011], LR [2009], DNV [2014], Gervaise et al. [2009] and Kuo et al. [2009] describe methodologies developed for such sloshing assessments based on sloshing model tests.

[2]Gaztransport&Technigaz

[3]Polymethyl methacrylate commonly known under the trademark **Plexiglas**

For large scale LNG ships decades of experience are available. This feedback enabled GTT to tune experimental scale factors from sloshing model tests performed in conditions for which sloshing incidents occurred (indentations of plywood boxes of NO96 containment system, permanent deformations of the stainless steel membrane corrugations of Mark III containment system). For less classical tank or ship designs when almost no feedback is available, as for tanks of LNG as a fuel that can be used for any kind of commercial ship or for small scale applications in general, a scaling based on dimensional analysis is applied: $P^{fs} = \frac{\mu\lambda^2}{\tau^2} \times P^{ms} = \mu \times \lambda \times P^{ms}$, where P is the pressure and ^{fs} and ^{ms} stand respectively for full scale and model scale.

This pressure scaling derived from the three fundamental scales $(1/\lambda, 1/\mu, 1/\tau)$ would be perfectly accurate if liquid and gas flows during sloshing model tests were in complete similarity with respective liquid and gas flows at full scale. This would be the case if at both scales these flows were entirely described by the simplest approximation of the problem represented by incompressible Euler equations. Under this assumption only the density of the different fluids matters. A common dimensionless form of this simplified problem can then be used at both scales exhibiting a single dimensionless number, DR.

The reality is more complex and the sloshing model test as described above must be considered as an approximation of reality. Firstly, there are phenomena in LNG tanks that are not modelled at model tests (see for instance Kaminski and Bogaert [2010] and Brosset et al. [2009] about the Sloshel JIP which was done to improve the understanding of some of those phenomena). For instance phase change occurs at full scale between LNG and its vapor, especially driven by the quick local gas compression or expansion, which might modify the impact loads but is not taken into account at model scale. Secondly, other properties of the fluids than densities are involved, especially during impacts, which cannot be scaled adequately at model scale biasing their influence on the flow with regard to full scale.

The liquid compressibility is involved at every contact point between the liquid and the wall when there is a normal velocity of the liquid particle with regard to the wall (impact). A pressure wave is then emitted from this point propagating through the liquid at the speed of sound which is possibly significantly reduced due to the presence of bubbles. The gas compressibility is involved in two different situations. Firstly, while the gas escapes in between an approaching wave and the wall. At first, the gas flow is incompressible as the gas escapes at a sufficient rate to keep the same density in the remaining available space in between the wave and the wall. As this space is getting smaller and smaller, the gas is forced to accelerate. Significant fractions of Mach number can be reached. When the gas cannot escape sufficiently quickly any longer, its density and therefore its pressure increases. Secondly, while the gas is entrapped in a cavity, it must comply with

the space provided by the much denser liquid. Its compressibility acts like a non-linear spring inducing oscillations of the cavity volume and pressure and modifying back the liquid flow. Under a higher level of approximation taking care of both the liquid and the gas compressibility additionally to their density, the common dimensionless form of the problem at both scales would now exhibit two additional dimensionless numbers, M_L and M_G, respectively the Mach number within the liquid and within the gas.

Furthermore, the liquid and gas viscosities and the surface tension at the interface are also involved at both scales. They are directly related to phenomena generating local perturbations of the global flow which do not repeat well when accurately repeating the same sloshing conditions at a given scale. These phenomena are (1) the development of free surface instabilities, especially generated by the shearing gas flow in between a wave and a wall just before any impact; (2) the fall of droplets onto the free surface after any impact splashing and (3) the generation of bubbles into the liquid. They are the sources of the local variability of the flow that causes the well-known local variability of impact pressure measurements. The problem should thus be modelled with a higher level of approximation at both scales adding Reynolds numbers, Re_L and Re_G respectively in liquid and gas, and Weber number We to the already long list of dimensionless numbers governing the common dimensionless problem.

A perfect similarity between gas and liquid flows at both scales would therefore require not only that the time scale imposed by the forced motions is the square root of the geometrical scale but also the equality of all mentioned dimensionless numbers at small and full scales. Each of these equalities imposes a direct down-scaling of the corresponding fluid property from full scale to model scale. Among them, only DR is really kept the same at both scales with the right choice of the gas density inside the model tank. None of the other properties can adequately be down-scaled from the values at full scale. For instance, the liquid and gas are much too stiff at small scale; the surface tension at the gas-liquid interface is also much higher at small scale than in the reality, leading to less fragmentation during the development of free surface instabilities or during splashing after impact and proportionally larger bubbles. Therefore, as these phenomena are the main causes of the variability of the flow, statistics carried out from the measured pressure peaks at model scale do not necessarily well represent statistics that would reflect the variability of the pressures at full scale.

Eventually, all these issues raise questions about the relevance of sloshing model tests. Nevertheless to address these concerns, comparisons between full scale measurements on board a 148300 m^3 membrane LNG carrier and sloshing model tests mimicking the conditions for which sloshing was experienced on board, showed that despite all the mentioned issues, sloshing model tests remain conservative on a long-term basis, which is the most important conclusion from

a design perspective. The study was performed within the Full Scale Measurement (FSM) JIP led by DNV and described in Lund-Johansen et al. [2011] and Pasquier and C.-F.Berthon [2012]. More precisely, statistical distributions representative of the ship operational profile over four years of measurements proved to be more conservative when built from model tests than from full scale measurements. Comparison of the design pressure defined at a probability 10^{-3} per year showed a safety margin for both curves. However, the study also showed that sloshing model tests were not always totally representative of the reality when comparisons were based on a short-term basis.

As numerical simulations are far from being mature enough to be used as a substitution tool for sloshing tests, the previously listed scaling issues related to the use of sloshing model tests motivate further studies on scaling in the context of liquid impacts. Multiple objectives are sought: to improve the conditions of sloshing tests for a better representation of the reality; to better derive design loads from biased measured pressures; to shorten the duration of a test campaign but with a better capture of the most violent events, enriching efficiently the tail of the statistical pressure distribution.

4.1.1 Context of the paper

Three sloshing model test campaigns have been carried out with model tanks having internal dimensions representing those of a transverse slice of tank 2 of a 152000 m^3 LNG carrier (2D tank), respectively at scales 1:40, 1:20 and 1:10. Whatever the scale, the same filling ratio of 20% of the tank height has been studied. Same transverse full-scale excitations (three degrees of freedom) have been used to adequately derive amplitude- and time-similar forced excitations at the three different scales (amplitudes are divided by λ and times are divided by $\tau = \sqrt{\lambda}$). The tests have been performed with water and different ullage gases at ambient temperature and atmospheric pressure, providing a large range of gas-to-liquid density ratios (DR). Whatever the scale a regular and rectangular array of pressure sensors was installed on one side of the tank covering the impacted area; a high speed video camera, synchronized with the data acquisition system, was fixed to the same side of the tank in order to capture the wave shapes right before and during impacts; additionally, a HD camera, also fixed to the tank, recorded global deformations of the free surface during the complete duration of the tests.

Thus, these sloshing test campaigns made it possible to study the variability of the flow when repeating accurately the same conditions, the influence of the liquid and gas properties and the influence of scale. This paper is the third of a series of five papers, gathering most important results from these test campaigns.

The first paper (Karimi et al. [2015b]) focused on the consequences on the

global flow of forcing the motions at different scales, with different ullage gases, with a time scale related to the geometrical scale by $\tau = \sqrt{\lambda}$. It was based on comparison of results at scales 1:40 and 1:20 for irregular excitations derived from calculated ship motions on a given sea state with a significant wave height of 6 m. It showed that, if a small uncertainty window is introduced, impacts always happen at the same instants when the same condition is repeated at a given scale. When comparing two different scales the impacts happen at time-similar instants. They are referred to as coincident impacts. This regularity does not deteriorate over time even for long duration tests (50 minutes at scale 1:40). The random perturbations brought to the global flow by the development of free surface instabilities or by the fall of droplets are damped quickly and are overcome by the regularity brought by the imposed motions. This process prevents a progressive randomization of the global flow. Moreover, changing the ullage gas does not affect this regularity of the flow when keeping the same motions imposed to the tank. Therefore, the small variations of the global flow induced by the differences between gas properties especially during impacts are also damped quickly enough to be overcome by the regularity brought by the imposed motions. This prevents a progressive general divergence of the global flow.

The second paper (Karimi et al. [2016]) presents the influence of DR on the wave shapes just before impacts but prior to any compression of the gas, as observed during sloshing tests at scale 1:20 for short regular sway excitations of the tank stopped after a unique impact. Such short excitations, referred to as Single Impact Wave excitations or SIW, lead to very accurately repeatable wave shapes before impact and enable a deterministic comparison of the wave shapes generated by the same conditions but with different ullage gases. Actually, the wave front keeps smooth and precisely repeatable from the trough to the base of the crest. The corresponding measured pressures induced by the trough run-up are also repeatable. Only around the crest, where free surface instabilities develop due to the shearing gas flow, some differences can be distinguished. As a consequence, variations of the pressure signals induced by the crest impact are significant. When repeating the same excitation with two different liquids and choosing the ullage gases in order to get matching DRs, the wave front keeps smooth and its shape remains precisely the same from the trough to the base of the crest although discrepancies around the crest can be observed due to different developments of free surface instabilities. Therefore this smooth shape of the wave front is independent of the liquid density and only depends on DR. When repeating the same condition with water but with different ullage gases, it is observed that the larger the DR, the less advanced the breaking process is. The gas seems to impede the breaking process. This includes a slightly reduced upward speed of the trough run-up for larger DR. This mitigating role of the gas

is clearly due to a transfer of mechanical energy from the liquid to the gas. As already stated in Braeunig et al. [2009] but only based on numerical simulations at that time, changing the DR leads to changing the impact conditions and therefore the nature of impact. This could as well magnify the impact pressures or mitigate them when increasing the DR depending on the initial wave shape chosen. Complying with density ratio similarity is therefore necessary during sloshing model tests to prevent any systematic bias in the impact conditions and consequently in the pressure statistics.

The fourth and the fifth paper are in preparation. In the fourth paper, the notion of dominant impact introduced in this paper will be fully explained. Taking benefit of the short inertial flow memory observed in Karimi et al. [2015a], the fifth paper will show that the characteristics of a given impact obtained during irregular tests can be conserved when generated by a short sequence of excitations extracted from the original motions before the impact time. The influence of this excitation duration on the variability, therefore on the pressure statistics, will be presented. Possible changes on the way to perform sloshing model tests will be envisaged.

4.1.2 Objectives of current paper and overview

In the second paper of the series, the intention was to discriminate the effect of DR from the other properties of the gas and especially from the gas compressibility. Therefore the comparison was to be made before any compression of the gas, thus before any impact. This led naturally to a comparison mainly based on pictures extracted from high speed videos. In the present paper quantitative results based on measured pressures are presented comparing irregular tests at different scales with the same gas or at a given scale with different gases. The comparisons are based on series of 10 tests for each studied condition defined by a scale and an ullage gas. Due to the variability of the local pressure measurements, the comparisons are necessarily based on statistics. Doing so, one must be aware that when changing the scale or the ullage gas, not only the most influential properties of the gas on the global wave shape matter, like its density or its compressibility, but also surface tension or/and viscosity which directly modify the local phenomena responsible for the variability (free surface instability, splashing, bubbles creation).

During the different test campaigns, the rectangular arrays of pressure sensors were not homothetic at the different scales. The comparisons have therefore been made on the largest rectangular area common to the three scales after scaling to scale 1:10. Pressure sensors used were the same during the different test campaigns at different scales. Furthermore, whatever the scale studied, the distance between two consecutive sensors was also kept to 10 mm within every

row and column of the rectangular sensor arrays. Therefore, the comparisons are made on averaged pressures calculated on homothetic rectangular subareas of the common area. These subareas of different sizes and different locations can be considered as virtual sensors of different sizes capturing the spatial distributions of the impact loads. After a short description of the different test set-ups and test conditions, the different subareas defined for the comparisons are presented and the assumptions for averaging the pressure on these subareas are explained.

It was already mentioned that whatever the scale or the ullage gas, impacts coincide at the same times when repeating similar irregular excitations. Therefore, each impact of our different series of tests has been identified by a reference time (considering a small uncertainty window), conventionally defined at scale 1:10, or by an index number. This will be referred to as impact identification or simply as impact ID. This important notion is explained next in this paper. Contrarily to SIW leading to accurately repeatable global wave shapes, the wave shape before impact for a given ID might significantly vary as shown later.

The current paper presents comparisons of tests at different scales and with different ullage gases based on statistics of pressure peaks as calculated on the different subareas. At first these comparisons rely on global statistics mixing all impact IDs together, as it is normally done during post-processing of sloshing model tests for any sloshing assessment of LNG tank on a floating structure. This method presents the advantage of using statistics on a larger sample of pressures. Other presented comparisons rely on statistics based on the notion of impact ID which present the general advantage of having more homogeneous samples to post-process but also the drawback in the case of our study to handle samples limited to a maximum of ten values. This small size of the samples obliged us to limit most of the time the presented results to the maximum values of each sample.

In the last part of the paper, it is shown that there are dominant IDs in the total collection of IDs for an irregular condition. When increasing the number of repetitions of an irregular test, the number of IDs involved in the N highest recorded pressures keeps decreasing, down to a few units. These dominant IDs are those which repeat the most frequently but also those which reach the highest pressures. Therefore they are responsible for the tail of the statistical distribution of pressure peaks.

4.2 Test Setup

The first descriptions of the test setup and the adopted measures to achieve the desired accuracy were mentioned in Karimi et al. [2015b] and Karimi et al. [2016]. Here a summary of the essential parts including complementary details will be added especially since in this paper, the results of another model test at scale

1:10 were used which were not utilized in the two earlier studies.

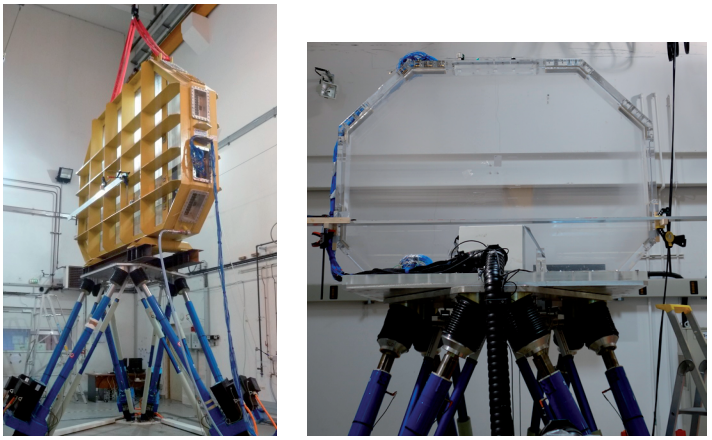

(a) (b)

Fig. 4.1. 2D tanks mounted on the hexapods at (a) scale 1:10 and (b) scale 1:20

The results of 3 sloshing model test campaigns were used in the current study. The model tests were carried out at scales 1:10, 1:20, and 1:40 and were all performed at GTT's laboratory. At each scale a tank was used as a model of a transverse slice of tank 2 of a LNG carrier with GTT's membrane containment system technology with the total capacity of 152000 m^3. See Fig. 4.1 for the general shape of the tanks at scales 1:10 and 1:20. The tank at scale 1:40's design was identical to the tank at scale 1:20. The tank at scale 1:10 had been designed by MARIN for the ComFlow project [4] and taken over by GTT after the project was finished. The structure of the tank is made of steel. The transverse walls are made of PMMA. The weight of the empty tank was 4.9 tons. The tanks at scale 1:20 and 1:40 were entirely made of PMMA plates with the thickness of 50 mm which allowed observation and made hydro-structural interactions insignificant during wave impacts. In this study only tank fill levels of 20% of the tank height were considered. Low fill levels are of interest due to more severe impacts and higher induced pressures (see BV [2011]). For the internal tank dimensions at the three scales see Fig. 4.2.

The tests were meant to be 2D and the only applied tank motions included sway, heave, and roll. A different hexapod was used for each campaign due to the difference in tank weights and the allowable hexapod payloads and motions. Tests at scale 1:10 were performed by an Aquilon type hexapod with the payload

[4] See ComFlow-3 project's website

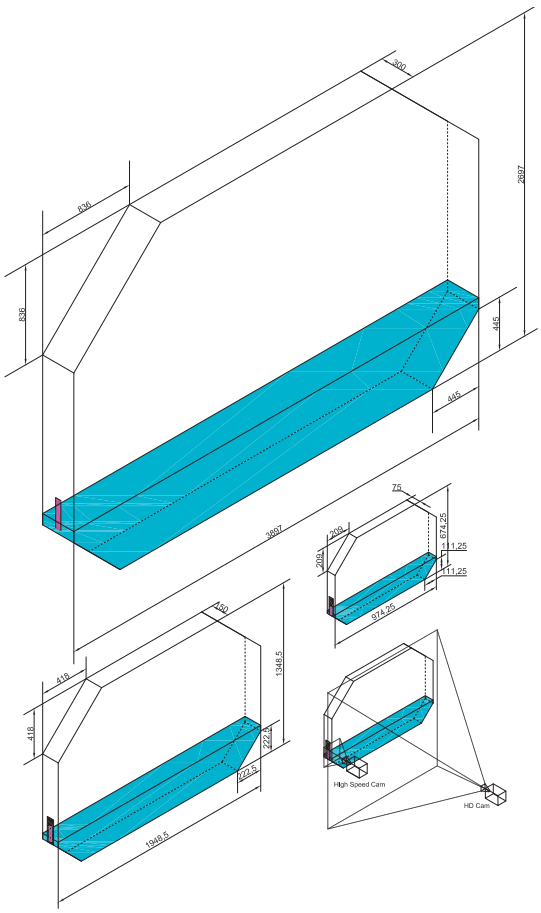

Fig. 4.2. Isometric illustration of internal tank dimensions from the largest to the smallest tank respectively at scales 1:10, 1:20 and 1:40. Schematic locations of HD and high-speed cameras are shown with respect to tank at scale 1:40.

capacity of 6 tons; tests at scale 1:20 were performed by a Sirocco type hexapod with max payload of 2 tons and finally the tests at scale 1:40 were carried out by a Mistral type hexapod with max payload of 1 ton. All three hexapods were manufactured by Symétrie [5]. The types of motions used in this study[6] were irregular.

[5]See Symétrie's website for complete technical details on the hexapods

[6] Irregular motions corresponding to H_s of 2 and 4 m and single impact waves were tested

Irregular tank motions were based on ship motions at full scale calculated by PRINCIPIA's DIODORE[7] for 5 hour sea states based on JONSWAP spectrum found from the assumption of zero crossing period T_z of 8.5 s, heading of 270 ° and significant wave height H_s of 6 m. The motions were coupled with sloshing in the tanks. After calculating the ship motions at the location of the tank slice, sway, heave, and roll motions were kept and scaled for the model tests. The ship motions were down-scaled by dividing the amplitudes by λ and time by $\sqrt{\lambda}$. These motions were defined at the middle of the bottom of the 2D tanks which was called the *center of rotation*. Irregular tank motions corresponding to one chosen sea state were repeated several times to obtain better statistical samples for further studies. In this study the collections of tests with 10 repetitions were considered.

Three types of cameras were used at 3 test campaigns. High-speed cameras were used to visually capture the impact geometry a few milliseconds before and after the impact. For tests at scale 1:10 and 1:20, a Photron SA5 high-speed camera was installed, looking at the sensor array. This camera had a resolution of 896×760 pixels with ~ 2 pix/mm at scale 1:10 and a resolution of 1024×1024 pixels with ~ 2.66 pix/mm at scale 1:20 and the global electronic shutter was adjustable from 16.7 ms to 1 μs independent of the frame rate. At scale 1:40, a Phantom V7.2 high-speed camera was used at the corresponding side. For this camera the resolution was 704×600 pixels with ~ 3.56 pix/mm and the exposure of 130 μs. Both high-speed cameras recorded at 4000 fps. The recordings of the high-speed cameras were utilized in the current study as well as in Karimi et al. [2016] and briefly in Karimi et al. [2015b]. To capture global videos of fluid free surface, the same HD camera (Canon XF105) was used for tests at scale 1:20 and 1:40[8] without capturing close-up details of impacts. This camera's shutter speed could have been adjusted between 1/18 and 1/2000 of a second depending on the frame rate. At both scales the same frame rate of 25 fps was used. The resolution at scale 1:20 was 960×576 pixels with ~ 0.5 pix/mm whereas at scale 1:40 the resolution was 1920×1080 pixels with ~ 1 pix/mm. The recordings of this HD camera were mainly used for qualitative comparisons presented by Karimi et al. [2015b] and were not used in the current study. A simple camera was also used to control the fill level. For all the cameras, dedicated wooden supports were made and installed. All the cameras were kept completely fixed on the supports throughout the tests (see Fig. 4.2 for schematic positions of high-speed and HD cameras and the corresponding observation windows). The high-speed cameras were activated when impact pressures exceeded a threshold used for the camera system. The HD camera captured the tank motions during the entire

but the results were not used in this study

[7] See PRINCIPIA's website for more information on DIODORE

[8] the global fluid flow was not monitored at scale 1:10

duration of the model tests. At the test campaign at scale 1:10, halogen lamps were used to provide clear and bright videos. Those lamps were not used for the next campaigns since considerable heat led to water evaporation in a preliminary series of tests at scale 1:40 which led to change in fill level that could spoil the repeatability of the tests. As a workaround and for tests at scale 1:20 and 1:40, arrays of LED lamps were installed which solved the evaporation problem.

Piezo-electric PCB sensors (112A21 and 112M361) were installed on modules in arrays of 25×5, 21×6, and 15×4 respectively at scales 1:10, 1:20, and 1:40 as depicted by Fig. 4.3. The horizontal and vertical distance between the centers of all the sensors was 10 mm for all the tests at all 3 scales. All the pressure sensors sampled at 40 kHz. During the tests, the pressure measurement system was being activated with the definition of a pressure threshold which triggered the pressure measurement system. None of the wave impacts on the module with maximum pressures lower than this threshold were recorded. In order to perform statistical comparisons between the measured loads on the modules, a common area had to be defined on the modules at 3 scales. This common area is shown in Fig. 4.3 after up-scaling the modules at scale 1:20 and 1:40 to scale 1:10 and superimposing all the 3 sensor modules. This common area is further subdivided into 63 subareas in rectangular or square shapes and different sizes which are all shown in Fig. 4.4. The defined subareas had surfaces of 800 mm^2 (A1-A12), 1600 mm^2 (A13-A28) , 2400 mm^2 (A29-A36), 3200 mm^2 (A37-A47), 4000 mm^2 (A48-A51), 4800 mm^2 (A52-A57) , 6400 mm^2 (A58-A60), 8000 mm^2 (A61-A62), and 9600 mm^2 (A63) when measured at scale 1:10. A63 corresponds to the total common area size. These subareas enable the comparison between the corresponding loads at different scales. Subareas are also defined to verify the effect of area size and location in the resulting pressures as well as the influence of changing the ullage gas and scale on the loads. Smaller subareas reflect the more local phenomena even though the pressure sensors themselves, as the smallest available sensors, represent the most local measurements available. The largest subareas give an idea about the global loadings during sloshing impacts. Local phenomena are masked and not represented in the pressure signals calculated on the larger areas as will be explained later on.

Measures taken to ensure repeatability and accuracy of tank alignment, motions, fill level, and environmental conditions at model tests at scale 1:20 and 1:40 were identical and were elaborated in Karimi et al. [2015b] and Karimi et al. [2016] and for the sake of brevity will not be repeated. For the model test at scale 1:10, the fill level was accurately adjusted based on the level markers and the laser apparatus was not used to verify the tank alignment. The rest of the procedure was identical. At scale 1:10, the only utilized gas was air and the tank did not need to be gas-tight. At the other scales, the use of several gases and gas mixtures with adjusted densities required tank gas-tightness which was tested

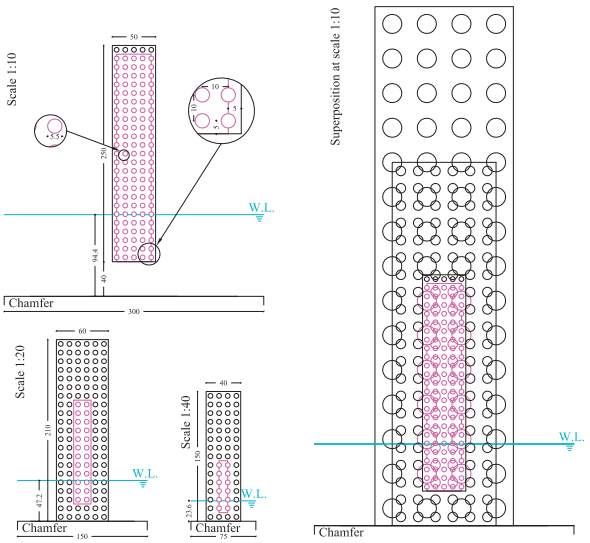

Fig. 4.3. Sensor modules and the defined common area at scales 1:10, 1:20 and 1:40 and the superposition of sensor modules after bringing all the geometries to scale 1:10

with Nidron 5 (a mixture of 95% nitrogen and 5% hydrogen). The tests with helium were more prone to leakage and as a result, leakage tests with helium were also performed.

With the exception of model tests at scale 1:10 which were performed only with water and air, other gases and gas mixtures were also used at scales 1:20 and 1:40. With water as liquid, the adopted ullage gases included helium (He), air, two mixtures of sulfur hexafluoride (SF_6) and N_2 (Mix_2 with a density of $2\,kg/m^3$ and Mix_4 with a density of $4\,kg/m^3$), and pure SF_6. Ullage pressure was atmospheric for all the performed tests. At scale 1:20 several tests were performed with a solution (with water) of sodium polytungstate (SPT) (with a density of $1800\,kg/m^3$) as liquid and air and Mix_2 as ullage gas. The results of the latter combination with heavier liquid were not used in this study but were referred to and used in Karimi et al. [2015b] and Karimi et al. [2016]. Lists of the series of tests which were used in this study are given in Table 4.1.

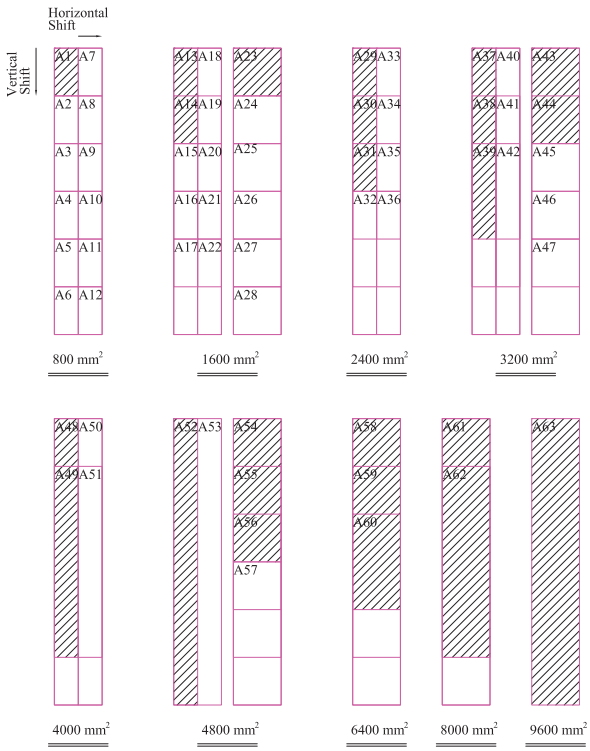

Fig. 4.4. Numbering, shape and position of 63 defined subareas (A1-A63) on the common area between the modules at 3 different scales

4.3 Average Pressure Definitions

The only initial pressure data came from measured signals at sensor level. Definition of subareas meant that average pressure signals on those areas were to be found based on measured data. In this study the process was done by finding the force signals on each area and the following division by the total surface area in order to calculate the average pressure over the whole area. The force signal on each area was found by identifying the sensors which should have been taken into account, multiplying the pressure signal by the contributory area of each pressure sensor and finally addition of all the smaller force signals.

This procedure is illustrated by Fig. 4.5 and for subarea A14 as an example (For the size and location of all the defined subareas see Fig. 4.4). The subarea

Table 4.1. Different series of 2D tests performed at 3 different scales of 1:10, 1:20 and 1:40 and the number of repetitions at each group

Scale	Group	Gas	Liquid	$\rho_g(kg/m^3)$	$\rho_l(kg/m^3)$	DR (-)	$n_{reps.}$
1:10	1	air	water	1.15	997	0.0012	10
1:20	1	helium	water	0.18	997	0.0002	10
	2	air	water	1.15	997	0.0012	10
	3	Mix_2	water	2.00	997	0.0020	10
	4	Mix_4	water	4.00	997	0.0040	10
1:40	1	helium	water	0.18	997	0.0002	10
	2	air	water	1.15	997	0.0012	10
	3	Mix_2	water	2.00	997	0.0020	10
	4	SF_6	water	6.00	997	0.0060	10

size is 1600 mm^2 at scale 1:10, 400 mm^2 at scale 1:20, and 100 mm^2 at scale 1:40. There are respectively 24, 4, and 2, sensors at scales 1:10, 1:20, and 1:40 which can be used to find the average pressure on the whole area. The sensor numbers are mentioned for further reference.

As is shown in Fig. 4.5 for some sensors, the contributory area is equal to 100 mm^2 as the sensors lie fully inside the defined boundaries for A14 such as the middle column of sensors at scale 1:10 and all the sensors at scale 1:20. Some other sensors lie partially within the boundaries of the subarea. For those sensors the contributory area is 50 mm^2 as it is the case with the first and the second column of sensors at scale 1:10 and both sensors at scale 1:40. Knowing the contributory area of each sensor, the average pressure signals on A14 and at all the 3 scales can be calculated as follows:

$$\begin{aligned}
&\bar{P}_{A14,Scale1:10}(t) = \\
&((P_{61}(t) + P_{66}(t) + P_{71}(t) + P_{76}(t) + P_{81}(t) + P_{86}(t) + P_{91}(t) + P_{96}(t)) \times 50\,mm^2 + \\
&\ (P_{62}(t) + P_{67}(t) + P_{72}(t) + P_{77}(t) + P_{82}(t) + P_{87}(t) + P_{92}(t) + P_{97}(t)) \times 100\,mm^2 + \\
&\ (P_{63}(t) + P_{68}(t) + P_{73}(t) + P_{78}(t) + P_{83}(t) + P_{88}(t) + P_{93}(t) + P_{98}(t)) \times 50\,mm^2) \div \\
&\ (8 \times 50\,mm^2 + 8 \times 100\,mm^2 + 8 \times 50\,mm^2)
\end{aligned}$$

$$\begin{aligned}
&\bar{P}_{A14,Scale1:20}(t) = \\
&((P_{53}(t) + P_{59}(t) + P_{65}(t) + P_{71}(t)) \times 100\,mm^2) \div (4 \times 100\,mm^2) = \\
&\ (P_{53}(t) + P_{59}(t) + P_{65}(t) + P_{71}(t)) \div 4
\end{aligned}$$

$$\begin{aligned}
&\bar{P}_{A14,Scale1:40}(t) = \\
&((P_{19}(t) + P_{23}(t)) \times 50\,mm^2) \div (2 \times 50\,mm^2) = \\
&\ (P_{19}(t) + P_{23}(t)) \div 2
\end{aligned}$$

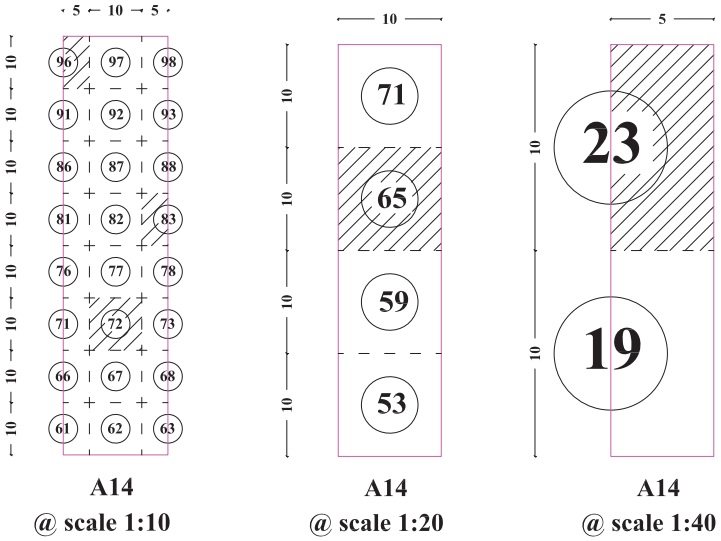

Fig. 4.5. Subarea A14 and the sensors that are used to calculate the average pressure on this area at each scale. The contributory area of each sensor is either 100 mm^2 or 50 mm^2. The shaded areas show the contributory areas of sensors 72, 83 and 96 at scale 1:10, sensor 65 at scale 1:20 and sensor 23 at scale 1:40. Sensor numbering convention was different at each scale and is mentioned to clarify the definition. Geometries at scale 1:40 and 1:20 have been up-scaled to scale 1:10. Measurements are in mm.

The result of this calculation at scale 1:20 and for one selected impact is demonstrated in Fig. 4.6. What should be mentioned is that some information are naturally lost in the averaging process. As shown in Fig. 4.6 in the demonstrated impact, a local phenomenon which is stronger at the top of A14 compared to the bottom, leads to higher measured pressures at the top sensors of 71 and 65 and weaker pressure signals on sensors 59 and 53. The averaging process masks such differences. It means that in order to study more local phenomena it is essential to consider smaller sizes of subareas. On the other hand whenever global phenomena are of interest, large subarea sizes would be satisfactory and more interesting.

Another point is the number of pressure sensors per subarea per scale and the spacial distribution of the sensors. In the previous example for A14, the ratio between the sensing area of all pressure sensors (considering the diameter of the sensing area of each sensor is 5.5 mm^2, see Fig. 4.3) is the same at all the 3 scales and is equal to 0.2376 but there are respectively 24, 4, and 2 pressure

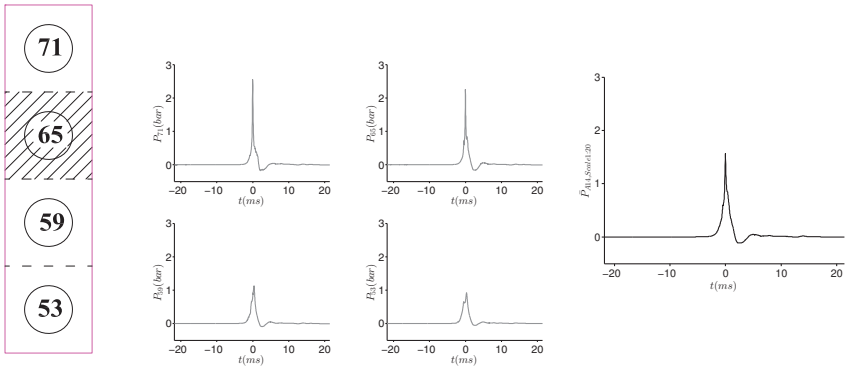

Fig. 4.6. Definition of average pressures masks local phenomena captured by each sensor at a more local level. Demonstration is done at scale 1:20.

sensors per area at scales 1:10, 1:20, and 1:40. More sensors at scale 1:10 and their distribution would mean that averaged pressures found at scale 1:10 will be more accurate since most of the phenomena which take place in this area can be captured with many available sensors which are distributed in such a way that they cover all parts and corners of A14. At scale 1:20 or 1:40 there would be a greater chance to miss the local phenomena. This aspect is however not considered in the present study.

4.4 Impact Coincidence and Impact ID

The notion of *Impact Coincidence* was first introduced in Karimi et al. [2015b] to verify the representativeness of model tests and perform more relevant verifications of the influence of different ullage gases on sloshing wave impacts. The idea of impact coincidence is based on the global flow which always keeps the same phase regardless of already tested range of DR and scale. Comparing different scales would include scaling of impact times based on the time scale factor of $\tau = \sqrt{\lambda}$. In this study all the impact times where brought to scale 1:10. The idea of in-phase global flow means that when comparing two model tests, wave impacts on either side of the tank would occur at the same exact times (with a small tolerance) regardless of tested range and scale since the impacts occur potentially when the global flow reaches either side of the wall which could lead to wave breaking on the walls. Based on this notion, if an impact occurs in one test at a certain time and if the same test is repeated again, the same impact with the matching nature and geometry (since global flow is also repeated with the same or scaled geometry and kinematics) should be expected at about this

exact time.

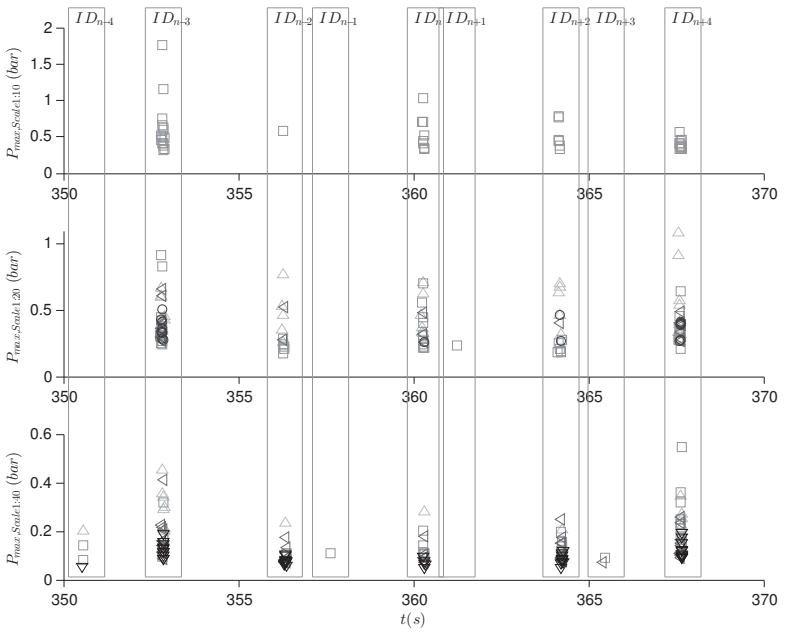

Fig. 4.7. Definition of impact ID based on the notion of impact coincidence observed in repetitions of long sloshing model tests. ($\triangle$: $DR = 0.0002$, $\square$: $DR = 0.0012$, $\triangleleft$: $DR = 0.002$, $\circ$: $DR = 0.004$, $\triangledown$: $DR = 0.006$)

This notion enables us to study the impacts of the corresponding tests based on their time of occurrence. Impacts that occur at the same exact times are relevant. This enables us to track down every impact between different sloshing model tests regardless of scale or ullage gas (in the tested range). In order to facilitate reference to the impacts that are relevant, it can be said that they belong to the same group or that they have the same ID[9] number among the impacts. Impacts with the same ID can be easily tracked down and related to each other as shown in Fig. 4.7 as an example. In this figure it is seen that some impacts are only recorded in one scale (take ID_{n+1} which was only recorded at scale 1:20; ID_{n-4}, ID_{n-1} and ID_{n+3} which were only recorded at scale 1:40) but nevertheless define an impact ID. This is due to both definition of different

[9]Identification

P_{th} (pressure threshold) for the measurement system in different model tests and variability of impact pressures which would mask some impacts in some tests.

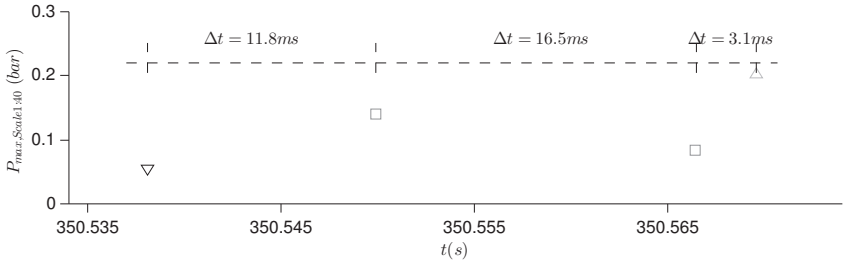

Fig. 4.8. Coincident impacts from 4 different sloshing model tests all corresponding to ID_{n-4} presented in Fig. 4.7. Impacts which were less than 50 ms (50 ms at scale 1:10) apart in time were considered coincident and belonged to the same ID. $\triangle$: $DR = 0.0002$, $\square$: $DR = 0.0012$, $\triangledown$: $DR = 0.006$

Considering impact ID_{n-4} of Fig. 4.7 and having a closer look in Fig. 4.8 it is observed that 4 impacts have been captured in 4 repetitions of the same tank motions but twice with air, once with helium and once with SF_6. The impacts are at each other's proximity in time but the decision whether they belong to the same group of impacts or in other words have the same ID number depends on the tolerance that is chosen. In this study every two consecutive impacts which occur with a time difference less that 50 ms were considered to belong to the same group and have the same ID number. 50 ms time difference was considered for time at scale 1:10 which means that the tolerance at scale 1:20 was $50/\sqrt{2}$ ms and at scale 1:40 it was 25 ms.

For a more detailed account of *Impact Coincidence* and the involved parameters see Karimi et al. [2015b]

4.5 Initial Results and Verifications

As mentioned earlier, in every test only the impacts where maximum induced pressure at sensor level exceeded a certain pressure threshold (P_{th}) were recorded and the rest of the impacts were measured but not recorded. The adopted pressure thresholds at each test were selected based on the previous experiences in GTT and the conditions of each campaign. Selection of high thresholds would have neglected valuable information and selection of very low thresholds would have led to capturing a large amount of data as well as recording every mild and uninteresting touch of the sensor module by single droplets. Having said that,

lower thresholds were more interesting since extra information could be filtered at any time but the discarded impacts could not be retrieved again. A list of selected thresholds for each group of tests and the number of measured impacts is given by Table 4.2.

Table 4.2. P_{th} (pressure threshold) used for different series of model tests and the number of recorded impacts (events) for every repetition of each group.

Scale	Group	Gas	Liquid	$P_{th}(bar)$	*rep.*1	*rep.*2	*rep.*3	*rep.*4	*rep.*5	*rep.*6	*rep.*7	*rep.*8	*rep.*9	*rep.*10
1:10	1	air	water	0.32	258	250	246	237	243	252	241	251	253	251
1:20	1	helium	water	0.25	429	390	411	420	429	410	398	399	433	425
	2	air	water	0.25	265	288	291	253	274	287	268	264	269	267
	3	Mix_2	water	0.25	218	243	224	219	234	234	207	229	213	208
	4	Mix_4	water	0.25	175	150	154	146	165	146	162	172	157	162
1:40	1	helium	water	0.20	216	200	192	181	190	189	197	184	205	205
	2	air	water	0.08	482	488	514	512	486	482	516	482	489	488
	3	Mix_2	water	0.07	528	515	526	490	487	514	505	501	499	509
	4	SF_6	water	0.05	567	556	559	576	575	583	568	573	559	575

4.5.1 Effect of Pressure Threshold (P_{th})

Based on Table 4.2 at scale 1:20 where the P_{th} for all the tests is the same and equal to 0.25 bar, number of recorded impacts decreases when testing with heavier gases. It means that in those tests there are less impacts with maximum measured pressure at sensor level higher than 0.25 bar. This could imply that using heavier gases would decrease impact pressures if considered altogether in a collection. This does not have any information on every impact so it cannot be said whether using a heavier gas would decrease the impact pressure for each impact.

The number of measured impacts as a function of P_{th} for each scale and ullage gas can be verified. This comparison is depicted by Fig. 4.9 for thresholds up to 2 bar. The value of N shown in this figure is the average number of impacts recorded for 10 repetitions in each series of tests, for the chosen P_{th}. From the figure it can be seen that for every N, the values of P_{th} at scales 1:20 and 1:40 has a ratio close to 2 for ullage gases of helium, air and Mix_2. Between the thresholds at scale 1:10 and 1:20 with the ullage gas of air, a ratio close to 1.13 seems to exist. Between the thresholds at scale 1:10 and 1:40 with the ullage gas of air, a ratio close to 2.26 is observed. The observation can be clarified further by finding the average value of P_{th} , corresponding to any number of recorded impacts (N) for each group of tests as shown in Table 4.3.

In Table 4.3 and considering the two scales of 1:20 and 1:40 and the three common ullage gases of helium, air and Mix_2 (groups 1 through 3 at each scale),

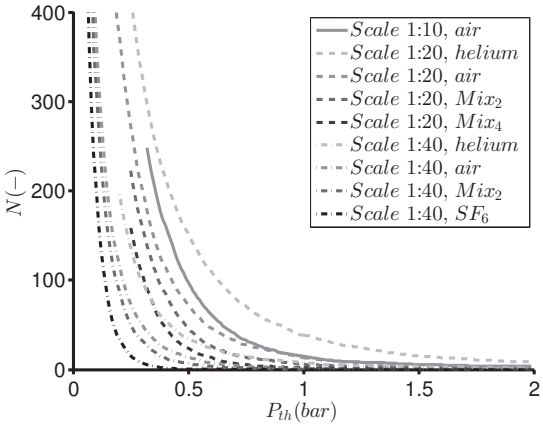

Fig. 4.9. Effect of varying P_{th} on number of measured impacts in each series of tests. The curves depict N, the average number of impacts found from 10 repetitions in each series.

Table 4.3. P_{th}(bar) corresponding to the number of recorded impacts for each group of tests.

Scale	Group	$N=$ 400	$N=$ 350	$N=$ 300	$N=$ 250	$N=$ 200	$N=$ 180	$N=$ 160	$N=$ 140	$N=$ 120	$N=$ 100	$N=$ 80	$N=$ 60	$N=$ 40	$N=$ 20	$N=$ 10	$N=$ 5
1:10	1	-	-	-	-	0.36	0.38	0.40	0.43	0.46	0.50	0.54	0.61	0.70	0.90	1.15	1.63
1:20	1	-	0.29	0.32	0.36	0.42	0.45	0.48	0.52	0.57	0.63	0.71	0.82	0.99	1.33	1.90	2.61
	2	-	-	-	0.26	0.30	0.32	0.34	0.36	0.39	0.43	0.48	0.54	0.64	0.89	1.11	1.46
	3	-	-	-	-	0.26	0.28	0.30	0.32	0.34	0.37	0.41	0.46	0.52	0.66	0.86	1.06
	4	-	-	-	-	-	-	-	0.27	0.29	0.31	0.34	0.37	0.42	0.52	0.63	0.77
1:40	1	-	-	-	-	-	0.21	0.23	0.25	0.27	0.30	0.34	0.38	0.46	0.65	0.90	1.21
	2	0.09	0.10	0.12	0.13	0.15	0.16	0.17	0.18	0.20	0.21	0.24	0.28	0.33	0.43	0.55	0.71
	3	0.08	0.09	0.10	0.12	0.13	0.14	0.15	0.16	0.17	0.19	0.21	0.23	0.28	0.35	0.44	0.55
	4	0.07	0.07	0.08	0.09	0.10	0.10	0.11	0.12	0.13	0.14	0.15	0.17	0.19	0.23	0.28	0.34

the required thresholds to obtain the same number of impacts for the same gas at scale 1:20 are indeed almost twice the thresholds at scale 1:40 to obtain the same number of impacts. This implies that considering a number of impacts, the ratio between the thresholds at scale 1:20 to scale 1:40 for each of those three ullage gases does not change much. It should be noted that this ratio of 2 can not be generalized further since the comparison between the thresholds at two scales is not based on a completely fair procedure. A fair comparison can be done only if the sensor sizes are comparable at the two scales which is not the case.

To make up for this shortcoming subareas can be defined with the scaled sizes at the two scales and the number of events based on those subareas can be counted and compared. The problem would be that a new threshold should be defined based on the newly defined areas but only impacts can be considered which have already been selected based on another threshold at the pressure sensor level. There would be no clear correlation between this threshold at sensor level and a pressure threshold defined at the level of the defined subareas. This would mean that the bookkeeping of the number of impacts over the desired thresholds at the level of subareas would not work properly and consequently the comparison would not be valid. Again and as it was mentioned before, between the thresholds at scale 1:10 and 1:20 with the ullage gas of air as well as between the thresholds at scale 1:10 and 1:40 with the ullage gas of air, other constant ratios can be found. What is interesting is that the ratios are almost constant over the range of N as it can be seen in Table 4.3.

4.5.2 3D Effects

All the 3 performed model test campaigns were performed with 3 DOF motions and were intended to be 2D. This symmetry was to be achieved in global and local flow geometry, kinematics, and subsequently the resultant impact loads. In practice the generated wave impacts were not completely 2D.

According to high-speed camera recordings the flow was reasonably 2D both globally and locally but 3D effects were observed which were manifested in terms of slightly twisted wave fronts as depicted by Fig. 4.10(a) or free surface instabilities for otherwise 2D breaking wave fronts as shown by Fig. 4.10(b). The first example was rare and severe irregularities in tank geometries and alignments were ruled out but the effect due to free surface instabilities was commonly observed.

On the influence of tank width on 2D sloshing model tests Schreier and Mehl [2012] elaborate that by increasing the 2D tank width, 3D effects appear which even affect the measured pressures and recommend to keep the ratio of tank width to length up to 0.1 which is also the case in all the three model test campaigns.

4.5.3 Impact ID Repeatability

Repeatability in sloshing model tests is usually studied through monitoring global fluid flow in tanks (see Karimi et al. [2015b]) and statistical results based on pressure measurements. In this study another level of comparison was possible thanks to the availability of high-speed cameras and the notion of impact coincidence which was introduced earlier. This meant that impacts of the same nature which had the same ID number for which high-speed video recordings were available could be closely observed. These observations showed that even though global fluid flow was highly repeatable, local flow in long sloshing tests was variable.

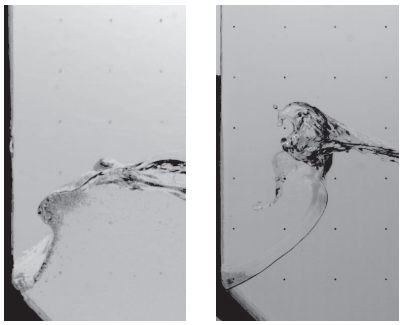

(a) (b)

Fig. 4.10. 3D effects observed with high-speed video recordings during the performed sloshing model tests (a) 3D twisted wave front at scale 1:40 (b) 2D wave front but with 3D free surface instabilities recorded at scale 1:20

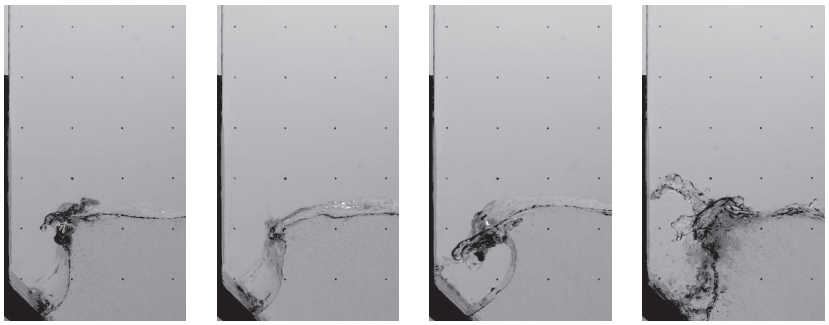

(a) (b) (c) (d)

Fig. 4.11. Variability of geometry and free surface instabilities in 4 breaking waves corresponding to the same ID captured in 4 repetitions of group 1 (with helium) of tests at scale 1:20.

Fig. 4.11 shows the local flow for 4 impacts of the same ID, which belong to group 1 of tests at scale 1:20. The global shapes are quite similar but locally and at the wave crest and front, considerable differences are observed. In Fig. 4.11 (c) the impact type is even changing as a gas pocket is being formed earlier compared to the other impacts. Different types of 3D effects are also observed in the depicted four repetitions. Similar discrepancies were observed for all the measured impacts as far as high-speed recordings were available and provided clues on the variability of wave shapes with the same IDs in long sloshing model

tests. The variability caused due to variability of impact geometry and kinematics, even when the same impact is considered, is expected to lead to variability of the resultant impact pressures.

4.6 Statistics of Pressure Peak Collections

Table 4.1 listed the series of tests that were performed at each scale with each ullage gas. Table 4.2 listed the number of impacts measured for every repetition from different series of tests and the corresponding P_{th}. For each event measured at each test, a pressure peak measured at sensor level is available which reflects the most severe local phenomena that took place in that impact. There are also pressure peaks found from averaged pressure signals on the defined subareas. Those calculated pressure peaks reflect a range of phenomena from local to global which depend on the location and size of the defined areas. The collection of all the pressure peaks (measured or calculated) found from all the repetitions in each series of tests (a maximum of 10 repetitions where used in this study for each series of tests) represents the collective distribution and severity of local or global phenomena (depending on the choice of subarea to be studied) that occur during the considered series of tests. Using many repetitions to make the collection of pressure peaks is due to large variabilities that are associated with sloshing. If such collections are found and compared on the same subarea at the same scale but for different ullage gases, the effect of ullage gas on the severity of local or global phenomena can be studied statistically. The comparison of pressure peak collections on the same subarea and with the same ullage gas but at different scales, helps to investigate the scaling effects of pressures. It should be noted that in the latter comparison, only the gas-liquid density ratio would match between the different scales. The bias due to the other parameters such as compressibility would still exist.

In this study the comparison of pressure peaks is done at the most local and the most global levels available. The most local level is represented by measured pressure peaks (P_{max}) at sensor level whereas the most global level is represented by collections of calculated pressure peaks on A63 ($\bar{P}_{A63,max}$) which is the largest defined subarea. The collections of 1000 highest pressure peaks for each series of tests are used and summarized by their probability density functions. The comparisons of collections of pressure peaks are done in two steps. First the effect of changing the ullage gas at each scale is studied. At this step only the results at scales 1:20 and 1:40 are considered since at scale 1:10 the tests were performed only with air. At the second step by considering the results with three ullage gases of helium, air and Mix_2, scaling effects are observed.

4.6.1 Effect of Different Ullage Gases at Each Scale

Fig. 4.12 shows a comparison of probability density function of 1000 highest pressure peaks at scale 1:20 found from series of tests with four ullage gases of helium, air, Mix_2 and Mix_4 at sensor level and on A63 respectively representing the most local and the most global phenomena that could be measured. Each series of tests with each gas consisted of 10 repetitions. It can be observed that considering both sizes, the probability density functions are gradually shifted towards the higher pressure by decreasing the ullage gas density. The most probable pressures also increase by reducing the ullage gas density. The tails of the distributions are also thicker with lighter gases. It should be kept in mind that other relevant properties of ullage gases other than density change as well.

A similar comparison was made at scale 1:40 summarized in Fig. 4.13, this time considering four series of tests with helium, air, Mix_2 and SF_6. Again by reducing the ullage gas density (along with other ullage gas properties), higher pressure values become more probable both at sensor level and on A63. The most probable pressure peak is also modified for each series.

From the increase of pressure peaks on A63 by reducing the ullage gas density, it appears that the breaking waves are slowed down in a global level by heavier gases. This is in line with the results presented in Karimi et al. [2016] which were obtained using single impact waves (SIW). Change of pressure peaks at sensor level by changing the ullage gas would be much more complicated to describe. Not only the transfer of energy between the liquid and gas phases plays a role at this local level, other gas and liquid properties come into play. The resultant is a statistical change of pressure peaks with an inverse relation between the change of pressures and the ullage gas density. In the interpretation of these results it should be noted that collections of pressure peaks were compared without considering the origin of such pressure peaks in terms of breaking wave category, shape, kinematics etc.

4.6.2 Scale Effects

Using the collection of pressure peaks which were considered in the previous section it can be verified whether scaling the pressures by the geometrical scale of λ is conservative or not since this is considered to be the case in many practical applications. This verification can be conducted for any chosen subarea on the selected common area. Normally and in practice, severe loads with long return periods are of interest. These are the loads which are not normally measured within the limited duration of model tests. It means that in order to predict them, a distribution should be fitted to the collections of pressure peaks and then severe loads are found by extrapolation. Such a study needs considerable reasoning on choosing the most relevant distribution, a debate which is ongoing

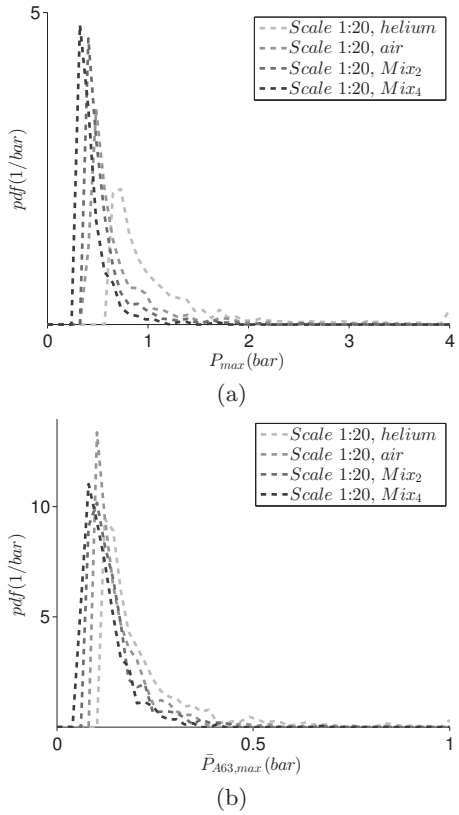

Fig. 4.12. Probability density function of 1000 highest pressure peaks at scale 1:20 obtained from series of tests with helium, air, Mix_2 and Mix_4 (a) at sensor level representing the most local phenomena (b) on A63 representing the most global phenomena that could be measured. Each series of tests with each gas consists of 10 repetitions.

and is out of the scope of this paper. Instead and regardless of the fitted distributions, probability density functions of the pressure peaks can be compared for the corresponding cases at different scales. Such a comparison for the most locally measured pressures at sensor level is given by Fig. 4.14 for three ullage gases. All the pressure peaks have been scaled to scale 1:10 with a factor of 2 for peaks at scale 1:20 and a factor of 4 for peaks at scale 1:40. Fig. 4.14 shows that at sensor level and for three gases of helium, air and Mix_2 probability density functions

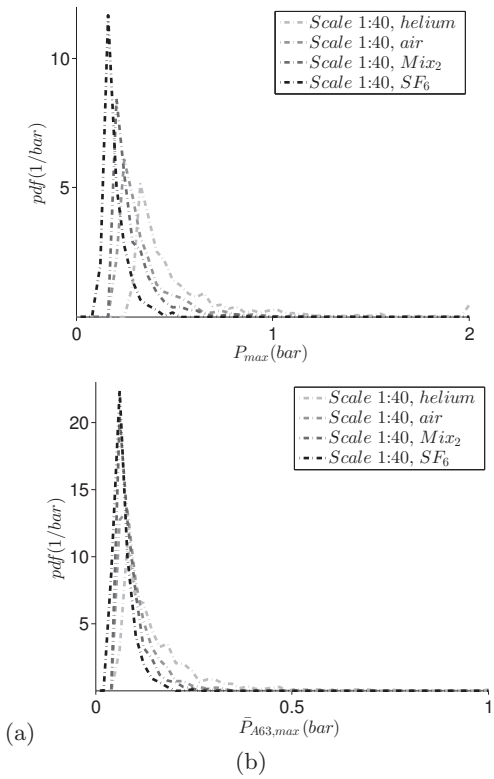

Fig. 4.13. Probability density function of 1000 highest pressure peaks at scale 1:40 obtained from series of tests with helium, air, Mix_2 and SF_6 (a) at sensor level representing the most local phenomena (b) on A63 representing the most global phenomena that could be measured. Each series of tests with each gas consist of 10 repetitions.

of 1000 pressure peaks are almost matching at scales 1:20 and 1:40. Comparing the results at scale 1:10 with air with the results at smaller scales with air shows a relative conservatism of smaller model scale results. An important point to consider is that in this comparison a certain bias exists due to the fact that the same sensors with the same sensing areas are used for the model tests. This can imply that at smaller scales a bigger pressure averaging effect should exist which could be potentially less conservative. Normally if we had smaller sensors at scale 1:20 and 1:40 in order to have the right sensor size with respect to scale 1:10, we would expect higher pressures at scale 1:20 and 1:40. Despite this bias, the

conservatism is observed in the comparison between scales 1:10 vs 1:20 on the one hand and results at scales 1:10 and 1:40 on the other hand.

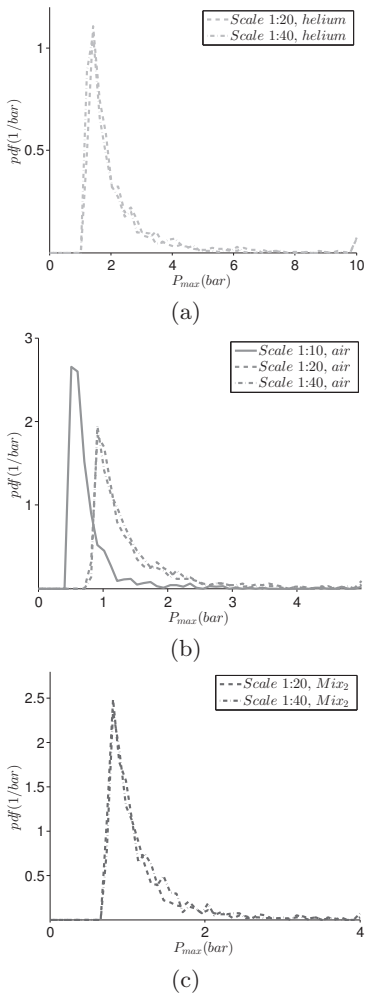

Fig. 4.14. Probability density function of 1000 highest pressure peaks at sensor level at scales 1:10, 1:20 and 1:40 obtained from series of tests with (a) helium (b) air and (c) Mix_2. All the pressure peaks have been scaled to scale 1:10 with a factor of 2 for peaks at scale 1:20 and a factor of 4 for peaks at scale 1:40. Each series of tests with each gas consists of 10 repetitions.

Fig. 4.15 shows a similar comparison but this time on subarea A63. In this comparison a statistical conservatism of model test results in terms of governing distributions of pressure peaks is observed. The pressure distributions found from smaller scales, are clearly shifted towards higher pressures. The most probable pressure peaks are also overestimated if found from model test results. In this comparison the bias of using the same pressure sensor size is less present (although not completely gone) since the area that is used for the comparison is exactly the same but still the pressures measured at sensor level are used for finding the average pressure peaks.

In order to focus further on the highest measured pressure peaks and given the 10 repetitions (each repetition corresponding to 5 hours at full-scale) in each series of tests at each scale, pressure peaks with return periods up to 50 hours can be found in each series and can be compared with the pressures corresponding to the same return periods in other series.

This comparison done for A63 can be summarized in 3 graphs depicted in Fig. 4.16. At each graph, 500 highest and sorted pressure peaks obtained from tests with air at a larger scale have been used as reference and have been compared with the same number of highest and sorted pressure peaks found from tests with other gases at a smaller scale. All the pressures have been scaled by the geometrical scale λ with respect to tests at scale 1:10. In other words pressure peaks at scale 1:20 have all been multiplied by a factor 2 and pressure peaks at scale 1:40 have all been multiplied by a factor 4. It should be noted that in each collection of sorted peaks, the highest pressure corresponds to a return period of 50 hours, the second highest pressure corresponds to a return period of 50/2 = 25 hours, the third highest pressure corresponds to a return period of 50/3 = 16.66 hours and so forth.

Since in practice sloshing model tests are done with the same gas-liquid density ratio, it is important to focus more on series of tests at different scales with the same ullage gases. Considering the subarea A63, and based on Fig. 4.16(a) and (b) pressures obtained from model tests with air at scales 1:20 and 1:40 when multiplied by respectively 2 and 4, give conservative predictions about the pressures with similar return periods at scale 1:10. In Fig. 4.16(c) and comparing the two scales of 1:20 and 1:40 with air, the 5 highest scaled results of the test at scale 1:40 are not conservative in predicting the pressures with the same return periods at scale 1:20.

It can also be noted from graphs of Fig. 4.16 that at scales 1:20 and 1:40 and by considering any return period, lighter ullage gases give higher expected pressures.

The discussion presented here is also covered for different sets of tests and a fewer number of common areas by Karimi et al. [2013a] and Karimi et al. [2014a]. In this study and considering more defined subareas the comparison

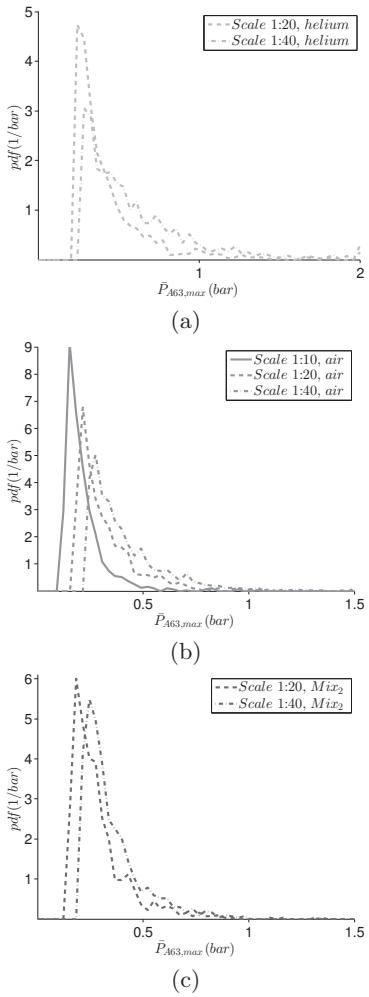

Fig. 4.15. Probability density function of 1000 highest pressure peaks on A63 at scales 1:10, 1:20 and 1:40 obtained from series of tests with (a) helium (b) air and (c) Mix_2. All the pressure peaks have been scaled to scale 1:10 with a factor of 2 for peaks at scale 1:20 and a factor of 4 for peaks at scale 1:40. Each series of tests with each gas consists of 10 repetitions.

can be made by focusing on the highest pressures obtained from each group of tests on each area. This comparison is done between tests with the same density

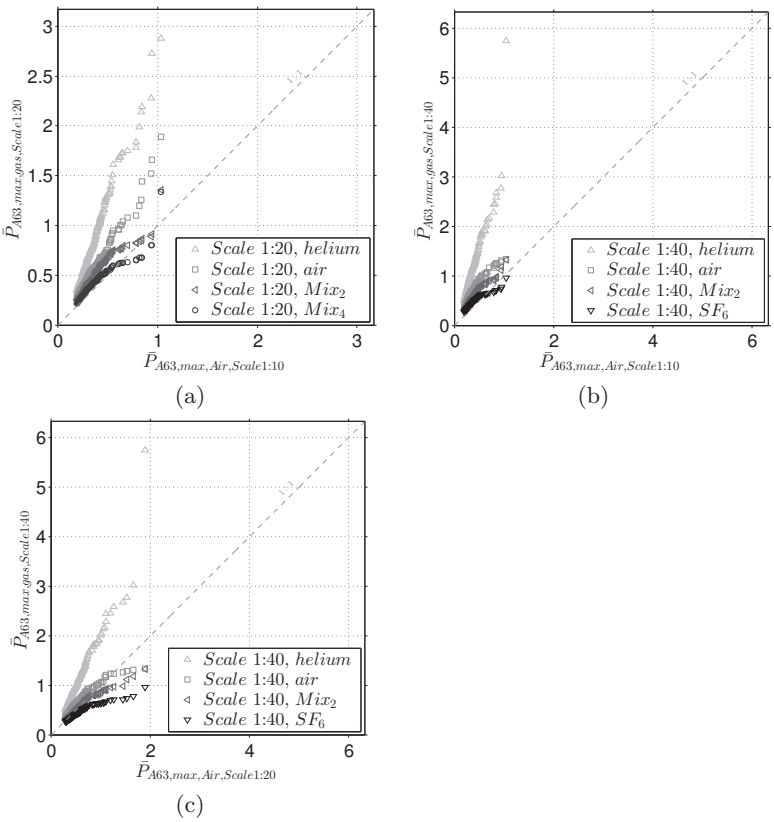

Fig. 4.16. Investigation of conservatism of scaling pressure peaks (multiplying pressures by the geometrical scale of λ) on A63 by comparing calculated pressure peaks with the same return periods found from 10 repetitions of irregular tests with the total duration of 50 hours. All the pressures have been scaled to scale 1:10 (a) Pressures with air at scale 1:10 compared with pressures at scale 1:20 (b) Pressures with air at scale 1:10 compared with pressures at scale 1:40 (c) Pressures with air at scale 1:20 compared with pressures at scale 1:40.

ratio at different scales which correspond to a return period of 50 hours. By the requirement of the same density ratio, 5 comparisons on every defined subarea can be done between series of tests with air (3 comparisons), tests with helium (1 comparison) and tests with Mix_2 (1 comparison). The results of such comparisons are shown in Table 4.4.

Table 4.4. Maximum impact pressures on 63 common areas compared in 5 groups with the same ullage gases of air, helium and Mix_2 at scales 1:10, 1:20 and 1:40. The impact pressures have been brought to scale 1:10 after scaling (pressures at scale 1:20 were multiplied by 2 and pressures at scale 1:40 were multiplied by 4). The cases where measurements underestimate the values at larger scale have been highlighted.

Ullage Gas	Air	Air	Air	He	Mix_2
Large Scale vs. Small Scale	1:10 vs. 1:20	1:10 vs. 1:40	1:20 vs. 1:40	1:20 vs. 1:40	1:20 vs. 1:40
An	$P_{An,max,RP=50h}$ (bar)				
A01	02.50 vs. 03.21	02.50 vs. 06.73	03.21 vs. 06.73	07.33 vs. 20.19	01.73 vs. 02.25
A02	02.33 vs. 04.40	02.33 vs. 03.35	**04.40 vs. 03.35**	05.31 vs. 13.67	01.94 vs. 03.44
A03	01.37 vs. 03.50	01.37 vs. 04.37	03.50 vs. 04.37	09.16 vs. 09.36	01.87 vs. 03.14
A04	01.23 vs. 02.87	01.23 vs. 03.60	02.87 vs. 03.60	**14.25 vs. 04.67**	03.04 vs. 04.89
A05	02.15 vs. 04.54	02.15 vs. 02.62	**04.54 vs. 02.62**	03.51 vs. 03.87	02.43 vs. 02.66
A06	**02.47 vs. 02.16**	02.47 vs. 02.67	02.16 vs. 02.67	06.57 vs. 06.85	01.99 vs. 02.31
A07	02.33 vs. 04.78	02.33 vs. 04.09	**04.78 vs. 04.09**	11.10 vs. 11.79	01.63 vs. 02.40
A08	01.85 vs. 04.60	01.85 vs. 02.99	**04.60 vs. 02.99**	05.20 vs. 13.87	02.11 vs. 04.57
A09	01.38 vs. 04.52	01.38 vs. 04.76	04.52 vs. 04.76	11.75 vs. 13.03	02.14 vs. 02.57
A10	02.07 vs. 02.52	02.07 vs. 03.06	02.52 vs. 03.06	03.88 vs. 16.18	02.36 vs. 04.00
A11	02.25 vs. 03.99	02.25 vs. 02.52	**03.99 vs. 02.52**	04.21 vs. 05.67	02.05 vs. 03.29
A12	**02.93 vs. 02.58**	**02.93 vs. 02.65**	02.58 vs. 02.65	03.35 vs. 14.09	02.02 vs. 02.07
A13	02.01 vs. 02.65	02.01 vs. 03.86	02.65 vs. 03.86	04.50 vs. 10.95	01.66 vs. 01.82
A14	01.70 vs. 03.95	01.70 vs. 02.50	**03.95 vs. 02.50**	06.22 vs. 10.55	01.67 vs. 02.20
A15	01.13 vs. 02.59	01.13 vs. 02.82	02.59 vs. 02.82	**07.12 vs. 06.99**	01.57 vs. 02.52
A16	01.08 vs. 03.09	01.08 vs. 02.41	**03.09 vs. 02.41**	**08.57 vs. 03.90**	02.22 vs. 03.06
A17	02.21 vs. 02.84	**02.21 vs. 01.96**	02.84 vs. 01.96	03.29 vs. 04.44	**02.11 vs. 01.87**
A18	01.94 vs. 03.31	01.94 vs. 02.62	**03.31 vs. 02.62**	06.58 vs. 09.19	01.54 vs. 02.29
A19	01.53 vs. 04.35	01.53 vs. 02.42	**04.35 vs. 02.42**	07.26 vs. 12.71	01.71 vs. 02.67
A20	01.13 vs. 03.11	01.13 vs. 02.77	**03.11 vs. 02.77**	06.74 vs. 08.14	01.92 vs. 02.44
A21	01.42 vs. 02.94	01.42 vs. 02.25	**02.94 vs. 02.25**	03.99 vs. 09.12	02.01 vs. 02.58
A22	02.59 vs. 02.83	**02.59 vs. 02.19**	**02.83 vs. 02.19**	03.40 vs. 07.04	01.86 vs. 02.08
A23	02.16 vs. 03.71	02.16 vs. 05.06	03.71 vs. 05.06	09.21 vs. 10.48	01.50 vs. 01.89
A24	02.09 vs. 03.60	02.09 vs. 02.50	**03.60 vs. 02.50**	04.91 vs. 11.66	01.76 vs. 02.43
A25	01.36 vs. 03.44	01.36 vs. 02.73	**03.44 vs. 02.73**	**10.13 vs. 08.23**	**02.00 vs. 01.98**
A26	01.59 vs. 02.58	01.59 vs. 02.61	02.58 vs. 02.61	08.63 vs. 09.24	02.34 vs. 03.41
A27	02.19 vs. 03.13	**02.19 vs. 01.95**	**03.13 vs. 01.95**	**03.79 vs. 03.62**	02.20 vs. 02.55
A28	**02.69 vs. 02.37**	**02.69 vs. 02.47**	02.37 vs. 02.47	03.31 vs. 08.18	01.82 vs. 01.90
A29	01.62 vs. 02.93	01.62 vs. 02.81	**02.93 vs. 02.81**	04.15 vs. 08.76	**01.63 vs. 01.54**
A30	01.38 vs. 03.19	01.38 vs. 02.01	**03.19 vs. 02.01**	04.90 vs. 08.56	01.55 vs. 01.73
A31	00.95 vs. 02.23	00.95 vs. 02.10	**02.23 vs. 02.10**	**05.71 vs. 05.67**	01.52 vs. 02.15
A32	01.48 vs. 02.69	01.48 vs. 02.02	**02.69 vs. 02.02**	**06.24 vs. 03.44**	01.84 vs. 02.24
A33	01.59 vs. 03.26	01.59 vs. 02.23	**03.26 vs. 02.23**	04.84 vs. 09.95	01.58 vs. 01.78
A34	01.32 vs. 03.48	01.32 vs. 01.88	**03.48 vs. 01.88**	05.42 vs. 10.02	01.62 vs. 01.83
A35	01.02 vs. 02.41	01.02 vs. 02.30	**02.41 vs. 02.30**	04.91 vs. 06.45	01.57 vs. 02.01
A36	01.73 vs. 02.60	01.73 vs. 02.14	**02.60 vs. 02.14**	03.52 vs. 06.24	01.73 vs. 01.90
A37	01.39 vs. 02.62	01.39 vs. 02.23	**02.62 vs. 02.23**	03.67 vs. 07.71	**01.54 vs. 01.33**
A38	01.17 vs. 02.64	01.17 vs. 01.70	**02.64 vs. 01.70**	04.28 vs. 07.16	01.42 vs. 01.65
A39	01.11 vs. 02.21	01.11 vs. 01.88	**02.21 vs. 01.88**	04.67 vs. 04.91	01.40 vs. 01.81
A40	01.35 vs. 02.87	01.35 vs. 01.92	**02.87 vs. 01.92**	04.06 vs. 08.64	**01.54 vs. 01.37**
A41	01.14 vs. 02.86	01.14 vs. 01.72	**02.86 vs. 01.72**	04.38 vs. 08.29	01.49 vs. 01.59
A42	01.30 vs. 02.12	01.30 vs. 01.98	**02.12 vs. 01.98**	03.93 vs. 05.44	01.39 vs. 01.64
A43	01.88 vs. 02.74	01.88 vs. 02.94	02.74 vs. 02.94	05.54 vs. 08.17	**01.59 vs. 01.50**
A44	01.58 vs. 03.47	01.58 vs. 01.97	**03.47 vs. 01.97**	06.53 vs. 09.91	**01.69 vs. 01.60**
A45	01.13 vs. 02.55	01.13 vs. 02.39	**02.55 vs. 02.39**	05.99 vs. 06.37	01.51 vs. 01.80
A46	01.19 vs. 02.79	01.19 vs. 02.10	**02.79 vs. 02.10**	**05.66 vs. 05.46**	01.96 vs. 02.21
A47	02.34 vs. 02.74	**02.34 vs. 01.88**	**02.74 vs. 01.88**	03.12 vs. 04.24	**01.96 vs. 01.85**
A48	01.23 vs. 02.29	01.23 vs. 01.86	**02.29 vs. 01.86**	03.42 vs. 06.77	**01.44 vs. 01.32**
A49	01.02 vs. 02.26	01.02 vs. 01.51	**02.26 vs. 01.51**	03.74 vs. 06.26	01.32 vs. 01.48
A50	01.16 vs. 02.50	01.16 vs. 01.68	**02.50 vs. 01.68**	03.50 vs. 07.53	**01.45 vs. 01.37**
A51	01.04 vs. 02.45	01.04 vs. 01.58	**02.45 vs. 01.58**	03.70 vs. 07.11	01.38 vs. 01.42
A52	01.09 vs. 02.04	01.09 vs. 01.62	**02.04 vs. 01.62**	03.11 vs. 06.08	**01.35 vs. 01.29**
A53	01.02 vs. 02.22	01.02 vs. 01.48	**02.22 vs. 01.48**	03.08 vs. 06.68	**01.37 vs. 01.36**
A54	01.53 vs. 02.65	01.53 vs. 02.19	**02.65 vs. 02.19**	04.35 vs. 08.17	**01.60 vs. 01.38**
A55	01.31 vs. 02.86	01.31 vs. 01.68	**02.86 vs. 01.68**	04.97 vs. 08.08	**01.58 vs. 01.43**
A56	00.95 vs. 02.11	00.95 vs. 02.10	**02.11 vs. 02.10**	04.44 vs. 05.27	01.36 vs. 01.60
A57	01.57 vs. 02.64	01.57 vs. 01.86	**02.64 vs. 01.86**	**04.29 vs. 03.82**	**01.69 vs. 01.64**
A58	01.30 vs. 02.39	01.30 vs. 01.77	**02.39 vs. 01.77**	03.73 vs. 07.23	**01.54 vs. 01.33**
A59	01.12 vs. 02.39	01.12 vs. 01.57	**02.39 vs. 01.57**	04.06 vs. 06.82	**01.45 vs. 01.43**
A60	01.18 vs. 02.16	01.18 vs. 01.85	**02.16 vs. 01.85**	03.59 vs. 04.59	01.30 vs. 01.43
A61	01.15 vs. 02.11	01.15 vs. 01.50	**02.11 vs. 01.50**	03.25 vs. 06.40	**01.44 vs. 01.31**
A62	00.99 vs. 02.07	00.99 vs. 01.48	**02.07 vs. 01.48**	03.46 vs. 05.96	01.35 vs. 01.42
A63	01.04 vs. 01.89	01.04 vs. 01.34	**01.89 vs. 01.34**	02.88 vs. 05.75	**01.36 vs. 01.33**

The table shows mostly conservative model test results except for the comparison between tests with air at scales 1:20 and 1:40 where on most of the areas, model test results are non-conservative after scaling the pressures using the geometric scale.

Table 4.5. Maximum impact pressures on 9 subarea sizes compared in 5 groups with the same ullag gases of air, helium and Mix_2 at scales 1:10, 1:20 and 1:40. The impact pressures have been brought to scale 1:10 after scaling (pressures at scale 1:20 were multiplied by 2 and pressures at scale 1:40 were multiplied by 4). The cases were measurements underestimate the measurements at larger scale have been highlighted.

Ullage Gas	Air	Air	Air	He	Mix_2
Large Scale vs. Small Scale	1:10 vs. 1:20	1:10 vs. 1:40	1:20 vs. 1:40	1:20 vs. 1:40	1:20 vs. 1:40
$Subarea\ Size\ n$	$\bar{P}_{Subarea\ Size\ n,max}(bar), RP = 50$ hours				
$Subarea\ Size\ 1$	02.93 vs. 04.78	02.93 vs. 06.73	04.78 vs. 06.73	14.25 vs. 20.19	03.04 vs. 04.89
$Subarea\ Size\ 2$	02.69 vs. 04.35	02.69 vs. 05.06	04.35 vs. 05.06	10.13 vs. 12.71	02.34 vs. 03.41
$Subarea\ Size\ 3$	01.73 vs. 03.48	01.73 vs. 02.81	**03.48 vs. 02.81**	06.24 vs. 10.02	01.84 vs. 02.24
$Subarea\ Size\ 4$	02.34 vs. 03.47	02.34 vs. 02.94	**03.47 vs. 02.94**	06.53 vs. 09.91	01.96 vs. 02.21
$Subarea\ Size\ 5$	01.23 vs. 02.50	01.23 vs. 01.86	**02.50 vs. 01.86**	03.74 vs. 07.53	01.45 vs. 01.48
$Subarea\ Size\ 6$	01.57 vs. 02.86	01.57 vs. 02.19	**02.86 vs. 02.19**	04.97 vs. 08.17	**01.69 vs. 01.64**
$Subarea\ Size\ 7$	01.30 vs. 02.39	01.30 vs. 01.85	**02.39 vs. 01.85**	04.06 vs. 07.23	**01.54 vs. 01.43**
$Subarea\ Size\ 8$	01.15 vs. 02.11	01.15 vs. 01.50	**02.11 vs. 01.50**	03.46 vs. 06.40	**01.44 vs. 01.42**
$Subarea\ Size\ 9$	01.04 vs. 01.89	01.04 vs. 01.34	**01.89 vs. 01.34**	02.88 vs. 05.75	**01.36 vs. 01.33**

This comparison can also be done between the collection of pressure peaks on the same corresponding size of subareas. According to Fig. 4.4 there are 9 sizes of subareas with size (at scale 1:10) of 800 mm^2 corresponding to A1-A12, size of 1600 mm^2 for A17-A28, size of 2400 mm^2 corresponding to A29-A36, size of 3200 mm^2 for A37-A47, size of 4000 mm^2 for A48-A51, size of 4800 mm^2 for A52-A57, size of 6400 mm^2 for A58-A60, size of 8000 mm^2 for A61-A62 and finally size of 9600 mm^2 corresponding to A63. If the samples of pressure peaks are found and sorted on each size of subareas, pressures with the same return period up to 50 hours can still be directly compared. A comparison similar to what was presented in Table 4.4 but this time based on the same size of subareas is presented in Table 4.5. Based on this table the results of tests at scale 1:40 and 1:20 are conservative in predicting the pressures at scale 1:10. This is also true when comparing tests with helium at scales 1:20 and 1:40. Comparing the results at scales 1:20 and 1:40 with Mix_2 at scales 1:20 and 1:40 shows slightly non-conservative predictions on the largest sizes of defined subareas. Comparing pressures with air at scales 1:20 and 1:40 show most of the observed non-conservative predictions.

4.7 Impact Pressures and Scaling Studied based on Impact IDs

In 90 sloshing tests that were performed according to Table 4.1, 1922 impact IDs were identified with a tolerance of 50 ms between the impact times (quantified at scale 1:10). In the following section all or part of those impact IDs were used in order to verify the effect of ullage gas on breaking wave impacts and pressure scaling.

4.7.1 The effect of ullage gas at scales 1:20 and 1:40

Tests at scale 1:20

At scale 1:20 40 tests were performed with 4 ullage gases of helium, air, Mix_2 and Mix_4 (10 repetitions with each gas). In those 40 tests 10688 events (wave impacts with a maximum pressure larger than 0.25 bar) were recorded (this number is simply the sum of the number of impacts at scale 1:20 according to Table 4.2). 1319 IDs out of the total 1922 detected IDs could be found among the 10688 events. Clearly not all the IDs had been captured in every test. This is normal and is considered to be due to the pressure threshold used in the measurement system as well as the variability associated with sloshing impacts.

In order to study the effect of changing the ullage gas on recorded impact IDs, first every ID for which there is at least one measurement with every ullage gas is selected. At scale 1:20 377 IDs were found for which there were recorded impacts with each ullage gas. For any of those 377 IDs and on each 63 subarea, a maximum pressure could be found for each gas out of all the corresponding 10 repetitions with that gas denoted as $\bar{P}_{An,ID,max10,gas,Scale1:20}$. This gave a 377×4 matrix for each subarea which became the basis for the later comparisons at this scale. Every row of the prepared matrix corresponded to one ID for which there was at least one recorded impact with each gas and every column corresponded to one of the four ullage gases.

It was considered that using the average of measured pressures for each ID and for each gas could have been another interesting parameter to compare but since there were not equal numbers of recordings for each ID and each gas and since the lack of data could not have been taken into account in the statistical post-processing, this comparison was ruled out. Comparison of the statistical distributions of pressure peaks for each ID and for each gas was not considered either since the number of repetitions (10) gave at most 10 values for each ID which was not enough.

Using every prepared 377×4 matrix for each area, the effect of ullage gas on the maximum pressures obtained for each ID can first be compared visually. Such

a comparison is shown for A63 in Fig. 4.17.

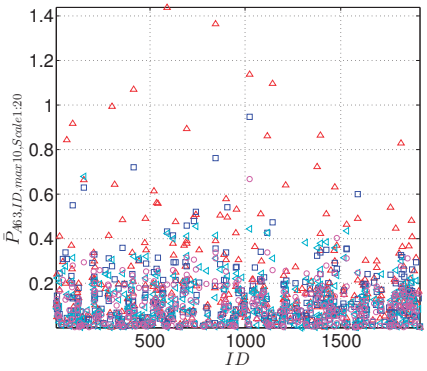

(a)

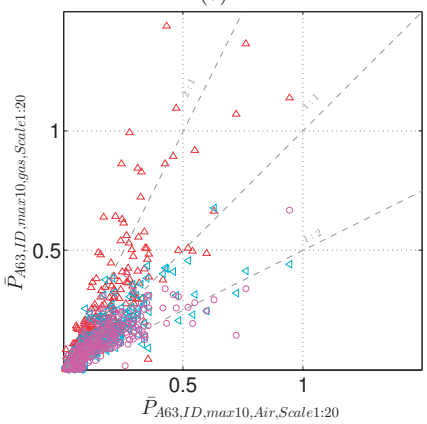

(b)

Fig. 4.17. Visual comparison of maximum pressures on A63 for common IDs with different ullage gases at scale 1:20 (a)Maximum pressures obtained in 377 common IDs with 4 ullage gases at scale 1:20 (b) In the abscissa maximum pressures obtained in 377 common IDs with air. In the ordinate maximum pressures obtained in the corresponding common impacts but with 3 other ullage gases. $\triangle$: helium, $\square$: air, $\triangleleft$: Mix_2, $\circ$: Mix_4.

Fig. 4.17 (a) shows the maximum pressures obtained for 377 common IDs with 4 ullage gases on A63. The zone of highest pressures is dominated by impacts with helium with occasional presence of high pressures due to impacts

with air. The same graph is rearranged in Fig. 4.17 (b) where the maximum pressures on A63 with air and for 377 common impacts are in the abscissa. In the ordinate the maximum pressures obtained with the three other ullage gases corresponding to the same exact IDs were plotted. It is observed that maximum highest pressures for each gas are dominated by more or less the same IDs. In other words impact IDs which are responsible for highest pressures on A63 with one gas, are responsible for the generation of the highest impact pressures with other ullage gases as well. Again it is clear that the highest reached pressures were obtained with helium for the considered IDs.

Among the 377 selected IDs it can be verified for what percentage of the total impacts, the maximum is achieved by each gas. This comparison can be done for each one of the 63 subareas separately as shown in Fig. 4.18 (a). It is clear that not for all the IDs lighter ullage gas leads to higher maximum pressures. This is true about all the studied areas even though the the percentages seemed to depend on the subarea size and location. Still for a larger percentage of the considered IDs, the maximum pressure (obtained from 10 repetitions) is obtained with helium. This percentage includes the most severe impacts as observed in the previous figure. There are around 20-30 percent of the IDs (depending on the subarea) for which maximum pressures are obtained with air. There is almost equal percentages of impact IDs for which the maximum is obtained with either Mix_2 and Mix_4 even though those seem to be milder impacts. For instance considering A63, the most severe ID for which the maximum pressure was achieved by Mix_4 recorded 0.40 bars with this gas (0.37, 0.26 and 0.24 were the maxima reached for the same ID with helium, air and Mix_2 respectively). On the other hand and on A63, the maximum achieved for one ID with helium is 1.44 bar which is much larger (0.43, 0.42 and 0.19 were the maxima reached for the same ID with air, Mix_2 and Mix_4 respectively). For another impact ID and considering A63 the maximum pressures achieved by helium, air, Mix_2 and Mix_4 were respectively 0.08, 0.15, 0.20, 0.26 bars. This supports the idea presented in Karimi et al. [2016] that changing the ullage gas could change the impact type which could in turn lead to impact types which lead to higher pressures.

The absolute variability of pressure peaks achieved for all 377 selected IDs on 63 areas can also be compared for different ullage gases as presented in Fig. 4.18 (b). This variability is measured in terms of standard deviation of the maximum pressures. The absolute variability as measured this way decreases strongly by using heavier ullage gas. Variability is again a function of area size and location as higher areas show larger variabilities compared to lower subareas on the selected common area.

The fact that for some impact IDs and after 10 repetitions maximum pressures were obtained with heavier gas rather than the lightest gas of helium is important for further consideration. According to Karimi et al. [2016] and for

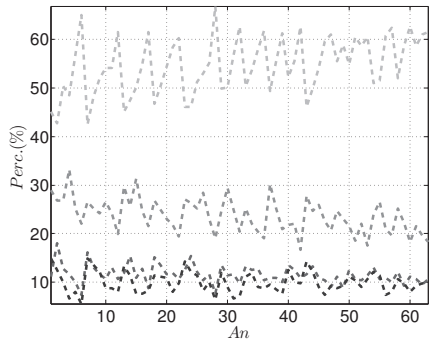

(a)

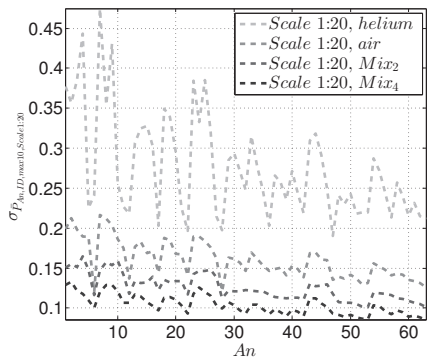

(b)

Fig. 4.18. For the 63 subareas, (a) percentage of IDs among the 377 common IDs at scale 1:20 for which the maximum is achieved by each ullage gas after 10 repetitions with each gas (b) standard deviation of maximum pressures obtained for 377 common IDs for 4 ullage gases at scale 1:20. The maximum pressures for each ID and for each gas is found from 10 repetitions for each gas. The use of lines in these graphs is only for better readability. There is no continuity between the connected points except for the areas of the same size.

the verified SIW (single impact waves) it was shown that wave fronts and slightly wave troughs were slowed down more by heavier gases. This meant that in case of heavier ullage gases, more energy is transferred from the liquid phase to the gas phase which in turn would lead to smaller levels of energy in the liquid and consequently smaller pressures. Nevertheless it was observed that the mentioned

process leads to a change of impact geometry which was considered to be important for the resulting pressures. It was speculated that in some cases this could lead to a change of impact type which could potentially lead to higher pressures with heavier gas. Something that should be kept in mind is the variability of impact geometries in sloshing model tests even for the same impact ID and with the same ullage gas as depicted in Fig. 4.11. The associated variability could lead to variations about the typical impact shape for each ID and with each gas which could also have significant effects on resultant pressures.

Considering the knowledge about the impact IDs and by the use of high-speed video recordings, the shape of the typical severe impact types can be studied. The impacts for which maximum pressures are not obtained with the lightest gas were also interesting cases for comparison. Similar to what was plotted in Fig. 4.17(b) with data from tests with air in abscissa, a new graph can be plotted with maximum pressures on A63 for 453 common IDs with tests with helium in abscissa and the maximum pressures for the corresponding IDs with Mix_4 in ordinate as shown in Fig. 4.19.

According to Fig. 4.19 two groups of interesting impact IDs were further investigated using high-speed video recordings. The first group included impacts for which the lighter gas of helium induced higher pressures and those with the highest induced pressure in the comparison. For the first group, it was observed that for pressures larger than 0.4 bars with helium, increase of pressure in IDs recorded with helium does not lead to considerable increase of pressure for the corresponding IDs with Mix_4. At this range pressures obtained with Mix_4 are almost constant. The second group includes IDs for which the heavier gas of Mix_4 induced higher pressures. There are only a few IDs in the second groups of impacts but in some cases the maximum pressures obtained with the heavier gas are proportionally much larger than those obtained with helium. The range and intensity of impact pressures in the second group is much smaller than the range and intensity observed in the first group. In terms of impact types it was observed that most of the impacts in the first groups were of small gas pocket or flip-through type. Similarities between impact geometries in the first group were also observed. In the second group of impacts broken and slosh wave impacts (breaking before the impact) were observed even though near flip-through impacts in the available videos with Mix_4 were also recorded. One aspect that should be noted in this study is that the shown snapshots are merely one recorded case with one ullage gas. Variability of the impact shape corresponding to each ID should be also kept in mind and studied further.

Tests at scale 1:40

At scale 1:40 40 tests were performed with 4 ullage gases of helium, air, Mix_2 and SF_6 (10 repetition with each gas). In those 40 tests 17663 events (wave

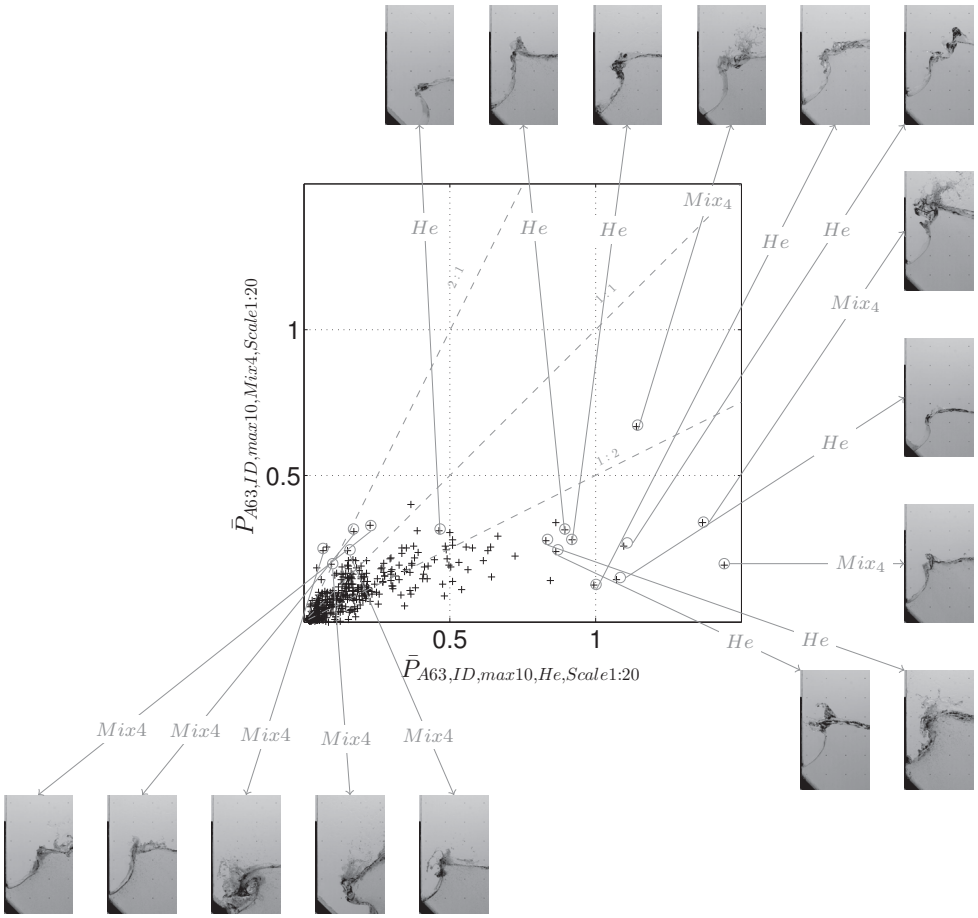

Fig. 4.19. In the abscissa maximum pressures on A63 obtained in 453 common IDs with helium at scale 1:20. In the ordinate maximum pressures obtained in the corresponding common impacts with Mix_4 at the same scale. For each selected impact a representative snapshot of the high-speed video recording has been shown. The choice of ullage gas for images was based on image availability.

impacts with maximum pressures larger than the chosen pressure thresholds) were recorded (this number is the sum of the number of impacts at scale 1:40 according to Table 4.2). 1487 IDs out of the total 1922 detected IDs could be

found among the 17663 events. Again not all the IDs were captured at scale 1:40 due to the pressure thresholds used and the variability associated with sloshing impacts.

Similar to the process adopted for analysis at scale 1:20, every ID for which there is at least one measurement with every ullage gas is selected. At scale 1:40 486 IDs were found for which there were recorded impacts with each ullage gas. For any of those 486 IDs and on each subarea, a maximum pressure could be found for each gas out of 10 repetitions with that gas which is denoted as $\bar{P}_{An,ID,max10,gas,Scale1:40}$. This gave a 486×4 matrix for each subarea which was the basis for the later comparisons at this scale. Again every row of the prepared matrix corresponded to one ID for which there was at least one recorded impact with each gas and every column corresponded to one of the four ullage gases.

Using every prepared 486×4 data matrix for each area, the effect of ullage gas on the maximum pressures obtained for each ID was first compared visually. Such a comparison is shown for A63 in Fig. 4.20.

Fig. 4.20 (a) shows the maximum pressures obtained for 486 common IDs with 4 ullage gases on A63. The zone of highest pressures is still dominated by impacts with helium (similar to what was observed at scale 1:20). This graph is rearranged in Fig. 4.20 (b) where the maximum pressures on A63 with air and for 486 common impacts are shown in the abscissa. In the ordinate the maximum pressures obtained with the three other ullage gases corresponding to the same exact IDs were plotted. Quite similar to what was observed at scale 1:20, that maximum highest pressures for each gas are dominated by more or less the same IDs. In other words impact IDs which are responsible for highest pressures on A63 with one gas, are responsible for the generation of the highest impact pressures with other ullage gases as well. It is also clear that the highest pressures were obtained with helium for the considered IDs.

Among the 486 selected IDs it can be verified for what percentage of the total impacts, the maximum is achieved by each gas. This comparison can be done for each on of the 63 subareas separately as shown in Fig. 4.21 (a). It is clear that not for all the IDs lighter ullage gas leads to higher maximum pressures. This is true about all the studied areas even though the percentages seemed to depend on the subarea size and location. Still for a larger percentage of the considered IDs, the maximum pressure (obtained from 10 repetitions) is obtained with helium. This percentage includes the most severe impacts as observed in the previous figure. There are smaller percentages of IDs (depending on the subarea) for which maximum pressures are obtained with air, Mix_2. Interestingly and specially for smaller subareas at the top of the common area, there are larger percentages of impacts for which the maximum is obtained with the heaviest ullage gas which is SF_6. This was not really expected as the consensus is that heavier ullage gas always leads to less severe impacts and resultant pressures.

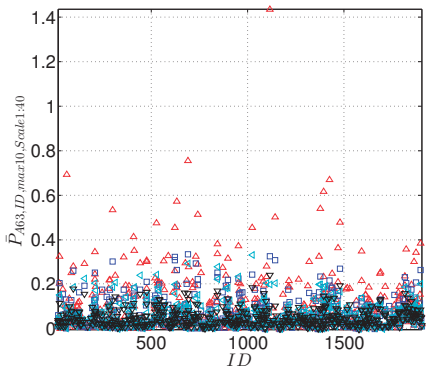

(a)

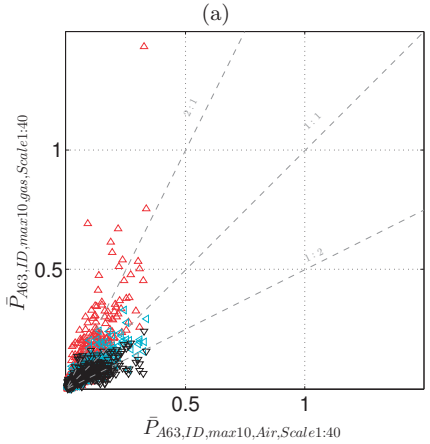

(b)

Fig. 4.20. Visual comparison of maximum pressures on A63 for common IDs with different ullage gases at scale 1:40 (a) Maximum pressures obtained in 486 common IDs with 4 ullage gases at scale 1:40 (b) In the abscissa maximum pressures obtained in 486 common IDs with air. In the ordinate maximum pressures obtained in the corresponding common impacts but with 3 other ullage gases. $\triangle$: helium, $\square$: air, $\triangleleft$: Mix_2, $\triangledown$: SF_6.

Nevertheless those impacts for which the maximum is achieved by SF_6 are not the most severe ones. For instance considering A63, the most severe ID for which the maximum pressure was achieved by SF_6 recorded 0.16 bars with this gas (0.09, 0.10, 0.11 were the maximums reached for the same ID with helium, air

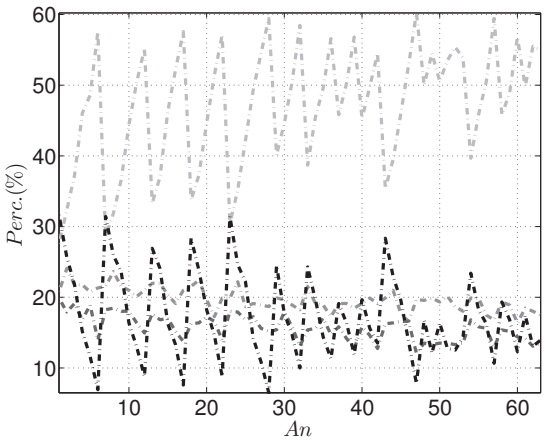

(a)

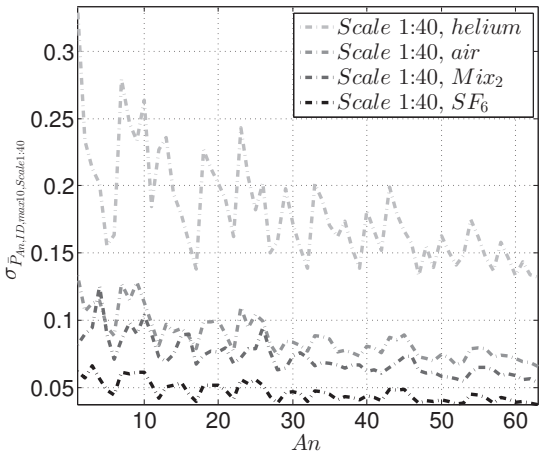

(b)

Fig. 4.21. For the 63 subareas, (a) percentage of IDs among the 486 common IDs at scale 1:40 for which the maximum is achieved by each ullage gas after 10 repetitions with each gas (b) standard deviation of maximum pressures obtained for 486 common IDs for 4 ullage gases at scale 1:40. The maximum pressure for each ID and for each gas is found from 10 repetitions for each gas. The use of lines in these graphs is only for better readability. There is no continuity between the connected points except for the areas of the same size.

and Mix_2 respectively). On the other hand and on A63, the maximum achieved for one ID with helium is 1.44 bar which is much larger (0.33, 0.20 and 0.24 were the maximums reached for the same ID with air, Mix_2 and SF_6 respectively).

The absolute variability of pressure peaks achieved for all 486 selected IDs, on 63 areas was compared for different ullage gases as presented in Fig. 4.21 (b). As before the variability is measured in terms of standard deviation of the maximum pressures. The absolute variability as measured this way decreases strongly by using heavier ullage gas. Variability is again a function of area size and location as higher areas show larger variabilities compared to lower subareas on the selected common area. This also confirmed the observation made based on the results at scale 1:20.

Since similar to what was observed at scale 1:20, for some impact IDs and after 10 repetitions maximum pressures were obtained with heaviest gas rather than the lightest gas of helium. Once more based on the knowledge about the impact IDs and by the use of high-speed video recordings, the shape of the typical severe impact types is studied. The impacts for which maximum pressures are not obtained with the lightest gas were also interesting cases for comparison. Similar to what was plotted in Fig. 4.20(b) with data from tests with air in abscissa, a new graph is plotted with maximum pressures on A63 for 513 common IDs with tests with helium in abscissa and the maximum pressures for the corresponding IDs with SF_6 in ordinate as shown in Fig. 4.22.

Similar to the comparison shown in Fig. 4.19 at scale 1:20, the shape of the typical severe impact types was studied. Similar to what was plotted in Fig. 4.20(b) with data from tests with air in abscissa, a new graph can be plotted with maximum pressures on A63 for 513 common IDs with tests with helium in abscissa and the maximum pressures for the corresponding IDs with SF_6 in ordinate as shown in Fig. 4.22.

According to Fig. 4.22 two groups of impact IDs were further investigated using high-speed video recordings. The first group included impacts for which the lighter gas of helium induced higher pressures and those with the highest induced pressure in the comparison. For the first group, it was observed that for pressures larger than 0.25 bars with helium, increase of pressure in IDs recorded with helium does not lead to considerable increase of pressure for the corresponding IDs with SF_6. At this range pressures obtained with SF_6 were almost constant. The second group includes IDs for which the heavier gas of SF_5 induced higher pressures. There are less IDs in the second groups of impacts. The range of impact pressures in the second group is much smaller than the range observed in the first group. In terms of impact types it was observed that similar to scale 1:20, the impacts in the first groups were of small gas pocket or flip-through type. In the second group of impacts only broken wave impacts were observed.

Based on what is observed in Fig. 4.19 and Fig. 4.22 it can be concluded

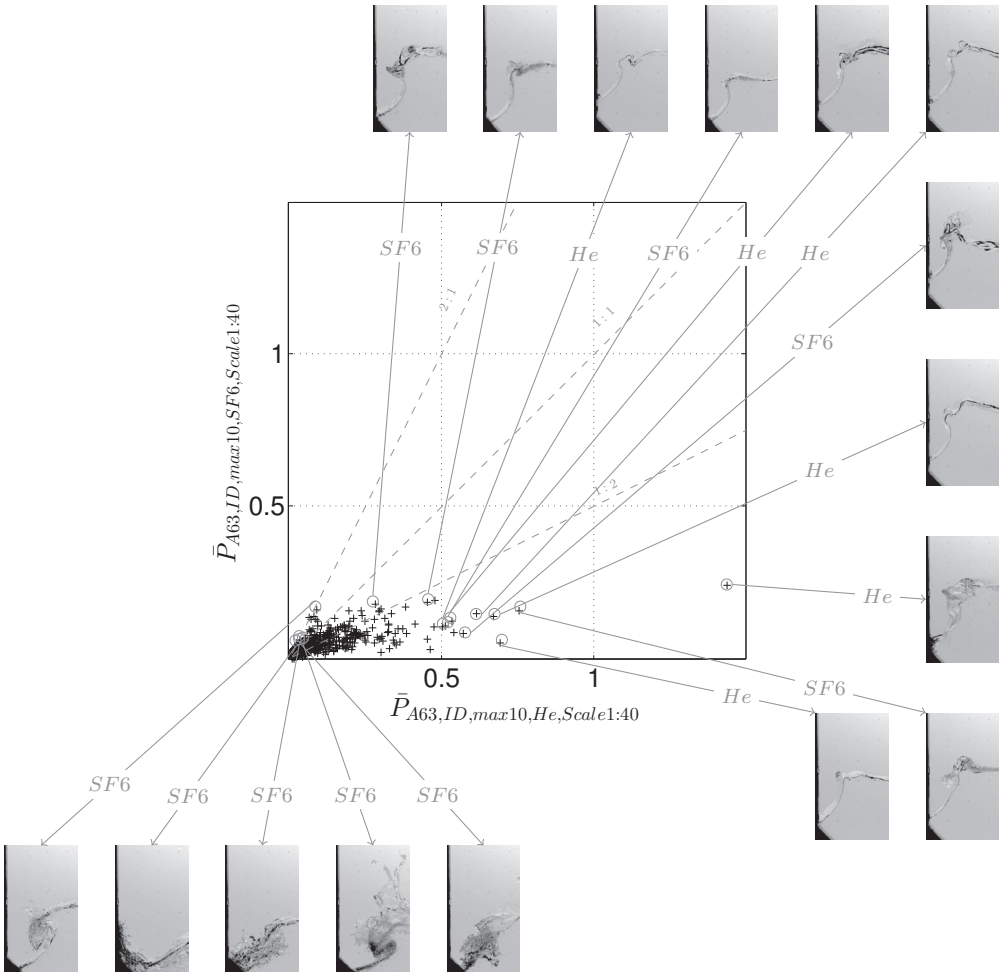

Fig. 4.22. In the abscissa maximum pressures on A63 obtained in 513 common IDs with helium at scale 1:40. In the ordinate maximum pressures obtained in the corresponding common impacts with SF_6 at the same scale. For each selected impact a representative snapshot of the high-speed video recording has been shown. The choice of ullage gas for images was based on image availability.

that that higher pressures with heavier gas are usually observed for impact types (such as broken wave impact type) were density ratio cannot play a significant role in effecting the impact energy. For impact types such as flip-through or

gas pocket density ratio plays a more important role. Heavier gases reduce the impact energy due to the interaction between gas and liquid which consequently leads to lower impact energies and in general lower impact pressures. The change of pressure due to change of ullage gas density can be studied further.

Scaling of highest pressure per ID

Using the same impact IDs which are captured in the model tests at different scales, maximum pressures on the common areas can be compared. The main interest would be to compare model tests with the same density ratio at different scales since this criterion is respected in practical sloshing model tests. In line with statistical verification of conservatism of Froude scaling which was presented in Table 4.4 and Table 4.5, 5 different comparisons can be made. This time as mentioned comparison is done based on the common IDs of the model tests. In order to do this and for each comparison, first the common IDs for which there is at least one measured impact per ID per scale are found. The maximum pressure per subarea per common ID is then found for each group (see Table 4.1) of tests at each scale.

Fig. 4.23(a), (b) and (c) show the comparison on A63 for model tests with air between scale 1:10 and 1:20, scale 1:10 and 1:40 and scale 1:20 and 1:40 respectively. The number of common IDs for those comparisons are respectively 458, 439 and 818. At each graph the maximum pressures for the common IDs obtained at the larger scale (abscissa) are plotted versus the maximum pressures for corresponding IDs at the smaller scale. The pressures as used in the graphs have not been scaled.

In Fig. 4.23(a) which compares the pressure peaks at scales 1:10 and 1:20, when the pressure is high for an ID at scale 1:10, generally the pressure is also high at scale 1:20. On the other hand for some common IDs, moderate pressures at scale 1:10 are matched with high pressures at scale 1:20. In other words moderate impacts at scale 1:10 become severe impacts at scale 1:20. In the given example in particular the maximum pressure at scale 1:20 was reached with the same ID that recorded moderate pressures at scale 1:10. No clear scaling trend is obvious from the graph.

Fig. 4.23(b) compares the pressure peaks at scales 1:10 and 1:40. Similar to the previous figure, when the pressure is high for an ID at scale 1:10, generally the pressure is also high at scale 1:40. Again for some common IDs, moderate pressures at scale 1:10 are matched with high pressures at scale 1:40. It can be said again that moderate impacts at scale 1:10 become severe impacts at scale 1:40. For higher pressure ranges the scatter around scaling based on the factor of 4 is more obvious but this trend is not valid for moderate and low pressure ranges.

Fig. 4.23(c) compares the pressure peaks at scales 1:20 and 1:40. Here it seems that especially for higher pressures at scale 1:20, the pressures for the corresponding IDs are rather low and not conservative with respect to scaling with the factor of 2. It can be stated that generally the higher pressures at scale 1:20, correspond to higher pressures at scale 1:40. As observed before in the other graphs as well, for some common IDs, moderate and even low pressures at scale 1:20 are matched with high pressures at scale 1:40.

The observation in the three presented graphs can be summarized as:

- There is a trend that IDs that generate high pressures at larger scale also generate high pressures at smaller scale,
- IDs which generate low pressures at the larger scale can sometimes induced high pressures at the smaller scale,
- No real scaling trend could be observed from the comparisons. The relation between the pressures at two scales also seems to vary depending on pressure intensities.

There are 435 common IDs between the model tests at 3 scales with air. Based on the maximum pressures found for the common IDs on each area and at each scale variability of maximum pressures can be studied by calculating the coefficient of variation (CV) of those 435 pressure peaks on each area and at each scale. It should be mentioned again that at each scale and for each gas 10 repetitions exist and as a result on each area and for each ID at that scale, there could be up to 10 measurements but in the mentioned graphs, only the maximum of those measurements for each ID was used. The comparison of relative variability of pressure peaks on 435 common IDs for 63 subareas is shown in Fig. 4.23(d).

According to this comparison variability is much larger for the subareas in the upper parts of the largest common area. The variability decreases on the lower subareas. This trend is valid regardless of scale. The variability is evidently less at scale 1:40 compared to scales 1:10 and 1:20 on all the studied subareas. Variability at scale 1:20 is also lower compared to scale 1:10 and considering most of the common areas especially the higher areas. There are only a few exceptions where variability is slightly higher at scale 1:20 compared to scale 1:10. In predicting the full-scale pressures this variability could be crucial as the scale difference is much larger in practice (normally model tests are conducted at scale 1:40).

Two similar comparisons can be done with tests with helium and Mix_2 at scales 1:20 and 1:40 which are presented in Fig. 4.24. With regard to Fig. 4.24(a) and (b) the conclusions already cited for tests with air are valid. The graphs show

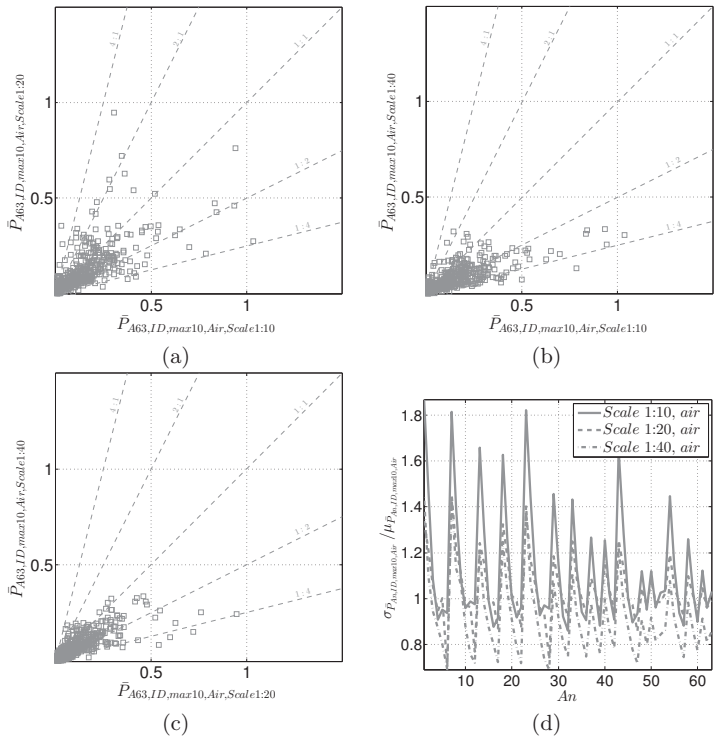

Fig. 4.23. (a) In the abscissa maximum pressures obtained for 458 common IDs with air at scale 1:10. In the ordinate maximum pressures obtained in the corresponding common impacts with air at scale 1:20. (b) In the abscissa maximum pressures obtained for 439 common IDs with air at scale 1:10. In the ordinate maximum pressures obtained in the corresponding common impacts with air at scale 1:40 (c) In the abscissa maximum pressures obtained for 818 common IDs with air at scale 1:20. In the ordinate maximum pressures obtained in the corresponding common impacts with air at scale 1:40. Pressures in (a), (b) and (c) have not been scaled (d) Coefficient of variation of the maximum pressures obtained for the 435 common IDs at scales 1:10, 1:20 and 1:40 on 63 subareas. The use of lines in this graph is only for better readability. There is no continuity between the connected points except for the areas of the same size.

less scatter in comparison for Mix_2 as is expected from less variability with heavier ullage gas that was shown in Fig. 4.18(b) and Fig. 4.21(b).

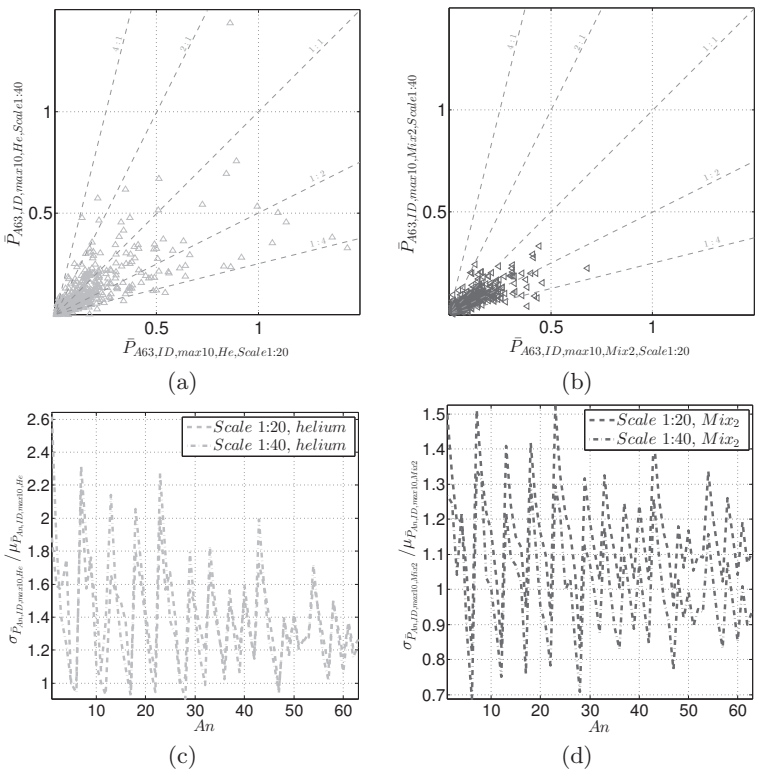

Fig. 4.24. (a) In the abscissa maximum pressures obtained in 503 common IDs with helium at scale 1:20. In the ordinate maximum pressures obtained with the corresponding common impacts with helium at scale 1:40 (b) In the abscissa maximum pressures obtained in 551 common IDs with Mix_2 at scale 1:20. In the ordinate maximum pressures obtained in the corresponding common impacts with Mix_2 at scale 1:40. Pressures in (a), (b) have not been scaled. (c) Coefficient of variation of the maximum pressures obtained for the 503 common IDs at scales 1:20 and 1:40 on 63 subareas with helium. (d) Coefficient of variation of the maximum pressures obtained for the 551 common IDs at scales 1:20 and 1:40 on 63 subareas with Mix_2. The use of lines in the last two graphs is only for better readability. There is no continuity between the connected points except for the areas of the same size.

The relative variability of the pressure peaks is also compared on 63 subareas and for 503 common IDs for tests with helium and 551 common IDs with Mix_2

at scales 1:20 and 1:40 as shown in Fig. 4.24(c) and (d) respectively. Variability at smaller scale with helium at scale 1:40 is very close to that of scale 1:20. This variability is slightly larger on higher subareas at smaller scale which is in contradiction with what was observed with air. Nevertheless on the largest subareas, variability is larger at the larger scale. The comparison with Mix_2 shows that variability is lower in all the subareas at smaller scale confirming the general trend that variability appeared to be less at smaller scale based on tests with air.

4.8 Dominant IDs

Based on Fig. 4.17(b) and Fig. 4.20(b) as 4.23(a), 4.23(b) and 4.23(c) it was clear that there are certain impact IDs which are responsible for highest loads. This was true considering different gases at the same scale or regarding tests with the same gases at two different scales. Those impact IDs deserve further investigation in the collections of all pressure peaks obtained from repetitions of long sloshing model tests. It was verified which impact IDs were present in the 20[10] highest pressure peaks on A63, obtained from 10 repetitions of irregular tests with air at scales 1:10, 1:20 and 1:40 as shown in Fig. 4.25.

Fig. 4.25 shows that the highest 20 pressure peaks are dominated by respectively 13, 13 and 14 impact IDs respectively at scales 1:10, 1:20 and 1:40. Four IDs of 693, 844, 1116 and 1142 are important in all 3 scales. Which means the severe impacts at larger scales remain crucial in smaller scales as well which is crucial for representativeness of model tests.

IDs 96, 302, 732 and 1023 are important in 2 scales rather than 3. The rest of the 20 IDs only appear at 1 scale. It is important to observe that some of the IDs are repeated several times among the top 20 pressure peaks. At scale 1:10, ID 844, 1142, and 1919 are present 5, 2 and 3 times among the highest 20 peaks. At scale 1:20, ID 96, 154, 414, 844 and 1023 are repeated 4, 2, 2, 2 and 2 times respectively. At scale 1:40, ID 96, 210, 302, 622, 693 and 844 are repeated twice each. This observation implies that if more repetitions of long model tests were available, the 20 highest pressure peaks for each sample could have been dominated by a fewer number of IDs with a larger frequency. This idea was tested and proven to be valid which will be presented later in this section.

At scale 1:20, it was also verified which impact IDs were present in the 20 highest pressure peaks on A63, obtained from 10 repetitions of irregular tests with helium, air, Mix_2 and Mix_4 as shown in Fig. 4.26. This was done in order to observe whether those peaks will still be dominated by the same impact IDs as the ullage gas changes. This was proven to be true as ID 693, 844 and 1116

[10]The choice of 20 was done for the sake of brevity and clarity of the presentation

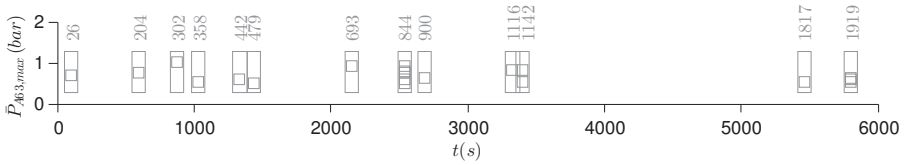

(a) *Scale 1:10*

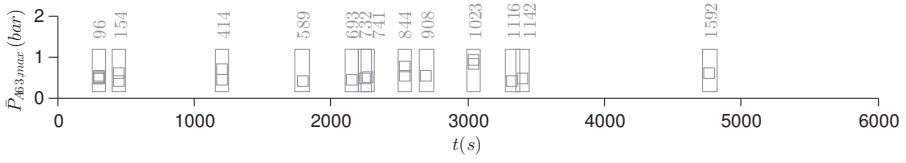

(b) *Scale 1:20*

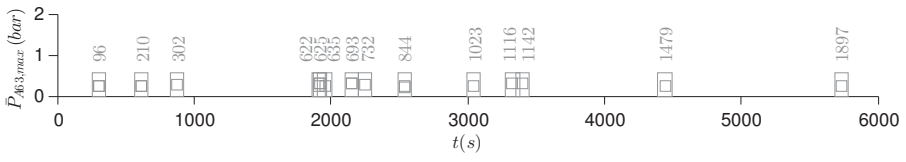

(c) *Scale 1:40*

Fig. 4.25. Dominant IDs among the 20 highest pressure peaks on A63 found from 10 repetitions of tests at scales (a) 1:10, (b) 1:20 and (c) 1:40 all with air. There are common dominant IDs in tests at different scales. Pressures have not been scaled.

were important for tests with all 4 gases. These IDs were also repeated when comparing 3 scales in Fig. 4.25.

At scale 1:20 and other than the introduced 10 repetitions for every gas which were used for the analyses throughout the study, there were 39 more repetitions of the model test with air which made it possible to investigate whether on a given area, by increasing the number of repetitions the number of IDs present in impacts of highest peak pressures would decrease or not as suggested by Fig. 4.25 and Fig. 4.26. This verification was done with the 49 available repetitions. The 500, 400, 300, 200 and 100 highest pressure peaks on A1 and A63 were found progressively from 1, 2, 3, ... and eventually all 49 repetitions and the number of IDs which were present among those peaks were determined. The choice of A1 and A63 as the smallest and largest common areas was for the sake of generality. It was observed that as expected by increasing the number of repetitions the number of present IDs in any highest number of pressure peaks was reduced.

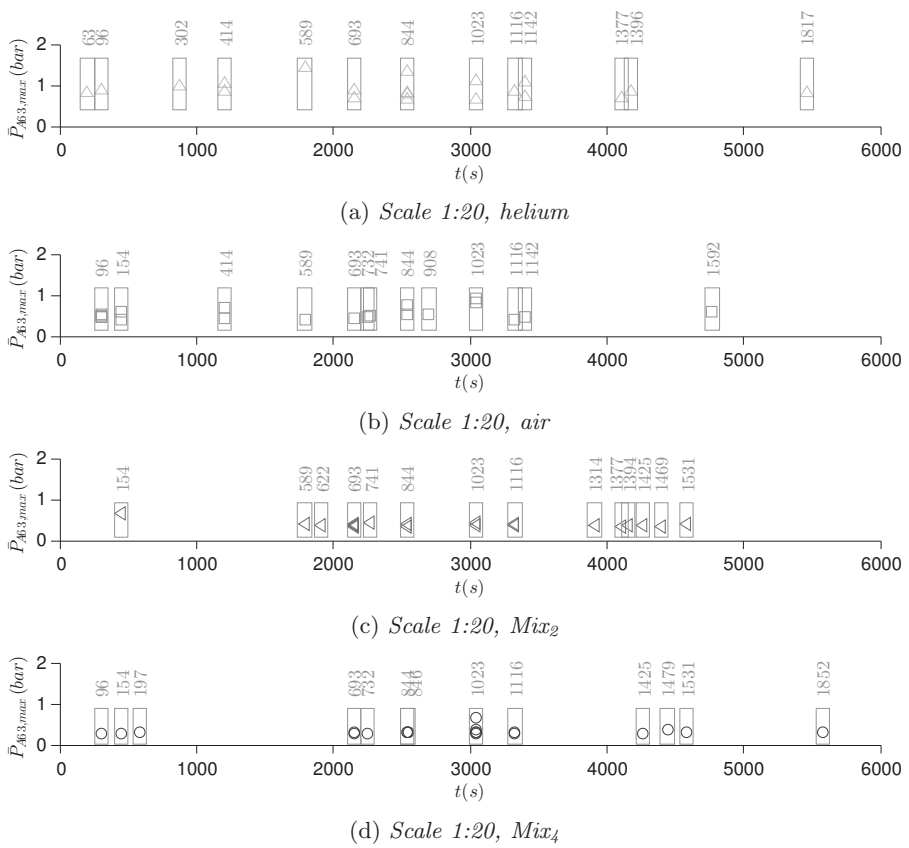

Fig. 4.26. Dominant IDs among the 20 highest pressure peaks on A63 found from 10 repetitions of tests with (a) helium, (b) air, (c) Mix_2 and (d) Mix_4 at scale 1:20. There are common dominant IDs in tests with different ullage gases.

The results are shown in Fig. 4.27. This means that as expected there are a few impact IDs which dominate highest pressure peaks. The number of those influential IDs decreases continuously as the number of model test repetitions increase meaning that if model test repetitions could increase there would be further reductions of the number of IDs which would leave one single important impact (or impacts depending on how many pressure peaks are considered and how many repetitions are available) of importance. Since extreme loads are of

importance in ULS[11] analysis of sloshing impacts, those single impacts if found can provide the ultimate loads that can be caused by any test condition and so knowledge on the behavior and statistical distribution of loads caused by those impacts which can be ideally found from many repetitions are more important than the knowledge gained about all the impacts by a few repetitions. It should be noted that repetitions of sloshing model tests are time consuming and the recent result shows that repetitions of long tests might not have any benefit on the prediction of severe sloshing loads as most of the gained data will not be used to predict the extreme loads.

In Fig. 4.27 the slope of the curves is not always negative as by addition of new model test repetitions, new IDs are occasionally added to the collection of dominant IDs. Nevertheless the overall trend is always downwards. The trend shows a sudden decline in the number of IDs for the first repetitions and then the trend becomes milder but still decreasing. In both Fig. 4.27(a) and Fig. 4.27(b) the trends are similar which means that single dominant IDs are important considering both local and global phenomena.

The persistence of those dominant impacts is also of importance. It should be shown that if the number of dominant IDs is reducing by increasing the number of repetitions, it is the same IDs that are dominant throughout the process. In other words the list of dominant impacts should become narrower. This was demonstrated in 4.27(a) and Fig. 4.27(b) for 100 highest pressure peaks. The total number of dominant IDs for any number of repetitions is broken into two parts. The number of IDs which were also dominant with one less repetition of the model test, depicted by light gray and the number of IDs which are new and were not dominant with one less repetition depicted by darker gray. It is shown that as the repetitions are few, there are new IDs which are added to the list of dominant IDs but after increasing the number of repetitions there are hardly any new IDs added to the list of dominant impacts. In other words, the dominant IDs persist and stay dominant by increasing the number of repetitions. It is seen that after 10 repetitions not many new IDs are added which means that a few repetitions could prove sufficient in order to find the list of important IDs. The correspondence of the maximum number of test repetitions and the minimum number of dominant IDs among the highest 100 (or any other number of highest peaks) means that some of those IDs are repeated several times. In the presented cases there are 40 dominant IDs among 100 highest pressure peaks on A1 after 49 repetitions and there are 28 dominant IDs among 100 highest pressure peaks on A63 after the same number of repetitions.

Fig. 4.28 demonstrates the frequency of dominant IDs (33 IDs on A28 and 28 on A63) among the 100 highest pressure peaks found from 49 repetitions. The number of IDs is presented by ID' to emphasize that the ID numbers were found

[11] Ultimate Limit State

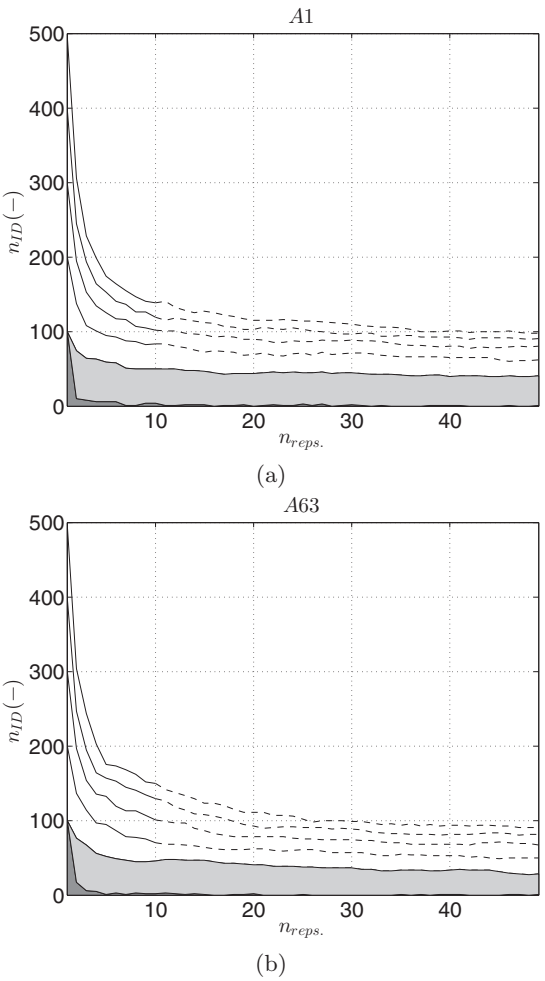

Fig. 4.27. Number of present IDs among the highest 500, 400, 300, 200 and 100 pressure peaks found from 1-49 repetitions of the same 3DOF tank motions on (a) A1 and (b) A63. Increasing the number of repetitions will reduced the number of dominant IDs. Light gray section indicates the number of dominant IDs which belong to the group of dominant IDs with one less repetition. The darker gray section indicates the number of dominant IDs which do not belong to the group of dominant IDs with one less repetition.

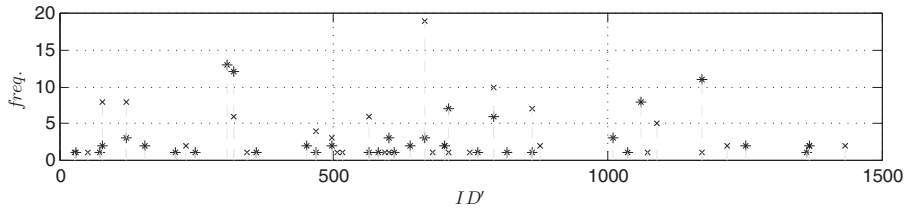

Fig. 4.28. Frequency of dominant IDs in the 100 highest pressure peaks on A28 (∗) and A63(×) found from 49 repetitions of 3DOF tank motions. Several IDs have a considerably larger frequency.

specifically for the 49 repetitions and not taking into account other tests and so cannot be compared with the previous ID numbers. It is seen that indeed some dominant IDs have a much higher frequency than the rest. The highest frequency is observed on A63 where an ID is repeated 19 times among the top 100. There are impacts which are repeated only once or twice. It is interesting that certain IDs with a high frequency for A63, are of low frequency for A28 which means that those IDs are more important for A63 than for A28. The opposite is true as well. Some impacts are solely important on one area and not important at all on the other which means that for a given tank motion (corresponding to a sea state) different dominant IDs could be of importance on different areas.

To obtain an insight on the pressures associated with the 100 highest pressure peaks on A28 and A63 and the relation with the frequency of each ID, all 100 pressure peaks on both areas are plotted versus the frequency of the associated impact ID as depicted on Fig. 4.29. On Fig. 4.29 (a) corresponding to A28, it is seen that impacts with higher frequencies are often associated with higher pressures as well. This is more clear on Fig. 4.29 (b). Impacts with frequencies of 1 or 2 cover the lower range of pressure peaks which means that by performing more repetitions, those IDs will disappear from the list of dominant IDs.

4.9 Discussion and Conclusions

2D sloshing model tests were performed at scales 1:40, 1:20 and 1:10 with water at the fill level equal to 20% of the tank height. The model tanks represented a transverse slice of tank 2 of a four-tank LNG carrier with a capacity of 152000 m^3. Different ullage gases were used depending on the scale: only air at scale 1:10; helium, air, Mix_2 (namely a mixture of SF_6 and N_2 with DR = 2 kg/m^3) and Mix_4 (namely a mixture of the same gases with DR = 4 kg/m^3) at scale 1:20; helium, air, Mix_2 and SF_6 at scale 1:40. For each model tank, the main instrumentation

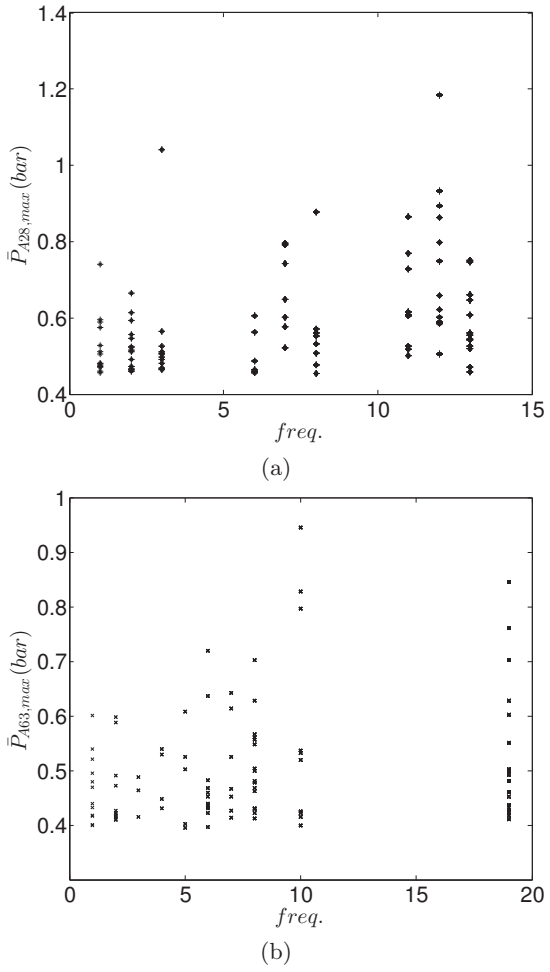

Fig. 4.29. 100 Maximum peak pressures on (a) A28 (∗) and (b) A63 (×), found from 49 repetitions of the same 3DOF tank motions and their distribution based on IDs with different frequencies. IDs with larger frequency appear to be associated with larger peaks.

consisted of a rectangular array of pressure sensors with an acquisition frequency of 40 kHz and a high speed camera recording at 4000 fps. The sensor array was installed on one vertical wall of the tank and covered the impact area around the

free surface. The video camera was fixed to the tank on the same side as the sensor array in order to capture wave shapes before and during impacts. The camera and the data acquisition system were synchronized. Only irregular excitations were studied corresponding, after due down-scaling, to the same motions of the LNG carrier in a beam sea condition for a five-hour sea-state of significant wave height H_s of 6 m.

The influence of ullage gas and scale was analysed through pressure peak statistics from repetitions of 10 tests for each studied condition defined by a couple (scale, ullage gas). Only peaks over a pressure threshold were post-processed. An impact was defined as an event for which at least one sensor recorded a peak exceeding the threshold. It was shown that whatever the condition and whatever the threshold, the number of impacts during a test varies only slightly (a few percent) when repeating the test. In order to perform relevant comparisons at different scales, the pressures were averaged on scaled subareas of different locations and sizes from the pressure measurements before any statistical post-processing. The range of locations and sizes covered by the subareas reflects the spatial distribution of the loaded areas during all tested impacts.

The density of the studied ullage gases were around 0.2, 1.2, 2.0, 4.0 and 6.0 kg/m^3 at ambient conditions for respectively helium, air, Mix_2, Mix_4 and SF_6. As a general rule, the heavier the gas, the more compressible it is. But one must keep in mind that when changing the scale or the ullage gas, not only the most influential properties of the gas on the global wave shape matter, like its density or its compressibility, but also surface tension or/and viscosity which directly modify the local phenomena responsible for the variability (free surface instability, splashing, bubbles creation) and thus of the final statistics. In the following conclusions, the gases are often ranked through their density in order to discriminate them easily. This does not mean that only the density matters.

The comparisons rely both on global statistics mixing all impacts of the series together and on statistics by impact at the same reference time, namely by impact ID. The first method gathers larger sample of pressures but from very different kinds of impacts. The second method is based on more homogeneous samples, although it has been shown that there is still a significant variability of the global wave shapes before impact for a given ID. With the second method, the samples are necessarily small (less or equal to ten) which obliged us to limit the comparisons to the maximum values of each sample.

The author would have liked to conclude this study with simple statements such as: the heavier the gas, the smaller the impact loads or the smaller the scale the more conservative the results with the natural pressure scaling from dimensional analysis. Unfortunately, despite these statements can be remembered as general trends, as often when sloshing is involved results are not as simple.

4.9.1 Influence of ullage gas

The following results concerning the influence of ullage gas have been obtained at both scales of 1:40 and 1:20, for which different gases were studied.

From statistics on samples mixing all impact IDs together, it was concluded that:

- At the same scale and with the same pressure threshold (P_{th}), the lighter the gas, the larger the number of recorded impacts. In order to record the same number of impacts, the threshold must be higher for lighter gases.
- Whatever the size of the subareas on which the pressure is averaged, the probability density functions obtained with the 1000 highest pressure peaks for the different ullage gases show that the most probable pressure is larger for lighter gases. Moreover the tail of the distribution is thicker for lighter gases, which means that larger maximum pressures can be expected for a large return period with lighter gases. Actually, for almost all the return periods in the studied range (maximum return period is 50 hours at full scale as we considered 10 repetitions of a 5 hour-full-scale excitation), Quantile-Quantile plots showed that the lighter the ullage gas, the larger the pressures.

By comparing the maximum pressure obtained from each series of 10 tests with a different ullage gas but for each impact ID at a time, it was concluded that:

- For a given ID, it is not always the lightest gas that leads to the largest pressure. Nevertheless, whatever the location and size of the subarea considered for averaging the pressure, percentage of IDs for which the maximum pressure is reached with helium is much larger than with air, which is larger than with Mix_2.
- At scale 1:20, for which results with Mix_4 are also available, the percentage of IDs giving a maximum pressure with Mix_4 is roughly the same as with Mix_2 whatever the subarea considered. At scale 1:40, for which results with SF_6 are also available, the percentage of IDs giving a maximum pressure with SF_6 is sometimes as large as with He for small sizes of the subareas. Here there is clearly another influence than that of DR but the other fluid properties involved have not been clearly identified yet.
- The impact IDs for which a heavy gas enables the highest pressure are never severe impacts.
- Based on results observed at scale 1:20 with different ullage gases but with repeatable SIW conditions, it was shown in Karimi et al. [2016] that the

ullage gas tends to impede the wave breaking process. The heavier the gas, the larger the mitigation. It was concluded that this could as well magnify the impact pressures or mitigate them when increasing the DR depending on the initial wave shape chosen. For a given impact ID, there is a certain variability of the wave shape before impact; nevertheless, the most probable shape is very likely directly influenced by the DR in the same way as for SIWs. Available high speed videos have been analyzed in order to possibly substantiate this explanation. Pictures extracted from the films showing the wave shapes before impacts for some selected impacts have been given. Unfortunately and as not all videos were systematically recorded for all impacts during these test campaigns, no definitive conclusions could really be brought.

- Nevertheless, it was noticed that the highest recorded pressures always happen with the same wave shapes corresponding to flip-through impacts or small gas pocket impacts. Some local particularities have been observed on the interaction between the upward jet from the trough and the impinging crest.

- Whatever the location and size of the subarea considered for averaging the pressures, the absolute variability of the maximum pressure, as measured by the standard deviation, is larger with lighter ullage gas. It had already been observed in Karimi et al. [2016] that for the same global wave impact shape before impact, the liquid excrescences at the crest level and the liquid fragmentation around the crest due to the development of free surface instabilities seemed larger for lighter gases. The two results lead to the conclusion that the more disturbed and fragmented the free surface near the impact zone, the larger the variability.

- The variability of maximum pressures depends both on the size of subareas as well as their location with respect to wave impacts. Generally the larger the area or the lower the subarea is located, the smaller the variability of maximum pressures but again both influences must be considered simultaneously.

4.9.2 Influence of scale

The following results concerning the influence of the scale have been obtained either by comparing the three scales with air or by comparing scale 1:20 and scale 1:40 either with helium or Mix_2. The discrepancies with regard to scaling by a scale factor which is the geometric scale are compared.

Keeping the same gas at different scales ensures keeping the same DR. This is important as it enables to keep the most probable wave shape the same for

a given impact ID (see discussion on this statement in the previous paragraph). Furthermore this rule has already been adopted by most laboratories performing sloshing model tests for real sloshing assessment of LNG membrane tanks. As it was already mentioned, a perfect similarity between gas and liquid flows at two different scales would require not only that the time scale imposed by the forced motions is the square root of the geometric scale but also the equality of all involved dimensionless numbers at both scales. Therefore, additionally to DR, M_L, M_G, Re_L, Re_G and We should be kept the same. These relations link the properties of the fluids (liquid and gas) at full scale to the perfectly scaled properties of fluids at model scale enabling the perfect match between the flows. For instance with regard to compressibilities, the perfectly scaled speed of sound in gas and liquid at model scale should be derived from the speed of sound in the chosen gas and liquid at full scale , ${c_l}^{ms} = \frac{1}{\sqrt{\lambda}}{c_l}^{fs}$ and ${c_g}^{ms} = \frac{1}{\sqrt{\lambda}}{c_g}^{fs}$. By considering these relations and according to the adopted model tests comparing two scales with the same liquid and gas it is noted that the same liquid and gas at model tests are stiffer. Discrepancies regarding all other parameters exist in the model tests.

From statistics on samples mixing all impact IDs together and based on scaling the pressures by scale factors taken to be equal to geometric scales it was observed that:

Most of the time, scaling the maximum expected pressure at a given return period from small scale to large scale with the geometric scale is conservative whatever the gas involved or the size of the loaded area.

- For the two smallest loaded areas studied (800 mm^2 and 1600 mm^2 at scale 1:10), whatever the gas, this conservatism showed no exception.

- When studying helium as ullage gas, whatever the size of the loaded area, this conservatism showed no exception.

- When studying Mix_2 or air as ullage gases, for the tail of the distributions, therefore for the largest pressures obtained with the largest return periods, the conservatism tends to get reduced for larger sizes of the subareas. Slightly non-conservative predictions from scale 1:40 to scale 1:20 have even been obtained for all large subareas with air.

This suggests a mixed influence of liquid and gas compressibility. Liquid compressibility is involved very locally in the impact area (see Lafeber et al. [2012b] for a phenomenological description and Guilcher et al. [2013] and Guilcher et al. [2014], for numerical simulations of the phenomenon). Its influence is therefore dominant for small sizes of the loaded areas. Gas compressibility is mostly involved when gas pockets are entrapped, therefore for larger sizes of the

loaded areas. Furthermore, as observed in Maillard and Brosset [2009] during 2D sloshing model tests with different ullage gases, including helium, the number of gas-pocket impacts involved with helium is much less than with any much heavier gas like air. It seems that lighter gases tend to escape more easily and therefore avoid being entrapped. Therefore the role of gas compressibility in the general statistics of impact pressures with helium is reduced whatever the size of the loaded area. These preliminary explanations must be confirmed by further studies, both experimentally and numerically.

– For those cases for which scaling from a smaller scale to a larger scale using the geometric scale is always conservative whatever the size of the loaded area (1:40 vs. 1:10 with air, 1:20 vs. 1:10 with air, 1:40 vs. 1:20 with helium) when considering all locations of subareas of similar size together, there are some locations for which the direct comparison is not conservative. These locations always correspond to subareas located on the lower part or the middle part of the sensor arrays.

By comparing the maximum pressure obtained from each series of 10 tests with a different scale and the same ullage gas but for each impact ID at a time, it was concluded that:

– When scaling the pressures using the scale factor from a given scale to a larger scale, there is a larger proportion of impact IDs leading to a conservative result in terms of the maximum pressure. This has been shown only for the largest subarea but the result is general,

– There is a trend that IDs that generate high pressures at larger scale also generate high pressures at smaller scale,

– IDs which generate low pressures at the larger scale can sometimes induce high pressures at the smaller scale. As a result mild impacts at the larger scale can become violent ones at the smaller scale,

– No clear scaling trend could be observed from the comparisons,

– Whatever the size of the loaded area, when using air or Mix_2 as ullage gas, the larger the scale, the larger the variability of the impact loads. This result is not so clear with helium for which the opposite can happen, especially for the small sizes of the loaded area. This result suggests that the surface tension at the interface might be involved in the phenomena bringing some variability of the flow. Viscosity might also play a role especially when the gas density is small. These preliminary explanations must be confirmed by further studies, both experimentally and numerically.

Finally, it was also shown that there are dominant IDs among the total collection of IDs for an irregular condition. When increasing the number of repetitions of an irregular test, the number of IDs involved in the N highest recorded pressures keeps decreasing, down to a few IDs. These dominant IDs are those which repeat the most frequently but also those which reach the highest pressures. Therefore they are responsible of the tail of the statistical distribution of pressure peaks. This observation may open a door to significant improvements in the methodology for sloshing assessment and will be studied further.

Chapter 5

Dominant Impacts in Sloshing Model Tests

abstract

[1]Using the notion of dominant IDs that was briefly discussed in Karimi et al. [2017] and using more repetitions of one test condition at scale 1:20 it was shown that the tail of the pressure peak sample from all the repetitions on any impacted area is governed only by a few dominant IDs. Each dominant ID was shown to have its own unique variation of impact shapes and a unique distribution of pressure peaks. An alternative way was suggested for the estimation of the exceedance probability of any pressure level during a sloshing model test based on the notion of impact IDs and dominant IDs which is different from the current approach that is based on the collection of all pressure peaks from all the repetitions of the same test condition.

[1]This chapter is based on: *Dominant Impacts in Sloshing Model Tests*. M. R. Karimi, L. Brosset, M. L. Kaminski and J.-M. Ghidaglia which has been submitted to European Journal of Mechanics - B/Fluids.

5.1 Introduction

A sloshing model test represents an imperfect experimental model at small scale of the problem of sloshing in membrane LNG tanks of floating structures such as LNG carriers, offshore terminals (FLNGs and FSRUs), bunker ships, LNG feeders or any other ship such as cruise ships, container ships, bulk carriers using a dedicated tank for LNG as fuel. For a sloshing assessment of a new project of floating structure with LNG tanks, the sloshing model tank has an internal geometry which represents at small scale the internal geometry of the most exposed tank of the project. The geometrical scale is taken in most sloshing laboratories at 1:40. The tank is put on an accurate Stewart platform (hexapod) to impose six-degree-of-freedom motions down-scaled from ship motion calculations. All accelerations have to be the same at both scales. Based on dimensional analysis, a time scale which is the square root of the geometrical scale is imposed on the model. Therefore, the down-scaling process of the ship motions consists of dividing all amplitudes of the three translations by 40 and the time for the six degrees of freedom by $\sqrt{40}$. The liquid inside the model tank is water. As the density of the gas or the vapor inside the tank has an influence on the flow (see Karimi et al. [2015b] and Karimi et al. [2016]), the ullage gas inside the model tank is chosen as a mixture of selected gases in order to get the same gas-to-liquid density ratio (DR) at small scale as at full scale. The loads generated by the impacts on the tank walls are recorded by numerous pressure sensors placed in the most exposed parts of the tank.

This experimental model represents imperfectly the full scale reality because some of the phenomena occurring at full scale are disregarded at model scale such as for instance phase change which is present at full scale, as LNG is always in a state close to thermo-dynamic equilibrium with its vapor, but not at model scale with the use of non-condensible gases. Furthermore there are other causes of imperfection of the model. Different physical phenomena happen at both scales, especially during the impacts, involving properties of the liquid and gas (or vapor) like compressibility, viscosity or surface tension that cannot be properly scaled because there is no real liquid or gas that could match the required properties. These imperfections of the experimental model are expected to lead to flows that are not in complete similarity with the flows at full scale and the pressure scaling based on dimensional analysis assuming the perfect similarity would also be biased.

5.1.1 Context of the Study

In order to study and quantify these biases with regard to a complete similarity, many model test campaigns have been performed in GTT using three model tanks representing respectively at scale 1:10, 1:20 and 1:40 a transverse slice

of the tank 2 of a 152000 m3 four-tank LNG carrier. The slice is located in the middle of the real tank. As the thickness of the slice is much smaller than the two transverse dimensions and only 3 DOF motions are applied, the model tanks are often referred to as 2D tanks. During these different test campaigns, the fluids used inside the tanks were most of the time water and air but tests have also been performed at scale 1:20 and 1:40 with different ullage gases. A focus has been made on the filling level of 20% of the tank height and a forced excitation down-scaled, whatever the scale, from the ship motions calculated at scale one for a beam sea condition with a sea state defined with a JONSWAP spectrum, a significant wave height Hs of 6 m and a zero up-crossing period Tz of 8.5 s. The ship motions have been calculated taking into account the coupling with the cargo motions according to a linear multimodal approach for the cargo motions. Only the three degrees of freedom in the plane of the tank (sway, heave and roll) have been retained. At each scale the instrumentation was at least comprised of a rectangular array of pressure sensors covering the impacted area on one longitudinal wall of the tank, a high speed camera synchronized with the data acquisition system and scrutinizing the same side of the tank as the sensors in the impacted area in order to capture the shapes of the impacting waves before and after the impacts and a HD camera looking at the complete width of the tank at the level of the free surface at rest in order to follow the global free surface shape during the complete duration of the tests.

The main results obtained from these sloshing model test campaigns have been described through five different papers:

Karimi et al. [2015b] focused on the consequences on the global flow of forcing the motions at different scales, possibly with different ullage gases. It was based on comparison of results at scales 1:40 and 1:20 with the forced excitations described above. It showed that, if a small uncertainty window is introduced, impacts always happen at the same instants when the same condition is repeated at a given scale. When comparing two different scales the impacts happen at time-similar instants. They are referred to as coincident impacts. This regularity does not deteriorate over time even for long duration tests (almost 50 minutes at scale 1:40). The random perturbations brought to the global flow by the development of free surface instabilities or by the fall of droplets or by the creation of bubbles vanish quickly enough to be overcome by the regularity brought by the imposed motions. This balance prevents a progressive randomization of the global flow. Moreover, changing the ullage gas does not affect this regularity of the flow when keeping the same motions imposed on the tank. Therefore, the small variations of the global flow induced by the differences between gas properties especially during impacts are also damped quickly enough to be overcome by the regularity brought by the imposed motions. This prevents a progressive general divergence of the global flow. Each impact obtained during a series of repetitions of the same

condition can be identified by a reference time (considering a small uncertainty window), conventionally defined at scale 1, or by an index. This index is referred to as an impact identification or simply as an impact ID.

Karimi et al. [2016] presented the influence of DR on the wave shapes just before impacts and prior to any compression of the gas, as observed during sloshing tests at scale 1:20 for short regular sway excitations of the tank stopped after a single impact. The intention was to distinguish between the effect of DR and the other properties of the gas and especially from the gas compressibility. Therefore the comparison was to be made before any compression of the gas, thus before any impact recorded by the pressure sensors. This led naturally to a comparison mainly based on pictures extracted from high speed videos. Short regular sway excitations, referred to as Single Impact Wave excitations or SIWs, lead to very accurately repeatable wave shapes before impact and enabled a deterministic comparison of the wave shapes generated by the same conditions except for the ullage gases. Actually, the wave front keeps smooth and precisely repeatable from the trough to the base of the crest. The corresponding measured pressures induced by the trough run-up are also repeatable. Only around the crest, where free surface instabilities develop due to the shearing gas flow, some differences can be distinguished. As a consequence, variations of the pressure signals induced by the crest impact are significant. When repeating the same SIW excitation with two liquids of different density and choosing the ullage gases in order to get matching DRs, the wave front keeps smooth and its shape remains precisely the same from the trough to the base of the crest in both cases although discrepancies around the crest can be observed due to different developments of free surface instabilities. Therefore this smooth shape of the wave front is independent of the liquid density and only depends on DR. When repeating the same condition with water but with different ullage gases, it is observed that the larger the DR, the less advanced the breaking process is. The gas seems to impede the breaking process. This includes a slightly reduced upward speed of the trough run-up for larger DR. This mitigating role of the gas is clearly due to a transfer of mechanical energy from the liquid to the gas. Therefore, changing the DR leads to changing the impact conditions and thus the nature of impact. This may as well magnify the impact pressures or mitigate them when increasing the DR depending on the initial wave shape chosen. Complying with density ratio similarity is therefore necessary during sloshing model tests to prevent any systematic bias in the impact conditions and consequently in the pressure statistics.

In Karimi et al. [2017] quantitative results based on measured pressures were presented comparing irregular tests at 20% fill level of the tank height at three different scales with the same gas or at a given scale with different gases. Doing so, one must keep in mind that when changing the scale or the ullage gas, not only the most influential properties of the gas on the global wave shape matter,

like its density or its compressibility, but also surface tension or/and viscosity which directly modify the local phenomena responsible of the variability (free surface instability, splashing, bubbles creation) become important. Due to the variability of the local pressure measurements, the comparisons were necessarily based on statistics. They have been built from series of 10 tests for each studied condition defined by a scale and a ullage gas. As the rectangular arrays of pressure sensors were not homothetic at the different scales, the comparisons have been made on the largest rectangular area common to the three scales after scaling at scale 1:10 and the smaller subareas defined on that common area. As the pressure sensors and the distance between two consecutive sensors within every row and column of the rectangular sensor arrays (10 mm) were the same at different scales, the comparisons were made on averaged pressures calculated on homothetic rectangular subareas of the common area. The samples of pressure peaks calculated on the subareas and built for the statistical comparisons were either derived from all impacts occurring during all repetitions of the studied condition, as it is normally done during post-processing of sloshing model tests for any sloshing assessment of LNG tank on a floating structure, or, for the first time, derived only from selected impact IDs. The study showed that simple statements like: the heavier the gas, the smaller the impact loads or the smaller the scale the more conservative the results with pressure scaling based on dimensional analysis can be remembered as general trends but as often when sloshing is involved many exceptions to these trends were observed which have been carefully listed.

In Karimi et al. [Submitted to EJMBF in 2017b] it is shown that the characteristics of any given impact obtained during repetitions of an irregular test, including statistics of the local pressure peaks for the same impact ID, are conserved when generated by only a short excitation corresponding to the original motions before the impact time. Whatever the impact ID studied, there is a minimum duration for the short excitation before the impact for which the state of the flow before this duration has no influence any more at the impact time. This suggests the existence of an effective flow memory (m_e): at a given time t everything that happened before $t - m_e$ has no influence any longer on the flow after t. This confirmed the notion of flow memory that had been mentioned in Karimi et al. [2015a]. This result has been confirmed during sloshing tests with 3D tanks and with high filling levels and can therefore be considered as general Frihat et al. [2016]. The irregular tests with a short excitation mimicking the original motions just before the impact time of the selected impact ID have been named singularization tests.

The present paper is coming back on a notion shortly introduced in Karimi et al. [2017]: there are dominant IDs in the total collection of IDs for repetitions of an irregular condition. When increasing the number of repetitions, the number of IDs involved in the n highest recorded pressures keeps decreasing, down to a

few ones. Therefore they are responsible for the tail of the statistical distribution of pressure peaks. The statistical properties for all dominant IDs of the selected condition are also studied. Moreover, it is shown that unlike the SIWs leading to accurately repeatable global wave shapes, the wave shape before impact for a given ID varies significantly. This shows that the variability brought to the flow by each impact does not damp completely in between two impacts. Finally, an alternative way of building the maximum value distribution of pressure peaks than that used during a sloshing assessment for design purpose is proposed. Both methods eventually lead to very similar distributions in the tail region.

5.2 Test Setup

The tests were at scale 1:20 and were performed in GTT. The tank was a model of a transverse slice of Tank 2 of an LNG carrier using membrane containment system technology with the total capacity of 152,000 m^3. In this study only the tank fill level of 20% of the tank height was considered due to more severe impacts and higher induced pressures (see BV [2011]). The tests were all performed with water and air. For the internal tank dimensions see Fig. 5.1.

The tests were 2D and only 3 motions of sway, heave, and roll in the tank plane were applied . The tests were performed by a Sirocco type hexapod with the maximum payload of 2 tons made by Symétrie [2]. The types of motions used in this study were irregular. Irregular tank motions were based on ship motions at full-scale calculated by PRINCIPIA's DIODORE[3] for 5 hour sea states based on JONSWAP spectrum found from the assumption of zero crossing period T_z of 8.5 s, heading of 270 ° and significant wave height H_s of 6 m. The motions were coupled with sloshing in the tanks. In order to find the model test tank motions, the full-scale motion amplitudes and time had been down-scaled by factors λ and $\sqrt{\lambda}$ respectively with $\lambda = 1 : 20$. These motions were defined for the middle of the bottom of the 2D tanks.

The main camera that was used in this campaign was a high-speed camera. The high-speed camera was used to record impact geometries a few milliseconds before and after each impact. A Phantom V7.2 high-speed camera was used in this model test. For this camera the resolution was 608×600 pixels with ~ 3.56 pix/mm and the exposure of 130 μs. The high-speed camera recorded at 4000 fps. The fill level was monitored regularly with a simple camera. The high-speed camera was activated when impact pressures exceeded a threshold used for the camera system. LED lamps were installed to illuminate the background.

PCB sensors were installed on the sensor module in an array of 21×6. The

[2]See Symétrie's website for complete technical details on the hexapods
[3]See PRINCIPIA's website for more information on DIODORE

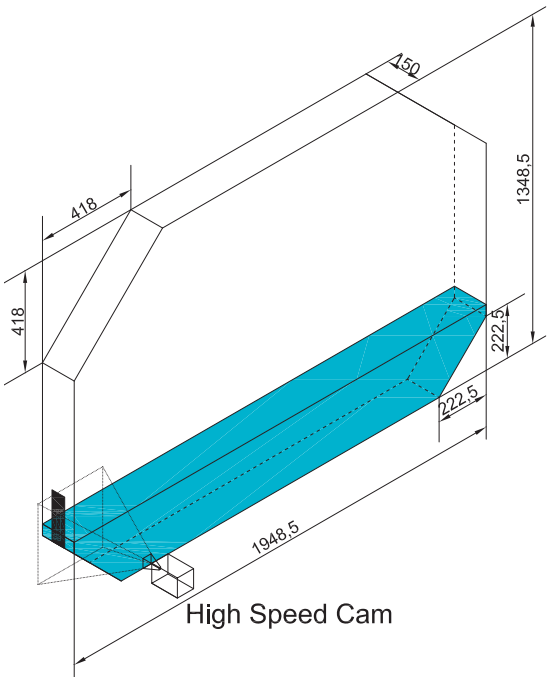

Fig. 5.1. Dimensions of the model tank and the schematic position of the high-speed camera and sensor module

horizontal and vertical distance between the centers of all the adjacent sensors was 10 mm. All the pressure sensors sampled at 40 kHz. The data acquisition system recorded the pressure signals from the sensors only for short sequences (events) including at least one pressure exceeding a chosen pressure threshold. This pressure threshold was 0.16 bar throughout the campaign. In order to perform the post-processing on the measured loads 5 areas were defined on the module. The areas are shown in Fig. 5.2. The defined areas of A1-A4 had surface areas of 3000 mm^2 at scale 1:20 corresponding to 1 m $\times$ 1.2 m at full-scale equivalent of the NO96 panel size. A5 had the size of 12000 mm^2 at scale 1:20. Smaller subareas provide insight on the more local phenomena even though the pressure sensors themselves, as the smallest available sensors, represent the most local measurements available. The largest subarea A5 gives an idea about the global loadings during sloshing impacts. Local phenomena are masked and not represented in the pressure signals calculated on the larger areas.

For a complete explanation of model test, equipment and the taken mea-

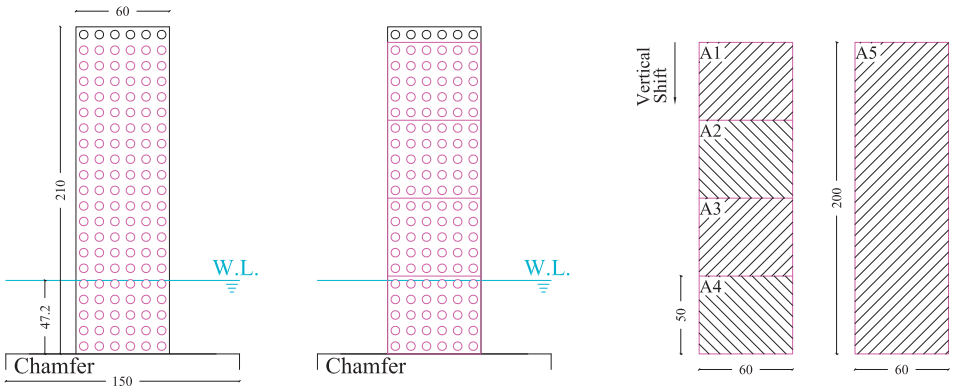

Fig. 5.2. The sensor module, water level and the defined subareas utilized in post-processing

sures to ensure repeatability and proper test conditions see Karimi et al. [2015b], Karimi et al. [2016] and Karimi et al. [2017] with similar procedures.

5.3 Dominant Impacts

In Karimi et al. [2017] and using 10 and then 49 repetitions of the same test condition it was shown that the tail of the statistical sample (largest values of the sorted sample) of pressure peaks on the selected area found from all recorded events of those tests was dominated by only a few impact IDs. The tail of the statistical sample was defined as the highest 100, 200, 300, 400 and 500 pressure peaks respectively. Those impact IDs were then called the dominant IDs. The list of dominant IDs depended on the size of the defined tail and the list of dominant IDs of the larger tails included the dominant IDs of the shorter tails. In this study more repetitions of the same test condition were used to further identify and study the dominant IDs.

296 repetitions were performed with water and air. Fig. 5.3 shows the maxi-

mum pressure peak on subarea A5 per model test as recorded in every repetition of the same model test. This maximum pressure peak is variable for different repetitions.

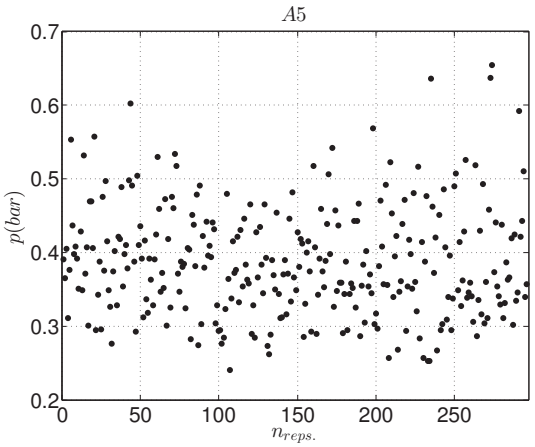

Fig. 5.3. The maximum pressure peak on subarea A5 recorded in each model test

The maximum pressure peak that is recorded on A5 for all repetitions, can also be found and plotted progressively as shown in Fig. 5.4 as a function of the number of repetitions. After a slight sharp increase with a few repetitions, this maximum increases slightly again until the last performed repetition. This maximum does not change for 190 tests as shown in the middle of graph. Fig. 5.5 also shows that considering the high pressure peaks, there are only a few IDs which can exceed such levels. Most of the measured IDs do not and cannot cause high pressures. On the other hand this means that there are only a few impact IDs which are responsible for the highest recorded pressures.

The pressure sample's tail was defined as the highest 100, 200, 300, 400 and 500 pressure peaks. The impact IDs which were present in the tail and the number of repetitions per each impact ID in the tail were monitored progressively in the sample of pressure peaks found from 1, 2, 3, ... , and 296 repetitions. The results confirmed the observations presented in Karimi et al. [2017]. It was observed that by increasing the number of repetitions the number of dominant IDs in the tail reduced whatever the size considered for defining the tail and for all the defined subareas as shown in Fig. 5.6, Fig. 5.7, Fig. 5.8, Fig. 5.9 and Fig. 5.10.

What is also of importance is that as the number of dominant IDs reduced by increasing the number of repetitions, it was the same IDs that were dominant throughout the process. In other words new IDs were rarely reintroduced to the

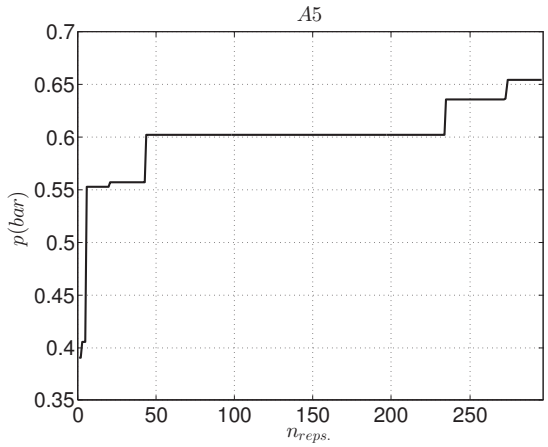

Fig. 5.4. The maximum pressure peak on subarea A5 recorded in all repetitions of the model tests

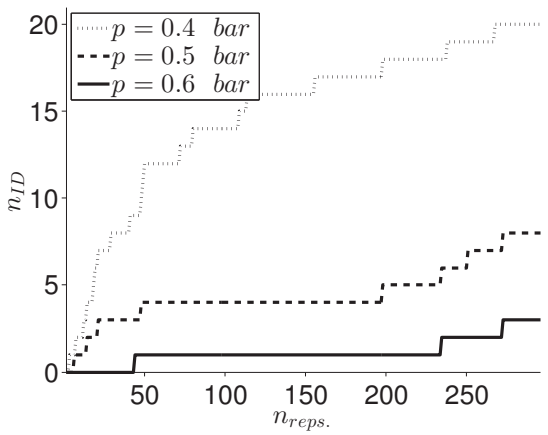

Fig. 5.5. The number of impact IDs which exceed the pressure level of 0.4, 0.5 and 0.6 bar on subarea A5 found after 1, 2, ... and 296 repetitions of the same model test

initial list of dominant IDs and the original list only became shorter. This showed that certain IDs have a higher probability of inducing severe impact pressures.

Fig. 5.11 illustrates the number of occurrences of each dominant ID among

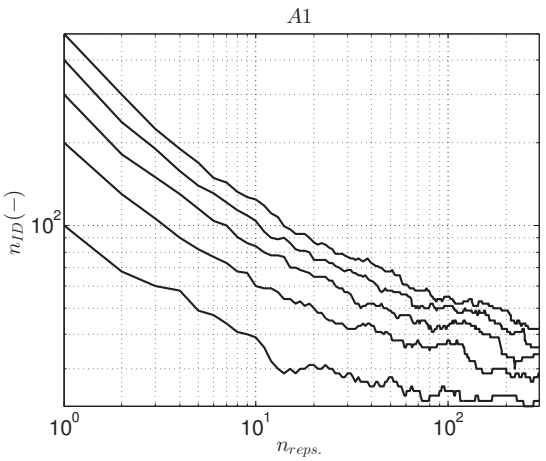

Fig. 5.6. Number of impact IDs among the highest 500, 400, 300, 200 and 100 pressure peaks found from 1-296 repetitions of the same 2D sloshing test condition on subarea A1. Increasing the number of repetitions reduced the number of dominant IDs.

the 100 highest pressure peaks on subareas A1-A5 found from 296 repetitions. Certain dominant IDs have a much higher number of occurrences than the others. The highest number of occurrences of an ID among the top 100 pressure peaks observed on A5 is 40. It was also observed that certain IDs with a high number of occurrences on certain subareas (A1, A2, A3 or A4) were of low or even zero number of occurrences for A5 implying that those IDs were important on the considered area rather that on A5.

The pressure peaks induced by dominant IDs among 100 highest pressure peaks on A1-A5 vs. the number of occurrences of each dominant ID was also studied as shown in Fig. 5.12. It is seen that on A4 as well as on A5 there is one dominant ID which has quite a larger frequency of occurrence compared to the rest. This ID is also associated with slightly higher pressure peaks. On A1-A3, the frequencies of occurrences for different IDs are closer and there are IDs with smaller frequencies which create the highest pressures as well. In the same figure, for all the subareas and considering the smallest impact pressure per subarea, it can be seen that the rest of the impact IDs during the model test never reached that pressure level.

The dominance of the pressure samples' tails by only a few IDs makes it interesting to study the statistical as well as physical properties of those dominant IDs. In order to estimate the most extreme loads that can be measured in a

sloshing model test condition and on each area studying the dominant impacts on that area would be important.

5.3.1 Variability of Wave Shape before Impact for a Given ID

In this study and thanks to the presence of the high-speed camera it was possible to observe each dominant ID in each repetition of the test condition. It could be seen that indeed there was a variation of impact geometry for any considered dominant ID. This observation was also true for any impact ID regardless of being dominant or not. There appears to be a correlation between impact geometry and the induced pressure which means that the variability of impact shape led to variability of impact pressure. The impact geometries for 5 dominant IDs found from 6 repetitions are shown in Fig. 5.13, Fig. 5.14, Fig. 5.15, Fig. 5.16 and Fig. 5.17. In the selection of images for each dominant ID occasions where the impact pressures were mild, average or rather high were chosen. For each ID, the images are chosen so that the wave troughs are at roughly the same level in order to make a rather fair comparison of the wave fronts.

From the comparison of the wave shapes right before the moment of impact it

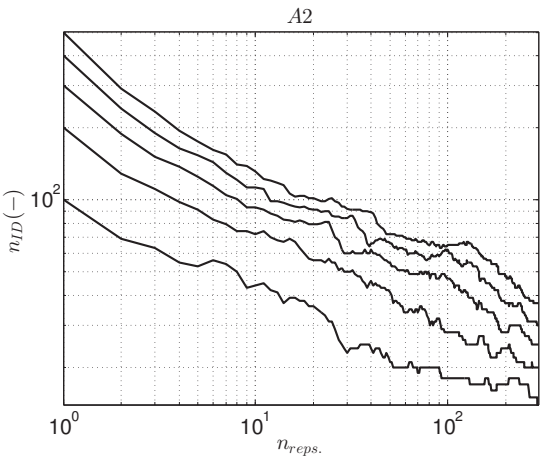

Fig. 5.7. Number of impact IDs among the highest 500, 400, 300, 200 and 100 pressure peaks found from 1-296 repetitions of the same 2D sloshing test condition on subarea A2. Increasing the number of repetitions reduced the number of dominant IDs.

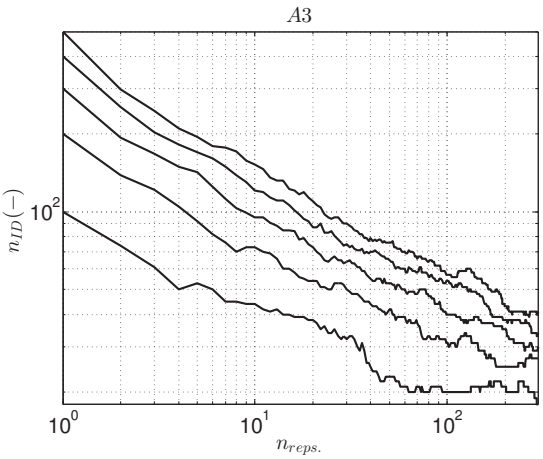

Fig. 5.8. Number of impact IDs among the highest 500, 400, 300, 200 and 100 pressure peaks found from 1-296 repetitions of the same 2D sloshing test condition on subarea A3. Increasing the number of repetitions reduced the number of dominant IDs.

appears that when the wave breaks earlier or when the wave hardly breaks (slosh impact), the impact pressure is less as shown in Fig. 5.13 trough Fig. 5.17. If there is a most probable shape for each ID, variations of wave shape around this most probable shape leads to variations of impact pressures around the most probable impact pressure.

As an example, for ID 3205 there were more images available as shown in Fig. 5.18 and by considering the pressure peaks corresponding to this dominant ID a sort of correlation between the impact pressures and impact shapes can be investigated although this correlation is not totally without exceptions. The general trend for this ID is that early breaking waves (early relative to the other repetitions of the wave shape for the same impact ID) are mostly associated with lower pressures and vice versa.

The most important message is that the wave shapes corresponding to each ID show a large variability compared to carefully generated single impact waves (SIW's for example as described in Karimi et al. [2016]). Such variabilities lead to variability of the associated loads which must be considered as statistical samples with their unique governing statistical distribution.

5.3.2 Statistical Properties

According to Fig. 5.10 and after 296 repetitions, 17 dominant IDs are present among the 100 pressure peaks on A5. The *probability density functions(pdf)* of the pressure peaks on A5 corresponding to those 17 IDs are shown in Fig. 5.19. Each probability density function of p has been found based on the normalized histogram of p.

The bin width h for each histogram was found according to FreedmanDiaconis rule: $h = 2 \times IQR(p) \times n^{-1/3}$ where n was the sample size and $IQR(p)$ represented the interquartile range of p defined as the difference between the 3rd and the first quartiles of the sample p. The number of bins in each histogram was then found based on $\frac{max(p)-min(p)}{h}$. After finding the histogram of each sample, the probability density function is estimated by dividing the frequency of each bin by $n \times h$. The area covered by the pdf was then equal to 1.

The illustrated probability density functions of the pressure peaks on A5 corresponding to the dominant IDs, show firstly the variabilities of impact pressures corresponding to the same ID. Each dominant ID by definition dominates the tail of the pressure sample and so induces the highest pressures that can be observed by repeating the same test condition. Nevertheless those dominant IDs can also induce mild impacts. This variability of pressures induced by the same ID may be

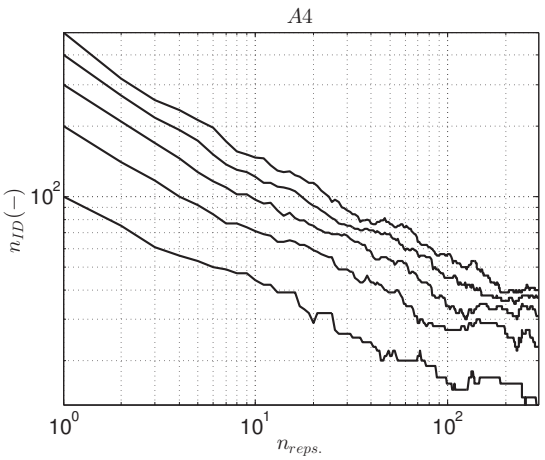

Fig. 5.9. Number of impact IDs among the highest 500, 400, 300, 200 and 100 pressure peaks found from 1-296 repetitions of the same 2D sloshing test condition on subarea A4. Increasing the number of repetitions reduced the number of dominant IDs.

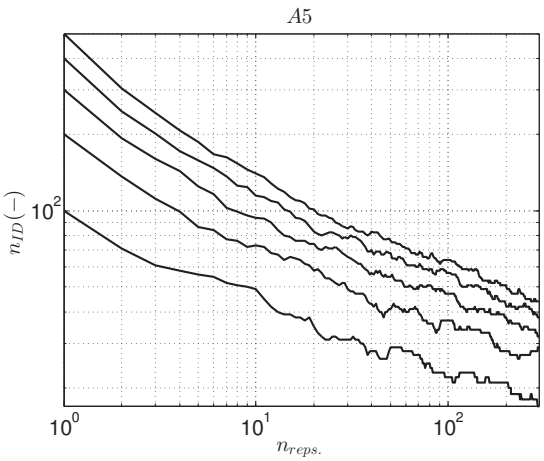

Fig. 5.10. Number of impact IDs among the highest 500, 400, 300, 200 and 100 pressure peaks found from 1-296 repetitions of the same 2D sloshing test condition on subarea A5. Increasing the number of repetitions reduced the number of dominant IDs.

attributed to the limited number of pressure sensors which could lead to missing some of the ongoing phenomena. This statement is more relevant about smaller loaded areas. With respect to a large area such as A5, this large variability should be mostly attributed to variability of wave shape and kinematics of the same IDs.

Considering the probability density functions presented in Fig. 5.19 it is evident that a most probable impact pressure peak exists for every impact ID. This most probable impact pressure peak may be attributed to a most probable impact shape. Variations of the geometry around this most probable shape may lead to variations of impact pressures around the most probable impact pressure. Empirical cumulative distribution functions of all dominant impacts are plotted as shown in Fig. 5.20.

It is seen that in terms of range of pressures and the associated probabilities there is a similarity between all dominant impacts with the exception of $ID\,2595$ which seems to have a considerably higher probability of exceedance for higher pressures. The empirical cdf of the pressure peaks associated with this dominant impact stands out among the rest. This ID happens to be the one with the highest frequency as shown in Fig. 5.11e.

Considering the similarity between the distributions of pressure peaks of different dominant IDs it can be demonstrated that taking $ID\,1377$ for instance and generating the 95% confidence bounds based on the two sample K-S test,

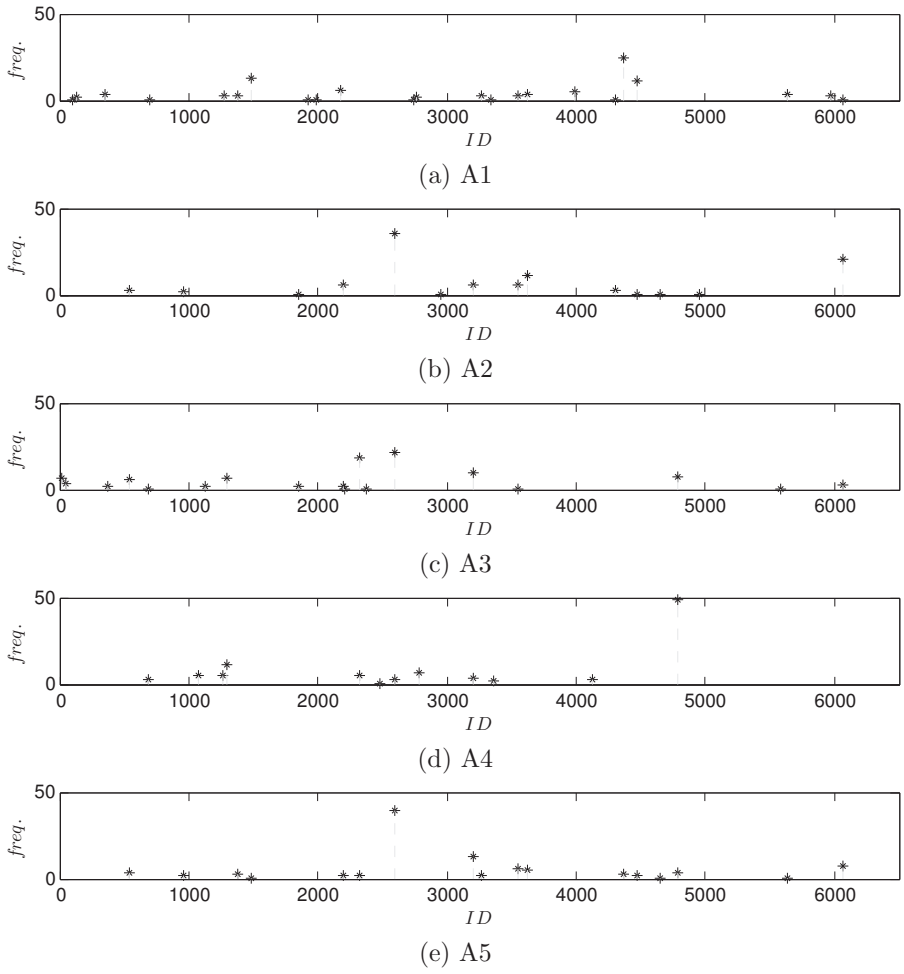

(a) A1

(b) A2

(c) A3

(d) A4

(e) A5

Fig. 5.11. Number of occurrences of dominant IDs in the 100 highest pressure peaks on subareas A1-A5 found from 296 repetitions of the same test condition. Several dominant IDs have a considerably larger frequency. The dominant IDs for different areas are different.

empirical cdf of 4 other IDs lie within these bounds and in other words the similarity between the distributions cannot be ruled out as shown in Fig. 5.21. This verification can be done for other dominant IDs and other similar statis-

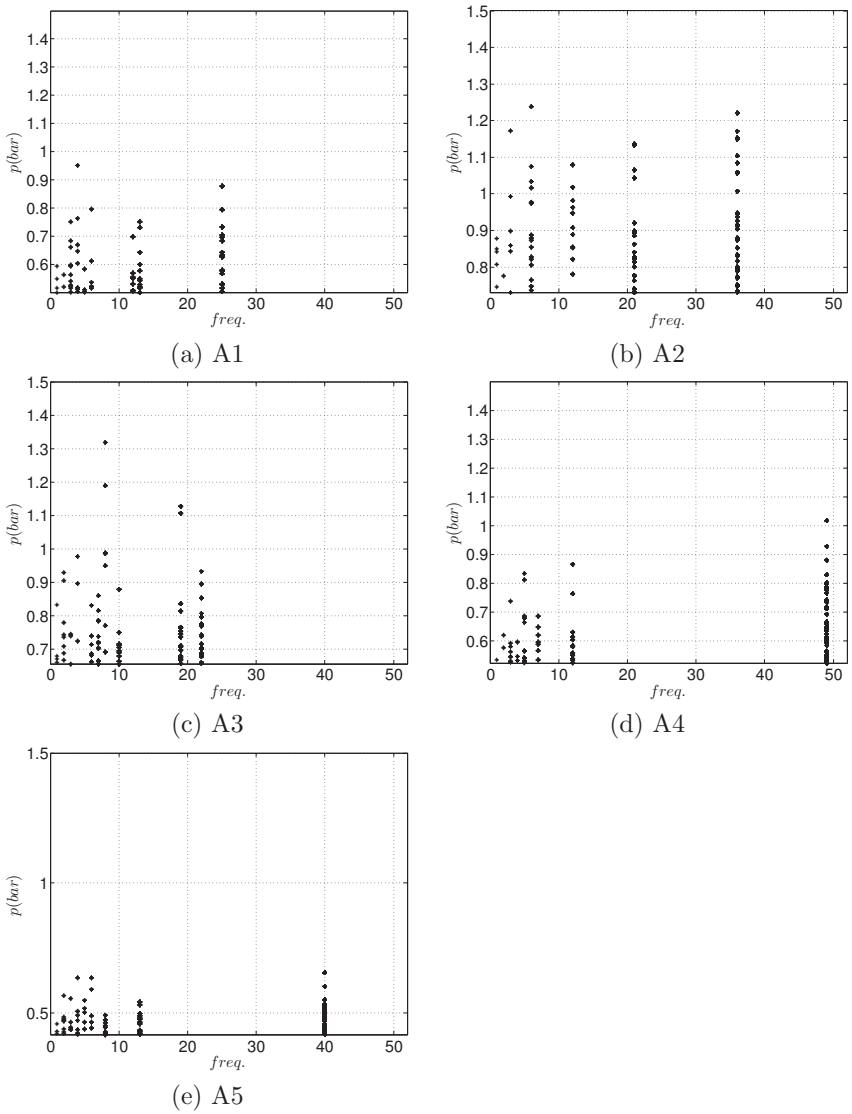

Fig. 5.12. The number of occurrences (frequency of occurrences) of the dominant IDs vs. the corresponding pressures for 100 maximum peak pressures on subareas A1-A5, found from 296 repetitions of the same test condition.

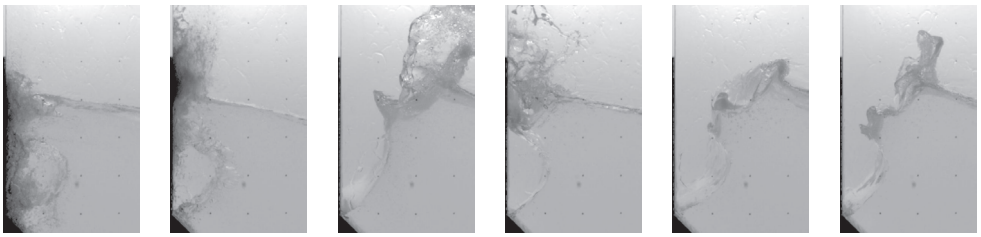

Fig. 5.13. Variation of impact shape for ID 543 found from 6 accurate repetitions of the same test condition. The maximum pressure values have been found on A5

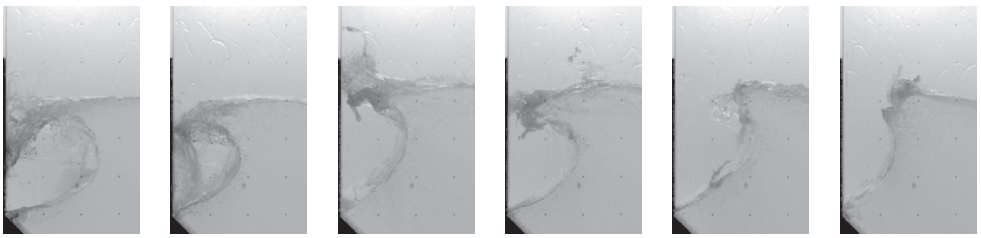

Fig. 5.14. Variation of impact shape for ID 1377 found from 6 accurate repetitions of the same test condition. The maximum pressure values have been found on A5

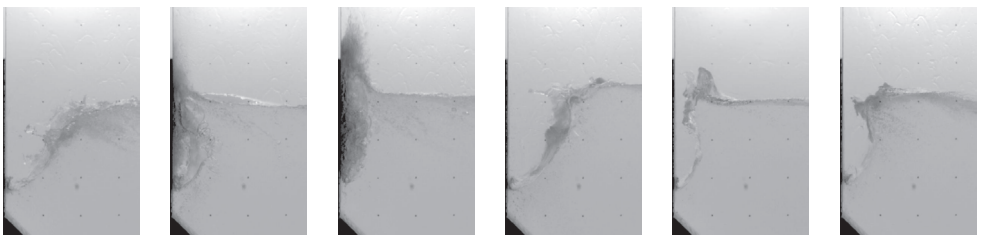

Fig. 5.15. Variation of impact shape for ID 2199 found from 6 accurate repetitions of the same test condition. The maximum pressure values have been found on A5

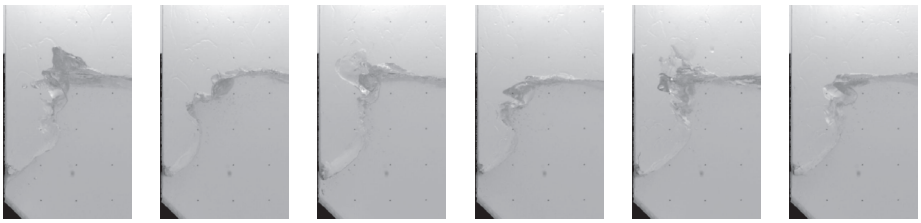

Fig. 5.16. Variation of impact shape for ID 2595 found from 6 accurate repetitions of the same test condition. The maximum pressure values have been found on A5

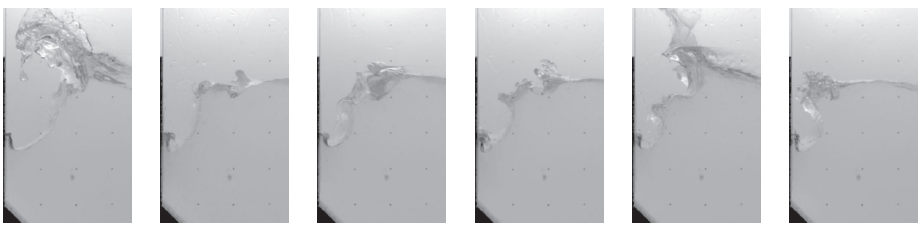

Fig. 5.17. Variation of impact shape for ID 3624 found from 6 accurate repetitions of the same test condition. The maximum pressure values have been found on A5

tical distributions can be found among which the statistical similarity between IDs, 543 vs. 6066 can be mentioned as another example. Besides the similarity it is important to note the unique statistical distribution of pressure peaks for every dominant ID. This is of course true for any impact ID regardless of being dominant or not.

5.4 Calculating the Probability of Exceedance

An important step in post-processing the results of every sloshing model test is to find the probability that a certain pressure level will be exceeded during one model test which is the equivalent of a five-hour sea state at full-scale. In practice all pressure peaks found from several repetitions of the same test condition form one sample. A statistical distribution is fitted to this sample that usually corresponds

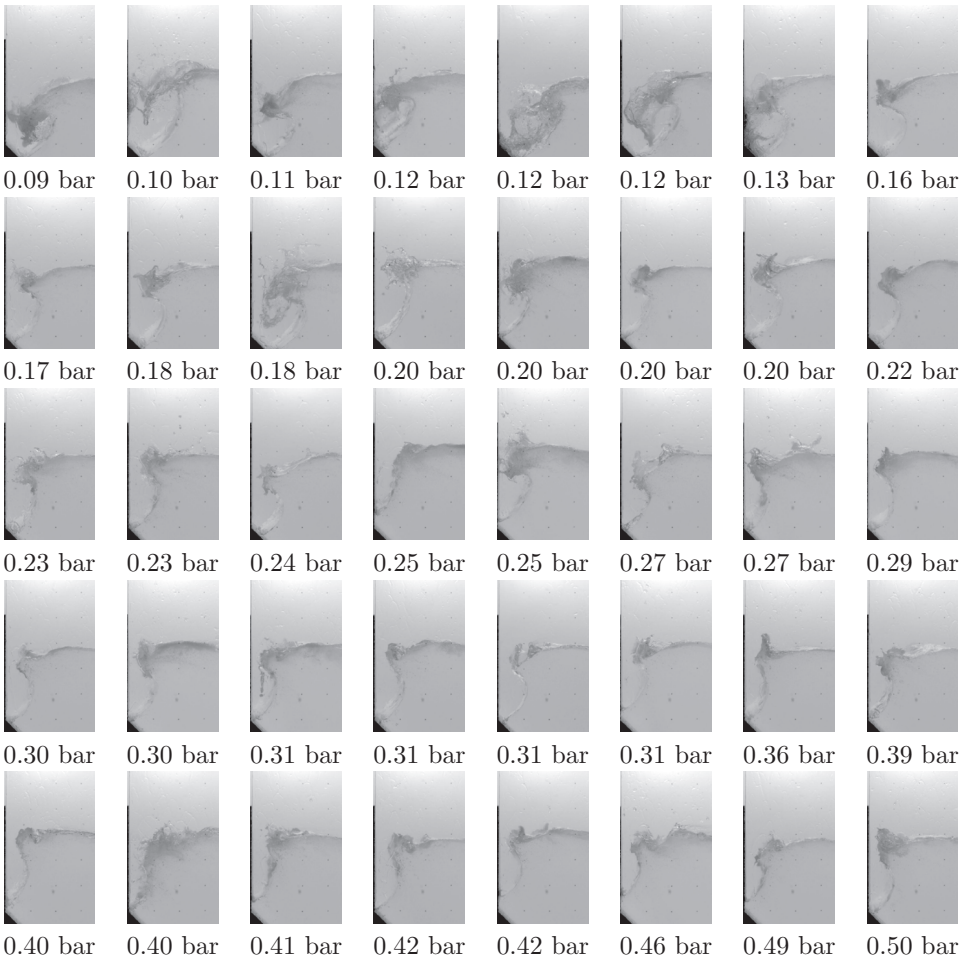

Fig. 5.18. Variation of impact shape for ID 3205 found from 40 accurate repetitions of the same test condition. The maximum pressure values have been found on A5

to Weibull or Generalized Pareto. In order to find the probability of exceedance during one model test, it is assumed that the statistical distribution of every event corresponds to the distribution of all the pressure peaks over time. In other words a sort of Ergodicity is assumed to exist in treating the pressure samples found from sloshing model tests.

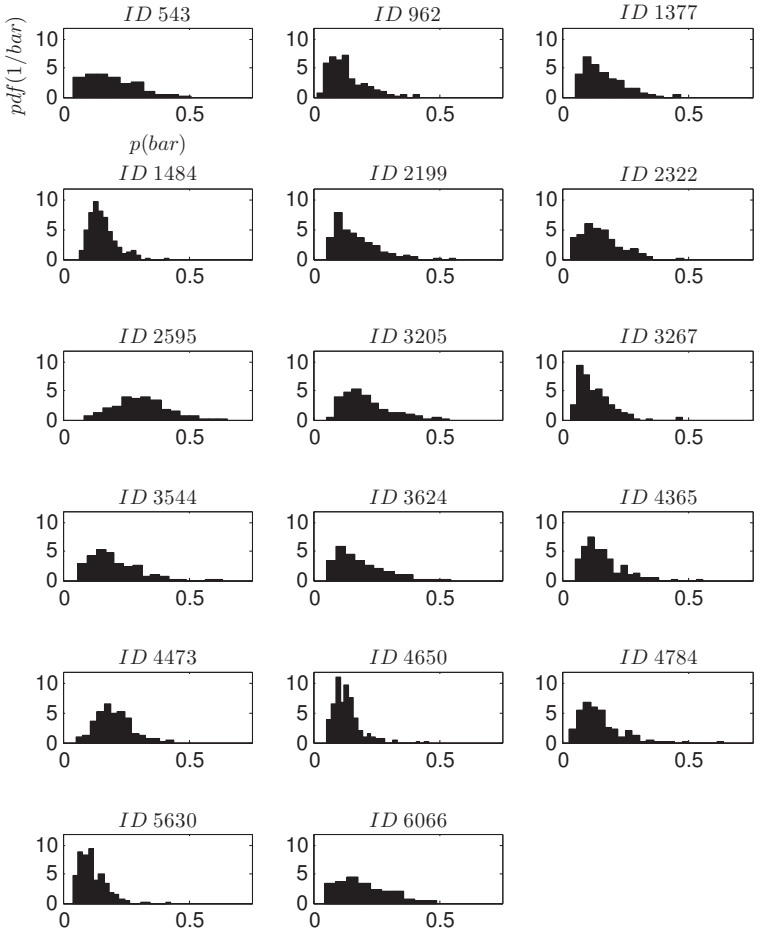

Fig. 5.19. The *probability density functions(pdf)* of the pressure peaks on A5 corresponding to 17 dominant IDs found from 296 repetitions of the same test condition

Earlier in this study it was shown that every detected dominant ID during one sloshing model test has a unique distribution. It can be shown that this distribution is not similar to the distribution found from the sample of all pres-

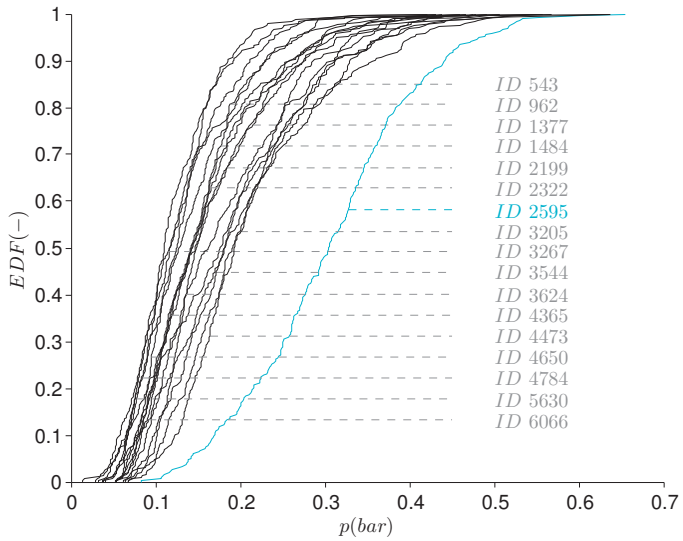

Fig. 5.20. Empirical cumulative distribution functions of pressure peak samples on A5 of 17 dominant impacts

sure peaks found from the repetitions of the same test condition. This is shown in Fig. 5.22. In this Figure the probability density function of pressure peaks found from 296 repetitions of one test condition is plotted next to the probability density functions of two dominant IDs. With the knowledge of each ID's statistical distribution, the probability of exceedance of every pressure level during one complete sloshing model test can be described based on the probability of exceedance of the detected impact IDs.

In the previous sections the statistics that were introduced were related to any dominant ID obtained for a given condition during sloshing model tests. The random variable X is the maximum measured pressure on a subarea during an event. By repeating N_T times the given condition, we were able to build a large sample of $X : (x_i)_{i=1,,N_P}$ where N_P is the total number of peaks for the chosen condition found from N_T repetitions and where the list of pressure peaks x_i are ranked from the largest x_1 to the smallest x_{N_P}. From this sample we built an empirical distribution that could be displayed as,

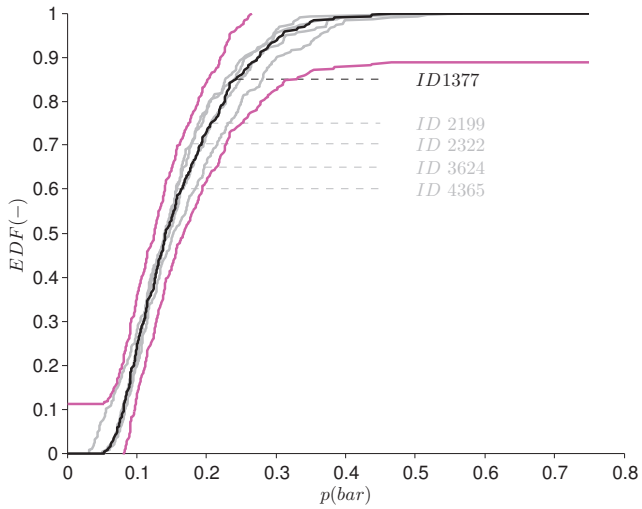

Fig. 5.21. Similarity between the empirical distribution functions of 5 dominant impacts. EDF of $ID\,1377$ was used as reference and edf of four other dominant IDs were compared using two sample K-S test. 95% confidence bounds have been plotted around the EDF of $ID\,1377$ based on the critical value of the two sample K-S test

$$\begin{aligned} E_E(x_i) = &\quad P(X \geq x_i) = \quad \frac{i}{N_P} \\ F_E(x_i) = &\quad P(X < x_i) = \quad 1 - E_E(x_i) \end{aligned}$$

Where $i = 1, , N_P$ and $E_E(x_i)$ and $F_E(x_i)$ are called *empirical exceedance probability function (EEPF)* and *empirical cumulative distribution function (ECDF)* respectively.

From a design point of view, we are interested in the probability to have no failure during the lifetime of the structure, that is to say a probability of survival after the total number of impacts N_{tot} that the structure will encounter during its life. Here as we only considered one condition in our experimental study, we have to imagine an operational scenario for the structure and a design objective. Let us consider that the structure will encounter that condition only once during its life (duration 5 hours at full scale corresponding to the duration of one test

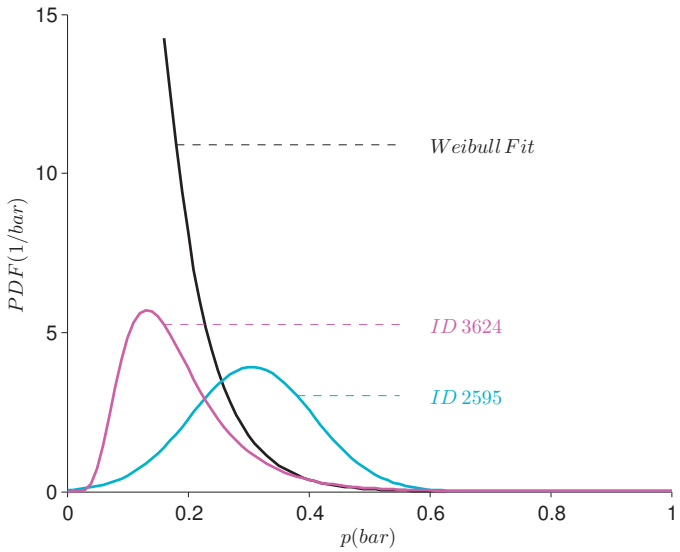

Fig. 5.22. Probability density functions of sloshing pressure peaks corresponding to $ID\,2595$ (—) and $ID\,3624$ (—) and all pressure peaks on A3 found from 296 repetitions of the same test condition with $p_{th} = 0.16\,bar$ (—),

after down-scaling) and that our design objective is that the floating structure will have no damage at all in that condition (short term approach), hence during the succession of $N_{tot} = N_P/N_T$ impacts it should experience, according to the average obtained from the N_T repetitions of the test.

We need to define a maximum value distribution. The usual way to build it is to consider a Bernoulli scheme. It means that we consider that at each impact the probability to have no new failure is $F_E(S) = 1 - E_E(S)$, where S denotes the design pressure, after down-scaling to the model scale, for the structural failure mode considered. After N_P/N_T impacts, the probability to have no failure at all is therefore given by $F_E(S)^{N_P/N_T}$, which defines a cumulative distribution function of the maximum values, $F1_{max}$, by:

$$F1_{max}(S) = \quad F_E(S)^{N_P/N_T} = \quad (1 - E_E(S))^{N_P/N_T}$$

Doing that, we assumed that each impact occurring when the structure sails in the chosen condition will induce a maximum pressure that is statistically governed

by the distribution derived from the tests (*ECDF*, *EEPF*).

Now we saw in the previous chapters, that the total sample of N_P pressure peaks obtained during the N_T repetitions of the test can be organized in a partition of N_{ID} samples, each one corresponding to an impact ID. The sub-sample of pressure peaks corresponding to the j^{th} impact ID for $j \in 1, , N_{ID}$, is composed of N_j peaks with

$$\sum_{j=1}^{N_{ID}} N_j = N_P$$

The empirical distribution of pressure peaks for the j^{th} impact ID can be defined by an empirical exceedance probability function $EEPF_j$ and an empirical cumulative distribution function $ECDF_j$ and for $j \in 1, , N_{ID}$:

$$\begin{aligned} E_{E_j}(x) = &\quad P(X_j \geq x) = \quad \frac{n_j(x)}{N_j} \\ F_{E_j}(x) = &\quad P(X_j < x) = \quad 1 - E_{E_j}(x) \end{aligned}$$

Where $E_{E_j}(x)$ is the empirical exceedance probability function of the j^{th} ID and $F_{E_j}(x)$ is the empirical cumulative distribution function of the j^{th} ID and $n_j(x)$ is the number of pressure peaks higher than or equal to x for the j^{th} ID. As the impact IDs enable us to define a partition of the total sample of pressure peaks, we have obviously,

$$E_E(x) = \frac{\sum_{j=1}^{N_{ID}} n_j(x)}{N_P} = \sum_{j=1}^{N_{ID}} \frac{N_j}{N_P} E_{E_j}(x)$$

The value $\frac{N_j}{N_P}$ measures the probability for a given impact obtained in the chosen condition to belong to the j^{th} ID. There is therefore a second way to calculate the probability to have no failure at all during the whole duration of the condition, considering that each impact during this time will belong to an ID. A second estimation of the cumulative distribution function of the maximum values $F2_{max}$ is given using a Bernoulli scheme for each ID, considering that there is an average $\frac{N_j}{N_T}$ impacts for the j^{th} ID for the duration of the condition.

Since every impact ID is experienced only once during one test condition a cumulative distribution function can be defined for any pressure level S during one test condition that can be expressed as:

$$F2_{max}(S) = \prod_{j=1}^{N_{ID}} (1 - E_{Ej}(S))^{\frac{N_j}{N_T}} = \prod_{j=1}^{N_{ID}} (1 - \frac{n_j(S)}{N_j})^{\frac{N_j}{N_T}}$$

in an ideal case, where the pressure threshold used for the acquisition system is 0, even the slightest pressures are measured and $N_j = N_T$. In this case,

$$F2_{max}(S) = \prod_{j=1}^{N_{ID}} (1 - E_{Ej}(S))^{1} = \prod_{j=1}^{N_{ID}} (1 - \frac{n_j(S)}{N_T})$$

The latter relation is idealistic and can hardly be achieved in reality. Considering that S corresponds to a design pressure, we can assume that both $E_E(S) = \sum_{j=1}^{N_{ID}} \frac{n_j(S)}{N_P}$ and $E_{Ej}(S) = \frac{n_j(S)}{N_j}$ are small with regard to 1. Now for $a << 1$, we can write $(1-a)^\alpha = 1 - \alpha \times a + O(a^2)$.

Therefore a good approximation of $F1_{max}(S)$ is achieved as,

$$F1_{max}(S) \approx 1 - \frac{N_P}{N_T} E_E(S) = 1 - \frac{N_P}{N_T} \frac{\sum_{j=1}^{N_{ID}} n_j(S)}{N_P} = 1 - \sum_{j=1}^{N_{ID}} \frac{n_j(S)}{N_T}$$

In a similar way we have a good approximation of $F2_{max}(S)$ as given by

$$F2_{max}(S) \approx \prod_{j=1}^{N_{ID}} (1 - \frac{N_j}{N_T} E_{E_j}(S)) = \prod_{j=1}^{N_{ID}} (1 - \frac{n_j(S)}{N_T})$$

As $\frac{n_j(S)}{N_T} << 1$, we can write

$$\prod_{j=1}^{N_{ID}} (1 - \frac{n_j(S)}{N_T}) = 1 - \sum_{j=1}^{N_{ID}} \frac{n_j(S)}{N_T} + O(\frac{max(n_j(s)^2), j \in 1, ..., N_{ID}}{N_T^2}) \approx 1 - \sum_{j=1}^{N_{ID}} \frac{n_j(S)}{N_T}$$

Hence

$$F1_{max}(S) \approx F2_{max}(S) \approx 1 - \sum_{j=1}^{N_{ID}} \frac{n_j(S)}{N_T}$$

If we consider a sub-sample of the total pressure peak sample defined by all peaks larger than S, these peaks belong to a short list of the total list of impact IDs, which represents, by definition, the dominant IDs for this tail of the peak distribution. If $Dom(S)$ denotes the list of indexes among $1, , N_{ID}$ for these dominant IDs, $n_j(S) = 0$ for $j \in 1, , N_{ID}$ and $j \notin Dom(S)$. hence we can write

$$F1_{max}(S) \approx F2_{max}(S) \approx 1 - \sum_{j \in Dom(S)} \frac{n_j(S)}{N_T}$$

Normally, during a sloshing assessment of a real project of LNG tank on a floating structure, we do not repeat enough times the different conditions to be studied in order to reach S by enough pressure peak measurements for a good evaluation of $E_E(S)$. Therefore, we have to fit the sample of pressure peaks by a statistical law. Usually the three-parameter Weibull distribution is used which is defined by the continuous EPF as $E(x) = exp(-(\frac{x-\mu}{\sigma})^{\xi})$, where (μ, σ, ξ) are respectively the location parameter, the scale factor and the shape parameter.

In that case the evaluation of the cumulative distribution function of the maximum values becomes: $F1_{max}(S) \approx 1 - \frac{N_P}{N_T} E(S)$.

For a real sloshing assessment, all conditions in terms of sea-state, ship/wave incidence, ship speed and fill level in the studied tank, that the structure is expected to encounter during its life are studied in order to build long-term statistics. The long-term probability of exceedance $EPFLT, E_{LT}(x)$, is built as a linear combination of the $EPFST_k$, $k \in 1, , N$, where $EPFST_k$ denotes the probability of exceedance $E_{ST_k}(x)$ for the condition k and N denotes the total number of conditions studied. The weighing factor of each $EPFST_k$ in the combination is the probability q_k to have one impact in the considered condition k: $E_{LT}(x) = \sum_{k=1}^{N} q_k E_{ST_k}(x)$.

5.5 Conclusions

This study elaborated the notion of dominant IDs that was identified in Karimi et al. [2017] using 296 repetitions of the same test condition. The tests were performed at scale 1:20 with a 2D tank which represented a slice of tank 2 of a 4 tank LNG carrier with a capacity of 152000 m^3. The tank fill level was chosen to be 20 % of the tank height. Water and air were used as liquid and gas. 3D tank motions of roll, sway and heave were applied on the tank and the test condition represented a 5-hour sea state at full-scale. Impact pressures were measured using an array of 21×6 sensors. The impacted area was divided into 5 subareas on which the measured pressure signals of each sloshing event were

averaged and the maximum of each pressure signal was found for each event. The collection of pressure peaks from all events of one repetition on each area formed the statistical sample per test and per that area. Impact shapes were recorded using a high-speed camera right before and slightly after each breaking wave impact.

It was shown that considering the sample of pressure peaks from the repetitions on any subarea,

- If the tail of the statistical sample of all the pressure peaks from all repetitions is defined by n largest peaks (highest 100, 200, 300, etc.), this tail is represented by only a few impact IDs, the dominant IDs. In other words, all of the pressure peaks in the tail belong to the measurements of a few impact IDs which are called the dominant IDs,
- By progressively increasing the number of repetitions of the same test condition, the number of dominant IDs in the tail decreased.

Considering each dominant ID, it was shown that

- The peaks that belong to each dominant ID have their own unique statistical distribution,
- Each ID seems to have its own variability in terms of impact shape,
- The distribution of every dominant ID is different from the collective distribution of all of the pressure peaks from all impacts.

It was shown that using the notion of dominant IDs the exceedance probability of any pressure level can be defined with an alternative method to the current approach used in the assessments which is based on one sample of all pressure peaks from all the repetitions. It was shown that both methods lead to identical results for the tail of the distribution of maximum values. The main difference of the method based on impact IDs is that the emphasis is put only on the IDs which will lead to the highest pressures, rather than all IDs since most of the impact IDs will not have any influence on the tail region.

Chapter 6

Singularization of Sloshing Impacts

abstract

[1]

This study elaborates the singularization technique first introduced by Karimi et al. [2015a]. With the singularization technique any impact ID from long sloshing model tests can be alternatively created with short sequences of tank motions. The resultant impact matches the target impact from long model tests both visually as well as in terms of statistical impact pressures. The conclusions are made based on sloshing model tests performed with a model tanks representing a slice of a real tank of LNG carrier at scale 1:20. The tests were performed with water and air at 20% (of tank height) fill level. The tanks were instrumented by high-speed cameras and pressure sensors.

One application is comparing statistical distributions of pressure peaks for selected impact IDs at different scales. Singularization helps to generate the relevant samples of pressure peaks for each ID in a short time. This helps to study the scaling biases or the influence of different parameters in sloshing model tests. Also in combination with the notion of dominant IDs developed in Karimi et al. [Submitted to EJMBF in 2017a], the singularization technique will enable to regenerate the tail of the long term empirical distribution of pressure peaks by first identifying the dominant impacts and then quickly generating the relevant statistical samples of the tail.

The results presented in this study with 2D tests, one impact ID and 5 impacted areas have been later confirmed to be valid for other impact IDs, much smaller impacted areas as well as for 3D tests.

[1]This chapter is based on: *Singularization of Sloshing Impacts*. M. R. Karimi, L. Brosset, M. L. Kaminski and J.-M. Ghidaglia which has been submitted to the European Journal of Mechanics - B/Fluids.

6.1 Introduction

When stored or transported, liquefied natural gas (LNG) is kept at atmospheric pressure and the temperature of $-163°C$. The design loads of the containment system include the loads induced by liquid impacts due to sloshing. These sloshing loads are assessed by means of sloshing model tests. A model tank made of smooth and rigid walls at a smaller scale of 1:λ (usually $\lambda = 40$), is placed on the platform of an accurate 6 DOF motion rig. The tank is partially filled with water. As the density of water is more than twice the density of LNG, a density scale $1 : \mu$ (μ is defined as ρ_{LNG}/ρ_{water}) representing the density ratio between LNG and water is introduced in the dimensional analysis. A heavy gas made of a mixture of sulfur hexafluoride (SF_6) and nitrogen (N_2) is used as ullage gas in the model tank. The mixture's density is adjusted so that the gas-liquid density ratio DR, defined as $DR = \frac{\rho_G}{\rho_L}$ matches that of the NG and LNG in real tanks (See Maillard and Brosset [2009]). The motions of the floating structure are calculated at full-scale by means of a classical boundary element method (BEM) taking into account the ship speed (usually under the approximation of the encounter frequency) and the coupling between the floating structure and the cargo motions. The motions are then applied by the rig to the model tank after having been down-scaled. A time scale $1 : \tau$ related to the geometric scale by $\tau = \sqrt{\lambda}$ is used in finding the tank motions at model-scale. Pressure sensors (typically 300 sensors in GTT for every sloshing test campaign) acquiring at high frequency (¿ 20 kHz) are regularly arranged in rectangular arrays located in the most exposed areas of the tank.

6.1.1 Representativeness of the Model Tests

When mild tank motions are applied to the model tank in order to avoid any wave breaking or any wave impact on the walls, liquid and gas flows can be considered as incompressible. The free surface remains smooth at any time without any free surface instability development as the shearing gas flow remains moderate. The liquid also remains free of bubble. In such conditions liquid and gas flows obtained experimentally at two different scales for scaled excitations (motion amplitudes scaled by $1 : \lambda$ and time by $1 : \sqrt{\lambda}$) are accurately repeatable at both scales provided that the sloshing rig is able to repeat accurately the same motions, and remain completely similar even after a long duration (considering the tank motion time shift see Karimi et al. [2015b]). Measured pressures at wall remain low in these conditions without impact but are also perfectly repeatable when measured with reliable sensors. Those pressures are purely hydrodynamic (without any compressibility influence). Pressure at any scale, including full-scale, can thus be directly found from measured pressures at a given model-scale, at scaled locations

and times, using the pressure scale derived from the three fundamental scales $(1:\lambda, 1:\mu, 1:\tau)$ by dimensional analysis: $p^{fs} = \frac{\mu\lambda^2}{\tau^2} \times p^{ms} = \mu \times \lambda \times p^{ms}$, where ^{fs} and ^{ms} denote full-scale and model-scale respectively. These ideal conditions are accurately described by incompressible isentropic Euler equations for two fluids without surface tension at the interface and can be numerically simulated with a good accuracy.

In realistic conditions with more violent tank motions, waves break on the tank walls. Under the more violent conditions, gas compressibility is involved while the ullage gas escapes just in front of a breaking wave crest or in between a wall and an impacting wave front or while it is entrapped in a gas pocket (see Bogaert et al. [2010b], Kimmoun et al. [2010], Lafeber et al. [2012a] for experimental evidence of gas compressibility influence ; see Bredmose et al. [2009], Guilcher et al. [2013], Guilcher et al. [2014], Costes et al. [2014] and Rafiee et al. [2015] for numerical simulations of such an influence).

Liquid compressibility is also involved at each direct impact resulting in propagation of a pressure wave towards the liquid as a result of the discontinuity of velocity between an impacting liquid particle and the wall (see Bredmose et al. [2009] and Lafeber et al. [2012b] for experimental evidence of liquid compressibility; see Guilcher et al. [2012] and Guilcher et al. [2014] for numerical simulations of this influence).

Other than gas and liquid compressibility, surface tension, viscosity and phase transition become important in real-life sloshing impacts. As a result for a complete similitude of the flows at two different scales, namely for having the same dimensionless formulation of the problem at both scales, in addition to $\tau = \sqrt{\lambda}$ and the similarity of DR at the two different scales, Mach number of the liquid (M_L) and the gas (M_G), Reynolds number of the liquid (Re_L) and the gas (Re_G) and the Weber number (We) must be kept the same at both scales. These different dimensionless numbers are defined by $M_L = U/c_L$, $M_G = U/c_G$, $Re_L = UL/\nu_L$, $Re_G = UL/\nu_G$ and $We = (\rho_L U^2 L)/\sigma$ where ρ_L is the liquid density, c_L and c_G are the speed of sound respectively in liquid and gas, ν_L and ν_G are kinematic viscosities respectively in liquid and gas and σ is the surface tension at the interface. L and U denote respectively a characteristic length and a characteristic velocity. If phase change occurs during impacts, the relevant parameters and dimensionless numbers should be respected too. As a result, a perfect similarity between the two scales (regardless of phase transition) would require the following additional conditions:

$c_L{}^{ms} = \frac{1}{\sqrt{\lambda}} c_L{}^{fs}$ and $c_G{}^{ms} = \frac{1}{\sqrt{\lambda}} c_G{}^{fs}$,
$\sigma^{ms} = \frac{1}{\mu\lambda^2} \sigma^{fs}$,
$\nu_L{}^{ms} = \frac{1}{\lambda^{3/2}} \nu_L{}^{ms}$ and $\nu_G{}^{ms} = \frac{1}{\lambda^{3/2}} \nu_G{}^{ms}$

Assuming λ=40 and μ=0.43, leads to the following ideal values :

${c_L}^{ms} = 0.16{c_L}^{fs}$ and ${c_G}^{ms} = 0.16{c_G}^{fs}$,
$\sigma^{ms} = 1.45 \times 10^{-3}\sigma^{fs}$,
${\nu_L}^{ms} = 3.95 \times 10^{-3}{\nu_L}^{ms}$ and ${\nu_G}^{ms} = 3.95 \times 10^{-3}{\nu_G}^{ms}$

In practice only DR is really kept the same at both scales with the right choice of the gas density inside the model tank. None of the other properties can be adequately down-scaled from the values at full-scale. With water and the mixture of SF_6 and N_2 as ullage gas inside the model tank instead of LNG and NG, the liquid and gas are way too stiff and viscous and the surface tension is way too large. The similarity between full-scale and model-scale is thus necessarily incomplete and the flow at model-scale is biased with regard to the flow at full-scale.

Moreover there is a variability of the fluid flow when a test at any scale with the exact same conditions and parameters is repeated. This variability can be observed at both local (close to impact zones) and global level (far from impact zones). These kinds of variabilities introduce inherent biases in the model tests. Such variabilities are constantly produced and dissipated. The variabilities and perturbations do not build up progressively during and until the end of each model test to lead to random global flows. Without this dissipation of variability during each impact sloshing model tests would not make sense (see Karimi et al. [2015b] and Karimi et al. [2016]). Since the variabilities at each scale are also influenced by viscosity, compressibility and surface tension, those variabilities are not properly scaled either. As a result of the bias in scaling the parameters and the bias of variability, the flow and hence the impact pressures can be considered as biased. It is assumed that tank motions would not pose another source of bias at this level of comparison. It should be noted that impact pressures can only be explained as statistical distributions and not absolute values. This is the direct consequence of the aforementioned variabilities (see Karimi et al. [2017] and Karimi et al. [Submitted to EJMBF in 2017a]).

There are therefore two main issues related to sloshing model tests: (1) the scaling of the flow and consequently of the measured pressures; (2) the variability of the flow and consequently of the impact loads when repeating carefully the same condition and also a combination of the two first: the scaling of the variability. Methodologies have been developed (Gervaise et al. [2009], LR [2009], BV [2011], DNV [2014] and ABS [2014]) aiming at deriving design loads for the containment systems from sloshing model tests taking care of these two issues.

Sloshing model tests try to recreate at small scale all conditions that the floating structure is expected to experience during its life, screening different possible loading conditions, sea states, ship speeds, wave incidences with regard to the floating structure and fill levels in the studied tank. To cope with the

variability of the pressure measurements, samples of pressure peaks are gathered for all conditions repeated as many times as necessary in order to enable relevant long term statistics. A scaling process is then proposed to derive design loads at a suitably low probability.

For large scale LNG ships decades of experience are available. This feedback enables GTT to tune experimental scaling factors from sloshing model tests performed in conditions for which sloshing incidents occurred (indentations of plywood boxes of NO96 containment system, permanent deformations of the stainless steel membrane corrugations of Mark III[2] containment system). For less classical tanks or ship designs when almost no feedback is available, as for tanks of LNG as a fuel that can be used for any kind of commercial ship or for small scale applications in general, the scaling derived from dimensional analysis with the no bias assumption is directly applied.

All these issues question the relevance of sloshing model tests. Nevertheless, comparisons between full scale measurements on board a 148 300 m3 membrane LNG carrier and sloshing model tests mimicking the conditions for which sloshing was experienced on board, showed that despite all mentioned defects, sloshing model tests remain conservative on a long-term basis - which is the most important from a design perspective (joint presentation of DNV-GL and GTT at Gastech2015). The study was performed within the Full Scale Measurement (FSM) JIP led by DNV and described in Lund-Johansen et al. [2011] and Pasquier and C.-F.Berthon [2012]. More precisely, statistical distributions representative of the ship operational profile over four years of measurements proved to be more conservative when built from model tests than from full scale measurements. Comparison of the design pressure defined at a probability 10-3 per year showed a safety margin for both curves. Nevertheless, the study also showed that sloshing model tests were not always totally representative of the reality when comparisons were based on a short-term basis. Another issue was that the comparison was only based on the statistics of the collection of pressure peaks as a whole and did not consider the individual impacts.

With the knowledge of all the biases surrounding sloshing model tests and as numerical simulations are far to be mature enough to be used as a substitution tool to sloshing tests, the different issues related to the use of sloshing model tests motivate further studies on scaling and on variability in the context of liquid impacts. R&D work on sloshing loads pursue multiple objectives: improve the conditions of sloshing tests for a better representation of the reality; better derive design loads from biased measured pressures; shorten the duration of a test campaign but with a better capture of the most violent events, enriching efficiently the tail of the statistical long term pressure distribution.

[2]See www.gtt.fr for description of NO96 and MarkIII containment systems

6.1.2 Impact Coincidence, Impact IDs, Dominant Impact IDs

A way to study the biases of the sloshing model tests would be to study each model test impact by impact. Since every model test is supposed to be a perfect copy (ideally) of the full-scale conditions, every single detail of the model test should be a model and copy of a similar detail at full-scale. This would not be achieved in reality as explained before; yet in order to study the biases, the comparable details at different scales can and must be compared. In order to propose a basis for such a comparison, an idea based on *Impact Coincidence* and *Impact ID* has been studied starting with Karimi et al. [2015b], Karimi et al. [2016], Karimi et al. [Submitted to EJMBF in 2017a] and Karimi et al. [Submitted to EJMBF in 2017a]. The goal so far is to suggest a new approach to look at the representativeness of the sloshing model tests and possibly evaluating the involved biases.

Currently the sloshing model test results are studied by comparing statistical samples from the whole tests at different scales. The problem is that too much information is lost (and basically discarded) in such comparisons and even if the model tests are totally irrelevant, this irrelevance cannot be established by analysing the statistical samples from the whole tests.

As it was mentioned with respect to the variabilities, they do not build up during and until the end of model tests. Their effects influence a short while after their creation and are dissipated gradually. The result of this dissipation is that the global flow (fluid flow far from the impact zones or basically far from the tank walls) is not random and can be reasonably scaled and does not depend much on the ullage gas and the liquid (see Karimi et al. [2015b]). As a result and for the same irregular excitations of sloshing model tests, impacts always happen at the some exact moments in time with regard to the initial time of the forced motions when considering a small uncertainty time window (Δt). This was also proven to be true regardless of the tested range of ullage gas densities. When comparing two different scales with scaled forced excitations the impacts happen at time-similar instants. The impacts that happen at the same exact times (or scaled times) are referred to as coincident impacts.

Δt of 30.070.0 ms at scale 1:20, 20.050.0 ms at scale 1:40, and 30.0120.0 ms when comparing scale 1:20 with scale 1:40 proved to be enough to detect almost all the possible impact coincidences as shown by Karimi et al. [2015b]. These coincident impacts when considering repetitions of the same irregular test at one or different scales are identified either by an index or a time which will be considered as their Impact ID. Every impact collected during the test repetitions belongs to one and only one impact ID. There are also dominant impact IDs in the total collection of IDs for an irregular condition. Indeed, when increasing the

number of repetitions of an irregular test, the number of IDs involved in the N highest recorded pressures keeps decreasing, down to a few IDs. These dominant IDs are those which generate the highest pressures and hence they are building up the tail of any statistical distribution which aims at describing the pressure peaks.

The impacts that belong to the same impact ID can be directly compared together as such impacts at different scales are supposed to be scaled copies of each other.

6.1.3 Overview of the Paper

For any impact ID occurring at a time t_{ID}, the process of variability production and regularization suggests that only previous impacts or wave breakings within a certain duration m_e before t_{ID} contributed to its shape variability and therefore its pressure variability. An impact occurring just before $t_{ID} - m_e$ will generate a certain variability on the next impacts but with less and less influence due to the regularization factors. At the instant t_{ID}, this influence can be considered as negligible. The duration m_e should be therefore considered as a an effective memory (flow memory) related to the considered impact ID. m_e is considered to be fluid-dependent and therefore scale-dependent.

It should be noted that starting from rest there is also a minimum duration for the singularized flow to be able to find the same pace with the reference global flow. This duration is shorter than m_e and can be called Inertial Flow Memory (IFM). A video proposed by Karimi et al. [2015a] illustrates this minimum duration by comparing three different durations of singularization. It can be watched here.

It was already shown by Karimi et al. [2015a] that for a given impact ID occurring at t_{ID}, a short sequence of the original irregular motions before the impact time is sufficient to generate a most probable shape before impact similar to the original one: the impact is thus singularized. Singularization tests related to the impact ID at t_{ID}, with a nominal duration d, are defined with tank motions composed of an extraction of the original irregular motions (for each degree of freedom) for the range $[t_{ID} - d, t_{ID} + \epsilon]$ (ϵ is a short margin taken after t_{ID}) completed by polynomial ramps joining the extracted signal with a continuous second derivative at both ends and enabling smooth start and stop of the sloshing rig. The results described in Karimi et al. [2015a] were based on singularization tests of variable nominal durations d with a 2D tank at scale 1:40 and high-speed video comparisons right before the moment of impact. The comparisons showed that, for the selected impact ID, a short duration ($d \approx 15s$) was sufficient to capture the main characteristics of the wave shape before impact. As the wave shapes varied around the most probable wave shape both for repetitions of the

reference irregular tests and for repetitions of the singularization tests, it was not possible only by visual judgement to evaluate whether the variability obtained on the wave shape and thus on the impact pressures was equivalent when comparing singularization tests and reference irregular tests. This is the main object of the present paper. The results will be consolidated this time based on statistics of the singularized impact. The effective memory m_e associated to an impact ID will be defined as the minimum required duration d for singularization tests to get an empirical statistical distribution which is equivalent of that obtained for the same ID from repetitions of the reference irregular test. The results show that for any given impact ID and at any scale and considering any impacted area, it is possible to define a duration m_e so that for any nominal duration $d \geq m_e$, the pressure peak samples obtained from the singularization tests are statistically equivalent to the reference pressure peak sample obtained for the same impact ID from long irregular model tests. Furthermore it is shown that the flow condition before this duration d of the singularization tests influences the statistics as long as $d < m_e$ but has no or negligible influence for $d \geq m_e$. It is therefore relevant to consider this duration m_e as a memory. For the impact ID that was studied at scale 1:20 and for the rather large impacted area that was considered, a duration of $m_e = 45s$ turned out to be large enough.

6.2 Test Setup

The main series of tests were at scale 1:20 and were performed in GTT. The tank was a model of a transverse slice of Tank 2 of an LNG carrier using membrane containment system technology with the total capacity of 152,000 m^3. In this study only tank fill levels of 20% of the tank height were considered due to more severe impacts and higher induced pressures (see BV [2011]). The tests were all performed with water and air. For the internal tank dimensions see Fig. 6.1.

The tests were 2D with 3 DOF applying sway, heave, and roll excitations. The tests were performed by a Sirocco type hexapod with the maximum payload of 2 tons made by Symétrie [3]. The types of motions used in this study were irregular. Irregular tank motions were based on ship motions at full-scale calculated by PRINCIPIA's DIODORE[4] for 5 hour sea states based on JONSWAP spectrum found from the assumption of zero crossing period T_z of 8.5 s, heading of 270 ° and significant wave height H_s of 6 m. The motions were coupled with sloshing in the tanks. In order to find the model test tank motions, the full-scale motion amplitudes and time had been down-scaled by factors λ and $\sqrt{\lambda}$ respectively. These motions were defined for the middle of the bottom of the 2D tanks which

[3] See Symétrie's website for complete technical details on the hexapods
[4] See PRINCIPIA's website for more information on DIODORE

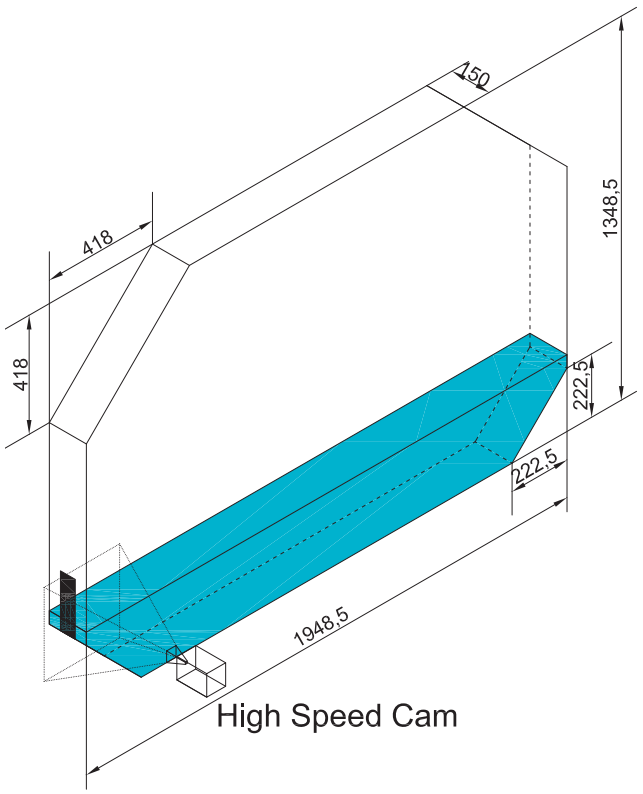

Fig. 6.1. Dimensions of the model tank at scale 1:20 and the schematic position of the high-speed camera and sensor module

was called the *center of rotation*.

The main camera that was used in this campaign was a high-speed camera. The high-speed camera was used to record the impact geometry a few milliseconds before and after the impact. A Phantom V7.2 high-speed camera was used in this model test. For this camera the resolution was 608×600 pixels with ~ 3.56 pix/mm and the exposure of 130 μs. The high-speed camera recorded at 4000 fps. The fill level was monitored regularly with a simple camera. The high-speed cameras was activated when impact pressures exceeded a threshold used for the camera system. LED lamps were installed to illuminate the background.

PCB sensors were installed on the sensor module in an array of 21×6. The horizontal and vertical distance between the centers of all the sensors was 10 mm.

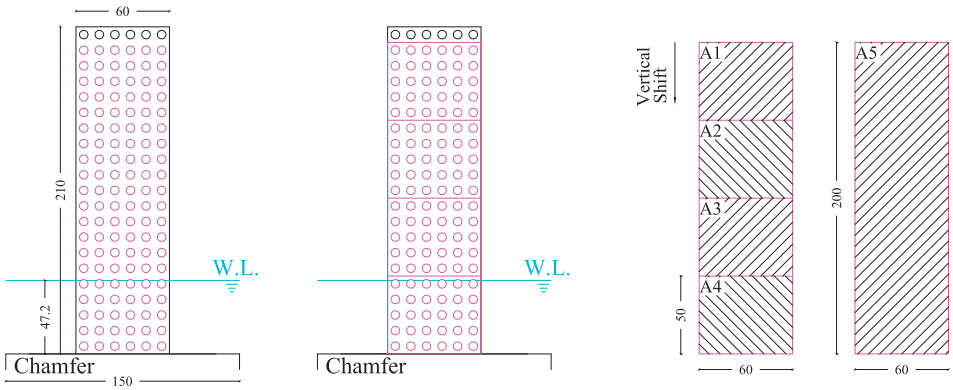

Fig. 6.2. The sensor module at scale 1:20, water level and the defined areas utilized in post-processing

All the pressure sensors sampled at 40 kHz. During the tests, the pressure measurement system was being activated with the definition of a pressure threshold which triggered the pressure measurement system. This pressure threshold was 0.16 bar throughout the campaign. In order to perform the post-processing on the measured loads 5 areas were defined on the module. The areas are shown in Fig. 6.2. The defined areas of A1-A4 had surface areas of 3000 mm^2 at scale 1:20 corresponding to 1 m $\times$ 1.2 m at full-scale equivalent of the NO96 panel size. A5 had the size of 12000 mm^2 at scale 1:20. Smaller areas are specially of interest in sloshing studies but were not introduced in this study to focus on defining the essential parameters rather than practical applications. Nevertheless conclusions drawn in this work can be extended to smaller areas as well. Smaller subareas reflect the more local phenomena even though the pressure sensors themselves, as the smallest available sensors, represent the most local measurements available. The largest subarea gives an idea about the global loadings during sloshing impacts. Local phenomena are masked and not represented in the pressure signals calculated on the larger areas.

For a complete account of model test, equipment and the taken measures to

ensure repeatability and proper test conditions see Karimi et al. [2015b], Karimi et al. [2016] and Karimi et al. [2017] with totally similar procedures.

6.3 The Target ID for Singularization

Although it was possible to try to singularize any selected sloshing impact (impact ID), a dominant ID was chosen for this purpose. It should be mentioned that the choice of a dominant ID was not fundamentally necessary and the results are meant to be generalized for any random impact ID. In Karimi et al. [Submitted to EJMBF in 2017a] 17 dominant IDs are mentioned and studied. Out of those 17 dominant IDs, ID 3624 (the same numbering is used by Karimi et al. [Submitted to EJMBF in 2017a]) was chosen to be singularized in this study. The choice of this ID was because,

- It was a dominant ID. The dominant IDs were responsible for generating the most severe impacts of sloshing model tests as reported in Karimi et al. [2017] and Karimi et al. [Submitted to EJMBF in 2017a]. Since in sloshing assessment methodologies, severe impacts are of importance, dominant IDs are naturally more interesting to study,

- It matched with the ID that was singularized at scale 1:40 and was introduced in Karimi et al. [2015a]. This was important for further scaling verifications,

- Its unique geometry particularly in the crest region made it a good target as the shape represented lots of small details that could help during comparison of the videos and specially for the detection of the target geometry.

The geometry of the chosen ID as well as the induced loads by that ID were targets of the singularization process and had to be generated using only short sequences of tank motions.

The shape of each ID in sloshing model tests is variable. This has been reported and partially studied by Karimi et al. [2017] and Karimi et al. [Submitted to EJMBF in 2017a]. The selected ID is no exception. The variability associated with the shape of this ID as recorded in different repetitions of irregular tests is demonstrated by Fig. 6.3 using 6 video recordings made by a high-speed camera. Each image corresponds to the same ID but in a different long sloshing model test. By the selection of these images for this ID, cases where the impact pressures were mild, moderate or rather high are shown. For each ID, the images are chosen so that the wave troughs are at the same level enabling the comparison of the wave fronts in a more representative manner.

From the images (and based on more recordings), a typical shape (a most probable shape) of the impact specially at the crest level characterized by a tongue of liquid forming a near double-crest can be seen. A small gas pocket is entrapped in almost all of the observed repetitions. The most probable shape of the chosen ID found from irregular tests was meant to be regenerated by singularization using short irregular tank motions. The impact shape was not the only feature that had to be regenerated.

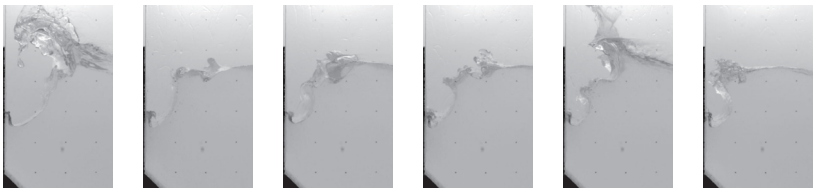

Fig. 6.3. Variation of impact geometry and conditions for the target ID found from 6 different irregular tests

Variations in impact shape and kinematics lead to variations of maximum induced loads. Fortunately those loads are not random. The loads generated by each ID was shown to have a unique governing distribution as shown in Karimi et al. [Submitted to EJMBF in 2017a]. Those distributions can be found by repeating the model tests multiple times. Those loads found based from 296 repetitions of irregular tank motions, ID 3624 and on the subarea A5 are shown in Fig. 6.4. Two variable log-normal distribution has been fitted to the data.

The ID generated by singularization had to also show the same pressure peak distribution on any loaded area. As shown by Karimi et al. [2015a], a short sequence of tank motions right before the moment of the chosen impact was enough to generate the similar impact geometry. In that study the distribution of the pressure peaks generated by singularization and by irregular waves were not compared which is the topic of the current study. The study started with determining or rather estimating the duration of the time trace of tank motions before the moment of the impact which was long enough for singularization.

6.4 Motion Signal Trimming

The duration of tank motions before the moment of impact that was long enough to generate the right geometry, kinematics and consequently same loads was indicated by m_e or effective memory. This effective memory was a duration in time before the moment of impact. The tank motions during the effective memory

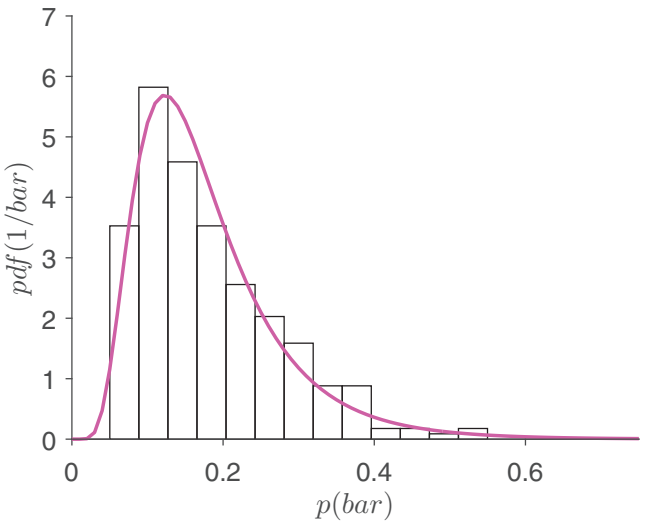

Fig. 6.4. The *probability density functions(pdf)* of the pressure peaks on subarea A5 corresponding to the target ID found from 296 repetitions of long irregular tests.

were the only tank motions before the moment of the target impact which were needed to generate that impact. In other words at the moment of impact, there was no memory of tank motions or the sources of variability before this duration. All the phenomena that could affect or influence the impact that had occurred before this duration, have been damped out or overcome by stronger phenomena by the impact time. The singularization could be summarized in finding the correct value or range of m_e. In other words this value was the most important unknown in the process that had to be determined.

In order to start the process the motion signals had to be trimmed near the moment of the target ID and mainly before it to estimate the unknown m_e. Before determining the m_e and since the duration was unknown, d was used to indicate the variable durations of singularization which were covered in order to find the right m_e.

A trimming process as used in this study is illustrated by Fig. 6.5 using the heave motion signal and with an assumed $d = 20s$. The motions start from the rest and the transmission to the trimmed part of the real motion signal was done using a ramp which guaranteed the smooth transition between the two parts and ensures the continuity of acceleration, velocity and displacement. The duration of 3s for this ramp proved to be enough. The trimmed part of the real signal

from irregular tank motions which was used had the duration d that was varied. The target impact was supposed to happen at the end of this trimmed part. The trimmed signal continued 1 s after the moment of the target ID, followed by another 3 s of ramp which again made a smooth transition to zero motions. The same procedure was repeated for 3 DOF motions of sway, heave and roll which summarized the motion signals to generate the target ID.

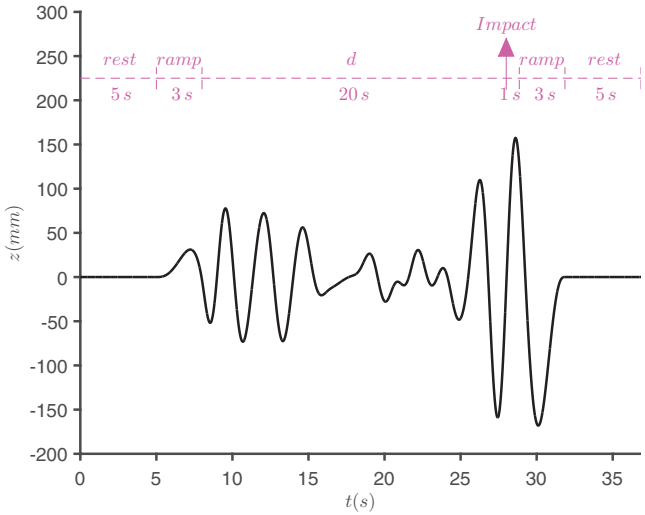

Fig. 6.5. Composition of the heave motion signal for generating the target ID. The real signal part has been trimmed from the long heave motions signal corresponding to irregular test which is in this case 20 s. The adequate length of the real signal before the impact time, m_e, was not known in the beginning and had to be determined by adjusting the variable d

The only clue about m_e came from Karimi et al. [2015a] which was done for the same ID but at scale 1:40 where a duration of at least 15 s was shown to enough to at least match the geometry and kinematics of the ID as far as the visual comparison was concerned. The value at scale 1:20 was thought to be roughly equal to $\sqrt{2}\times$ 15 s or 21 s.

As it was mentioned before m_e was unknown and had to be determined and in order to do so, short signals with variable durations of d had to be tested in order to find the acceptable range of d where $d \approx m_e$. This value of d had to give the right wave shape as well as the right statistics for the wave loads. The first requirement could be checked visually. However the second requirement could only be verified using many repetitions of the same impact which were needed to

build up a statistical sample which could then be compared with the statistical sample obtained from the target ID's loads measured from irregular model tests.

In order to save time in this process, it was decided to start with reasonably short durations of d, increase it incrementally and perform only a few repetitions for each duration in order to approach the target wave shape. For the durations which would give wave shapes similar to the target wave shape more repetitions were done in order to check the statistics as well. It should be noted that for small values of d, or basically for $d < m_e$ the duration of pause between the tests (d_p) was also influential.

6.5 Matching the Target ID Shapes

The shortest verified duration for d was 5 s which was then increased with 5 s increments up to 20 s followed by 30 s and 45 s. There was a pause of $d_p = 60s$ between consecutive tests of any duration. With very short durations of d (shorter than 5 s) not only the wave shape did not match with the target shape, the generated impact did not occur exactly at the expected time either. Increasing the duration of the trimmed signals led to the gradual evolution of breaking wave shapes towards the target shape. This gradual evolution right before the moment of impact is shown in Fig. 6.6. For the durations of 30 s and more the wave shape was similar to what was expected based on the target wave shape shown in Fig. 6.3.

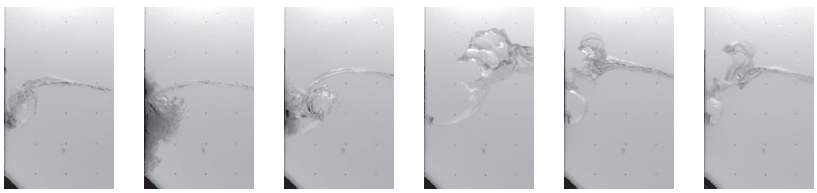

Fig. 6.6. Evolution of the breaking wave shape by increasing the estimated d from 5 s to 45 s. At around $d = 30$ s, the impact shape becomes similar to the target impact shape. The pause length between consecutive tests each test was 60 s

Regarding Fig. 6.6 it has to be noted again that the shape associated with each impact is variable (not random) but there is a most probable shape associated with each impact. It was this most probable shape that was used in the comparison.

Even though with the mentioned durations, breaking wave shapes were reasonably similar to the target wave shape, it was not clear at first whether the

durations of 30 s and more were in fact long enough to give the statistical properties similar to the target distribution but this first step gave an idea about the range of d and durations that had to be repeated at the next step to compare the statistical distributions of the generated impacts. At the end of the first step it was concluded that roughly $m_e \geq 30s$ and consequently tests with d of more than 30 s were repeated several times. The values of d which were repeated included 30s, 45s, 60s, 90s, 95s, 100s, 105s and 110s.

As it was mentioned before for tests in which $d < m_e$, the duration of pause between consecutive tests would become important. As a result and for smaller values of d, two pause durations of 60 s and 240 s were tested. Clearly one preliminary criterion to decide whether a duration of d was long enough or not was whether the pause duration was affecting the statistics or not.

6.6 Matching the Target ID Statistics

At first by varying the pause duration (between consecutive tests) for $d = 30s$ and $d = 60s$, the sensitivity of the statistics to the pause duration was tested. For $d \geq m_e$ it was expected that the pause duration would not influence the statistics. Naturally for $d < m_e$ the pause duration was expected to be important. All the statistical comparisons at this stage and later were done with respect to the statistical sample of pressure peaks on subarea A5 found for the same ID and from 296 repetitions of irregular tests. For all the samples, the empirical distribution functions or EDF were found and compared using the two sample K-S test with $\alpha = 5$.

At first it was tested whether the $d = 30s$ was a good estimation of m_e or not. Fig. 6.7 shows the EDFs of pressure peaks on A5 found with the duration of 30s and two pauses of 60 s and 240 s compared with the reference EDF found from repetitions of irregular tests. The pressure peak sample size with the pause of 60 s was 205 whereas the sample size with the pause of 240 s was 176. Using two sample K-S test with $\alpha = 5$ it was shown that the similarity between the distributions could be ruled out. This was an indication that in fact $m_e > 30s$ since different lengths of pause d_p had a clear influence on the statistics. Furthermore even with a long duration of d_p there was a clear discrepancy between the EDFs found from irregular tests and singularization tests.

A similar comparison with $d = 60s$, $d_p = 60s$ and $d_p = 240s$ was also performed. The comparison was also done on subarea A5. The pressure peak sample size with the pause of 60 s was 192 whereas the sample size with the pause of 240 s was 393. The EDFs of both samples were found and compared with EDF of the pressure peak samples on subarea A5 found from 296 irregular tests as shown in Fig. 6.8. The comparison was based on the two sample K-S test with $\alpha = 5$ and showed that the similarity of both statistical samples found from singularization

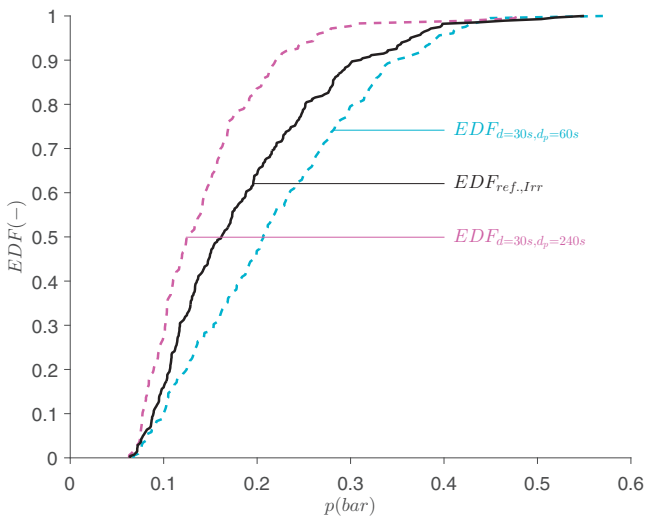

Fig. 6.7. The EDFs of the target ID on A5 found from 296 irregular tests and two singularizations with the estimation of $d = 30\,s$ and two different pause durations (between the consecutive singularizations) of 60 s and 240 s. The adopted $d = 30\,s$ was not enough and was too short. The duration of the pause between repetitions of short tests had an influence on the statistics of the pressure peak samples on A5.

tests had the sample found from irregular tests could not be ruled out. Furthermore the comparison confirmed that the duration of the pause had no influence on the statistics. In other words it was concluded that $30s < m_e \leq 60s$. Also it was clear that m_e could also be found more accurately. For the rest of the tests the duration of $d_p = 60s$ was adopted until the end.

For the values of d between 45 s and 110 s all with $d_p = 60s$ and on A5, similar comparisons were done between the samples of peak pressures found from singularization tests and irregular tests as summarized in Fig. 6.9. The pressure peak sample sizes for the repetitions with d of 45, 60, 90, 95, 100, 105 and 110 s were 194, 192, 391, 190, 190, 188 and 77 respectively. Using two sample K-S tests with $\alpha = 5$ it was observed that all the EDF were similar with each other as well as with the reference EDF. This suggested that a more accurate estimation of m_e was $30s < m_e \leq 45s$. Longer values of d were proved to be enough but unnecessary.

The previous comparisons were performed based on the pressure peaks found on subarea A5 which was the largest possible subarea according to the sensor

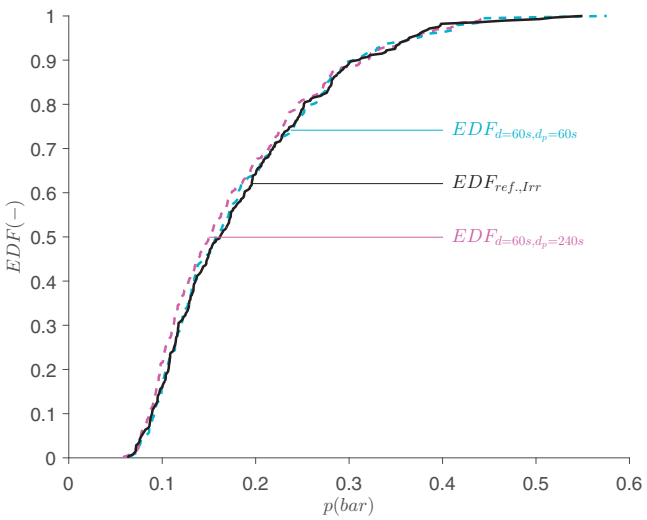

Fig. 6.8. The EDFs of the target ID on A5 found from 296 irregular tests and two singularizations with the estimation of $d = 60\,s$ and two different pause durations (between the consecutive singularizations) of 60 s and 240 s. The estimation of $d = 60s$ was larger than m_e. The duration of the pause between repetitions of tests with $d = 60s$ had no influence on the statistics of the pressure peak samples on A5.

module layout. In order to confirm the same finding on smaller subareas, two sample K-S test with $\alpha = 5$ was performed for different d, all with a pause of $d_p = 60s$ and for all the defined areas of A1-A5 as summarized in Table 6.1. The results were coherent with the previous observations with the exception on A3 and with $d = 90s$.

It is in fact shown that the chosen dominant ID could be regenerated with short sequences of tank motions rather than the whole history of long irregular tank motions. This was achieved by respecting only a short duration of tank motions right before the moment of the target impact (ID) that was called the effective memory or m_e of that impact. It was also shown that the range for the value of m_e could be found. The impact generated using this technique was shown to have similar kinematics and geometry with respect to the target ID which led to the same load distribution as found from irregular test.

It should be noted that this process could have been done for any impact ID and for any impacted area. However the duration of m_e could be slightly different for different IDs and different areas. As a rule, it can be said that

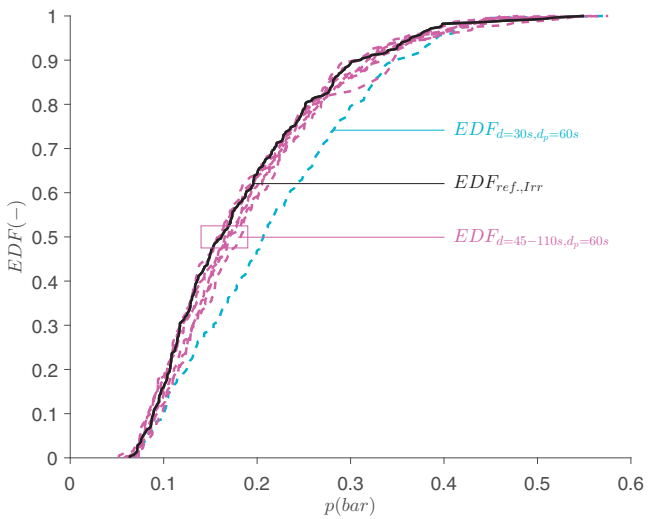

Fig. 6.9. The EDFs of the target ID on A5 found from 296 irregular tests and several singularizations with the estimation of d from 30 s to 110. Increasing the duration from 45 s up to 110 s did not change the EDF. The effective memory had to be $30s < m_e \leq 45s$. The d_p between all the tests was 60 s. The similarity of empirical distribution functions was verified with the two sample K-S test

d (s)	A1	A2	A3	A4	A5
30	1	0	0	0	0
45	1	1	1	1	1
60	1	1	1	1	1
90	1	1	0	1	1
95	1	1	1	1	1
100	1	1	1	1	1
105	1	1	1	1	1
110	1	1	1	1	1

Table 6.1. The result of the two sample K-S test between the reference edfs and edfs fround for different d with a pause of 60 s and for all the defined areas of A1-A5 corresponding to the target ID. 1 indicates matching distributions.

larger areas would be less sensitive to this duration whereas the smaller impacted areas, specially the ones which are subject to highly variable loads would be more

sensitive and would need longer durations of m_e thus reflecting the variabilities associated with global or local phenomena.

6.7 Comparison of the Same ID at Scales 1:20 and 1:40

Karimi et al. [2015a] described the process for singularization of a chosen impact ID at scale 1:40. In that study, the singularization was based on the visual comparison of the wave shapes generated by singularization with the most probable wave shape generated in irregular tests. The statistical comparison of pressure peak samples was not performed due to the lack of enough repetitions of irregular sloshing tests. However the adopted estimation of m_e for 2000 singularization tests was rather conservative in order to be able to trust the measured loads for later comparisons. Although d of about 15 s gave a good visual match of the singularized wave shapes, a d of 30 s was used for singularization tests. At scale 1:40 2000 repetitions of the singularization tests were performed to create a large sample. This sample would be the basis for the comparisons presented in this section.

The chosen ID at scale 1:40 corresponded to the impact ID at scale 1:20 which was introduced and singularizaed in this study. This match was the basis for the comparison of the same ID at different scales. The aim was to observe the change of breaking wave shape and impact as well as the statistical properties of the pressure peak samples from one scale to the other and for the same ID. It should be noted that this comparison could have been done without using singularization and only based on many repetitions of irregular tests, tracking down the corresponding IDs, building the statistical samples of loads on the corresponding areas for the corresponding IDs and then comparing the statistical samples. However repetitions of irregular tests would take a long time and at the time of preparation of this study, enough repetitions of irregular tests at scale 1:40 were not yet available. Nevertheless it was shown previously that the samples found from singularization tests could be trusted to be quite representative given that certain requirements are fulfilled.

The model tests at scale 1:40 were performed with 60 sensors arranged in a 15×4 array of PCB sensors similar to the sensors that were used at scale 1:20. All the properties of the sensors, sensor sizes and the vertical and horizontal spaces between the sensors as well as the acquisition frequencies were identical to those of the model test at scale 1:20 and will not be repeated here. The sensor module at scale 1:40 is shown in Fig. 6.10 next to the sensor module at scale 1:20. The sensor module at scale 1:40 can be scaled and superimposed on the module at scale 1:20. The subareas of A1-A5 can be identified on both modules. The loads

on those common areas could be compared for the chosen ID at scales 1:20 and 1:40.

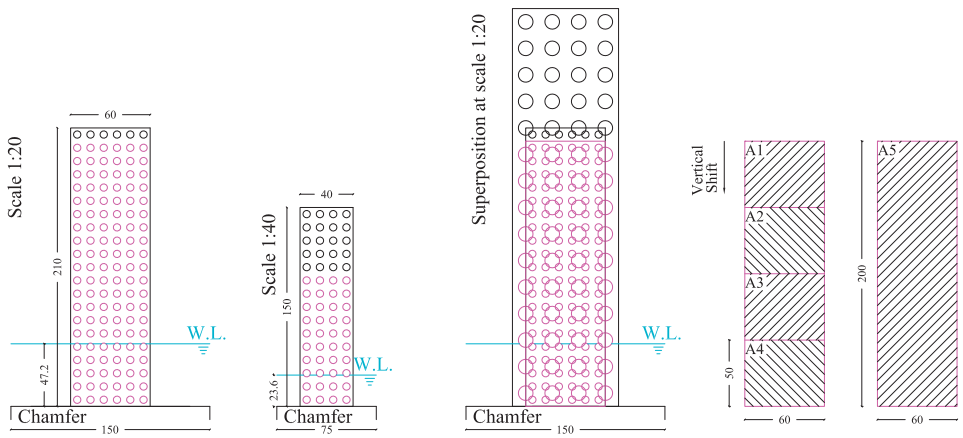

Fig. 6.10. The sensor modules at scale 1:20 and 1:40, water level and the defined common subareas. The dimensions are in mm

All of the 2000 singularization repetitions at scale 1:40 were done with $d = 30s$. This duration is thought to be enough by considering the m_e at scale 1:20. The m_e at scale 1:20 was found to be in the following range, $30s \leq m_e \leq 45s$. An estimation of the adequate m_e at scale 1:40 would be found by scaling the previous range by $\sqrt{2}$ which would give a new range at scale 1:40 as $21.2s \leq m_e \leq 31.8s$. Thus the choice of $d = 30s$ is considered to be adequate.

The 2000 singularization tests With $d = 30s$ at scale 1:40 generated a large sample of pressure peaks and high-speed video recordings. A selection of 6 high-speed video recordings at scale 1:40 is shown in Fig. 6.11. These images shown that again a typical wave shape is repeated for the same ID at scale 1:40. The comparison of these images with the corresponding ones at scale 1:20 (see Fig. 6.3) showed that the typical wave shapes for the same ID at two different scales are quite similar. The entrapment of a small gas pocket is also observed at scale 1:40. The small tongue of liquid at the crest location is also seen at scale 1:40. Free surface instabilities are much less and almost do not exist at the smaller

scale.

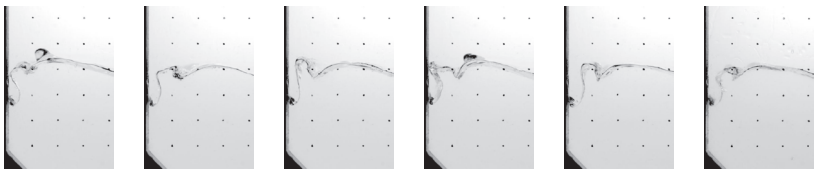

Fig. 6.11. Variation of impact geometry and conditions for the target ID found from 6 different singularization tests at scale 1:40

As observed at scale 1:20, wave shapes are also variable for the same ID at scale 1:40. This variability of breaking wave shapes was reflected in the measured loads and led to a distribution of pressure peaks that could be captured well with 2000 repetitions of singularization tests. The samples of pressure peaks on A1-A5 corresponding to the target ID at scale 1:40 were compared with the corresponding pressure peak samples found on the same subareas, for the same ID at scale 1:20.

As mentioned before the comparison of impact loads corresponding to the singularized ID on the common subareas of A1-A5 at scales 1:20 and 1:40 was done statistically. The sample size at scale 1:40 was 2000 corresponding to $m_e = 30s$. At scale 1:20 the sample size was 192 corresponding to $m_e = 60s$. At first the probability density functions of the impact loads found based on normalized histograms (probability density functions) were compared as shown in Fig. 6.12. The comparison of probability density functions is done on the common subareas A1-A5, before and after scaling the pressure peaks at scale 1:40 with the scale factor 2.

Before scaling the pressure peaks at scale 1:40 it can be seen that the most probable values for pressures are quite close despite the scale difference. This is true on all 5 subareas. The probability of more severe pressures are still higher at scale 1:20. After multiplying the pressures at scale 1:40 with the factor 2, the most probable pressure based on the results at the smaller scaler of 1:40 clearly shift towards more severe values. The probability density functions based on the scaled pressure peaks at scale 1:40 also show a higher probability for more severe pressures. This implies a conservatism regarding the model test results scaling based on the geometric scale.

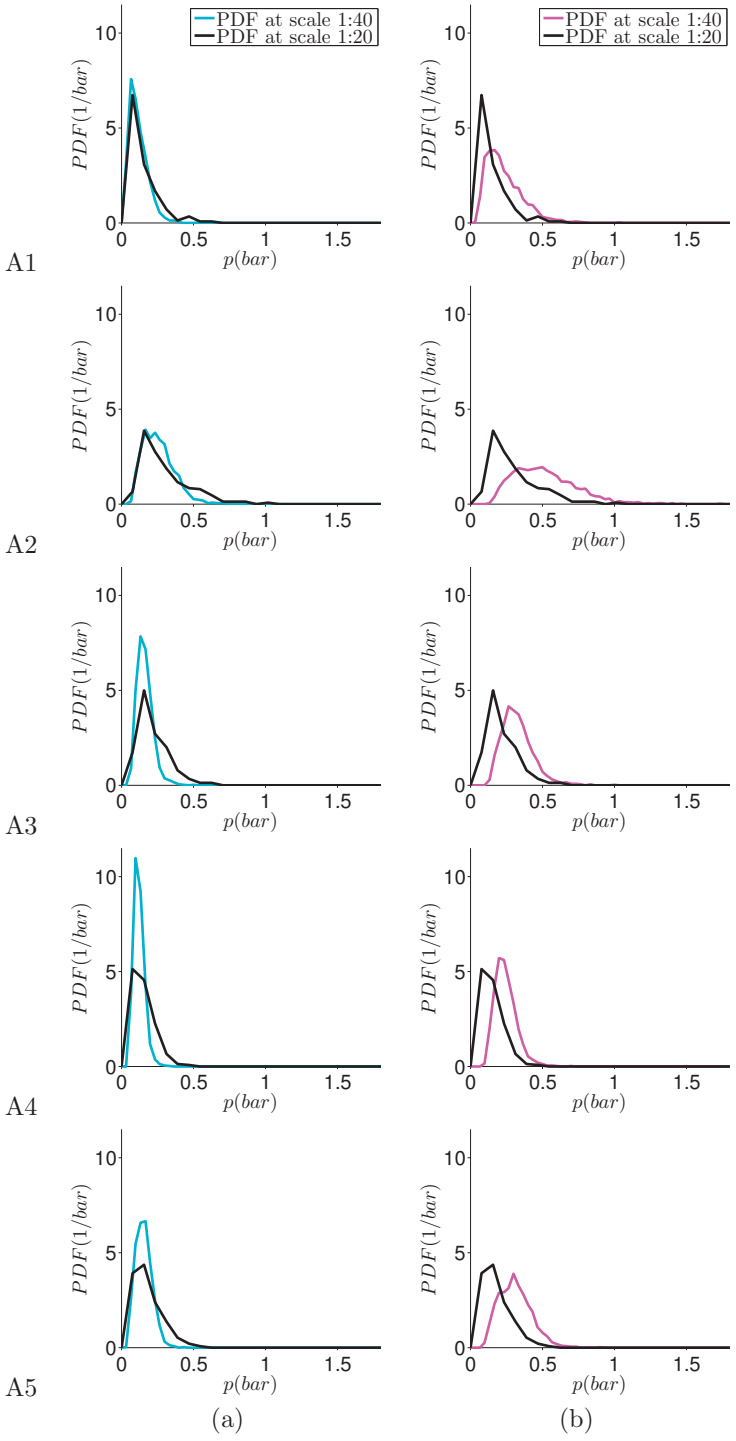

Fig. 6.12. Probability density functions of pressure peaks corresponding to the target ID at scales 1:20 and 1:40 (a) pressures at scale 1:40 have not been scaled (b) pressures at scale 1:40 have been scaled by the factor 2

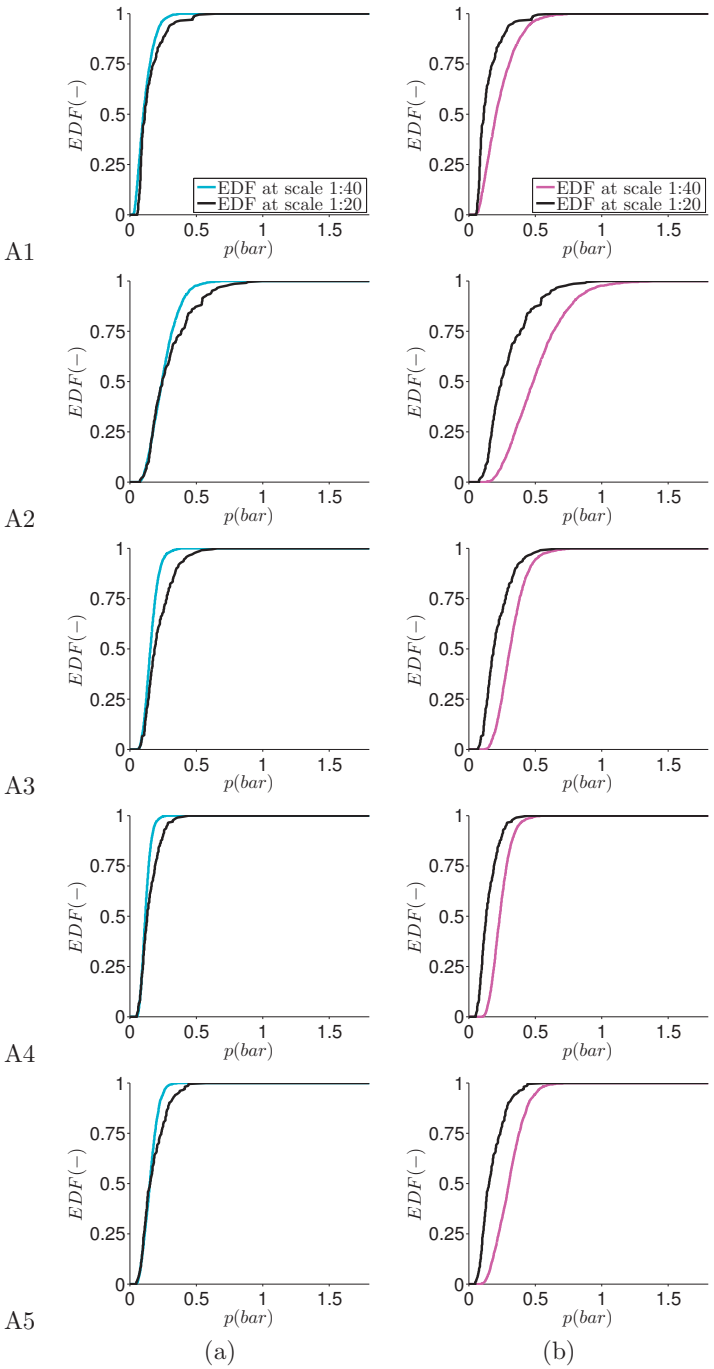

Fig. 6.13. Empirical distribution functions (EDFs) of pressure peaks corresponding to the target ID at scales 1:20 and 1:40 (a) pressures at scale 1:40 have not been scaled (b) pressures at scale 1:40 have been scaled by the factor 2

Fig. 6.13 compares the EDFs of the pressure peaks on the common subareas of A1-A5 before and after scaling the pressure peaks at scale 1:40 by the factor 2. It can be observed that for different levels of probability (different percentiles) and after scaling the loads at scale 1:40, the predicted load levels at scale 1:40 are higher than those measured at scale 1:20. This could imply a sort of conservatism in model test results. It can also be seen that after scaling the loads, the load distribution found from the model test is not totally representative of the load distribution at scale 1:20.

Based on Fig. 6.12 and 6.13 and considering the maximum loads of the same impact ID at two different scales of 1:20 and 1:40 and the five common subareas of A1-A5 it can be said that the distributions of pressure peaks are different at two different scales. This is to say that the impact loads generated by the tests at a smaller scale are not representative of the impact loads of the same impact at the larger scale. This does not come as a surprise since several biases in scaling the physical properties of gas and liquid exist. Yet when the pressure peaks found at the smaller scale were scaled with the geometric scale factor of 2, the resultant distributions proved to be conservative. This was only investigated for one impact ID but it should be kept in mind that the studied impact ID was a dominant ID.

It should be mentioned that the observed conservatism was established after mastering the governing distributions of the impact loads. Those distributions were found by many measurements of the sloshing loads at two different scales corresponding to the same ID. This means that not every repetition at the smaller scale would give conservative results after being scaled by the geometric scale. There is a probability associated with such conservatism for each repetition that can be found based on the observed distributions.

Considering the given distributions a probability can be defined as,

$$\int_0^{+\infty} (\int_0^p PDF_{20}(p)dp) PDF_{40}(p)dp \tag{6.1}$$

Which can be simplified as,

$$\int_0^{+\infty} EDF_{20}(p) PDF_{40}(p)dp \tag{6.2}$$

Which represents the reliability of the conservatism of a sloshing model test result considering one impact ID. In the definition of the probability density function for the results at model scale, the used scale factor should be considered.

6.8 Conclusions

The present study showed that the singularization technique for any given impact ID that was introduced by Karimi et al. [2015a] for the first time is an efficient tool for collecting a large sample of pressure peaks in a short time corresponding to that impact ID. The collected sample was shown to be statistically equivalent to the reference sample of pressure peaks for the same impact ID collected from many repetitions of the corresponding long irregular test. A parametric study was performed at scale 1:20 for a selected impact ID by performing singularization tests of progressively increasing durations d with many repetitions of each singularization test. The duration d indicated the duration of the trimmed part of the original long tank motions (in 3DOF in this study) right before the moment of the selected impact ID that was used in singularization tests. The results showed that for any given impact ID, at each scale and on each loaded area, it is possible to define a duration called the effective memory or m_e so that for any duration $d \geq m_e$:

- The most probable wave shape for the singularized impact ID look the same as the most probable shaped of the same impact ID obtained from long irregular tests,

- The samples of pressure peaks of the selected impact ID obtained from the singularization tests are statistically equivalent to the reference sample obtained for the same ID from long irregular tests.

Furthermore it was shown that tank motions or other sources of variability that occur before this duration d of the singularization tests influences the wave shape and its statistics as long as $d < m_e$ but has no or negligible influence for $d \geq m_e$. It is therefore relevant to consider this duration m_e as a memory. The range of $30s < m_e \leq 45s$ was shown to be enough for the impact ID studied at scale 1:20. The duration of m_e could vary depending on the type of impact, scale, size of the loaded area, location of the loaded area and the properties of ullage gas and liquid. This new tool will allow different applications that could change the way of performing a sloshing assessment:

- A first application has already been illustrated in the paper. It consists of comparing statistical empirical distributions of pressure peaks for selected impact IDs at different scales. This enables to directly study not only the bias that would induce a direct scaling based on dimensional analysis on the pressures at a given probability level of occurrence but also the bias on the direct scaling of pressure variability. For the impact IDs studied so far at both scales, it turns out that at each probability level the direct scaling

is conservative but the authors do not believe that this is a general law. More cases in more varied conditions are to be studied.,

- Combined with the notion of dominant impact IDs developed in Karimi et al. [Submitted to EJMBF in 2017a], the singularization technique will enable to regenerate the tail of the long term empirical distribution of pressure peaks by first identifying the dominant impacts and then quickly generating the relevant statistical samples of the tail by using the singularization technique in order to reach directly the right level of probability for design purposes without using uncertain extrapolations by a best fitted statistical law. For each sloshing test condition only the short sequences of singularization tests for the dominant impact IDs have to be repeated as many times as necessary. The main difficulty lies in the quick but relevant selection of the dominant impact IDs for each condition,
- It can be used to tune the numerical modes with thousands of more realistic waves that can and must be simulated with short sequences of tank motions,
- Singularization will help identify damping effects in sloshing model tests,
- It appears that only a short duration of tank motions determine the impact types and their severity. This gives an indication on the required sensitivity of sloshing prediction tools,
- Finally, the singularization technique will also help analyse the correlation between tank motions and impact pressures.

  Later studies which were conducted in the course of the publication of this paper at 20% fill level and 2D tanks at two scales of 1:40 and 1:20 showed that the technique works for different IDs and ullage gases and even loaded areas as small as the pressure sensors. Furthermore the singularization technique has also been used successfully for 3D tests with different tanks and different fill levels including high fills (see Frihat et al. [2016] and Brosset [2016]).

Bibliography

H. N. Abramson. The Dynamic Behavior of Liquids in Moving Containers, with Applications to Space Vehicle Technology. Technical Report NASA-SP-106, NASA, Jan 1966.

American Bureau of Shipping ABS. Strength Assessment of Membrane-type LNG Containment Systems under Sloshing Loads. Guidance notes, American Bureau of Shipping, February 2014.

Y. Ahn, S. Y. Kim, K. H. Kim, S. W. Lee, Y. Kim, and J. J. Park. Study on the Effect of Density Ratio of Liquid and Gas in Sloshing Experiment. In *Proceedings of the Twenty-second International Offshore and Polar Engineering Conference*, volume 3, pages 311 – 317, 2012.

H. Bogaert, L. Brosset, and M. L. Kaminski. Interaction Between Wave Impacts and Corrugations of Markiii Containment System for LNG Carriers: Findings from the Sloshel Project. In *Proceedings of the Twentieth International Offshore and Polar Engineering Conference*, volume 3, pages 109 – 118, 2010a.

H. Bogaert, S. Léonard, L. Brosset, and M. L. Kaminski. Sloshing and Scaling : Results from the Sloshel Project. In *Proceedings of the Twentieth International Offshore and Polar Engineering Conference*, volume 3, pages 88 – 97, 2010b.

J. P. Braeunig, L. Brosset, F. Dias, and J. M. Ghidaglia. Phenomenological Study of Liquid Impacts Through 2D Compressible Two-fluid Numerical Simulations. In *Proceedings of the Nineteenth International Offshore and Polar Engineering Conference*, volume 3, pages 21 – 29, 2009.

H. Bredmose, D.H. Peregrine, and G.N. Bullock. Violent Breaking Wave Impacts. Part 2: Modeling the Effect of Air. *Journal of Fluid Mechanics*, 641:389 –430, 2009.

L. Brosset. Official discussion to the report of Committee v.2 - Natural Gas Storage and Transportation. Proc. of the 19th Intl. Ship and Offshore Structures Congress (ISSC), 2016.

L. Brosset, Z. Mravak, M.L. Kaminski, S. Collins, and T. Finnigan. Overview of Sloshel Project. In *Proceedings of the nineteenth International Offshore and Polar Engineering Conference*, pages 115 – 124, 2009.

Bureau Veritas BV. Design Sloshing Loads for LNG Membrane Tanks. Guidance Note NI 554 DT R00 E, Bureau Veritas, May 2011.

M.J. Cooker and D.H.Peregrine. Violent Water Motion at Breaking-Wave Impact. *Coastal Engineering Proceedings*, 1(22), 1990.

J. Costes, J.-M. Ghidaglia, and A.A. Mrabet. On the Simulation of Liquid Impacts on a Flat Rigid Wall by a 2D Parallel Finite Volume Solver. In *Proceedings of the Twenty-fourth International Offshore and Polar Engineering Conference*, pages 246 – 256, 2014.

F. Dias, J. M. Ghidaglia, and G. Le Coq. On the Fluid Dynamics Models for Sloshing. In *Proceedings of the Seventeenth International Offshore and Polar Engineering Conference*, volume 3, pages 1080 – 1088, 2007.

Det Norske Veritas DNV. Sloshing Analysis of LNG Membrane Tanks. Classification Notes No. 30.9, Det Norske Veritas, August 2014.

P. G. Drazin and W. H. Reid. *Hydrodynamic Stability*. Cambridge University Press, 2004.

O.M. Faltinsen and A.N. Timokha. *Sloshing*. Cambridge University Press, 2014.

M. Frihat, M.R. Karimi, L. Brosset, and J.-M. Ghidaglia. Variability of Impact Pressures Induced by Sloshing Investigated Through the Concept of Singularization. In *Proc. of the 26th Int. Offshore and Polar Eng. Conf. (ISOPE), Rhodes, Greece*, 2016.

E. Gervaise, P. E. De Sèze, and S. Maillard. Reliability-Based Methodology for Sloshing Assessment of Membrane LNG vessels. *International Journal of Offshore and Polar Engineering*, 19(4):254 – 263, 2009.

P. M. Guilcher, L. Brosset, N. Couty, and D. Le Touzé. Simulations of Breaking Wave Impacts on a Rigid Wall at Two Different Scales with a Two Phase Fluid Compressible SPH Model. In *Proceedings of the Twenty-second International Offshore and Polar Engineering Conference*, volume 3, pages 460 – 472, 2012.

P. M. Guilcher, L. Brosset, N. Couty, and D. Le Touzé. Simulations of Breaking Wave Impacts on a Rigid Wall at Two Different Scales with a Two Phase Fluid Compressible SPH Model. *Int. Journal of Offshore and Polar Eng.*, 23(4):241 – 253, 2013.

P. M. Guilcher, Y. Jus, N. Couty, L. Brosset, Y.M. Scolan, and D. Le Touzé. 2D Simulations of Breaking Wave Impacts on a Flat Rigid Wall. Part 1: Influence of the Wave Shape. In *Proceedings of the Twenty-Fourth International Offshore and Polar Engineering Conference*, volume 3, pages 232 – 245, 2014.

M.L. Kaminski and H. Bogaert. Full-Scale Sloshing Impact Tests-Part I. *International Journal of Offshore and Polar Engineering*, 20(1):24, 2010.

M. R. Karimi and L. Brosset. Global and Local Effects of Gas-Liquid Density Ratio on Shape and Kinematics of Sloshing Waves and Scaling Considerations. In *Proceedings of the Twenty-ninth International Workshop on Water Waves and Floating Bodies*, pages 97 – 100, 2014.

M. R. Karimi, C. Kosinski, and L. Brosset. Comparison of Sloshing Model Test Results at Scales 1:10 and 1:40. In *Proceedings of the Twenty-third International Offshore and Polar Engineering Conference*, volume 3, pages 224 – 234, 2013a.

M. R. Karimi, L. Brosset, J.-M. Ghidaglia, and M. L. Kaminski. A Study on Conservatism of Froude Scaling for Sloshing Model Tests. In *Proceedings of the Twenty-Fourth International Offshore and Polar Engineering Conference*, volume 3, pages 306 – 313, 2014a.

M. R. Karimi, L. Brosset, J.-M. Ghidaglia, and M. L. Kaminski. Singularization of Sloshing Impacts. In *Proceedings of the Thirtieth International Workshop on Water Waves and Floating Bodies*, 2015a.

M. R. Karimi, L. Brosset, J.-M. Ghidaglia, and M. L. Kaminski. Effect of Ullage Gas on Sloshing - Part I. Global Effects of Gas-Liquid Density Ratio. *European Journal of Mechanics B/Fluids*, 53:213 – 228, 2015b. doi: 10.1016/j.euromechflu.2015.05.006.

M. R. Karimi, L. Brosset, J.-M. Ghidaglia, and M. L. Kaminski. Effect of Ullage Gas on Sloshing - Part II. Local Effects of Gas-Liquid Density Ratio. *European Journal of Mechanics B/Fluids*, 57:82 – 100, 2016. doi: 10.1016/j.euromechflu.2015.11.011.

M. R. Karimi, L. Brosset, M.L. Kaminski, and J.-M. Ghidaglia. Effects of ullage gas and scale on sloshing loads. *European Journal of Mechanics B/Fluids*, 62: 59 – 85, 2017. doi: http://dx.doi.org/10.1016/j.euromechflu.2016.11.017.

M. R. Karimi, L. Brosset, M. L. Kaminski, and J.-M. Ghidaglia. Dominant Impacts in Sloshing Model Tests. *European Journal of Mechanics B/Fluids*, 0 (0):0, Submitted to EJMBF in 2017a.

M. R. Karimi, L. Brosset, M. L. Kaminski, and J.-M. Ghidaglia. Singularization of Sloshing Impacts. *European Journal of Mechanics B/Fluids*, 0(0):0, Submitted to EJMBF in 2017b.

M Reza Karimi, C Kosinski, L Brosset, et al. Comparison of sloshing model test results at scales 1: 10 and 1: 40. In *The Twenty-third International Offshore and Polar Engineering Conference*. International Society of Offshore and Polar Engineers, 2013b.

MR Karimi, L Brosset, J-M Ghidaglia, ML Kaminski, et al. A study on conservatism of froude scaling for sloshing model tests. In *The Twenty-fourth International Ocean and Polar Engineering Conference*. International Society of Offshore and Polar Engineers, 2014b.

O Kimmoun, A Ratouis, L Brosset, et al. Sloshing and scaling: experimental study in a wave canal at two different scales. In *The Twentieth International Offshore and Polar Engineering Conference*. International Society of Offshore and Polar Engineers, 2010.

J. F. Kuo, R. B. Campbell, Z. Ding, S. M. Hoie, A. J. Rinehart, R. E. Sandström, T. W. Yung, M. N. Greer, and M. A. Danaczko. LNG Tank Sloshing Assessment Methodology-the New Generation. *International Journal of Offshore and Polar Engineering*, 19(4):241 – 253, 2009.

W. Lafeber, L. Brosset, and H. Bogaert. Comparison of Wave Impact Tests at Large and Full Scale: Results from the Sloshel Project. In *Proceedings of the Twenty-second International Offshore and Polar Engineering Conference*, volume 3, pages 285 – 299, 2012a.

W. Lafeber, L. Brosset, and H. Bogaert. Elementary Loading Processes (ELP) involved in breaking wave impacts : Findings from the Sloshel project. In *Proceedings of the Twenty-second International Offshore and Polar Engineering Conference*, volume 3, pages 265 – 276, 2012b.

D. H. Lee, M. H. Kim, S. H. Kwon, J. W. Kim, and Y. B. Lee. A Parametric Sensitivity Study on LNG Tank Sloshing Loads by Numerical Simulations. *Ocean Engineering*, 34(1):3 – 9, 2007.

Lloyd's Register LR. Sloshing Assessment Guidance Document for Membrane Tank LNG Operations. Guidance Note version 2, Lloyd's Register, May 2009.

C. Lugni, M. Miozzi, M. Brocchini, and O. M. Faltinsen. Evolution of the air cavity during a depressurized wave impact. I. The kinematic flow field. *Physics of Fluids (1994-present)*, 22(5):056101, 2010.

Ø. Lund-Johansen, T. Østvold, C.-F. Berthon, and K. Pran. Full scale measurements of sloshing in LNG tanks. In *Proceedings of GASTECH Conference*, pages 21–24, 2011.

S. Maillard and L. Brosset. Influence of Density Ratio Between Liquid and Gas on Sloshing Model Test Results. *International Journal of Offshore and Polar Engineering*, 19(4):271 – 279, 2009.

R. Pasquier and C.-F. Berthon. Model Scale Test vs. Full Scale Measurement: Findings from the Full Scale Measurement of Sloshing Project. *Altamira*, 2010: 01–03, 2009.

R. Pasquier and C.-F.Berthon. Model Scale Test vs. Full Scale Measurement: Findings from the Full Scale Measurement of Sloshing Project. In *The Twenty-second International Offshore and Polar Engineering Conference*, volume 3, pages 277 – 284, 2012.

A. Rafiee, D. Dutykh, and F. Dias. Numerical Simulation of Wave Impact on a Rigid Wall Using a Two–Phase Compressible SPH Method. *Procedia IUTAM*, 18:123 – 137, 2015.

S. Schreier and B. Mehl. Experimental Investigation of 3D Sloshing Effects in Thin Rectangular Tanks. In *Proceedings of the Twenty-second International Offshore and Polar Engineering Conference*, volume 3, pages 433 – 439, 2012.

Y. M. Scolan. Some Aspects of the Flip-through Phenomenon: A Numerical Study Based on the Desingularized Technique. *Journal of Fluids and Structures*, 26:918 –953, 2010.

Y. M. Scolan, M. R. Karimi, F. Dias, J.-M. Ghidaglia, and J. Costes. Highly Nonlinear Wave in Tank with Small Density Ratio. In *Proceedings of the Twenty-ninth International Workshop on Water Waves and Floating Bodies*, pages 181 – 184, 2014.

T. W. Yung, Z. Ding, H. He, and R. E. Sandström. LNG Sloshing: Characteristics and Scaling Laws. *International Journal of Offshore and Polar Engineering*, 19(4):264, 2009.

T. W. Yung, R. E. Sandström, H. He, and M. K. Minta. On the Physics of Vapor/Liquid Interaction During Impact on Solids. *Journal of Ship Research*, 54(3):174 –183, 2010.